SYNTHESIS AND GAS SENSING PROPERTIES OF TRANSITION METAL DICHALCOGENIDES MATERIALS (TMDS)

Aanchal Alagh

DOCTORAL THESIS

Synthesis and Gas Sensing Properties of Transition Metal Dichalcogenides materials (TMDs)

PhD Thesis

Aanchal Alagh

Supervised by:

Dr. Fatima Ezahra Annanouch

and

Prof. Eduard Llobet Valero

Department of Electronic, Electrical and Automation Engineering

UNIVERSITAT ROVIRA i VIRGILI

Tarragona 2022

UNIVERSITAT ROVIRA i VIRGILI

FAIG CONSTAR que aquest treball, titulat “SYNTHESIS AND GAS SENSING PROPERTIES OF TRANSITION METAL DICHALCOGENIDE NANOMATERIALS”, que presenta Aanchal Alagh per a l’obtenció del títol de Doctor, ha estat realitzat sota la meva direcció al Departament d’Enginyeria Electrònica, Elèctrica i Automàtica d’ aquesta universitat.

HAGO CONSTAR que el presente trabajo, titulado “SYNTHESIS AND GAS SENSING PROPERTIES OF TRANSITION METAL DICHALCOGENIDE NANOMATERIALS”, que presenta Aanchal Alagh para la obtención del título de Doctor, ha sido realizado bajo mi dirección en el Departamento de Ingeniería Electrónica, Eléctrica i Automática de esta universidad.

I STATE that the present study, entitled “SYNTHESIS AND GAS SENSING PROPERTIES OF TRANSITION METAL DICHALCOGENIDE NANOMATERIALS”, presented by Aanchal Alagh for the award of the degree of Doctor, has been carried out under my supervision at the Department Electronic, Electric and Automation Engineering of this university.

Tarragona, 17th June, 2022

El/s director/s de la tesi doctoral

El/los director/es de la tesis doctoral

Doctoral Thesis Supervisor/s

Eduard Llobet Valero

Fatima Ezahra Annanouch

Acknowledgements

It is a pleasure to convey my thanks to all the people who have helped me throughout the amazing journey of my PhD.

First, I owe a deep debt of gratitude and thanks to my academic supervisor, Prof. Eduard Llobet Valero, for his constant support, guidance, and valuable scientific discussions. He always motivated me to think and work as an independent researcher. Besides that, I enjoyed an excellent working environment, in which they gave me direction, asking insightful questions and plenty of freedom to pursue my own ideas. Thank you for giving me an opportunity to work in such a wonderful research environment.

Further, I would like to express my deepest appreciation to my co-supervisor, Dr. Fatima Ezahra Annanouch for her constant support and motivation. Along with that I would also like to thank other Professors from my research group for their valuable scientific discussions during the group meetings, Dr. Xavier Vilanova, Dr. Alfonso Romero, Dr. Jose Luis.

I also very much appreciate the extensive support of collaborators especially, Dr. Carla Bittencourt from University of Mons in Belgium, who helped me with her expertise in XPS analysis. With her support I got an opportunity to conduct operando measurements in synchrotron facility in Barcelona. I would also like to thank other collaborators for helping me with their research expertise in different characterizations techniques, Dr. Polona Umek for HRTEM analysis, Dr. Frank Guell with Photoluminsecence spectroscopy and last but not the least Dr. Jean François Colomer.

I also want to convey my special thanks to Prof. Ludwig Bartels from the University of California, in the United States, for accepting me in his group to conduct my 3 months research secondment. I have learned a lot during those three months. Also, the group members have been very supportive throughout my stay. I would like to thank them all, Prachi, Xing and Hae-in.

I would also like to thank Mariana, Merce, Francesc, Eric and Rita from Servei de Recursos Científics i Técnics Servei (SRCiT) for their availability and help during material characterization with SEM, FESEM, Raman, XRD.

I am grateful and indebted to all fellow doctoral students and my colleagues for their help and providing a friendly environment throughout my PhD, Shuja, Juan, Eric, Ernesto, Miriam, Badi, Pineda, especially Xavi, who helped with the technical assistance. I would also like to thank all of them for helping me with things outside the lab translating Spanish to English. Thank you all for the wonderful time and excellent teamwork.

Also, I would like to thank my friends who became my family outside India and made it easier to survive and exciting at the same time, Jagriti, Ankur, Aakash, Alfonsina, Jitesh, Anand, Alba, Marta, Kandeel, Qasim, Rebecca, Hajar, Nisrin, Mariam, Saloni, Bakshinder. I would like to thank especially, Deepanshu and Shuja for encouraging me whenever I was going through a tough time and for always being there whenever I needed a family. I am blessed to meet all the friends and people who I have worked in this wonderful journey.

Above all, I am grateful my family for their unconditional love and endless support throughout my entire study and journey of life. My parents, Sangita and Tarvinder, have been my pillar of support and provided the foundation for my work. I consider myself the luckiest in the world to have such a loving family and I dedicate this dissertation to my parents.

Abstract

While technological advancements have improved an individual's lifestyle, they have equally contributed to the emergence of environmental challenges, such as pollution and global warming. In particular, the quantity of pollutant emissions in the atmosphere has increased considerably, leading to air pollution. Particulate matter and many hazardous gases, such as nitrogen dioxide (NO_2), ammonia (NH_3), carbon monoxide (CO), sulphur dioxide (SO_2), hydrogen sulphide (H_2S), carbon monoxide (CO), and ozone (O_3), are responsible for this phenomenon. These gases not only pose a threat to the environment but are also detrimental to human health, as they are a leading cause of ailments such as respiratory irritation syndrome, lung diseases, and bronchitis, only to name a few. The primary sources of pollutants that regularly deteriorate natural environmental conditions include continuously rising population, industrial emissions, automobile exhaust, and open burning of waste disposal. According to studies, air pollution is the leading cause of death, accounting for one out of every nine deaths each year. Furthermore, nearly 92% of the world's population lives in locations with poor air quality, putting them at significant risk of premature death. The detection of such gases is an urgent requirement, and experts all around the world are striving to develop a solution. In this context, cheap, miniaturized, portable, and durable gas sensors that allow precise measurements of air contaminants are required.

The most widely employed materials in gas sensing applications, semiconducting metal oxides, show significant drawbacks such as high-power consumption, poor long-term stability, limited selectivity and, particularly, high humidity cross-sensitivity. As a result, in the last few years, considerable efforts have been directed toward the development of room temperature gas sensors for application in consumer electronics, wearables and wireless sensing networks. Consequently, 2D materials such as transition-metal dichalcogenides (TMDs), have emerged as viable materials for gas sensing applications. These next-generation materials have the potential to improve the sensing parameters, such as sensitivity, selectivity, stability, and speed (response-recovery time) of gas-sensitive materials. This is owing to their inherent unique properties, which include nanoscale thickness, large specific surface area, abundant active edge sites, and high sensitivity to gas molecules at lower temperatures and even at room temperature.

The gas sensing materials investigated in this thesis can address the aforementioned issues, either in their pristine form or after some functionalization. In this respect, this thesis presents chemoresistive gas sensors based on various TMDs materials.

While the literature describes several methodologies for fabricating these 2D layered materials, achieving an edge enriched morphology is crucial for gas sensing applications. Therefore, the present doctoral thesis is dedicated to the development of these 2D layered materials to develop such a morphology with an aim to implant them as chemoresistive gas sensors. In this regard, a facile synthesis route is developed via a combination of the aerosol-assisted chemical vapour deposition (AA-CVD) method with/without H_2-free atmospheric pressure chemical vapour deposition (APCVD) to develop 3D assemblies of TMDs materials, such as WS_2, MoS_2, WSe_2, WS_2/Cu_2O, WS_2/PtO and WS_2/PdO.

In the line of research, the **first chapter** discusses the state-of-the-art and provides an overview of the conventional gas-sensitive materials studied in the literature. 2D materials that are advantageous for gas sensing applications are also discussed. This includes materials from Graphene to its descendants (Graphene oxide, GO, CNT) to several other 2D materials (black phosphorous, MXene, hBN). Among them, the advantages, and properties of using inorganic analogues of graphene, such as TMDs are elaborated. Also, the different synthesis approaches found in the literature are well-studied and detailed. In the end potential application of these next-generation materials in the field of electronics, spintronics, biomolecules detection and so on, is also studied.

The **second chapter** discusses the effect of two different morphologies of WS_2 (nanotriangles and nanoflakes) on the gas sensing properties, achieved by adopting a combination of AACVD and APCVD techniques. The results demonstrate that the final morphology of WS_2 films depends mainly on that of pre-deposited WO_3 layers. From the gas sensing point of view, the highest sensitivity was recorded for the WS_2 nanotriangles sensor, with an unprecedented ultra-low detection limit below 5 ppb. Additionally, this material has demonstrated its ability to detect 800 ppb of NO_2 even when operated at room temperature (25 °C). The high sensitivity observed for the WS_2 sensor is attributed to the porous surface and the increased number of sulphur edges in WS_2 NTs, which were created by the random 3D assembly of WS_2 nanosheets on WS_2 nanoneedles. Furthermore, WS_2 NTs have shown excellent response stability during long-term stability tests conducted over 8 months. Hence,

these results shed light on the important role played by the morphology in enhancing sensor performance.

Numerous reports in the literature suggest enhancing the gas sensing characteristics of TMDs by modifying their surface chemistry, either by noble metal decoration or functionalization with other materials, for instance, decoration with metal oxides. In this regard, the **third chapter** of this thesis focuses on improving the selectivity of WS_2NTs sensors for the detection of hydrogen sulphide gas. This gas is of particular interest as it poses serious threats to humans. Hence, a chemoresistive sensor was fabricated by using a hybrid material consisting of copper-oxide nanoparticles-decorated multi-layered tungsten disulfide nanostructures (Cu_2O/WS_2). The gas-sensing studies performed show that this hybrid nanomaterial has an excellent sensitivity towards hydrogen sulphide (11-times increase in response compared to that of pristine WS_2 sensor) at moderate temperature (150 °C). Additionally, functionalization of pristine WS_2 sensor with Cu_2O nanoparticles further enhances the gas sensing performance towards the targeted gas even at room temperature (13-times increase in response compared with that of pristine WS_2 sensor). Moreover, results obtained from humidity cross-sensitivity of Cu_2O/WS_2 sensor indicate superior gas sensing response (with a negligible decrease in response) as compared to pristine WS_2 sensor, when the ambient humidity is increased to 50%, which is rarely found in metal oxide-based sensors.

To further enhance the sensitivity of 2D layered TMDs materials at room temperature they were loaded with different metal oxides and the gas sensing properties of metal oxides loaded TMDs have been explored in the following **chapter- 4.** The sensing results revealed that loading of WS_2 nanosheets with either PtO or PdO ions significantly increases their gas response towards NO_2 (i.e., double the response as compared to pristine WS_2 sensor from 10% to 26.5%, thereby lowering the detection limit of the sensor (lower than 25 ppb after loading, which is far lower than that of pristine WS_2 gas sensor), at room temperature. Moreover, this study takes advantage of an appealing method for adding functionality to the transition metal dichalcogenide host matrix.

To elucidate the gas sensing properties of other TMDs material, tungsten diselenide (WSe_2), a tungsten-based dichalcogenide with close similarities to WS_2 was investigated and the corresponding results are presented in the **fifth chapter** of this thesis. Instead of sulfurization, the synthesis procedure uses the inclusion of H_2 gas during the APCVD process to selenize the WO_3 nanomaterial. The integration of as-synthesized, 3D WSe_2 with unique

structural arrangements resulted in exceptional gas sensing characteristics with dual selectivity towards NH_3 and NO_2 gas. Additionally, the selectivity of the sensor can be tuned by selecting its operating temperature (150°C for NH_3 and 100°C for NO_2). Moreover, when detecting NH_3 gas, the sensor demonstrated great resilience against high levels of ambient humidity (Rh = 50%), demonstrating its remarkable stability.

Following that, MoS_2, one of the significant and well-studied TMDs, is also investigated to highlight its gas sensing characteristics toward various gaseous pollutants such as NO_2 and NH_3. To build edge enriched 3D assemblies of MoS_2 nanosheets, the growth mechanism is examined in-depth, in the **sixth chapter** of this thesis. The synthesis was carried out using a single-step atmospheric pressure CVD method and the gas flow rate was explored as an important parameter to have such morphology. In contrast to earlier researched materials that demonstrated p-type behavior towards the same gases, this material's gas sensing characteristics exhibit an n-type semiconducting activity towards the analyzed gases (NO_2 and NH_3). Furthermore, it was revealed that the sensor's resistance to high levels of ambient humidity is enhanced by the vertical development of edge enriched MoS_2.

Finally, the research conducted in this thesis investigates a novel and simple method for fabricating these 2D layered materials with excellent scalability and reproducibility, as well as their use as gas-sensitive materials. Moreover, this research work exploits an attractive pathway to add functionality to the transition metal dichalcogenide host matrix. Also, a wide variety of analytical techniques have been used to characterise the surface morphology, topography, and chemical composition of the produced films. Furthermore, it was observed that by functionalizing and doping with different nanomaterials, significant improvements in sensitivity, selectivity, response/recovery time, and humidity tolerance were achieved.

LIST OF ACRONYMS

AACVD	aerosol-assisted chemical vapour deposition
APCVD	atmospheric pressure chemical vapor deposition
CVD	chemical vapor deposition
2D	two dimensional
TMDs	transition metal dichalcogenides
HR-TEM	high-resolution transmission electron microscopy
MBE	molecular beam epitaxy
MOX	metal oxide
PL	photoluminescence
SEM	scanning electron microscope
FESEM	field effect scanning electron microscope
TEM	transmission electron microscope
XPS	Xray spectroscopy
XRD	Xray Diffraction spectroscopy
NFs	nanoflowers
NTs	nanotriangles
WHO	world health organization
PdO	Palladium oxide
PtO	platinum oxide
WSe_2	tungsten diselenide
MoS_2	molybdenum sulphide
WS_2	tungsten disulfide
Cu_2O	copper oxide

Ppm	parts per million
Ppb	parts per billion
H_2	hydrogen
O_2	oxygen
H_2O	water
H_2S	hydrogen sulphide
NO_2	nitrogen dioxide
NH_3	ammonia
MFC	mass flow controller

TABLE OF CONTENTS

Chapter-1

Introduction

5.1 State of the art

According to the World Health Organization, anthropogenic air pollution is responsible for an estimated 7 million premature deaths worldwide in 2021 [1]. Inhalation of small pollutants prevalent in the air, which may swiftly permeate into the circulatory and respiratory systems, causing heart diseases, lung cancer and chronic obstructive pulmonary disease is killing millions of people every year [2]. As per statistics, air pollution is the biggest cause of death, accounting for one out of every nine fatalities each year. Unfortunately, around 92% of the world's population lives in places with poor air quality, leaving them in danger of death and disability. Apart from the toxic effects on human health, these gases pose serious environmental repercussions and are a leading cause of climate change, contributing to global warming, acid rain, and changes in soil quality, thereby affecting the growth of plants along with the groundwater quality [3]. According to the Organization for Economic Co-operation and Development (OECD), the economic consequences of air pollution are estimated to be in the billions of dollars each year globally. Several hazardous gases, such as nitrogen oxide (NO), nitrogen dioxide (NO_2), ammonia (NH_3), carbon monoxide (CO), sulphur dioxide (SO_2), hydrogen sulphide (H_2S), carbon monoxide (CO), and ozone, are major contributors to air damage (O_3).

Among all, one of the five key pollutants that degrades ambient air quality is nitrogen oxides (NOx), namely NO_2 [4] which is mainly produced by high-temperature combustion processes, common in industrial operations and automobile emissions. Moreover, NO_2 is associated with the formation of ground-level ozone, acid rain, and inorganic particulate matter in the stratosphere. It is a life-threatening pollutant that can cause respiratory problems, chronic bronchitis, asthma, and a variety of heart and lung diseases, depending on the duration of exposure [2][5]. As a result, the stipulated airborne acceptable exposure limit of NO_2 set by the Occupational Safety and Health Administration (OSHA) is 5 ppm, which cannot be exceeded. Furthermore, the American Industrial Hygiene Association has set a 5-minute emergency NO_2 exposure limit of 35 ppm, because exposure above this concentration might trigger skin issues

and respiratory problems [1]. As a result, it is now more important than ever to continuously monitor and analyse air quality.

H_2S is another toxic gas which is naturally found in crude petroleum, volcanoes, natural gas, hot springs etc [5]. It is also discharged as a by-product in more than 70 industries including food processing, water treatment, petroleum refining, natural gas production and paper mills to name a few [6][7]. It has a distinct odour depending on the concentration present; for example, at concentrations below 5 ppm, it has a characteristic rotten-egg stench, yet at higher concentrations beyond 100 ppm, it deadens the sense of smell, making it a silent threat for potential victims [8]. The health effects of such a deadly gas are determined by the concentration and time of exposure. For example, a little exposure to such a noxious gas can cause blurred vision, whereas when exposed to higher concentrations it might even lead to corneal ulcers, ultimately causing permanently impaired eyesight. Furthermore, at concentrations exceeding 100 ppm, the gas affects the human neurological system, causing paralysis and, in the case of prolonged exposure, it can even lead to death [9]. Apart from the health risks, sulphur compounds can also corrode steel, carbon, and other metallic surfaces, resulting in financial losses. As a result, the permissible concentration of H_2S (as suggested by the Scientific Advisory Board on Toxic Air Pollutants in the United States) is set between 20 and 100 parts per billion (ppb) [10]. In this regard, continual monitoring of H_2S gas levels is required to prevent leaks and minimize exposure.

Similarly, ammonia (NH_3) is a highly detrimental and poisonous gas that has a similar impact on human health as earlier mentioned for NO_2 and H_2S. However, it is the most widely used chemical in agriculture (for fertilisers), food manufacturing, and textile industries and has played a vital role in scientific research [11], also generated through vehicular emission [12]. It is a toxic gas that is detrimental to human health and the environment at higher concentrations [13]. When exposed at lower concentrations, it can cause coughing and irritation of the nose and throat, whereas, at higher concentrations it is highly toxic and can cause respiratory shocks which can even lead to death. Thus, the Occupational Safety and Health Administration (OSHA) has set a limit of 25 parts per million (ppm) (for 8 hr TWA) and 35 ppm (for 10 mins) above which it can cause significant health issues [14].

Table-1 gives an insight regarding the threshold values for some of these pollutant gases established by the European Union (EU) and the National Ambient Air Quality Standards (NAAQS) in the United States. To give a comparison, the LOD of some of the best performing

sensors that are reported in literature is also presented. Even though the published research shows that these MOS gas sensors can operate within these limits, these systems are still in the research and development stage.

Table 1 Threshold values for NO_2, SO_2, O_3, CO, CO_2, H_2S and NH_3 pollutants in the ambient atmosphere.

Pollutant	US Threshold Limits [1]	EU Threshold Limits [1]	LoD of the best-performing sensors reported in literature	References
NO_2	53 ppb	40 ppb	5 ppb	[15]
SO_2	75 ppb	130 ppb	38 ppb	[16]
O_3	70 ppb	120 ppb	20 ppb	[17]
CO	9 ppm	10 ppm	1 ppm	[18]
CO_2	N/A	N/A	150 ppb	[19]
H_2S	20-100 ppb	-	-	
NH_2	25 ppm	20 ppm	1 ppm	[11]

In this respect, gas sensors are employed as an environmental monitoring method in a variety of places. Nowadays, all the new constructions including offices, buildings, and industries are installed with gas sensors to detect the presence of toxic and harmful gases. Moreover, some researchers have even declared the first decade of the 21st century as a "**Sensor Decade**" [20]**.** Gas monitoring with drones, wearable gas sensing devices and the internet of things (IoT) sensor arrays for multi-gas sensing are some of the more contemporary applications of gas sensing products. As a result, the sensor industry has grown tremendously in recent years. The global sensor industry is estimated to be worth $190 billion by 2021 (**Figure. 1**), and it is predicted to reach $1 trillion by 2025 [20].

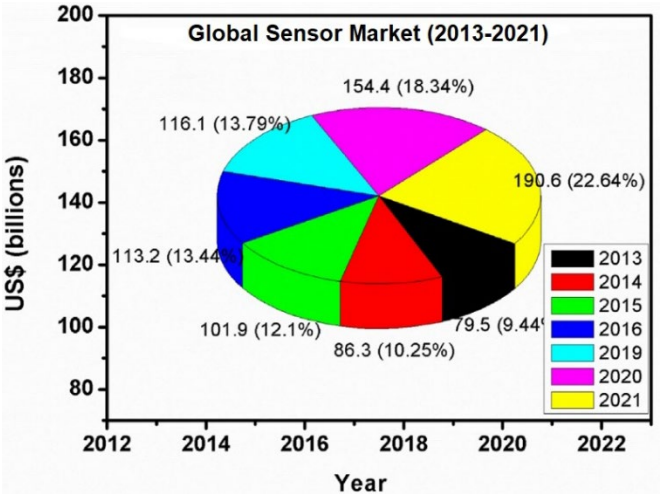

Figure 1 Global Sensor Market (2013-2021) demonstrates a spike in 2021.

5.2 Gas Sensors

A gas sensor is any device that can detect the presence and quantity of an analyte (such as poisonous or explosive gases and vapours, volatile organic compounds (VOCs), humidity, and odours) and generates an electrical or optical signal in response.

There are many different types of gas sensors that have been developed throughout the years using different sensing materials and methodologies. They are namely, infrared absorption, electrochemical, catalytic combustion, thermally conductive, solid electrolyte, paramagnetic and metal oxide semiconductor sensors.

While each variety has its own set of benefits, it also has its own set of limitations. Electrochemical sensors, for example, are the most widely used due to their selectivity, wide operating temperature range, and low cost. However, they have a few drawbacks, such as short life, limited storage period, and high temperature and humidity-dependent sensitivity, making them incompatible for many applications. **Table-2** presents a comparison between the different types of sensors based on different sensor parameters, given by Korotcenkov [12].

Table 2 Comparison of different types of gas sensors [12]

Parameters	Types of Gas Sensors				
	SMO Gas Sensors	Catalytic Combustion Gas Sensors	Electro Chemical Gas Sensors	Thermal Conductivity Gas Sensors	Infrared Absorption Gas Sensors
Sensitivity	E	G	G	P	E
Accuracy	G	G	G	G	E
Selectivity	F	P	G	P	E
Response Time	E	G	F	G	F
Stability	G	G	P	G	G
Durability	G	G	F	G	E
Maintenance	E	E	G	G	F
Cost	E	E	G	G	F
Suitability to portable instru-ments	E	G	F	G	P

E: excellent, G: good, F: Fair, P: Poor.

Among these, the chemoresistive type gas sensors have attracted major interest since they have a plethora of advantages over other sensors in terms of their ease of fabrication, simplicity of use, and low cost.

Chemoresistors are a class of gas sensors that consists of a gas-sensitive material which interacts with the analyte and generates some response as an electrical signal, which corresponds to the change in the electrical resistance/conductance. The change in resistance results from the change in the concentration of charge carriers due to the interaction of the sensing layer with the gas molecules[21].

An example of a typical chemoresistive gas sensor employed during this research work is demonstrated in **Figure. 2**. For this research work two varieties of substrates were used as demonstrated in **Figure. 2b** and **c**. The first is a silicon wafer, which is oxidised to form a silicon oxide layer on top (300 nm thick). On the front side, two platinum wire contacts were made on the deposited/grown material, using silver epoxy paste. On the back side, an alumina hotplate is pasted, which comprises a platinum screen printed heater to control the operating temperature of the sensor. Afterwards, the whole wafer, consisting of platinum electrodes and heater is wire bonded to a printed circuit board (PCB).

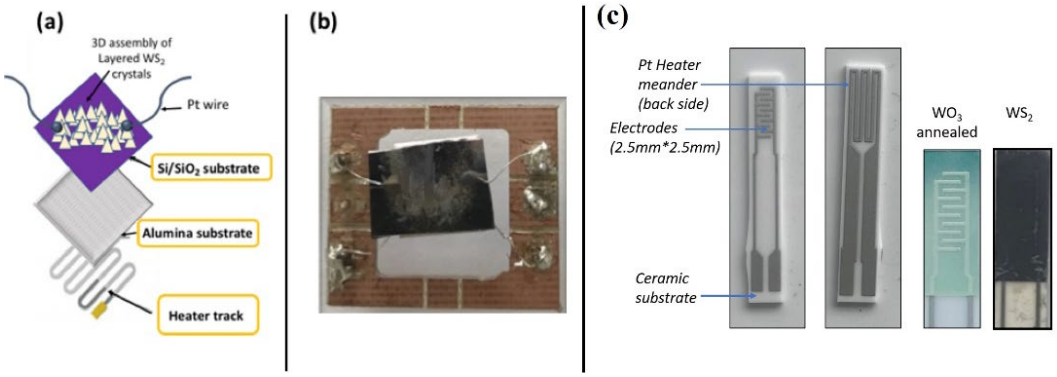

Figure 2 (a) Schematic and (b) a picture of WS_2 sensor fabricated over a silicon substrate. (c) Alumina transducer substrate was used to deposit WO_3 nanomaterial (green colour) and sulfurized to deposit WS_2 nanomaterial (black colour).

Several parameters govern a sensor's performance, such as response, sensitivity, selectivity, limit of detection (LoD), speed (response and recovery time) and stability. The gas sensing response of a sensor is defined as the percentile change in the baseline resistance of the sensor when exposed to a target gas. For instance, the response of a p-type material-based gas sensor towards an oxidising gas is calculated by using equation (1), while when exposed to a reducing gas, the sensor response is calculated by using equation (2).

$$Response(\%) = \frac{Rair - Rgas}{Rair} * 100 \quad (1)$$

$$Response(\%) = \frac{Rgas - Rair}{Rair} * 100 \quad (2)$$

Here Rair is the sensor resistance in the air whereas Rgas is the resistance in presence of analyte gas.

Selectivity refers to the characteristics of a gas sensor that determine whether it can distinguish and respond to a target gas amid a mixture of various gases. It is an important attribute for air quality sensors, since several gaseous species can produce variations in the electrical resistance of the sensor at ppb or ppt levels, much like the target gas.

The sensor's **limit of detection (LoD)** is defined as the lowest concentration of gas analyte that it can detect. It is a crucial factor to consider when developing sensors for detecting gaseous contaminants in real-time. **Table-1**, for example, shows the threshold limits for some of the pollutants found in the environment, as determined by the National Ambient Air Quality Standard (NAAQS) in the US and European ranges, as well as the current LoD of some of the best gas-sensitive materials documented in the literature.

The **response time** (Tres) is defined as the time taken by the sensor to obtain 90% of the total resistance change when exposed to the target gas and **recovery time** (Trec) is defined as the time taken by the sensor to retrieve 90% of the total resistance change upon removal of the target gas.

A sensor's **stability,** or repeatability, relates to its ability to deliver the same signal over time when exposed to the same quantities of a target gas.

A homemade gas sensing detection system was used for evaluating the sensing characteristics of different TMDs materials employed during this research work, namely, WS_2, MoS_2, WSe_2, WS_2/Cu_2O, WS_2/PdO and WS_2/PtO. A schematic diagram of the homemade gas sensing detection system is shown in **Figure.3**.

The sensors were either prepared on silicon substrates (oxidised previously) or on commercial alumina transducers. Depending on the type of substrate used to prepare the sensor, the testing chamber was chosen. The as-fabricated sensors (on commercial alumina) were then placed inside a homemade Teflon test chamber of 35 mL in volume. This testing chamber is capable of measuring 4 sensors simultaneously. It was connected to a fully automated, continuous gas flow measurement set-up able to supply diluted gas mixtures as well as humidified gas mixtures using a mass flow controller (Bronkhorst High-Tech B.V.) and electro valves. The gases employed for testing were used from calibrated gas cylinders balanced in dry synthetic air (Air Premier purity: 99.999%). The operating temperature of the sensor was controlled by connecting its heater to an external power supply (Agilent, model 3492A).

The sensing measurements were done by recording the change in electrical resistance of the sensor upon exposure to several different concentrations of target gases such as NO_2, NH_3, H_2, CO, H_2S and C_6H_6 at different operating temperatures (25°C, 100 °C and 150 °C). The sensors were initially kept in a dry airflow for a period of 2 h before any gas sensing measurements to stabilise their baseline resistance. Then the sensor was exposed to a given concentration of gaseous species for 10 mins followed by 50 min exposure to dry air to stabilise. The electrical resistance of the sensor was measured by using an Agilent-34972A multimeter. The gas flow and humidity were controlled using mass-flow controllers (MFC). Throughout the tests, the overall flow rate was maintained at 100 mL/min. To evaluate the humidity interference, certain tests were done in a humid environment (e.g., 50 % R.H or 70

% R.H at 25 °C). While the sensors were exposed to varying concentrations of the target gas the humidity level was kept constant.

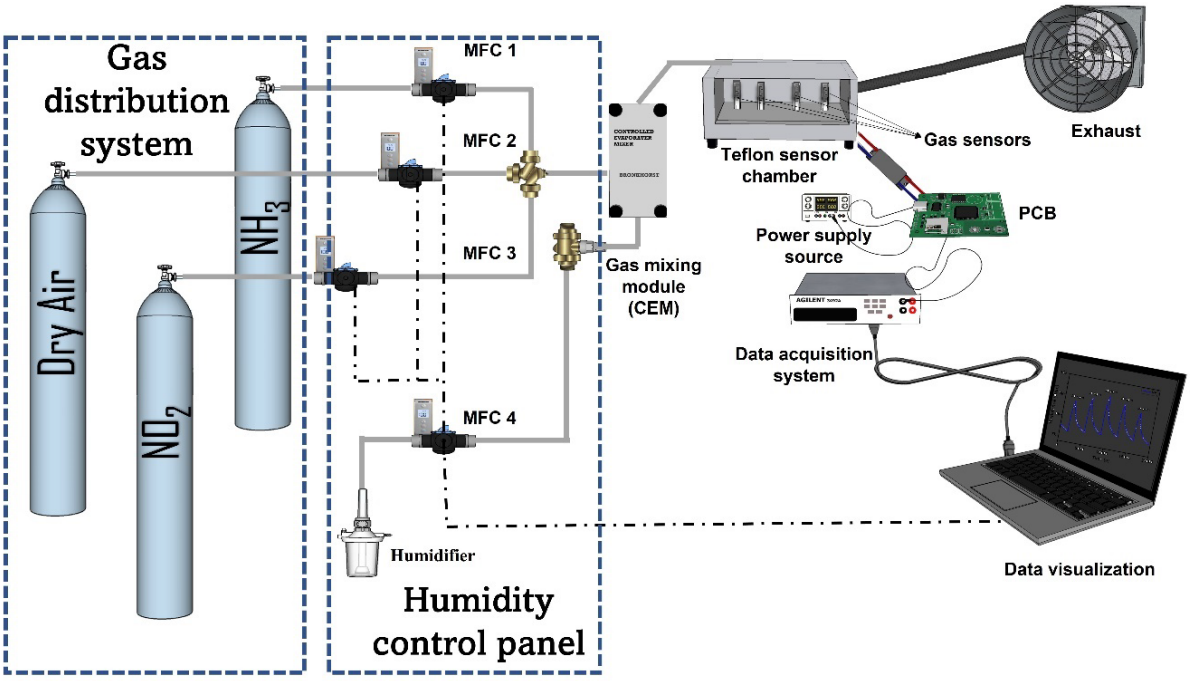

Figure 3 Schematic demonstrating a homemade gas sensing detection system.

5.3 Gas Sensitive Materials

In the past few years, extensive research has been conducted on gas-sensitive materials that can be employed in chemoresistors. These include investigations on conducting polymers (such as polyaniline or polypyrrole), nanomaterials such as nanoparticles, graphene, carbon nanotubes and metal oxide semiconductors. Metal oxide-based chemoresistors, on the other hand, have always been in high demand, and research to increase the performance of these materials has continued to this day. For instance, **Figure. 4** provides a comparison between some of the gas-sensitive materials commonly used in chemoresistors for NH_3 gas detection. As demonstrated, semiconducting metal oxides-based sensors outperform when compared to catalytic metal, conducting polymers, and optical sensors, as shown [12].

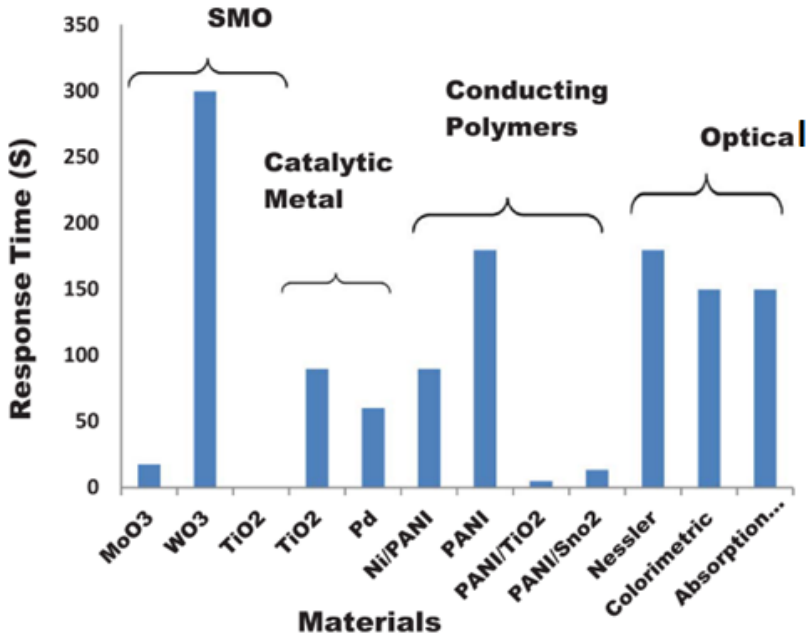

Figure 4 Comparison of several sensor materials for NH3 detection based on their response time [12]

5.3 Metal Oxide Gas Sensors

Metal oxide-based gas sensors have attracted wide attention for a variety of applications, including environmental monitoring, household safety, public security, medical sector, automotive and chemical industry.

There are several different methodologies for growing these materials, such as sol-gel, thermal oxidation, solvothermal, CVD, hydrothermal, and electrodeposition, where each one offers some advantages as well as has some limitations, for instance, the sol-gel technique is a commonly used method however precise control and choice of surfactants is crucial [22].

Although chemoresistive metal oxide-based gas sensors require a high operating temperature of around 300°C, several successful approaches to reduce power consumption have been developed, including i) light-activation ii) noble metal decoration, iii) hetero-junction engineering, and iv) non-oxide materials. On the other hand, noble metal decoration and hetero-junction engineering were more effective in altering the selectivity of the gas sensors, permitting good detection at a little lower temperature while being less effective in lowering the overall working temperature to near room temperature (RT). At room temperature, light-activated gas sensors function well, but light sources consume a lot of power. As a result, active gas sensing materials should be replaced with alternative, room-temperature-operating sensitive materials.

However, the lack of selectivity and high working temperature of traditional materials has resulted in a surge in demand for novel materials. Moreover, for effective monitoring of environmental contamination and large-scale application, it is essential to develop cheap, reliable, low-power, and miniaturized solid-state gas sensors that can detect and monitor trace level concentrations of these noxious gases in real-time for air-quality monitoring and human health protection.

5.5 Transition Metal Dichalcogenides - Overview

Graphene, with a honeycomb lattice structure, is the pioneer in the realm of 2D layered material. It is regarded as one of the most promising materials for post-silicon devices due to its high electron mobility and atomic thickness. It was first discovered by the Geim's group and has also been awarded the Nobel Prize in 2004 for mechanical exfoliation of a single atom thick graphene sheet from graphite. Since its discovery, scientists all around the world have been working to explore its applications in every field. Among them, one of the most promising fields is gas sensors, where a graphene-based sensor has been used to detect a single molecule of NO_2. Despite the exciting properties, its zero-bandgap nature limits its application in some areas such as in semiconductor electronics. To overcome this drawback, several methods have been explored to modify the band gap of graphene via electrical/chemical functionalization. However, these methods have their own disadvantages of increasing complexity and reducing carrier mobility. Moreover, for gas sensing applications, the main drawback of graphene-based gas sensors is their sluggish response and incomplete baseline recovery after a sensing process, thus degrading the reproducibility of the sensor.

Consequently, the surge for new materials has led to the exploitation of other 2D materials. Every year, the 2D library expands, which includes over 150 unique, layered materials that may be readily divided into sub-nanometer-thick materials to form atomic sheets with distinctive characteristics[23]. This includes materials such as transition-metal dichalcogenides (TMDs) which are regarded as the inorganic analogues of graphene (GR), hexagonal boron nitride (h-BN), black phosphorus (BP, also known as phosphorene), MXenes to name a few. Based on their chemical composition and structural arrangements, these 2D layered materials can be classified as metallic, semi-metallic, semiconducting, insulating, or superconducting, an illustration is shown in **Figure. 5**.

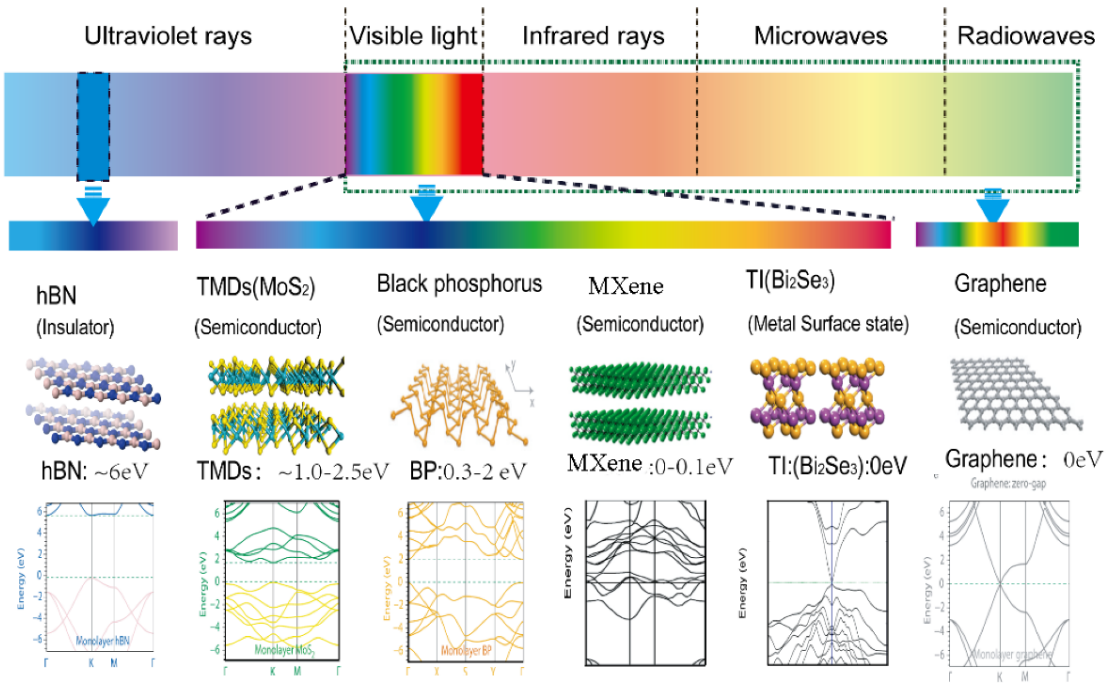

Figure 5 Spectral properties, atomic structures, and band diagrams of various 2D materials.

Among these materials, the first graphene descendants that attracted major attention are TMDs. They share many of the same characteristics as graphene, including transparency and flexibility, but unlike graphene, they exhibit exceptional electrical and chemical properties due to their semiconducting nature. As a result, they are becoming the target of research and have found plentiful applications spanning from nanoelectronics and nanophotonics to nanosensing [24]. Indeed, their properties like layer-dependent bandgap, a high surface-to-volume ratio which provides large active sites, high electrical conductivities, and low electrical noise make them a promising material for future technology. The highly reactive edge sites of transition metal dichalcogenides (TMDs) are particularly remarkable. For instance, for sensing applications, TMDs with a high d-orbital electron density at their edges can serve as chemically active sites for direct interaction with target gas molecules [25], as a result, they have attracted many researchers from the chemical and biosensing sector. Moreover, these materials can be easily altered by modifying the basal planes, dangling bonds at the edge site and surface functionalization by doping with different materials.

Apart from their exceptional chemical properties, TMDs exhibit exceptional physical properties such as high mechanical strength and good optical transparency. As a result, they are a good fit for the next generation of flexible and wearable electronics. Moreover, they have a significant potential to be turned into miniaturized, low-power transistors that are more efficient than the current silicon-based transistors [26].

The science of 2D materials is rapidly developing, and the quest for alternative 2D materials outside graphene is not restricted to only TMDs. In the constantly expanding worlds of 2D materials, new 2D materials such as silicene and phosphorene are formidable rivals. Several theoretical investigations have addressed the fundamental features of these novel 2D materials; however, due to stability concerns, experimental prospects are still in their infancy.

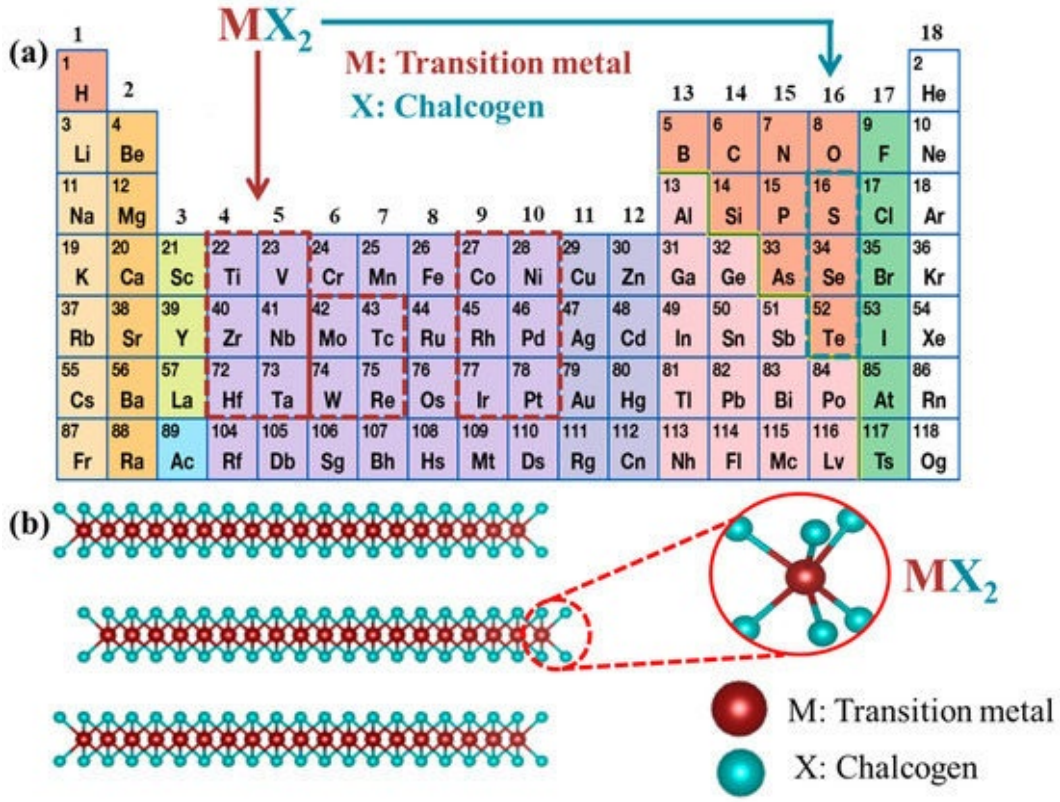

Figure 6 (a) Transition metal elements (M) that form layered structures are highlighted with red dotted box in the periodic table and Chalcogen elements (X) are indicated by the green dotted box, (b) illustration of MX_2 Layered structure.

5.6 TMDs Properties

5.6.1 Crystal and Band Structure

In total there are more than 40 different types of TMDCs which include metals (like VSe_2 and TiS_2), semimetals (such as $MoTe_2$ and WTe_2) and semiconductors (like WS_2, MoS_2 etc). Similar to GR, this class of materials has a layered structure. They are represented by the chemical formula MX_2 and have a X-M-X architecture, where M represent a transition metal atom (such as Mo, W, Re, V, Nb, Ti, Zr and so on), and X indicates a chalcogen atom (like S, Te, or Se), as shown in **Figure.6b**. In general, TMDs materials that belong to the groups IV-VII are in a layered structure, whereas the materials that are from groups VIII to X exist in a non-layered structure. A monolayer of WS_2 which is one of the principal materials of this

research work can be considered as a sandwich structure in the form of S-W-S. The S atoms are arranged in two hexagonal planes separated by a plane of metal atoms. The atoms in these three layers are bonded together by strong covalent intralayer bonds, while weak Van der Waals forces of attraction stack the layers on top of one other to create bulk materials. The sandwich has an interlayer spacing of ~6.5-7 Å, which makes it simpler to exfoliate the bulk material into a few layers by taking advantage of the weak interlayer attractions (vdW forces). The bond length of M-M bond lies in the range of 3.15-4.03 Å, which is dependent on the size of the metal and chalcogen atoms.

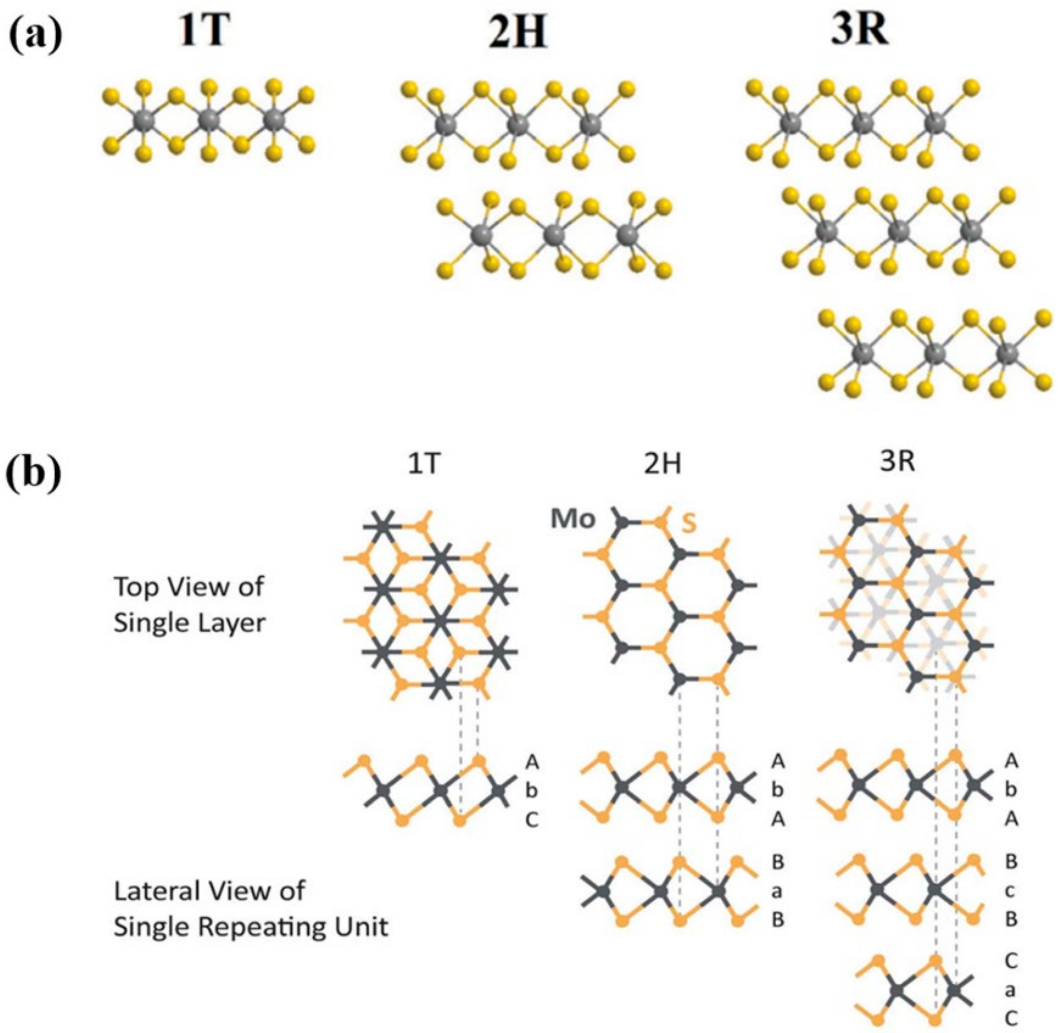

Figure 7 Metal coordination, stacking sequence and top view of the three polymorphs of TMDs, namely 1T, 2H and 3R.

The structures of 2D TMDs can be classified as trigonal prismatic (hexagonal, 2H; in monolayers, the prefix 2 is redundant) octahedral (tetragonal, T), or distorted phase (T′) depending on the arrangement of the atoms, as illustrated in **Figure. 7.** For instance, in H-phase WS_2 each W atoms are prismatically coordinated to six surrounding S atoms, resulting in a

hexagonal symmetry from the top view (**Figure 7a**). While in the case of the IT phase, a single layer has a trigonal chalcogen layer on the top with a trigonal antiprism layer (180-degree rotated structure) at the bottom, thereby resulting in a hexagonal symmetry from the top view. As the name suggests, in the distorted 1T′phase the metal atoms are distorted or dimerized as a result there is an atomic displacement of chalcogen atoms resulting in the structural modifications (as shown in **Figure 7a**). The bulk TMDs can be categorised into three different polymorphic structure based on different coordination phases and stacking sequence: 1T, 2H, and 3R, where the integers represent the number of layers in the stacking sequence while the letters correspond to the type of symmetry, namely, tetragonal (T), hexagonal (H), and rhombohedral (R), respectively [18]. The electronic property of the material varies among the different polymorphs. For instance, materials having the 2H or 3R crystal phase exhibit semiconducting properties while the 1T phase has semi-metallic or metallic behaviour. The different properties of each polymorph are summarised in **Table 3.**

Table 3 Properties of different TMD polymorphs.

	Polymorphs		
Properties	1T	2H	3R
Coordination Phase	Octahedral (Trigonal anti-prismatic)	Trigonal prismatic	Trigonal prismatic
No. of layers in stacking sequence	1	2	3
Electronic properties	Metallic	Semiconducting	Semiconducting
Types of symmetry	Tetragonal	Hexagonal	Rhombohedral
Stacking sequence	AbC	AbA BcB	AbA BcB CaC

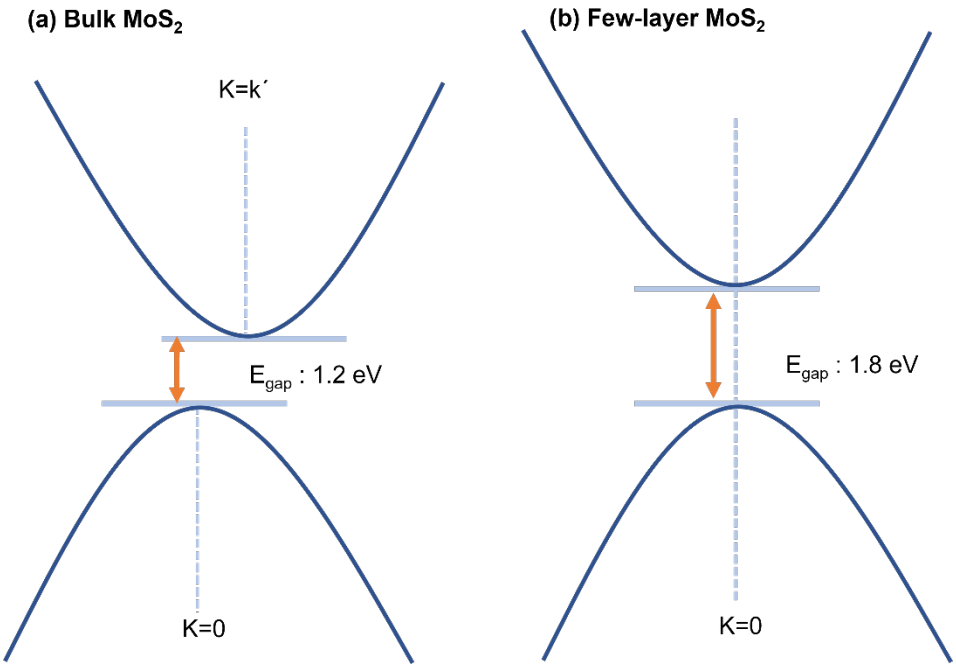

Figure 8 Energy band diagram of (a) Bulk MoS_2, (b) Few layered MoS_2.

At room temperature, the stable phase of the MX_2 material is the 2H phase whereas 1T is a metastable phase. Generally, TMDs materials belonging to group IV and V exists in 1T phase under ambient conditions.

5.6.2 Optical and electrical properties

Despite having structural similarities with graphene, having a wide range of bandgap in the visible and IR region, makes these materials a fit match for numerous applications. The bandgap of these materials falls in the range of 0-3 eV and can be tuned by varying – layer thickness, dopants, defects, and mechanical deformations. Also, as the thickness of these materials increases, the band gap reduces, and as the thickness falls from bulk to few layers or monolayer, the band gap transitions from indirect to direct, an illustration of the change in the bandgap is depicted in **Figure 8 5.** This transition from indirect to direct band gap results in a significant increase in Photoluminescence (PL), which is attributed to the quantum confinement and surface effects. The PL spectra are thickness-dependent and, therefore, it is obvious that the maximum PL intensity is observed when the thickness is reduced to the monolayer. **Table-4** compares the electronic band gap of the three materials studied in this thesis (namely WS_2, MoS_2 and WSe_2).

Table 4 Electronic properties of various TMDs

Material	Electronic Property	Band Gap
MoS_2	Semiconducting	Bulk: 1.2 eV Monolayer: 1.8 eV
WS_2	Semiconducting	Bulk: 1.4 eV Monolayer: 1.9 - 2.1 eV
WSe_2	Semiconducting	Bulk: 1.2 eV Monolayer: 1.7 eV
$MoTe_2$	Semimetal	Bulk: 1.1 eV Monolayer:

5.6.3 Mechanical Properties

Similar to graphene, TMDs are mechanically strong and flexible materials. For instance, WS_2 monolayer has three layers of atoms (chalcogen-metal-chalcogen), as a result 2D-WS_2 offers a more flexible stacking structure than graphene (S-W-S). Moreover, in suspended few-layer MoS_2 nanosheets, an extremely high Young's modulus *(E)* of ~ 0.33 ± 0.07 TPa has been found [64]. In another study, Bertolazzi et al. [65] found that single-layer MoS_2 has high in-plane stiffness and E, with values of ~180± 60 N m^{-1} and ~ 270 ± 100 GPa, respectively. The absence of stacking faults, high crystallinity, and defect-free nature of the atomically thin TMDs are attributed to the monolayer MoS_2 Young's modulus outperforming stainless steel (204 GPa) and graphene oxide (207 GPa) [66], which is attributed to the absence of stacking faults, high crystallinity, and defect-free nature of the atomically thin TMDs. Therefore, with these properties they are a promising material for near-term applications in flexible electronics.

5.6.4 Superconductivity

TMDs also have superconductivity, which is a fascinating characteristic. The intrinsic superconductivity of Group V TMDs such as NbSe and TaS has been fully explored in Ref. [59]. To achieve superconductivity in semiconducting multilayer TMDs such as 2H-MoS_2, WS_2, or $MoSe_2$ it requires the establishment of low-resistance metallic behavior [59]. This can be achieved by intercalation doping to boost electron concentration [125,126,127]. For instance, it has been observed that when metals were introduced into neighbouring MoS_2 layers in bulk MoS_2, the intercalation donated electrons to MoS_2, making the material metallic [128].

For instance, intercalation with calcium and strontium, resulted in Ca_xMoS and Sr_xMoS compounds, which showed superconducting properties at around ~4 K and 5.6 K, respectively.

Moreover, in recent studies, researchers looked at intrinsic superconductivity in the 1T MoS_2 phase without using electron injection [133]. It was found that the superconductivity of 1T-MoS_2 crystals was detected under 4 K based on magnetic and electrical studies, and the zero-temperature upper critical magnetic field of 1T-MoS_2 is calculated to be 5.02 T.

5.7 Synthesis of TMDs materials

Up to now, several techniques have been exploited to obtain controlled, homogeneous, large-scale growth of mono and few-layer TMDC material. These include various top-down and bottom-up approaches, wherein the top-down approach, atomically thin layers are obtained from bulk material via techniques like mechanical exfoliation, chemical exfoliation (such as Li-intercalation or ultrasonication-assisted liquid exfoliation)[27][28].

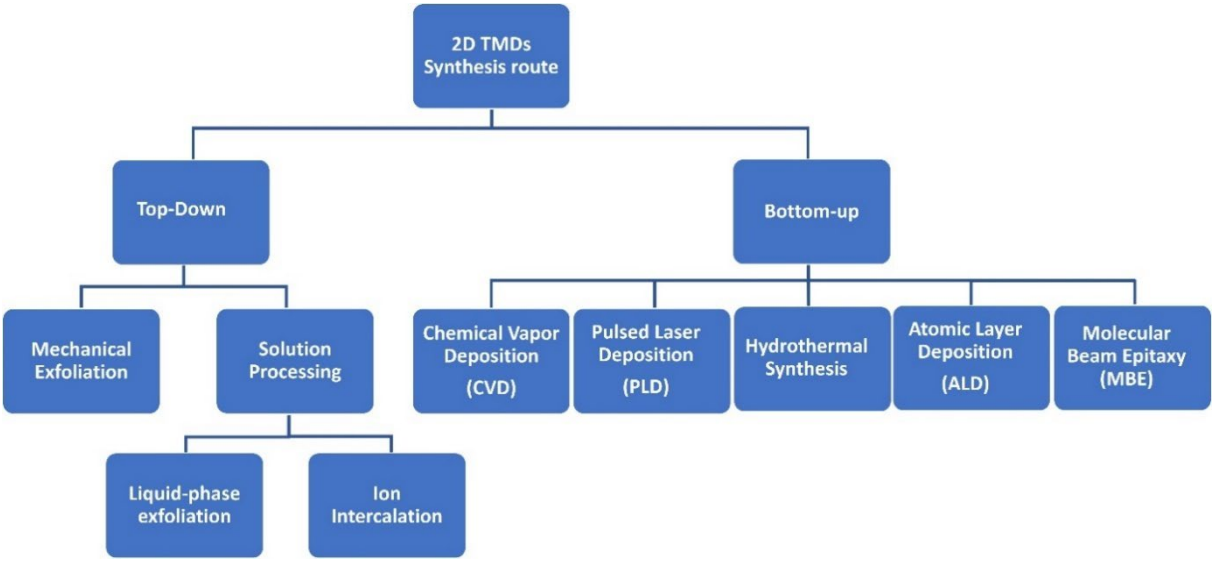

Figure 9 Overview of 2D TMDs synthesis techniques.

5.7.1 Top-down Approach

5.7.1.1 Mechanical exfoliation

Also known by the name ¨scotch-tape¨ method, it has been widely used owing to the ease of obtaining highly crystalline mono or few layered TMDs nanosheets from bulk material. It is known to be first used by Frindt in 1966, when a bulk MoS_2 was peeled down into thin molecular layers (~3.5 nm thick). While mechanical exfoliation produces high-quality mono-

or few-layered TMDs sheets, it is limited by its low yield of production. As a result, the technique is not fruitful for large-scale applications [29][27].

5.7.1.2 Solution Processing

In this context, **chemical exfoliation** provides an alternative route. As an example, **Figure 10** [29] shows an image of the two key routes adopted for chemical exfoliation to obtain atomically thin TMDs materials. Basically, in these techniques, either a liquid (solvent) or lithium ions are intercalated into the interlayer spacing of TMDC material. The l**iquid exfoliation technique** involves a series of steps, such as (a) dispersion of bulk TMDs material into a solvent such as water or alcohol, (b) followed by sonication for few hours, (c) centrifugations. This is followed by sonication or chemical reactions resulting in the intercalation of lithium ions in these materials [29]. Studies suggest that a solvent with the lowest enthalpy of mixing should be chosen to ensure optimal dispersion of the TMD material. The solvent's polarity, hydrogen bonding, and Hansen solubility factors must all be considered in this step [43, 44]. N-methyl pyrrolidone (NMP) and N-Cyclohexyl-2-pyrrolidone (CHP) are the two favoured strong solvents among the several available. However, because of their high boiling points and potentially harmful effects on the human body, both NMP and CHP are difficult to handle. Other mild solvents that can be utilized as dispersants for 2D TMDs include deionized water and alcohols [30].

In the **ion intercalation** process, the bulk TMDs material is immersed into a lithium containing solution (such as, n-butyllithium) for a long period (more than 24 hours). The lithium ion enhances the interlayer separation of the bulk material, making the hydrothermal exfoliation process easier. The ions stacked between the layers react rapidly with water during the exfoliation process, producing H_2 gas. As a result, microbubbles formed due to the production of H_2 gas which separates the multi-layered TMDs.

In another technique, **electrochemical cells** with lithium foil anodes can also be utilized to induce interlayer separation in 2D TMDs in addition to intercalation with lithium-containing solution [48, 49]. The lithium-ion that intercalates the bulk TMDs is produced by the galvanic discharge in the electrochemical cell. This technique is a more effective approach than chemical intercalation, and it also requires less time to process.

In comparison to the mechanical exfoliation technique, when the sheets are produced via the chemical exfoliation technique the yield is significantly enhanced, but material integrity is lost, and semiconducting characteristics are altered due to a change in structure induced by

lithium ions intercalating in between the exfoliated sheets. Moreover, the number of sheets produced via Liquid-phase exfoliation is generally multilayers (~ 4-6) and not monolayer [29]. Consequently, bottom-up approaches are more favoured for the synthesis of mono/multi layered materials.

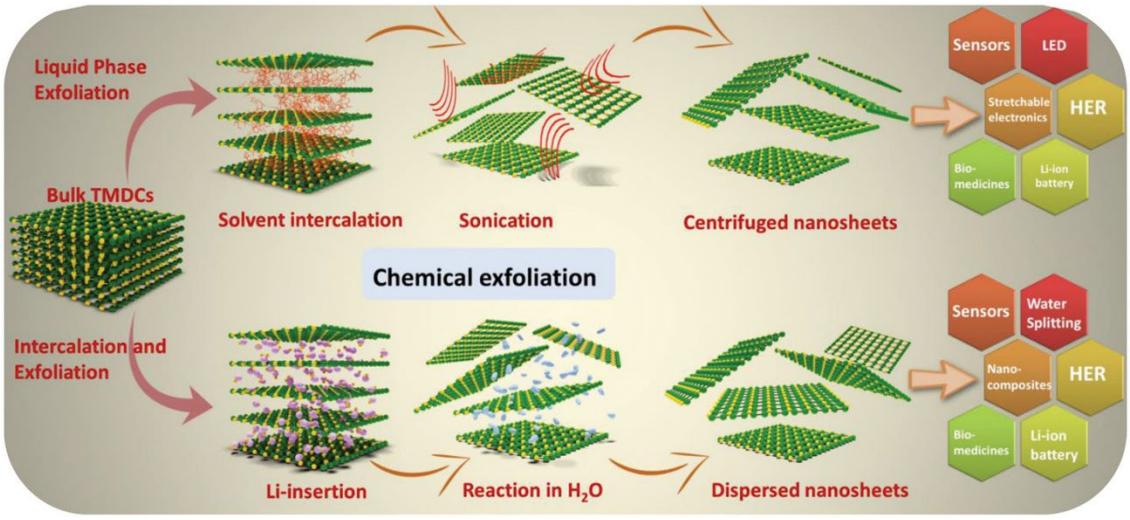

Figure 10 Chemical exfoliation approach to obtain atomically thin layer of TMDC materials [29].

5.7.2 Bottom-Up Approach

In case of bottom-up approach the material is grown via self-assembly of precursor molecules resulting into bulk material using techniques like chemical vapor deposition (CVD), pulsed laser deposition (PLD) physical vapor transport (PVT), MOCVD, ALD, MBE, and wet-chemical methods (such as hydrothermal, solvothermal). In comparison to the top-down approach, bottom-up approach provides more film uniformity over the grown substrates as well as produces films of high quality.

5.7.2.1 Chemical Vapor Deposition

The CVD process is one of the most efficient routes adopted to grow large scale of atomically thin 2D layered TMDs material. The most basic CVD method for growing 2D TMDs is the co-evaporation of metal oxides with chalcogen precursors, which results in vapor phase reaction and the generation of a stable 2D TMD over a suitable substrate. The growth mechanism varies depending on the synthesis process, as the growing material is influenced mostly by 3 parameters (a) substrate property, (b) Temperature for the deposition and (c) theatomicc gas flux used. Moreover, the final thickness of the grown material depends on the concentration of precursors used in the beginning as well as the duration of the growth process.

(a) **Substrate Property**: Nanoscale surface morphology and atomic planes terminating at the substrates, as well as lattice mismatching, affect the atomic layer of 2D materials. Moreover, research suggests that the surface energy of the substrate influences the nucleation and formation of 2D TMDs [80].

(b) **Temperature**: The growth temperature limits the reaction process. During the growth process, a randomly deposited adatom will normally travel to the energetically most favourable area if the growth temperature is high enough, that is, if the surface diffusion is fast enough, resulting in a 3D island development. While in the other scenario, when the substrate temperature is too low, however, an amorphous or polycrystalline film forms because the adatoms do not have enough kinetic energy to diffuse and reach the lowest potential energy location [81].

(c) **Atomic gas flux:** Another crucial characteristic for achieving high-quality 2D material films is atomic gas flow. Only a sufficiently high vapor pressure allows atomic gases to combine and be transported to the substrate. To avoid unwanted reactions during vaporized atom transfer to the substrate, vaporized atom stability is essential.

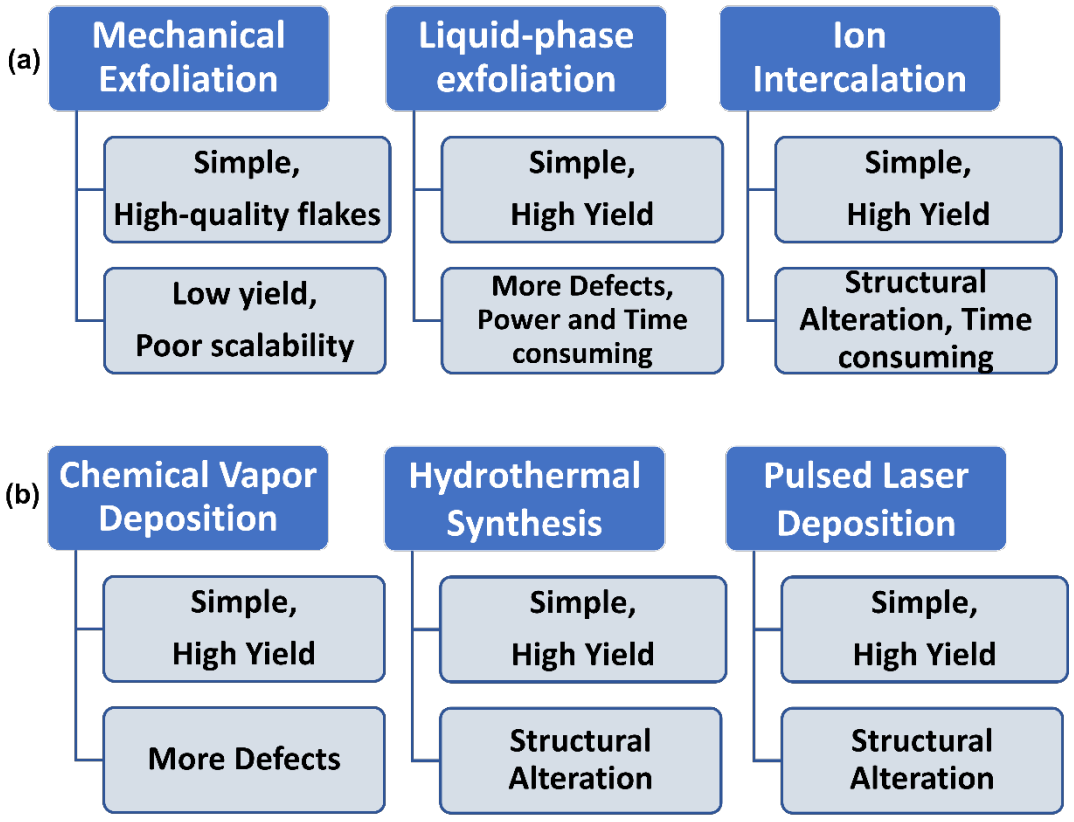

Figure 11 Comparison of advantages and limitations of some of the commonly used synthesis methods for TMDs growth where (a) top-down techniques, (b) bottom-up techniques

5.7.2.3 Pulsed Laser Deposition

The ablation of the desired bulk TMD leads to the creation of few-layer TMD films employing PLD [63–66]. During this process, a pulsed laser source is used to irradiate the bulk TMD, which is placed in a vacuum chamber. The irradiation of a high-intensity laser cause thinning of bulk TMDs which is subsequently deposited on a substrate. Due to the varying evaporation rates of the two ions, the approach permits control over the proportion of transition metal to chalcogenide ions (M:X) in the film. The defect in the produced few-layers TMD sample may be minimised by adjusting the M:X ratio [31].

5.7.2.3 Hydrothermal synthesis

The hydrothermal process is carried out in a sealed autoclave at elevated temperatures with high pressure. Although the method is simple with wide applicability, it results in the growth of TMDs materials with lateral sizes ranging from sub-micrometres to a few micrometres.

Moreover, the wet chemical routes are still in their preliminary stage where the electrical and optical properties of the as-synthesised material are not fully explored, hence these methods are in infancy.

Among all the above-mentioned techniques, the most widely used technique to grow layered materials for device application is **chemical vapour deposition** as it is a versatile method that offers several advantages over other techniques including, scalability, morphological control, controlled growth (lateral as well as vertical) and synthesis of high-quality films with interesting electronic and optical properties[32]. **Figure -11** summarises the advantages and limitations of some of the commonly used synthesis techniques used for fabricating 2D TMDs.

In this regard, viable techniques for large-scale multilayer semiconductor synthesis have yet to be devised. Hence, in this study a simple and facile route is explored to grow these next-generation materials directly over commercial substrates. For instance, pristine or metal-oxide decorated WS2 films were grown via a novel two-step technique wherein, at first, pristine or metal-oxide decorated WO3 nanomaterial was grown by using aerosol-assisted chemical vapor deposition technique which was later sulfurized to form pristine, or metal/oxide decorated WS2 films. The method is described in detail here. [33]

1. **First step deposition using aerosol-assisted chemical vapour deposition technique (AACVD)**

In the first step, either pristine or metal-oxide NPs loaded nanowires of WO_3 were grown, directly on a commercial alumina substrate, with screen-printed, interdigitated platinum electrodes on one side and a platinum resistor heater on the backside. It is a one-step growth process achieved via the AACVD method. This technique is widely used to deposit nano and microstructures of metal oxides. Pristine nanowires of WO_3 were grown using 50 mg of tungsten hexacarbonyl (WCO_6) dissolved in a solution of 15 mL acetone (CAS: 67–64–1) and 5 mL methanol (CAS: 67–56–1). The solution was kept in an ultrasonic bath for 20 min. After the solution was fully solubilised, it was placed in an ultrasonic bath to convert the solution to an aerosol. Nitrogen (N_2) was used as a carrier gas and the flow rate was set to 0.5 L/min to transport the aerosol to the deposition chamber, where the alumina substrate was kept. Before this, the deposition chamber was heated to a temperature of 400 ºC. The growth process took approximately 30 min to complete. Afterwards, the chamber was allowed to naturally cool down and later the substrate with WO_3 nanowires was annealed at 500 ºC for 2 h using a carbolite CWF 1200 muffle furnace. Annealing was done to remove any carbon residual left from the precursor, resulting in fully oxidised WO_3 nanowires. Metal-oxide NPs loaded nanowires were fabricated adopting the same procedure and equipment as described for the deposition of pristine WO_3 nanowires. However, the solution containing precursors and the amount of organic solvent used varied. For instance, in the case of PdO/WO_3, 25 mg of $W(CO)_6$ was dissolved in 9 mL acetone and 5 mg of palladium acetylacetonate ($Pd(C_5H_7O_2)_2$) was dissolved in 3 mL methanol separately. The solutions were then mixed and sonicated for 15–20 mins, whereas for PtO/WO_3, 25 mg of $W(CO)_6$ was dissolved in 9 mL acetone and 36 mg platinum acetylacetonate $Pt(O_2C_5H_7)_2$ was dissolved in 3 mL methanol separately. Again, the two solutions were then mixed and sonicated for 15–20 mins. After this, the same procedure was followed as described previously for growing pristine WO_3 nanowires. However, for growing metal-oxide-loaded nanowires the deposition chamber was heated to a temperature of 350 ºC only instead of 400 ºC.

2. **Second step deposition using atmospheric pressure chemical vapour deposition technique (CVD)**

In the second step of the synthesis, the as-grown WO_3 nanowires are sulfurized to form WS_2 nanomaterial using a quartz tube furnace via atmospheric pressure chemical vapour

deposition technique (CVD). This experiment is performed inside an in-house custom-built CVD reactor under hydrogen-free conditions. Preceding the sulfurization process, the quartz tube is flushed with 0.5 L/min of argon gas to remove any oxygen content present in the reactor. Two ceramic boats containing an equal amount of sulphur (S) powder each (>99.95%, Sigma Aldrich, CAS: 7704–34–9) are placed at different temperature zones of the deposition furnace. One of which is placed inside a secondary semi-sealed quartz tube next to the WO3 nanowires and the other sulphur boat is placed outside the secondary quartz tube. The boat outside the secondary quartz tube is placed upstream of the argon flow inside the bigger quartz tube. This promotes the double sulfurization of the as- grown WO3 nanowires. The furnace is then heated from room temper- ature to 900 ◦C with a heating rate of 40 ◦C/min to remove contaminants such as water or residual organics. This is done to obtain the nucleation of WS2. The growth of WS2 is achieved by allowing the reaction to proceed at 900 ◦C for 60 min under a constant flow of argon. It is vital to control all the growth parameters including the gas flow rate, heating rate and the quantity of sulphur powder used to obtain homogeneously sulfurized multi-layered films of WS2. After the growth phase, the furnace is cooled naturally to room temperature. Metal-oxide loaded nanowires were sulfurized adopting the same procedure and equipment as described for the sulfurization of pristine WO3 nanowires. **Figure 12 (a)** and **(b)** shows an image of the home-made setup used for the fabrication of these materials.

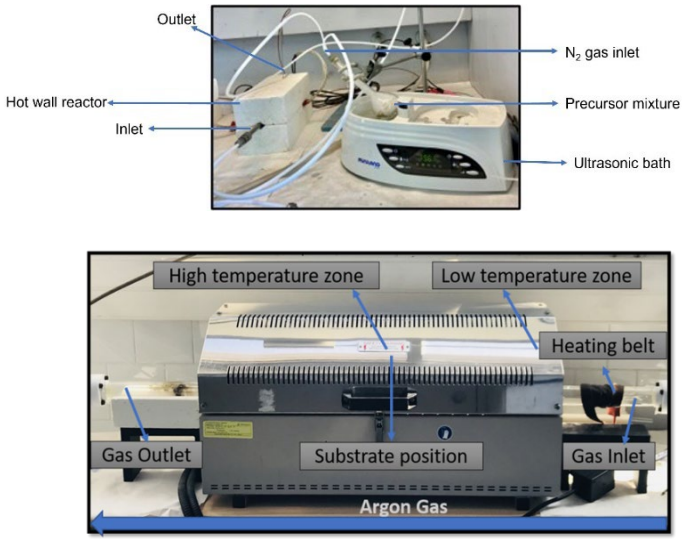

Figure 12 Homemade two-temperature zone furnace used for atmospheric pressure chemical vapor deposition (APCVD) for the sulfurization of pristine and functionalized WO3 to form doped and undoped WS_2 nanomaterial.

Moreover, a similar approach was adopted for growing also WSe_2 by simple selenization of WO_3 nanomaterial. However, the synthesis was carried out in the Namur

University and the as-synthesised material was later evaluated for its gas sensing properties. The synthesis process is detailed in Chapter-4 of this thesis.

In an attempt, to grow these 2D layered films in a single step, multilayered MoS_2 films were grown using the same homemade two temperature zone furnace via controlled growth at atmospheric pressure. The method is discussed in detail in **Chapter-5** of this thesis. Also, a schematic demonstrating the APCVD synthesis setup to grow multilayered films of MoS_2 and its growth temperature profile is demonstrated in **Figure-13**. Furthermore, the synthesis methods used in this work are not limited to the TMDCs shown and may be applied to a variety of other TMDs materials.

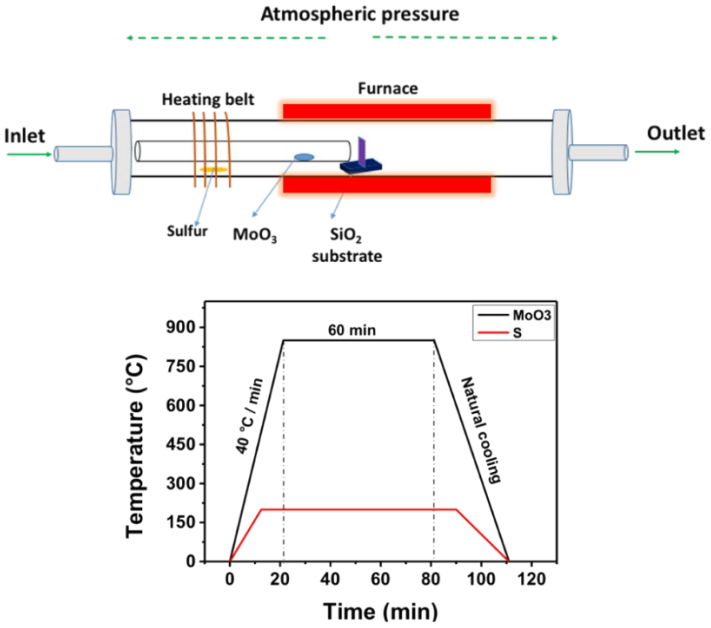

Figure 13 A schematic demonstrating the APCVD synthesis setup and MoS_2 growth temperature profile.

5.8 TMDs Applications

Among the wide variety of TMDs studied so far, Molybdenum/Tungsten Sulphide/Selenides (Mo/W/S_2/Se_2) are known to be chemically stable at ambient conditions and therefore have found niche applications in various sectors including energy storage, catalysis, photonic devices, chemical sensing, to name a few. For instance, multi-layered MoS_2 has been extensively studied for its transistor application, and potential applications in valleytronics, spintronics and sensing. As an example, **Figure-14** provides an illustration of the different kinds of devices fabricated employing various TMDs [32].

5.8.1 Optoelectronic devices

Owing to the broad range of bandgap energy from 1.1-2.1 eV, high absorption coefficient and ultrafast charge transfer, TMDs are a promising candidate for optoelectronic applications [34]. For instance, Lopez-Sanchez et al. [35] developed a monolayer MoS_2 phototransistor which is probed using a focussed laser beam. With a maximum external photoresponsivity of 880 AW^{-1} at a wavelength of 561 nm, the photodetector displayed an ultrasensitive behaviour and generated a photo response in the range of 400–680 nm. The direct band gap in monolayer MoS_2 resulted in a photoresponsivity that was 9000 times higher than that of multi-layered devices. The photodevice demonstrated a rise time and drop time of 4 s and 9 s, respectively, when the Vds = 8 V and Vg = 70 V was applied. The delayed transition from on to off state could be altered. The surroundings of the MoS_2 photodevice, such as O_2/H_2O molecule adsorption, may influence the sluggish change between the on and off states [35]. To overcome this, Zhang's group constructed a monolayer MoS_2 - based photodetector with an outstanding switching characteristic [36]. They reported the switching length of only 50 ms, for the current rise or decay process, which was significantly shorter than the value reported by Lopez-Sanchez and colleagues[37]. The calculated photoresponsivity, on the other hand, was extremely low, as it could only achieve 7.5 mA/W.

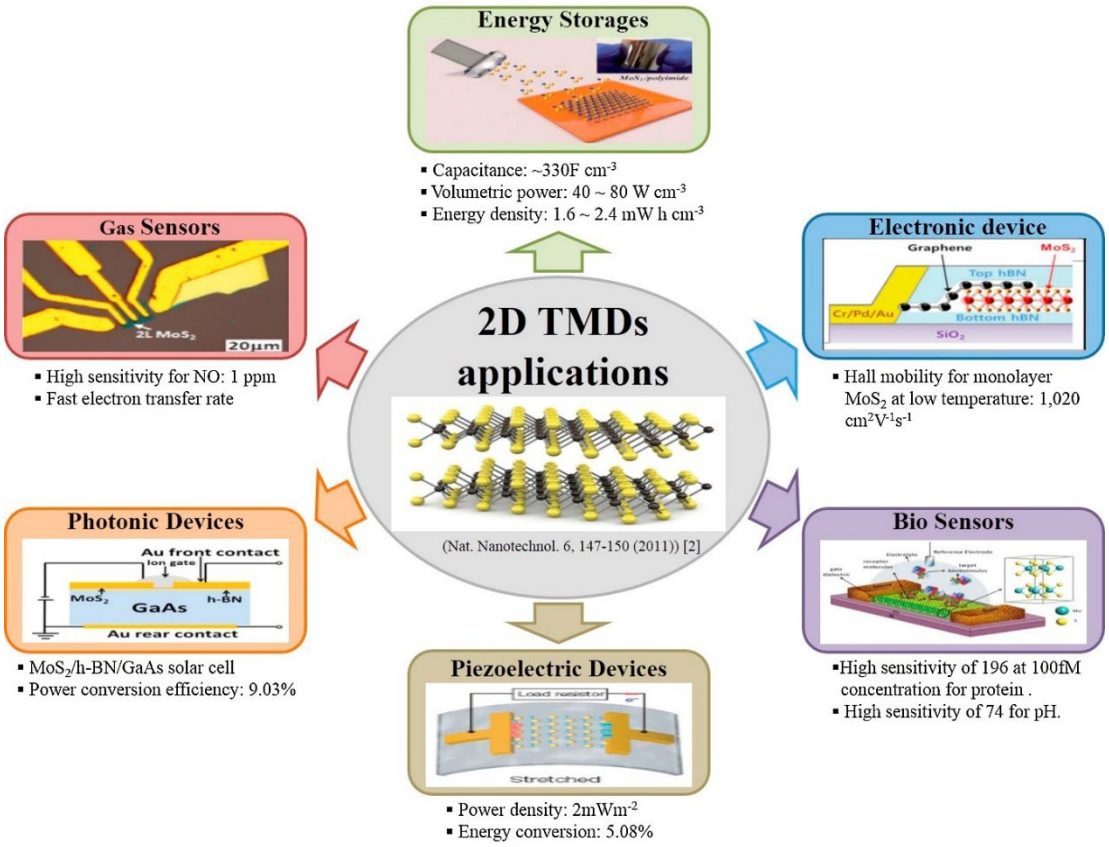

Figure 14 Different kinds of device fabricated employing various TMDs nanostructures.

5.8.2 Hydrogen Evolution Reaction (HER)

The production of new energy has been a prominent concern in academic society due to environmental damage resulting from the consumption of non-renewable fossil energy. One of the most efficient ways to generate clean hydrogen energy is by electrocatalytic hydrogen generation. Noble metals such as Pt have been the most effective electrocatalysts for hydrogen evolution reactions (HER) thus far. However, the scarcity of noble metals and their expensive price limits their use on a large-scale. As a result, the search for alternate new catalysts is on the horizon [28]. In this regard, MoS_2 is the first among the layered TMDs to emerge as an active hydrogen evolution reaction catalyst. In the 1970s, bulk MoS_2 was utilized as a HER catalyst, but it had weak catalytic activity (an onset potential of 90 meV and a Tafel slope of 692 mV/dec)[37]. However, in 2005, Nørskov's group demonstrated the application of MoS2 nanoparticles as an active HER catalyst [38]. Since then, 2D nanostructured TMDs have gained lots of attention from researchers worldwide as electrocatalysts for HER [39][40][41][42][43].

5.8.3 Biosystems: (Biosensors, Food Safety, Medical Diagnostics, and Drug Delivery)

Medical diagnostics, drug discovery, biosensing and food safety all rely on biomolecular detection. Apart from chemical and toxic gas detection, TMDs have evidenced significant growth in the field of **biosensing.** Due to the availability of a large specific surface area, these layered materials allow a large number of biomolecules to immobilize on their surface, resulting in high efficiency of biomolecules detection [44]. In this regard, many reports have demonstrated an increased sensitivity towards the detection of DNA, dopamine, glucose and so on [44]. Several studies have been published regarding the high sensitivity of MoS_2 based biosensors for the detection of DNA by taking advantage of the intrinsic fluorescence quenching properties of Mo ions [45]. For instance, MoS_2 based label-free FET biosensor has demonstrated a pH detection sensitivity that is 74 folds higher than graphene-based biosensors [46]. Similarly, WS_2 based biosensor has shown its capability for the detection of single-stranded DNA (ssDNA) chains via fluorescence quenching [44].

Not only this but TMDs have also been incorporated into the food industry where many reports have been published regarding the potential application of TMDs materials in food safety for pathogen and toxin detection. For example, Diphenylamine (DPA) is commonly used in the food sector to prevent pathogen growth on fruits and vegetables, also while storing food. It has poor water solubility, making it difficult to entirely remove it from the surfaces of fruits and vegetables. The presence of DPA in food items is hazardous to human health, as it can

cause significant disorders such as eczema, hypertension, and other diseases, emphasizing the necessity for a sensitive DPA detection system in the food business [47]. Sakthivel et al. [48] used a hydrothermal technique to fabricate europium-doped molybdenum diselenide nanoflowers (EuMoSe2) sensors that were disseminated on GCE for the electrochemical detection of DPA. The as-prepared sensor showed exceptional electrocatalytic activity toward DPA with a LOD of 8.8 nM. The sensor was tested to detect the presence of DPA in apple juice. It was observed that the sensor exhibited outstanding recovery rates for DPA boosted apple fruit juice, ranging from 97 % to 107 %.

The application of TMDs QDs has also been proposed for cancer radiation therapies. Experiments show that the cysteine protected WS_2 QDs have substantial catalytic activity in the reduction of H_2 O_2 and O_2, as well as exhibit wavelength dependant fluorescence. These characteristics made WS2 QDs a promising candidate for improving cell viability and removing reactive oxygen species from wounded cells. In vivo tests revealed that the WS_2 QDs could also protect DNA in irradiated cells from high-energy gamma-ray damage. By participating in catalytic processes and avoiding reactive oxygen species, the cysteine protected WS_2 QDs were able to restore superoxide dismutase and eliminate excess Methylenedioxyamphetamine from the liver and lung. Furthermore, around 80% of WS_2 QDs were efficiently removed by renal pathways a day after injection, and no significant toxicological effects were observed up to 30 days after injection, despite the relatively large injection dose [49].

5.8.4 Gas Sensing Application:

With the ever-growing economy, there is an increased demand for developing energy-efficient, cheap, miniaturised, reliable and portable sensors that have a high degree of sensitivity and selectivity for the next-generation technologies such as Internet-of-things and smart devices. The demand for small, low-cost gas sensors has prompted a surge in the quest for novel materials. Transition metal dichalcogenides (TMDs), which are graphene-like materials, have emerged as a viable material for the next generation of gas-sensitive materials. Additionally, the recent demonstration of scalable synthesis of 2D TMDs has shown that low-cost sensors can be developed. Furthermore, these materials have sparked a research boom in the future generation of flexible and wearable electronics.

For gas sensing applications, one major advantage that TMDs materials offer is that they operate at room temperature, unlike conventional metal oxides-based gas sensors.

Moreover, the high surface to volume ratio results in large active sites for gas adsorption thereby resulting in a high response. Their high electrical conductivities, and low electrical noise (a small change in carrier concentration induced by gas exposure induces significant changes in electrical conductivity). The highly reactive edge sites of transition metal dichalcogenides (TMDs) are particularly remarkable. TMDs with a high d-orbital electron density at their edges can serve as chemically active sites for direct interaction with target gas molecules. These outstanding properties make them a promising material for gas sensing applications. Moreover, these materials can be easily altered by modifying the basal planes, dangling bonds at the edge site and surface functionalization by doping with different materials to enhance their gas sensing properties. For instance, **Chapter-1** of this thesis demonstrates a WS_2 based gas sensor which has shown an unprecedented low detection limit below 5 ppb towards NO_2 gas detection. In this regard, **Table 5** summarises and compares some of the reported work on TMDs based gas sensors for the detection of Nitrogen dioxide gas from literature while also comparing the synthesis method. Moreover, owing to their diverse adsorption mechanism, NO_2 and NH_3 are the two flagship gases studied during this research work, for understanding the fundamental effect of gas sensing. Consequently, **Table-6** summarises all the results obtained during the development of this thesis.

Apart from NO_2, TMDs-based sensors have also been exploited for the detection of other toxic gases including VOCs and warfare agents. For instance, in a recent study, WSe_2 based sensor has demonstrated an enhanced sensitivity of 8.91 % towards 10 ppm dimethyl methyl phosphonate (DMMP) detection. DMMP is a well-known stimulant of the nerve agent sarin which is extremely harmful to humans. Moreover, the sensor has a fast response time of 100 s with 122-ppb limit of detection [50]. Whereas, on the other hand, the difficulty in developing VOC sensors is that VOC is made up of numerous compounds (such as benzene, ethylene glycol, formaldehyde, and others) with somewhat varied properties. For instance, a nanohybrid consisting of cubic Ag-MoS_2@m-CN nanohybrid is found to have multifunctional capabilities for VOC sensing. By studying molecules of n-butanol, isopropanol, benzene, and xylene gas, it was found that at 175°C, all VOC molecules had a short response time (7–15 s) with a recovery time of 6–9.5 s [51].

SI. no	Preparation methodology	Structure of material	Materials	Concentration (ppm)	Response /recovery time	Response	Operating temperature (C)	References
1	Hydrothermal	3D flower	MoS2	50	-/-	78%	150	
2	Hydrothermal-CTAB	3D flower	MoS2	50	-/-	60%	100	
3	Hydrothermal	nanosheets	WS2	0.1	-/-	9.3%	RT	
4	Hydrothermal	hollow	MoS2	100	79s/225s	40.3%	150	
5	Two step CVD	Bilayer	MoS2	1	11.3/5.3 minute	2.6%		
6	CVD	monolayer	MoS2	0.4	16s/65s	670%	RT (625 nm, 4 mW/cm^2)	
7	CVD	nanowires	MoS2	5	16s/172s	18.1%	60	
8	CVD	flakes	VA-MoS2	50	-/-	48.32%	100	
9	Chemical etching+ CVD	Nanosheet	MoS2/Psi	50	-/	28.4%	RT	
10	Aerogel conductometric	nanosheets	WS2/GA	2	100 s/300 s	3%	180	
11	Sulfurization	Vertically alligned	MoS2/ZnO NWs	50	5 min/-	31.2%	200	
12	Wet chemical	hybrid	MoS2-RGO	3	8 s/20 s	1.23	160	

SI. no	Preparation methodology	Structure of material	Materials	Concentration (ppm)	Response /recovery time (s)	Response	Operating temperature (C)	References
13	solvothermal	nanocomposite	RGO-MoS2-CdS	0.2	25 s/34 s	27.4%	75	
14	Redox reaction	nanoparticle	MoS2-Au	2.5	4/14 min	30%	RT	
15	Electrospinning	Nanofiber	WS2/	50	-/-	60%	100	
16	Wet chemical	Nanostructure	WS2	0.1	-/-	9.3%	RT	
17	Nucleation controlled	micro flowers	MoS2	100	79s/225s	40.3%	150	

References

[1] N. A. Isaac, I. Pikaar, and G. Biskos, “Metal oxide semiconducting nanomaterials for air quality gas sensors: operating principles, performance, and synthesis techniques,” *Microchimica Acta*, vol. 189, no. 5, 2022, doi: 10.1007/s00604-022-05254-0.

[2] T. W. Hesterberg, W. B. Bunn, R. O. McClellan, A. K. Hamade, C. M. Long, and P. A. Valberg, “Critical review of the human data on short-term nitrogen dioxide (NO2) exposures: Evidence for NO2 no-effect levels,” *Critical Reviews in Toxicology*, vol. 39, no. 9. pp. 743–781, 2009. doi: 10.3109/10408440903294945.

[3] أ. ث. ف. و. س. م. الدرس ,”تنمية الحكمة كمدخل للصمود النفسي لدى طلاب الملرحلة الثانوية المتفوقين عقليا“No Title”, □□□□□□, no. May 2001, 2019.

[4] S. Kumar, V. Pavelyev, P. Mishra, N. Tripathi, P. Sharma, and F. Calle, “A review on 2D transition metal di-chalcogenides and metal oxide nanostructures based NO2 gas sensors,” *Materials Science in Semiconductor Processing*, vol. 107, no. May 2019, p. 104865, 2020, doi: 10.1016/j.mssp.2019.104865.

[5] S. K. Pandey, K. H. Kim, and K. T. Tang, “A review of sensor-based methods for monitoring hydrogen sulfide,” *TrAC - Trends in Analytical Chemistry*, vol. 32, pp. 87–99, 2012, doi: 10.1016/j.trac.2011.08.008.

[6] A. Mirzaei, S. S. Kim, and H. W. Kim, “Resistance-based H2S gas sensors using metal oxide nanostructures: A review of recent advances,” *Journal of Hazardous Materials*, vol. 357, pp. 314–331, 2018, doi: 10.1016/j.jhazmat.2018.06.015.

[7] C. H. Moon, M. Zhang, N. V. Myung, and E. D. Haberer, “Highly sensitive hydrogen sulfide (H2S) gas sensors from viral-templated nanocrystalline gold nanowires,” *Nanotechnology*, vol. 25, no. 13, 2014, doi: 10.1088/0957-4484/25/13/135205.

[8] A. Mortezaali and R. Moradi, “The correlation between the substrate temperature and morphological ZnO nanostructures for H2S gas sensors,” *Sensors and Actuators, A: Physical*, vol. 206, pp. 30–34, 2014, doi: 10.1016/j.sna.2013.11.027.

[9] C. International and C. Assessment, “H2S human health aspects,” 2003.

[10] Y. Guo, M. Gong, Y. Li, Y. Liu, and X. Dou, “Sensitive, Selective, and Fast Detection of ppb-Level H2S Gas Boosted by ZnO-CuO Mesocrystal,” *Nanoscale Research Letters*, vol. 11, no. 1, 2016, doi: 10.1186/s11671-016-1688-y.

[11] B. Timmer, W. Olthuis, and A. van den Berg, “Ammonia sensors and their applications - A review,” *Sensors and Actuators, B: Chemical*, vol. 107, no. 2, pp. 666–677, 2005, doi: 10.1016/j.snb.2004.11.054.

[12] A. Dey, “Semiconductor metal oxide gas sensors: A review,” *Materials Science and Engineering B: Solid-State Materials for Advanced Technology*, vol. 229, no. November 2017, pp. 206–217, 2018, doi: 10.1016/j.mseb.2017.12.036.

[13] D. Punetha and S. K. Pandey, “Sensitivity Enhancement of Ammonia Gas Sensor Based on Hydrothermally Synthesized rGO/WO3 Nanocomposites,” *IEEE Sensors Journal*, vol. 20, no. 4, pp. 1738–1745, 2020, doi: 10.1109/JSEN.2019.2950781.

[14] H. Nanofibers *et al.*, "Effective Ammonia Detection Using n-ZnO / p-NiO," *IEEE Sensors Journal*, vol. 16, no. 8, pp. 2477–2483, 2016.

[15] R. E. *et al.*, "Synthesis and Characterization of Chromium-Doped Mesoporous Tungsten Oxide for Gas Sensing Applications," *Advanced Functional Materials*, vol. 17, no. 11. pp. 1801–1806, 2007.

[16] C. S. Prajapati and N. Bhat, "Growth Optimization, Morphological, Electrical and Sensing Characterization of V 2 O 5 Films for SO 2 Sensor Chip," *Proceedings of IEEE Sensors*, vol. 2018-Octob, pp. 6–9, 2018, doi: 10.1109/ICSENS.2018.8589650.

[17] L. F. da Silva *et al.*, "UV-enhanced ozone gas sensing response of ZnO-SnO2 heterojunctions at room temperature," *Sensors and Actuators, B: Chemical*, vol. 240, pp. 573–579, 2017, doi: 10.1016/j.snb.2016.08.158.

[18] C. Lin *et al.*, "High Performance Colorimetric Carbon Monoxide Sensor for Continuous Personal Exposure Monitoring," *ACS Sensors*, vol. 3, no. 2, pp. 327–333, 2018, doi: 10.1021/acssensors.7b00722.

[19] C. Willa, J. Yuan, M. Niederberger, and D. Koziej, "When Nanoparticles Meet Poly(Ionic Liquid)s: Chemoresistive CO2 Sensing at Room Temperature," *Advanced Functional Materials*, vol. 25, no. 17, pp. 2537–2542, 2015, doi: https://doi.org/10.1002/adfm.201500314.

[20] S. Dhall, B. R. Mehta, A. K. Tyagi, and K. Sood, "A review on environmental gas sensors: Materials and technologies," *Sensors International*, vol. 2, no. July, p. 100116, 2021, doi: 10.1016/j.sintl.2021.100116.

[21] A. Sharma and C. S. Rout, "Advances in understanding the gas sensing mechanisms byin situandoperandospectroscopy," *Journal of Materials Chemistry A*, vol. 9, no. 34, pp. 18175–18207, 2021, doi: 10.1039/d1ta05054k.

[22] A. Moumen, G. C. W. Kumarage, and E. Comini, "P-Type Metal Oxide Semiconductor Thin Films: Synthesis and Chemical Sensor Applications," *Sensors*, vol. 22, no. 4, 2022, doi: 10.3390/s22041359.

[23] G. Sanyal, A. Vaidyanathan, C. S. Rout, and B. Chakraborty, "Recent developments in two-dimensional layered tungsten dichalcogenides based materials for gas sensing applications," *Materials Today Communications*, vol. 28, no. June, p. 102717, 2021, doi: 10.1016/j.mtcomm.2021.102717.

[24] X. Zhang, S. Y. Teng, A. C. M. Loy, B. S. How, W. D. Leong, and X. Tao, "Transition metal dichalcogenides for the application of pollution reduction: A review," *Nanomaterials*, vol. 10, no. 6, 2020, doi: 10.3390/nano10061012.

[25] J. M. Suh *et al.*, "Edge-exposed WS2 on 1D nanostructures for highly selective NO2 sensor at room temperature," *Sensors and Actuators, B: Chemical*, vol. 333, no. 2, p. 129566, 2021, doi: 10.1016/j.snb.2021.129566.

[26] Y. H. Wang, K. J. Huang, and X. Wu, "Recent advances in transition-metal dichalcogenides based electrochemical biosensors: A review," *Biosensors and Bioelectronics*, vol. 97, no. May, pp. 305–316, 2017, doi: 10.1016/j.bios.2017.06.011.

[27] X. Li, J. Shan, W. Zhang, S. Su, L. Yuwen, and L. Wang, "Recent Advances in Synthesis and Biomedical Applications of Two-Dimensional Transition Metal Dichalcogenide Nanosheets," *Small*, vol. 13, no. 5. 2017. doi: 10.1002/smll.201602660.

[28] L. Yang *et al.*, "Properties, preparation and applications of low dimensional transition metal dichalcogenides," *Nanomaterials*, vol. 8, no. 7, pp. 1–52, 2018, doi: 10.3390/nano8070463.

[29] A. Raza *et al.*, "Advances in Liquid-Phase and Intercalation Exfoliations of Transition Metal Dichalcogenides to Produce 2D Framework," *Advanced Materials Interfaces*, vol. 8, no. 14, pp. 1–46, 2021, doi: 10.1002/admi.202002205.

[30] Cellulose Nanocrystal-Derived Hollow Mesoporous Carbon Spheres and their Application as a Metal-Free Catalyst, "ce d M us pt," *Nanotechnology*, pp. 0–22, 2019.

[31] Cellulose Nanocrystal-Derived Hollow Mesoporous Carbon Spheres and their Application as a Metal-Free Catalyst, "ce d M us pt," *Nanotechnology*, pp. 0–22, 2019.

[32] W. Choi, N. Choudhary, G. H. Han, J. Park, D. Akinwande, and Y. H. Lee, "Recent development of two-dimensional transition metal dichalcogenides and their applications," *Materials Today*, vol. 20, no. 3, pp. 116–130, 2017, doi: 10.1016/j.mattod.2016.10.002.

[33] A. Alagh *et al.*, "PdO and PtO loaded WS2 boosts NO2 gas sensing characteristics at room temperature," *Sensors and Actuators B: Chemical*, vol. 364, no. 2, p. 131905, 2022, doi: 10.1016/j.snb.2022.131905.

[34] JEAN-F. TOMB *et al.*, "Enhanced Reader.pdf," *Nature*, vol. 388. pp. 539–547, 1997.

[35] O. Lopez-Sanchez, D. Lembke, M. Kayci, A. Radenovic, and A. Kis, "Ultrasensitive photodetectors based on monolayer MoS 2," *Nature Nanotechnology*, vol. 8, no. 7, pp. 497–501, 2013, doi: 10.1038/nnano.2013.100.

[36] D. J. Late, B. Liu, H. S. S. R. Matte, V. P. Dravid, and C. N. R. Rao, "Hysteresis in single-layer MoS 2 field effect transistors," *ACS Nano*, vol. 6, no. 6, pp. 5635–5641, 2012, doi: 10.1021/nn301572c.

[37] Z. Yin *et al.*, "Single-layer MoS 2 phototransistors," *ACS Nano*, vol. 6, no. 1, pp. 74–80, 2012, doi: 10.1021/nn2024557.

[38] B. Hinnemann *et al.*, "Biomimetic hydrogen evolution: MoS2 nanoparticles as catalyst for hydrogen evolution," *J Am Chem Soc*, vol. 127, no. 15, pp. 5308–5309, 2005, doi: 10.1021/ja0504690.

[39] J. Deng *et al.*, "Triggering the electrocatalytic hydrogen evolution activity of the inert two-dimensional MoS2 surface via single-atom metal doping," *Energy and Environmental Science*, vol. 8, no. 5, pp. 1594–1601, 2015, doi: 10.1039/c5ee00751h.

[40] T. F. Jaramillo, K. P. Jørgensen, J. Bonde, J. H. Nielsen, S. Horch, and I. Chorkendorff, "Identification of active edge sites for electrochemical H2 evolution from MoS2 nanocatalysts," *Science (1979)*, vol. 317, no. 5834, pp. 100–102, 2007, doi: 10.1126/science.1141483.

[41] L. Liao *et al.*, "MoS2 formed on mesoporous graphene as a highly active catalyst for hydrogen evolution," *Advanced Functional Materials*, vol. 23, no. 42, pp. 5326–5333, 2013, doi: 10.1002/adfm.201300318.

[42] H. Wang *et al.*, "MoSe2 and WSe2 nanofilms with vertically aligned molecular layers on curved and rough surfaces," *Nano Letters*, vol. 13, no. 7, pp. 3426–3433, 2013, doi: 10.1021/nl401944f.

[43] D. Voiry *et al.*, "Conducting MoS2 nanosheets as catalysts for hydrogen evolution reaction," *Nano Letters*, vol. 13, no. 12, pp. 6222–6227, 2013, doi: 10.1021/nl403661s.

[44] W. Choi, N. Choudhary, G. H. Han, J. Park, D. Akinwande, and Y. H. Lee, "Recent development of two-dimensional transition metal dichalcogenides and their applications," *Materials Today*, vol. 20, no. 3, pp. 116–130, 2017, doi: 10.1016/j.mattod.2016.10.002.

[45] C. Zhu, Z. Zeng, H. Li, F. Li, C. Fan, and H. Zhang, "Single-layer MoS2-based nanoprobes for homogeneous detection of biomolecules," *J Am Chem Soc*, vol. 135, no. 16, pp. 5998–6001, 2013, doi: 10.1021/ja4019572.

[46] D. Sarkar, W. Liu, X. Xie, A. C. Anselmo, S. Mitragotri, and K. Banerjee, "MoS 2 Field-Effect Transistor for Next-," *ACS Nano*, vol. 8, no. 4, pp. 3992–4003, 2014.

[47] F. E. Annanouch, J. Casanova-Cháfer, A. Alagh, M. Alvarado, E. González, and E. Llobet, *Nanosensors for food logistics*. INC, 2022. doi: 10.1016/b978-0-12-824554-5.00022-7.

[48] A. K. C. Hau, T. H. Kwan, and P. K. T. Li, "Melamine toxicity and the kidney," *Journal of the American Society of Nephrology*, vol. 20, no. 2, pp. 245–250, 2009, doi: 10.1681/ASN.2008101065.

[49] X. Bai *et al.*, "Ultrasmall WS2 Quantum Dots with Visible Fluorescence for Protection of Cells and Animal Models from Radiation-Induced Damages," *ACS Biomaterials Science and Engineering*, vol. 3, no. 3, pp. 460–470, 2017, doi: 10.1021/acsbiomaterials.6b00714.

[50] B. Li *et al.*, "Enhanced dimethyl methylphosphonate detection based on two-dimensional WSe2nanosheets at room temperature," *Analyst*, vol. 145, no. 24, pp. 8059–8067, 2020, doi: 10.1039/d0an01671c.

[51] V. K. Tomer *et al.*, "Superior visible light photocatalysis and low-operating temperature VOCs sensor using cubic Ag(0)-MoS2 loaded g-CN 3D porous hybrid," *Applied Materials Today*, vol. 16, pp. 193–203, 2019, doi: 10.1016/j.apmt.2019.05.010.

[52] Y. Z. Chen *et al.*, "Low-Temperature and Ultrafast Synthesis of Patternable Few-Layer Transition Metal Dichacogenides with Controllable Stacking Alignment by a Microwave-Assisted Selenization Process," *Chemistry of Materials*, vol. 28, no. 4, pp. 1147–1154, 2016, doi: 10.1021/acs.chemmater.5b04579.

[53] H. Medina *et al.*, "Wafer-Scale Growth of WSe2 Monolayers Toward Phase-Engineered Hybrid WOx/WSe2 Films with Sub-ppb NOx Gas Sensing by a Low-Temperature Plasma-Assisted Selenization Process," *Chemistry of Materials*, vol. 29, no. 4, pp. 1587–1598, 2017, doi: 10.1021/acs.chemmater.6b04467.

[54] Y. Z. Chen, S. H. Lee, T. Y. Su, S. C. Wu, P. J. Chen, and Y. L. Chueh, "Phase-modulated 3D-hierarchical 1T/2H WSe2 nanoscrews by a plasma-assisted selenization process as high performance NO gas sensors with a ppb-level detection limit," *Journal of Materials Chemistry A*, vol. 7, no. 39, pp. 22314–22322, 2019, doi: 10.1039/c9ta05348d.

[55] D. Liu, Z. Tang, and Z. Zhang, "Comparative study on NO2 and H2S sensing mechanisms of gas sensors based on WS2 nanosheets," *Sensors and Actuators, B: Chemical*, vol. 303, no. 2, p. 127114, 2020, doi: 10.1016/j.snb.2019.127114.

[56] W. Yan *et al.*, "Conductometric gas sensing behavior of WS2 aerogel," *FlatChem*, vol. 5, pp. 1–8, 2017, doi: 10.1016/j.flatc.2017.08.003.

[57] B. Cho *et al.*, "Chemical Sensing of 2D Graphene/MoS2 Heterostructure device," *ACS Applied Materials and Interfaces*, vol. 7, no. 30, pp. 16775–16780, 2015, doi: 10.1021/acsami.5b04541.

[58] Z. Wang *et al.*, "Rational synthesis of molybdenum disulfide nanoparticles decorated reduced graphene oxide hybrids and their application for high-performance NO2 sensing," *Sensors and Actuators, B: Chemical*, vol. 260, no. 2, pp. 508–518, 2018, doi: 10.1016/j.snb.2017.12.181.

[59] W. Yan, M. A. Worsley, T. Pham, A. Zettl, C. Carraro, and R. Maboudian, "Effects of ambient humidity and temperature on the NO 2 sensing characteristics of WS 2 /graphene aerogel," *Applied Surface Science*, vol. 450, pp. 372–379, 2018, doi: 10.1016/j.apsusc.2018.04.185.

Chapter-2

CVD growth of self-assembled 2D and 1D WS_2 nanomaterials for the ultrasensitive detection of NO_2

Sensors & Actuators: B. Chemical 326 (2021) 128813

Contents lists available at ScienceDirect

Sensors and Actuators: B. Chemical

journal homepage: www.elsevier.com/locate/snb

CVD growth of self-assembled 2D and 1D WS_2 nanomaterials for the ultrasensitive detection of NO_2

Aanchal Alagh [a,1], Fatima Ezahra Annanouch [a,1], Polona Umek [b], Carla Bittencourt [c], Ayrton Sierra-Castillo [d], Emile Haye [e], Jean François Colomer [d,*], Eduard Llobet [a,*]

[a] Departament d'Enginyeria Electrònica, Universitat Rovira i Virgili, Països Catalans 26, 43007 Tarragona, Spain
[b] Condensed Matter Physics Department, Jožef Stefan Institute, Jamova cesta 39, 1000 Ljubljana, Slovenia
[c] Laboratory of Plasma-Surface Interaction Chemistry (PSI Chem), University of Mons, Av. Nicolas Copernic 1, 7000 Mons, Belgium
[d] Research Group on Carbon Nanostructures (CARBONNAGe), Namur Institute of Structured Matter (NISM), University of Namur, 61 Rue de Bruxelles, 5000 Namur, Belgium
[e] Laboratoire d'Analyse par Réaction Nucléaires (LARN), Namur Institute of Structured Matter (NISM), University of Namur, 61 Rue de Bruxelles, 5000 Namur, Belgium

ARTICLE INFO

Keywords:
Gas sensor
AACVD
CVD
WS_2
TMDs

ABSTRACT

Herein, we report for the first time on the facile synthesis of 2D layered WS_2 nanosheets assembled on 1D WS_2 nanostructures by combining the aerosol assisted chemical vapor deposition (AA-CVD) method with H_2-free atmospheric pressure CVD, for an ultrasensitive detection of NO_2. This synthesis strategy allows us a direct integration of the sensing material onto the sensor transducer with high growth yield and uniform coverage. Two different WS_2 morphologies (nanotriangles and nanoflakes) were prepared and investigated. The results show that the assembly of layered WS_2 nanosheets on a 3D architecture leads to an improvement in sensing performance by maintaining a high surface area in an accessible porous network. The sensors fabricated show stable, reproducible and remarkable responses towards NO_2 at ppb concentration levels. The highest sensitivity was recorded for WS_2 NT sensors, with an unprecedented ultra-low detection limit under 5 ppb. Additionally, this material has demonstrated its ability to detect 800 ppb of NO_2 even when operated at room temperature (25 °C). Regarding humidity cross-sensitivity, our WS_2 sensors remain stable and functional for detecting NO_2 at ppb levels (i.e., a moderate response decrease is observed) when ambient humidity is raised to 50%. An 8-month long-term stability study has been conducted, which indicates that WS_2-NT sensors show a very stable response to NO_2 over time.

1. Introduction

Anthropogenic air pollutants are having a negative impact in human health, since these are responsible for about 4.2 million premature deaths yearly, according to the World Health Organization. [1] Premature deaths related to ambient air pollution, occur mainly from heart disease, chronic obstructive pulmonary disease, lung cancer etc. For instance, nitrogen oxides (NO_x) and, particularly, NO_2 are among the five major pollutants that degrade ambient air quality. NO_x are generated from combustion processes, e.g. motor vehicle exhausts. NO_2 has a direct contribution to the formation of ground level ozone in the stratosphere, acid rain and inorganic ambient particulate matter. [2–5] Exposure to NO_2 may cause respiratory irritation, chronic bronchitis, and asthma (53 ppb set as the annual standard by the U.S. Environmental Protection Agency). [6]

The continuous and widespread monitoring of nitrogen dioxide would require using inexpensive sensing technologies. Nowadays, metal oxide chemoresistors or electrochemical cells are commercially available technologies for detecting NO_2 [4,6–9]. However, the reliable and selective detection of nitrogen dioxide at ppb levels is still far from what currently marketed inexpensive sensors can offer. Therefore, it is crucially important to develop a new generation of reliable, accurate and cost-effective gas sensors that can detect and monitor in real time low concentrations of NO_2 for air-quality monitoring and human health protection.

Inspired by the intensive research efforts devoted to the application

* Corresponding authors.
E-mail addresses: jean-francois.colomer@unamur.be (J.F. Colomer), eduard.llobet@urv.cat (E. Llobet).
[1] Authors with equal contributions to this work.

https://doi.org/10.1016/j.snb.2020.128813
Received 30 April 2020; Received in revised form 7 August 2020; Accepted 25 August 2020
Available online 6 September 2020

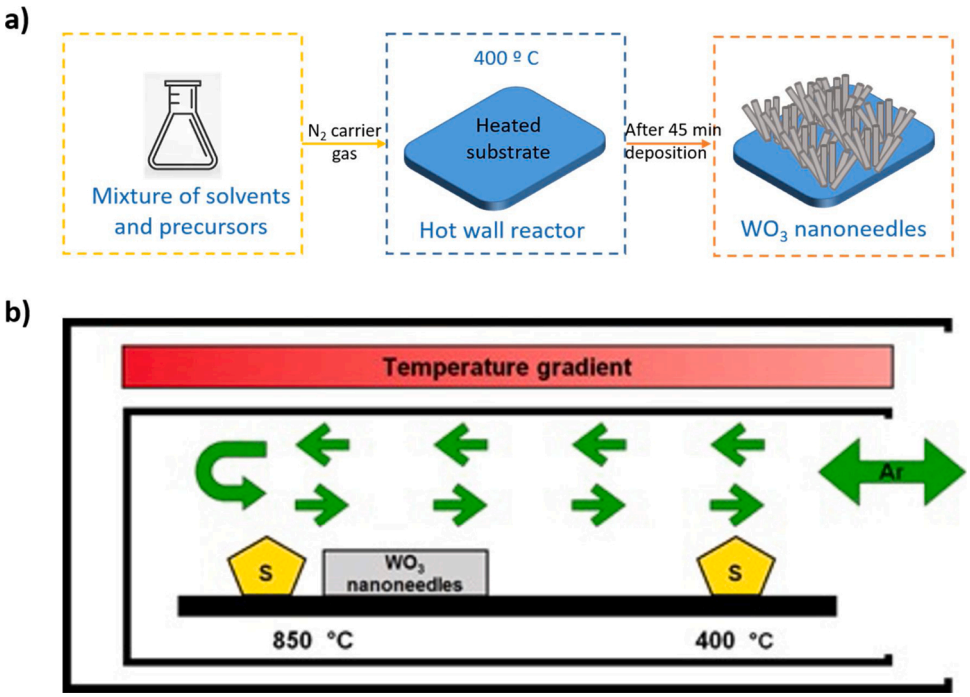

Fig. 1. (a) AACVD synthesis of WO_3 nanomaterials, (b) CVD synthesis of WS_2 nanomaterials.

of graphene nanomaterials for gas sensing, [10–13] 2D layered transition metal dichalcogenides (TMDs) materials have been receiving increasing attention and are becoming the target of research in gas sensing [14–17]. 2D TMDs consist of a metal atomic layer sandwiched between two atomic layers of a chalcogen material (e.g. S, Se, Te). TMDs often appear as many 2D layers stacked one above the other by Van der Waals forces of interaction [14].

Owing to their semiconducting properties, nanoscale thickness and large specific surface area, TMDs hold promise for addressing sensitivity, selectivity, stability and speed (response-recovery time) issues often encountered in gas sensitive materials. [18–20] Indeed, the thinning of the bulk material to a single or few layers leads to a drastic change of its inherent semiconductor properties, primarily due to the confinement of charge carriers in two dimensions (*x*- and *y*-directions) due to the low or absence of interactions in the z-direction [18].

Among the TMDs materials that have demonstrated their usefulness in gas sensing application, WS_2, MoS_2 and SnS_2 are the most studied [21–25]. They have shown promising results towards various gases and vapors of VOCs, at very low operating temperatures. Additionally, TMDs could be used as a scaffold material to which functional groups or complex molecules could be grafted to tune selectivity, employing different approaches such as plasma treatment, low-energy ion implantation/ substitutional doping, covalent or non-covalent functionalization. Such materials can be obtained by means of different routes including chemical or electrochemical Li-interaction and exfoliation [26–28], a mechanical cleavage method [24], liquid-phase exfoliation [29], chemical vapor deposition (CVD) [30], and a wet-chemical method [31].

Despite the past and current efforts to refine the sensing properties of these new materials and facilitate their integration to obtain functional gas sensor devices, TMDs are still facing many shortcomings such as low production yield, difficulties for their integration in standard transducing substrates and weak gas response. In fact, the adoption of these novel materials is somewhat limited by the synthesis processes currently employed to grow layered TMDs. As we mentioned above, there are numerous methods available for the synthesis of TMDs, however, they are subject to specific drawbacks. For instance, mechanical exfoliation produces high quality TMDs sheets, but the method cannot be scaled up for mass production, given its extremely low yield. In contrast, if the same sheets are produced via lithium intercalation exfoliation route, yield is substantially increased but with loss of material integrity and alteration of semiconducting properties due to a change in structure caused by lithium ions intercalating in between the exfoliated sheets [32]. Similarly, the production efficiency of TMD nanosheets is high if grown via hydrothermal or solvothermal processes at the cost of losses in crystalline quality. Moreover, most of the growth techniques described above do not allow the direct growth and integration of the desired material onto the sensor transducer, since they are not compatible with a variety of sensor substrates (e.g., ceramics, silicon, silicon MEMS or flexible polymers). Consequently, transfer techniques are needed to remove the material from its growth substrate and to place it onto the application one, which negatively affect fabrication costs as well as the stability of the sensing material (e.g. uncontrolled defects are generated in the transfer process or residues from solvents or polymers remain at the surface after the transfer process is completed). In an attempt to address the issue of poor gas responsiveness, Koo and co-workers reported that gas sensitivity could be ameliorated when the number of the 2D TMDs edges is increased, since higher catalytic activity locates at the edges rather than at the basal plane of the 2D sheets [15]. However, most of the techniques reported lead to the formation of materials with large basal planes and the assembly of 2D TMDs nanosheets into 3D nanostructures remains highly challenging.

Hence, to overcome all the above-mentioned drawbacks, we report for the first time the direct growth on standard ceramic transducers, of a 3D assembly of WS_2 nanosheets on 1D nanostructures, using a two step-CVD (it combines the aerosol-assisted CVD and CVD methods) for developing NO_2 chemoresistive sensors. The nanosheets are grown at atmospheric pressure under argon gas flow without H_2 assistance. This makes the process significantly simple and thermally safe. Two different morphologies were grown in the form of 3D assembly of 2D WS_2 nanoflakes (NFs) and/or nanotriangles (NTs) on WS_2 nanorods and/or nanoneedles respectively. Throughout the paper, these two morphologies are denoted as WS_2 NFs and/or WS_2 NTs respectively. Their phase composition, morphology, microstructure and chemical composition have been characterized. Moreover, the gas-sensing performance of these materials towards NO_2 have been studied under both dry and

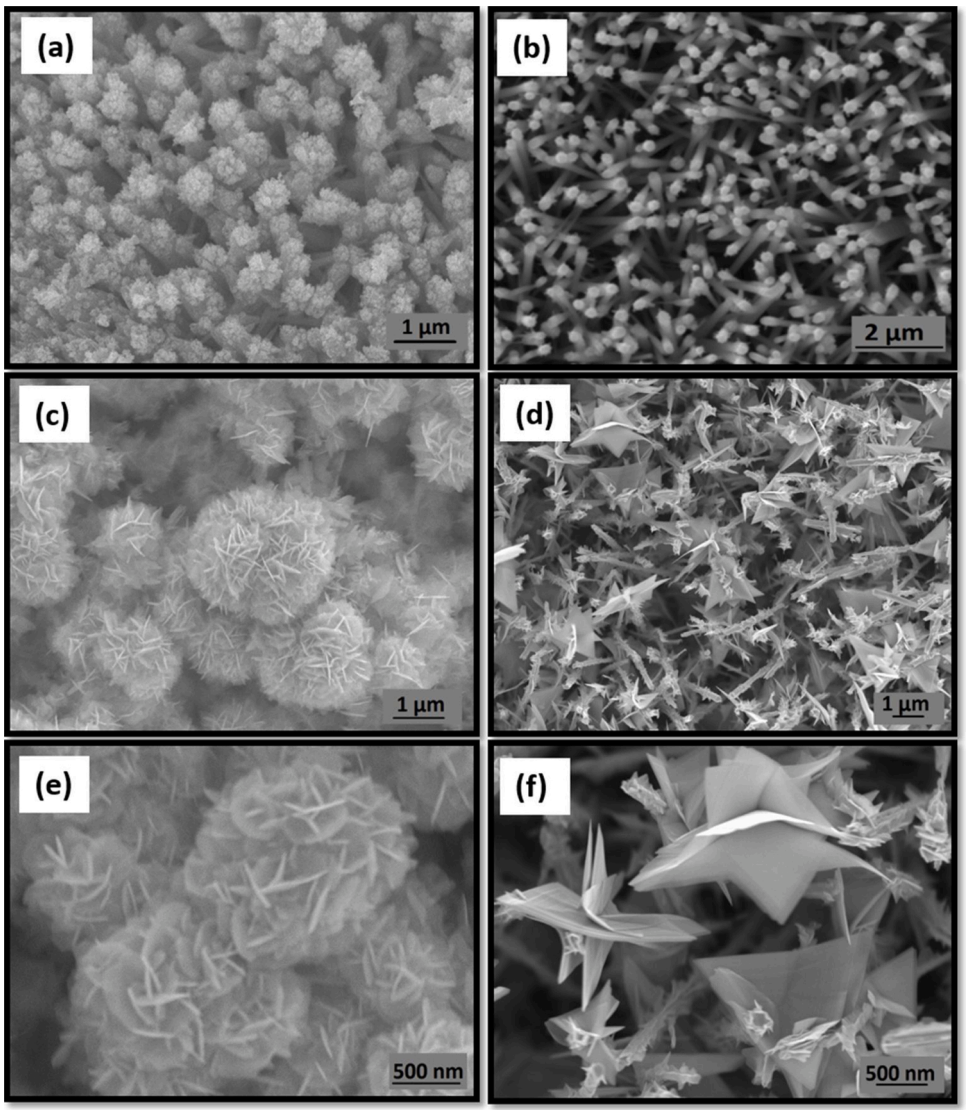

Fig. 2. SEM images of (a) WO_3 nanorods, (b) WO_3 nanoneedles, (c and e) WS_2 nanoflakes and (d and f) WS_2 nanotriangles.

humid atmospheres. WS_2 NT sensors exhibited very high NO_2 responses with good stability and, an unprecedented low detection limit below 5 ppb at low operating temperature was achieved. Furthermore, the response towards potentially interfering species such as H_2S, H_2 and NH_3 has been studied as well in order to assess NO_2 selectivity. Finally, a discussion on the NO_2 sensing mechanism for the 3D assembly of WS_2 nanosheets is given as well.

2. Experimental

2.1. Material synthesis

First step deposition: either WO_3 nanorods (NRs) or nanoneedles (NNs) were deposited directly on alumina substrates (Pt-interdigitated electrodes with a gap of 300 µm on the front side and Pt- resistive heater meander on the backside, the electrode area was 2.5 mm × 2.5 mm), via AACVD (Fig. 1a) using tungsten hexacarbonyl $W(CO)_6$ (50 mg, purity 97%) dissolved in a mixture of acetone and methanol in a ratio of 3:1. It is worth noting that by changing the nitrogen flow during the AACVD deposition, the obtained morphology can be varied from NRs to NNs. First, the substrates were cleaned with acetone, ethanol and distilled water, dried with air and then placed inside a CVD hot wall reactor. Next, the precursor along with the organic solvents were mixed in a glass flask, sonicated for 20 min and then placed in an ultrasonic bath, to convert the mixture to an aerosol. The deposition temperature was set to 400 °C. Nitrogen gas was used as a carrier gas (0.5 L/min to obtain NRs and 1 L/min to obtain NNs), in order to transport the aerosol to the heated zone inside the reactor. The duration of the complete growth process was kept under 45 min. After deposition, the samples were subjected to annealing at 500 °C for 3 h in dry, zero-grade air at a flow rate of 2 L/min.

Second step deposition: WS_2 was synthesized via the sulfurization of the previously grown WO_3 nanomaterial films using an atmospheric pressure CVD technique, as shown in Fig. 1b. For the two different morphologies of WO_3 nanostructures, the same method of sulfurization was adopted. For sulfurization of WO_3, S powders (99.5%), purchased from Alfa Aesar were used without any further purification. Prior to the sulfurization process, the quartz tube was flushed with 0.725 L/min of argon to remove any oxygen content in the reactor. Two ceramic boats were utilized each one loaded with 0.220 g of sulfur powder. The two boats were placed at different temperature zones of the deposition furnace such that one was positioned at the 40 °C temperature zone and the other at 850 °C temperature zone (total 0.440 g). WO_3 samples were placed at the 850 °C temperature zone in the downstream of the argon flow in the quartz tube reactor. The initial step of sulfurization process goes for a span of 30 min wherein the S powder set at the 850 °C zone

sublimates. The optimized second sulfurization step was performed by inserting the quartz tube in the hot zone of the furnace, such that the S powder which was initially placed at 40 °C reaches the 400 °C temperature zone. The WO_3 sample remained at 850 °C as the quartz reactor was moved over a few centimeters.

2.2. Material characterization techniques

The microstructure of the material was characterized using scanning electron microscopy (SEM-FEI Quanta 600). The chemical analysis has been performed by X-ray photoelectron spectroscopy (XPS), using a K-Alpha Thermo Scientific spectrometer. High-resolution transmission electron microscopy (HRTEM) (Jeol, JEM-2100) was used to analyze crystal structure at the atomic level. XRD measurements were made using a Bruker-AXS D8-Discover diffractometer. Lastly, RAMAN spectroscopy measurements were carried out using Renishaw in Via, laser 514 nm, ion argon-Novatech, 25 mW.

2.3. Gas sensing tests

The gas sensing properties of the different nanomaterials were measured by monitoring the change in electrical resistance of the sensors upon exposure to different target gaseous species (NO_2, NH_3, H_2S, H_2) at different operating temperatures (25 °C, 100 °C, 150 °C). A Teflon test chamber of 35 mL in volume was connected to a fully automated, continuous gas flow measurement set-up able to supply diluted gas mixtures. Sensors were placed inside this test chamber and their electrical resistance was measured using an Agilent-34972A multimeter. To control the operating temperature of a given sensor, its heater was connected to an external power supply (Agilent, model 3492A). The total flow rate was kept constant at a value of 100 mL/min throughout the measurements. Some experiments were conducted under a humid background. Since aging often helps achieving more stable responses, sensors were kept for a week at 150 °C under a flow of dry air before their gas sensing properties were investigated.

3. Results and discussion

3.1. Material synthesis and characterization

Tungsten trioxide NRs and/or NNs were directly deposited on alumina substrate using AACVD method. The as-deposited films were strongly adherent to the substrate, with dark blue color, which changed to light green after annealing (Fig. S1a). The color of the film was again changed to dark black after undergoing the process of sulfurization (Fig. S1b). The morphology of the synthesized material (WO_3 and WS_2) was examined using a scanning electron microscope. Fig. 2a and b show the SEM imaging results of the as-prepared material before it undergoes the sulfurization process. The results demonstrate that the starting material was composed of either thick nanorods with aggregates of nanoparticles at their tips (Fig. 2a) or thin and elongated nanoneedle structures (Fig. 2b). Besides, it is observed that the grown nanostructures are randomly oriented, tilted and with homogeneous distribution over the substrate.

Also, SEM images revealed that the morphology of WO_3 samples (NRs and NNs) changed due to the sulfurization process. These changes can be observed very well from the obtained images, as shown in Fig. 2c–f. It can be seen that WO_3 nanorods were transformed to a 3D assembly of 2D WS_2 NFs on WS_2 NRs, like flower structures with multilayered sheets as petals. In contrast, the WO_3 nanoneedles, were transformed to a 3D assembly of large WS_2 triangle-shaped crystals (NTs) on WS_2 nanoneedles. Furthermore, a consistent change in color for both deposited films is observed, which clearly indicates the formation of homogeneous and uniform film of WS_2. Thus, the final morphology of the WS_2 materials strongly depends on the morphology of the starting WO_3.

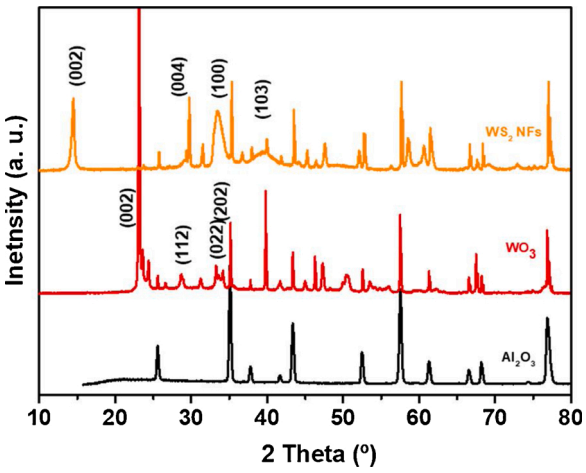

Fig. 3. XRD diffractograms for a bare Al_2O_3 substrate (lower patter), WO_3 NRs (middle pattern and WS_2 NFs (upper pattern).

WS_2 samples were investigated by using X-ray powder diffraction (XRD). The XRD diffractograms of a bare Al_2O_3 substrate was compared to those of WO_3 nanorods or WS_2 (coating Al_2O_3 substrates) in view of checking for the presence of tungsten oxide in sulfurized samples. Fig. 3 shows an XRD spectrum for WS_2 NFs. From the spectrum, it is clear that many reflection peaks can be perfectly indexed to the hexagonal P63/*mmc* space group, indicating that the structure of the WS_2 phase is 2H-WS_2 [33]. Besides, we noticed the presence of peaks belonging to alumina substrate [34]. Moreover, XRD did not detect any peaks corresponding to WO_3 impurities. Equivalent results were observed for WS_2 NT films (see Fig. S2, Supporting Information).

X-ray spectroscopy (XPS) was used to investigate the chemical states and stoichiometry of WO_3 and WS_2 films. Fig. 4 depicts an example of the W 4f, S 2p and O 1s core level spectra recorded for the WO_3 NNs, WS_2 NTs and WS_2 NFs. Considering the W 4f spectra of WO_3 NNs (Fig. 4a), three components are observed that are associated to the W $4f_{7/2}$ and W $4f_{5/2}$ spin orbit doublet, and a low intensity peak originating from the W $5p_{3/2}$ core level. For the WO_3 NNs, the W4f doublet is centered at 35.4 eV and 37.5 eV and the W 5p weak peak around 41 eV. These values are in good agreement with those found in the literature for W^{+6} in WO_3 stoichiometric films [35]. The W 4f spectrum can be properly fitted by a doublet, confirming the nature of WO_3 material with W only present in the six-valent state. Moreover, one can note the presence of oxygen and the absence of sulfur on this material. Concerning the WS_2 NTs and WS_2 NFs, the same features that are observed in the WO_3 can be observed with a binding energy shift of the different components. Here, the W4f doublet is centered at 32.7 eV and 34.8 eV and the W 5p weak peak around 38.2 eV. The perfect fitting of the spectra for both WS_2 NTs and WS_2 NFs by a doublet confirms the presence of WS_2 with values in good agreement with those found in the literature for W^{+6} in WS_2 stoichiometric films [35], without the presence of oxide. This is otherwise correlated with the quasi absence of oxygen and the presence of sulfur. Indeed, in the S 2p spectrum, the known doublet peaks, S $2p_{1/2}$ and S $2p_{3/2}$ at 163.4 and 162.2 eV, respectively, with a spin–orbit energy separation of 1.2 eV corresponding to WS_2 (S^{2-} oxidation state), can be seen in Fig. 4b. The experimental shape is very well fitted by a doublet demonstrating the presence of the unique phase WS_2. Considering the O 1s region (Fig. 4c), the difference between the two materials is well visible, with a lower intensity peak of oxygen in the WS_2 material around 533 eV, most likely related to physically adsorbed oxygen molecules. This can be compared to O 1s core level spectrum of WO_3 material with a main peak at 530.8 eV related to the WO_3 (O^{2-}oxidation state). Based on the XPS analysis, the complete conversion of WO_3 to WS_2 is demonstrated for both morphologies (at least for the sample depth probed by XPS, which is considered a surface analysis method),

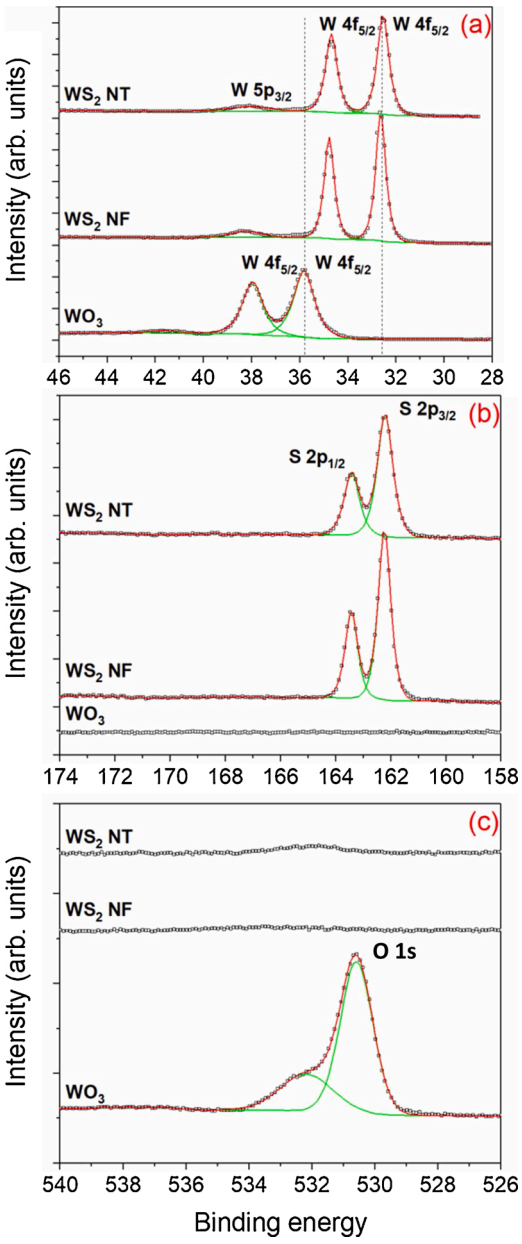

Fig. 4. XPS spectra of the W 4f (a), S 2p (b) and O 1s (c) core levels for WO_3 NNs (before the sulfurization reaction), WS_2 NFs and WS_2 NTs (i.e., after the sulfurization reaction).

since sulfurized materials show the same stoichiometry than that of a WS_2 single crystal.

The purity of the grown films was studied by using Raman spectroscopy, which is a powerful tool to evaluate the crystal quality [36] and to determine whether a TMD material is monolayer or multilayer. Fig. 5a shows an example of WO_3 NRs Raman spectrum. All the peaks (271 cm^{-1}, 327 cm^{-1}, 715 cm^{-1} and 805 cm^{-1}) are indicative of monoclinic tungsten trioxide phase, which is in a good accordance with our previous reported works. [37–39] Fig. 5b and c indicate the Raman spectra collected from WS_2 NTs and NFs films, respectively. Two important Raman peaks characteristic of 2H-WS_2 were observed in both samples: E^1_{2g} at 348.5 and A_{1g} at 414.5 cm^{-1} associated to WS_2 NTs, and E^1_{2g} at 349 and A_{1g} at 416.8 cm^{-1} appertained to WS_2 NFs. The E^1_{2g} mode corresponds to the in-plane vibration of W and S atoms and the A_{1g} mode indicates vibration of sulfides in out of plane direction. [40,41] The ratio of relative peak intensity $I[E^1_{2g}]/I[A_{1g}]$ for both samples turns out to be 0.89, revealing the formation of multilayered WS_2 [42]. In

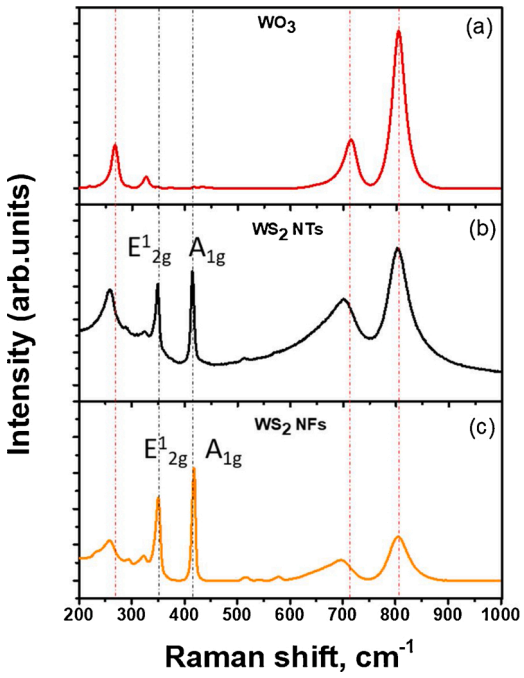

Fig. 5. Raman spectra of (a) WO_3 NRs, (b) WS_2 NTs and (c) WS_2 NFs.

contrast, at 700 cm^{-1} and 803 cm^{-1}, two broad peaks were detected with low intensity compared to WO_3 spectrum, indicating the presence of some WO_3 impurities. These results are indicative that Raman is more sensitive than XRD or XPS for detecting traces of tungsten oxide remnants within the WS_2 films. Additionally, it is clear that the morphology did not affect the composition and crystallinity of the WS_2 material.

Fig. 6 shows an example of TEM and HRTEM images obtained from a WS_2 NT sample. TEM analysis revealed that upon sulfurization of WO_3 nanoneedles (i) transformed to WS_2 nanoneedles (Fig. 6) and (ii) that sulfurization triggered the growth of WS_2 triangular nanosheets from side walls and tips of WS_2 nanoneedles (Fig. 6a and Fig. S3a), Supporting Information). Beside nanoneedles also nanotubes with diameters up to 20 nm were observed (Fig. S3b). The HRTEM image of a triangular WS_2 nanosheet with its corresponding FFT pattern show the hexagonal lattice structure with lattice *d*-spacing of 0.28 nm corresponding to the 2H-WS_2 (100) planes (PDF pattern 84-1398) (Fig. 6b). HRTEM images of the WS_2 nanoneedles tip and its sidewall (Fig. 6c and d) reveal the (002) crystal plane distances are expanded in comparison to the distance of 0.616 nm in PDF pattern 84-1398. For instance,*d*-spacings of (002) planes decrease from the outer side toward the inner part of the nanorod (Fig. 6d) from 0.68 to 0.62 nm. The lattice expansion may be connected to crystallographic defects, especially dislocations in the nanoneedles (see red arrows in Fig. 6c and d) [43,44]. TEM analysis did not reveal the presence of WO_3 impurities in the WS_2 materials.

Thus, XRD, XPS, and HRTEM results show good accordance in between them and support the total transformation of WO_3 nanomaterials to WS_2 ones. Moreover, these results were similar for the two morphologies (NFs and NTs) achieved. This apparent discrepancy with Raman results in which the presence of tungsten oxide traces are detected can be explained as follows. XPS is a method that only probes the surface of the sample while XRD and Raman probe the entire sample. Raman is far more sensitive than XRD. All these results taken together are indicative that some tungsten oxide traces remain in the core of the material.

3.2. Gas sensing results and discussion

The gas sensing performances of WS_2 NF or WS_2 NT sensors were examined towards different concentrations of NO_2 and other species

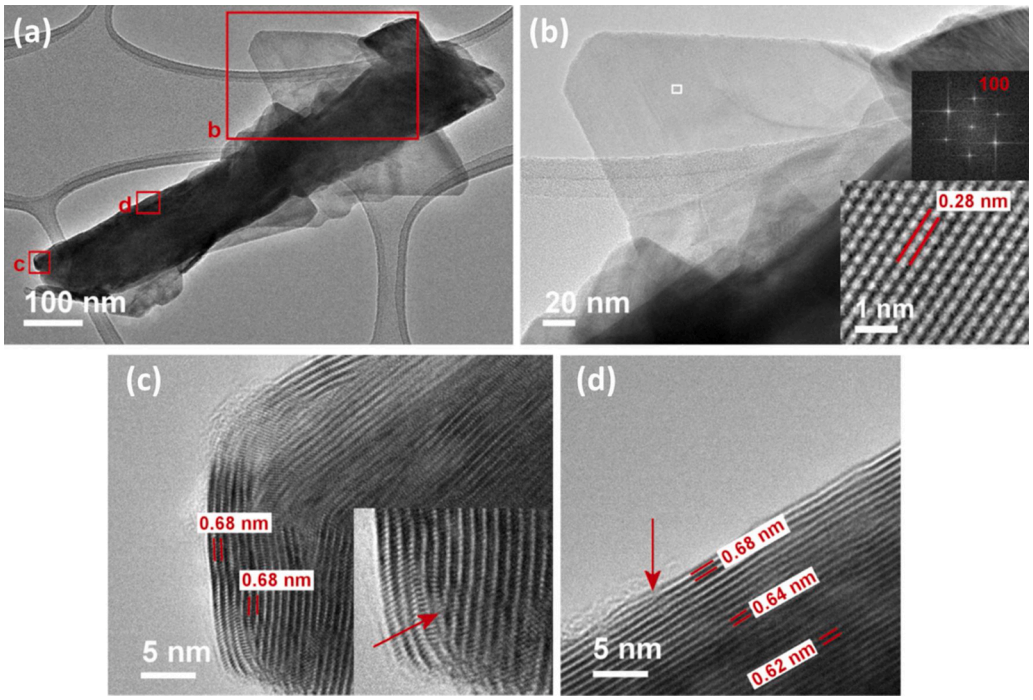

Fig. 6. TEM image of a WS_2 nanoneedles (a). Triangular WS_2 nanosheet growing from a nanoneedles longest side. The white frame in the image indicates the area where HRTEM image was taken (bottom inset); the upper inset is the corresponding FFT pattern (b). HRTEM images of the WS_2 nanoneedle end (c), and sidewall of the WS_2 nanoneedle (d). Arrows in panels (c) and (d) are pointing to dislocations. Red frames in panel (a) indicate the areas shown in HRTEM images (b), (c) and (d). (For interpretation of the references to colour in this figure legend, the reader is referred to the web version of this article.)

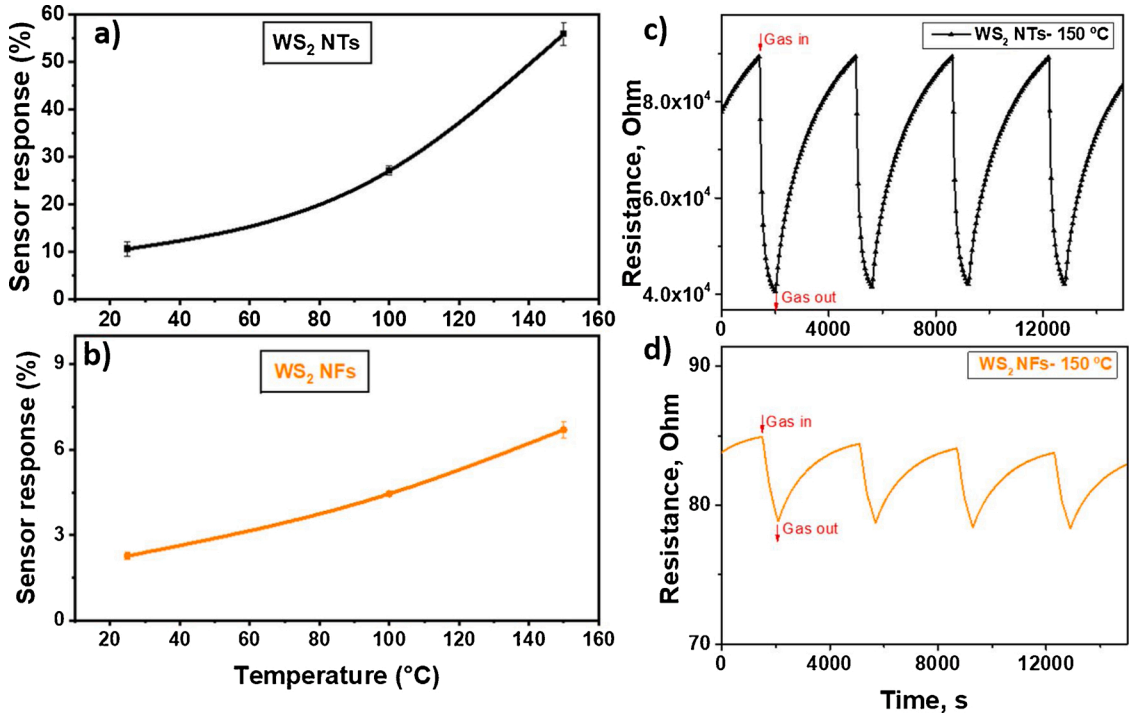

Fig. 7. (a and b) gas sensor response of WS_2 NTs and WS_2 NFs as a function of temperature, towards NO_2 at 800 ppb and 300 ppb, respectively and (c and d) electrical resistance change of both sensors operated at 150 °C, toward these concentrations.

such as H_2S, H_2 and NH_3. For all direct-current resistance measurements, the target gas was injected for 10 min into the test chamber where sensors were placed, which was followed by 50 min purging with a dry air flow for sensors to regain their initial baseline resistances. The equation used to calculate sensor response is as follows:

$$R = \frac{(R_{air} - R_{gas})}{R_{air}} * 100 \quad (1)$$

To study the effect of the operating temperature on sensor behavior, various NO_2 gas measurements were performed at temperatures ranging from 25 °C to 150 °C. Fig. 7, panels a) and b) depict the intensity of sensor responses as a function of the operating temperature. It is observed that sensor response for both morphologies, WS_2 NFs as well as WS_2 NTs increased almost linearly with the increase in operating temperature. This can be explained well by enhanced adsorption of gas molecules at higher temperatures. Indeed, as the temperature is

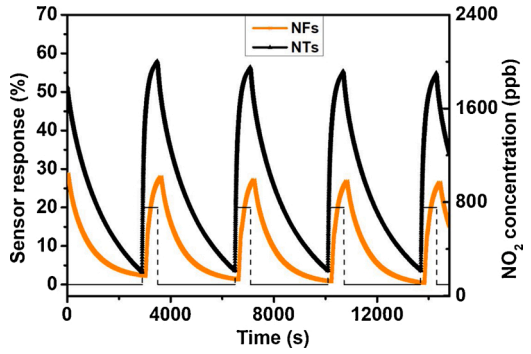

Fig. 8. WS_2 NFs (orange), WS_2 NTs (black) sensor responses (4 replicate response and recovery cycles) towards 800 ppb of NO_2 at the operating temperature of 150 °C.

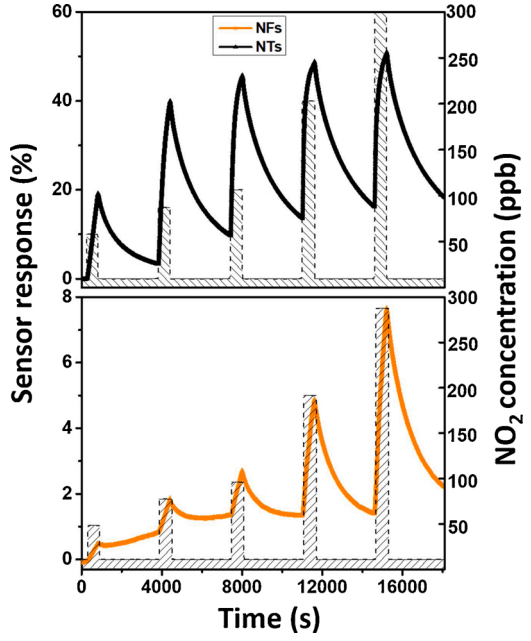

Fig. 9. WS_2 NF (orange), WS_2 NT (black) sensor response and recovery towards pulses of increasing concentrations of NO_2 gas (from 50 to 300 ppb). Sensors were operated at 150 °C.

increased the activation barrier is lowered which enhances the rate of gas adsorption on the surface, leading to a much higher response at an elevated temperature. However, measurements beyond 150 °C were not performed, since the evaporation of sulfur would start and the formation process of WO_3 will initiate leading to a formation of a WO_3/WS_2 composite. Thus, for subsequent studies, 150 °C was considered as the optimal working temperature for both types of sensors. This operating temperature is quite low in comparison to the standard operating temperatures for most metal oxide gas sensors. Fig.7, panels b) an c) show the evolution of the electrical resistance of the sensors operated at 150 °C under repeated exposure and recovery cycles of NO_2. As we can see WS_2 NT films are more resistive than WS_2 NF films, since the baseline resistance of WS_2 NTs is significantly higher than that of WS_2 NFs.

Fig. 8 shows typical repeated response and recovery cycles for WS_2 NF and WS_2 NT sensors towards 800 ppb of NO_2. As it is clear from the figure, sensors show a decrease in their electrical resistance when exposed to NO_2 (i.e., an oxidizing gas), indicating a p-type semiconducting behavior. This can be explained by the spontaneous adsorption of NO_2 gas molecules on the WS_2 surface, thereby withdrawing electrons via the valence band causing an increase in hole concentration and resulting in an overall decrease in the electrical resistance of the film. [45] Moreover, both sensors show stable, reproducible and remarkable responses towards 800 ppb of NO_2 gas. While the WS_2 NF sensor response is 26.6%, the response of the WS_2 NT sensor is significantly higher and reaches 56%.

Also, the sensors were exposed to consecutive concentration pulses of NO_2 that ranged from 50 to 300 ppb, as depicted in Fig. 9. During these measurements, the two sensor types were tested at five different concentrations of NO_2 at a constant operating temperature of 150 °C. A diluted mixture of NO_2 in dry air was injected for 10 min in steps of increasing concentrations of 50, 80, 100, 200 and 300 ppb. It is evident from the results obtained that there is an increase in response with each increment in analyte concentration. The WS_2 NF sensor response was calculated to be 0.16%, 0.96%, 2.28%, 3.41%, and 6.69% for 50, 80, 100, 200 and 300 ppb of nitrogen dioxide, respectively. In contrast, the response increased to higher values (19.6%, 38.04%, 39.3%, 40.265, 41.75%) for the WS_2 NTs sensor. Hence, WS_2 NTs are significantly more sensitive to NO_2 than WS_2 NFs. These results encouraged us to investigate the responses of WS_2 NTs towards NO_2 at concentrations lower than 50 ppb.

Fig. 10a and b present the responses of WS_2 NTs towards very low concentrations of NO_2 (5 ppb and 10 ppb) at 150 °C. It is clearly observed that the nanomaterial was able to detect such small concentrations with good responses and enough signal to noise ratio. For 5 ppb and 10 ppb of NO_2 the responses recorded were 3.20% and 7.23% respectively. It is worth noting that no responses above the noise level were obtained from WS_2 NFs at such low concentrations of NO_2. Hence, the detection limit is roughly 50 ppb of NO_2 for WS_2 NFs, while this detection limit is clearly below 5 ppb of NO_2 for WS_2 NTs. Indeed, considering the low noise levels observed in Fig. 10 a, the limit of detection for NO_2 lies in the ppt concentration levels. To the best of our knowledge, none of the reported works in the literature have achieved such a small detection limit of NO_2 gas (below 5 ppb) using a WS_2 nanomaterial. Fig. 10c depicts the response of WS_2 NTs to pulses of 10 and 20 ppb of nitrogen dioxide. Five consecutive replicate measurement sequences were performed to study repeatability. Similarly, Fig. 10d shows four replicate measurement sequences for concentration pulses ranging from 50 to 800 ppb of NO_2. From these results, it is clear that WS_2 NTs were able to discern between all the concentrations tested. Additionally, sensor responses were remarkably stable and reproducible, which can be attributed to the direct growth of the nanomaterial on the sensor transducer. While all the above-discussed measurements were performed at the operating temperature of 150 °C, Fig. 10e shows the responses towards 800 ppb of NO_2 of WS_2 NTs operated at room temperature. Despite the higher drift experienced in the baseline resistance, surely due to the difficulty of desorbing NO_2 molecules from the surface during the cleaning cycles at room temperature, the nanomaterial was able to detect NO_2 at room temperature with an acceptable and reproducible response of 10.6%. To further study the sensing performance of WS_2 NTs, its behavior in a humid environment was considered as well. The effect of ambient moisture was studied as it is well known that water vapor can affect sensor response by affecting its electrical resistance in a similar way to that of a reducing gas, resulting in an interfering effect for gas detection. Fig. 10f shows three replicate sensor response and recovery cycles towards 800 ppb of NO_2 for a WS_2 NT sensor operated at 150 °C in dry (~3% RH @ 25 °C) and humid (50% RH @ 25 °C) backgrounds. One can observe that under humid conditions, sensor remains fully functional with good and reproducible response. However, there is a tolerable decrease in response intensity, since response decreased from 56% to 30%. It is worth noting that most of the reported studies on layered TMD gas sensors have not studied the effect of ambient humidity on sensing performance, an essential aspect for the real application of gas sensors.

The response toward NH_3, H_2S, H_2 was studied as a way to assess the potential selectivity of the nanomaterials studied in the detection of NO_2. Typical sensor response and recovery signals for these reducing

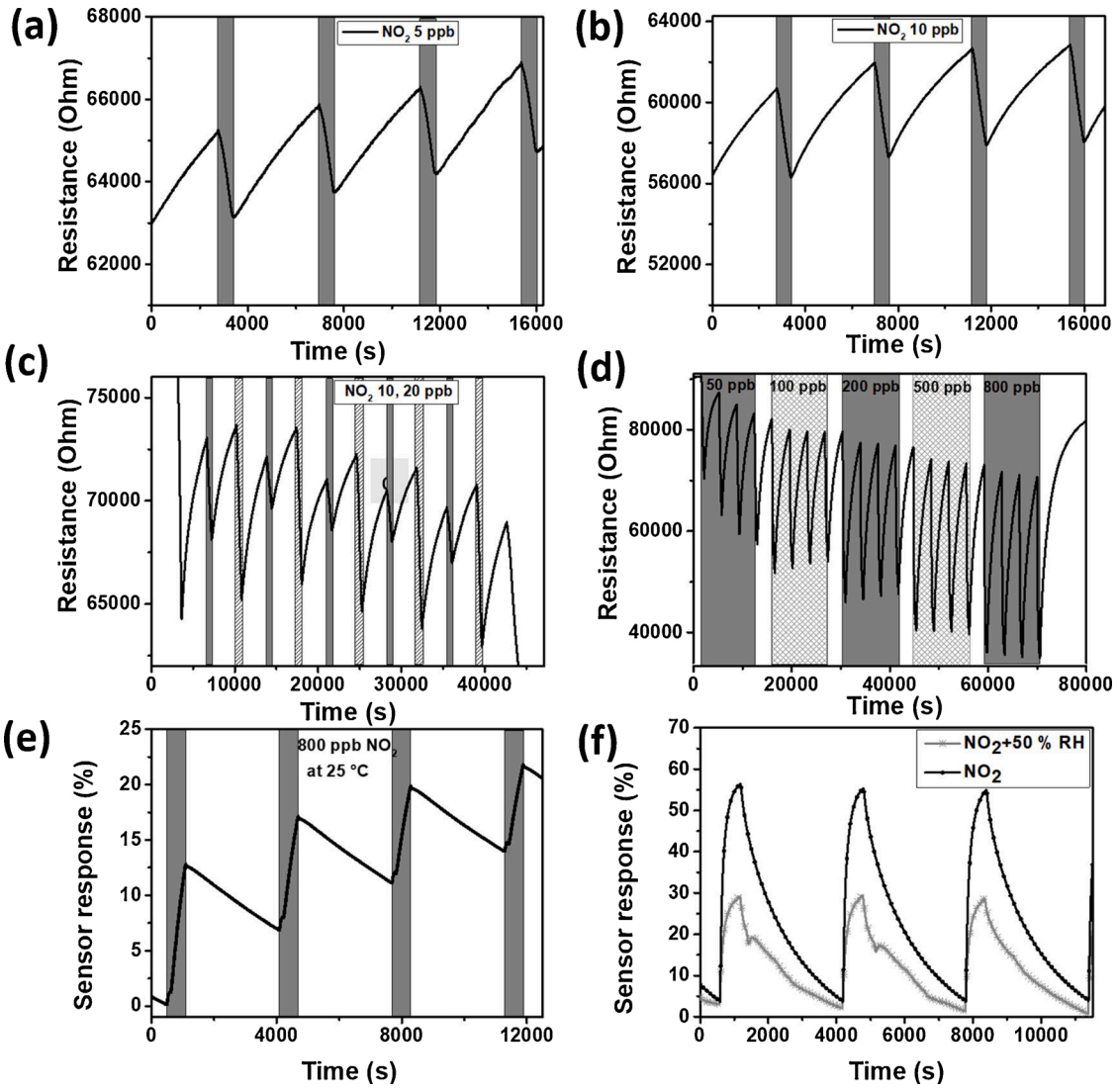

Fig. 10. Repeated response and recovery cycles for a WS_2 NT nanomaterial towards different concentrations of NO_2. Unless otherwise specified, the operating temperature was set to 150 °C. (a) 5 ppb; (b) 10 ppb; (c) five replicate measurements for consecutive 10 and 20 ppb pulses; (d) four replicate measurements for increasing concentration pulses ranging from 50 to 800 ppb; (e) four replicate measurements for 800 ppb pulses while operated at room temperature; (f) three replicate measurements for 800 ppb in dry and 50% RH backgrounds.

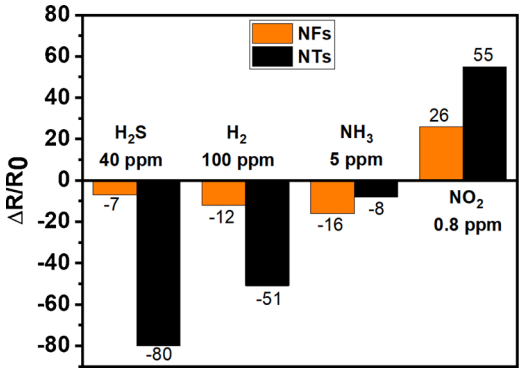

Fig. 11. Response histogram of WS_2 NFs and WS_2 NTs sensors operated at 150 °C.

species can be found in Fig. S4. The concentrations tested for these interfering species were chosen to be much higher than that of the target gas. Fig. 11 summarizes the obtained results. The responses towards these species are negative, because sensor resistance increases in the presence of these electron donor species, which further confirms the p-type behavior of our WS_2 nanomaterials. It is evident from the bar graph that both WS_2 NF and WS_2 NT sensors were highly sensitive and NO_2. NO_2 response is significantly higher than the one recorded for any of the other species tested. Besides, it is noticeable that WS_2 NTs sensor showed high responses to H_2S, however it must be stressed that the concentration tested for hydrogen sulfide was fifty times higher than the one for NO_2. These results are in line with previously reported theoretical studies indicating that the interaction of the NO_2 molecule with the surface of 2D TMDs is characterized by higher adsorption energy and charge transfer than for other molecules such as NH_3 or H_2S [21]. These results indicate that WS_2 sensors show potential for the selective detection of NO_2 traces, provided some surface functionalization is conducted to decrease the current cross-sensitivity experienced.

Based on the obtained results, sensor with large nanotriangular sheets assembled on 1D nanoneedles (WS_2 NTs) displayed the best NO_2 gas sensing performances. This can be attributed to the difference in the morphology, since it can have a huge impact on how gas molecules interact with and get adsorbed on the sensing surface. Further, the material characterization results showed that both nanomaterials are

Table 1
Comparison of the sensing properties to NO_2 of resistive gas sensors based on different WS_2 sensing materials.

Structure	Working temp. (℃)	Studied conc.	Response (%)	Sensitivity (Response%/ppm)	Detection limit	Reference
Nanotriangles	150	800 ppb	55.9	70	<5 ppb (experim.)	This work
Nanotriangles	25	800 ppb	10.6	13.2	N/A	This work
Nanoflakes	150	800 ppb	26.6	33.2	~50 ppb (experim.)	This work
Nanoflakes	25	300 ppb	0.5	1.7	N/A	This work
Nanosheets	NA	25 ppm	8.7	0.3	N/A	[26]
Nanosheets	25	5 ppm	68.4	13.7	0.1 ppm (experim)	[27]
Nanostructure (aerogel)	180	2 ppm	3	1.5	10 ppb (theoret.)	[28]
Nanostructure	25	5 ppm	2.5	0.5	N/A	[50]
Nanosheets	160	5 ppm	121	242	< 200 ppb (experim.)	[51]

N/A: Not available; experim.: experimentally measured; theoret.: theoretically calculated.

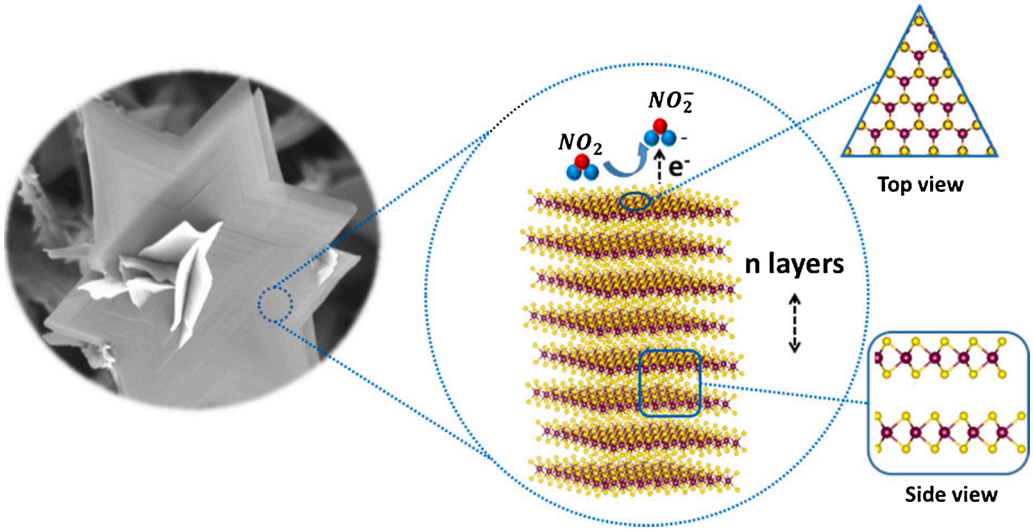

Fig. 12. Gas sensing mechanism of WS_2 nanosheets (W = pink, S = yellow) toward NO_2 gas molecules. (For interpretation of the references to colour in this figure legend, the reader is referred to the web version of this article.)

identical in terms of chemical composition and crystallographic phase, whereas the only difference was in their morphologies.

Table 1 summarizes the main results achieved and puts them in context with the state of the art. In this table, the performance in the detection of NO_2 reported here are compared against those in the literature NO_2 gas detection. From these results it is clear that sensors based on WS_2 NTs show very remarkable gas responses with high sensitivity an unprecedented detection limit below 5 ppb for NO_2 gas at 150 °C. The long-term stability of the NO_2 sensing properties for WS_2 materials was studied (see the Supporting Information, Fig. S5). It was found that WS_2-NTs show a very stable response to NO_2 over 8 months of tests.

3.3. NO_2 gas sensing mechanism

NO_2 molecules behave as electron acceptors and H_2S, H_2 or NH_3 behave as electron donors. The resistance of the WS_2 devices decreases in the presence of NO_2 and increases in the presence of the above mentioned electron donor species, which is indicative that our multilayer tungsten disulfide behaves as a p-type semiconducting material. While single layer WS_2 behaves usually as an n-type semiconductor, [46] the n-type or p-type nature of WS_2 depends on its morphology, nanostructure alignment on the substrate or even on the presence of few carbon atoms substituting sulfur atoms. [47] The p-type behavior of WS_2 achieved via the sulfurization of WO_3 has been reported previously. [48]

The nitrogen dioxide sensing mechanism in WS_2 NFs or NTs (Fig. 12) involves the adsorption of NO_2 molecules both on the edges of flakes or triangles and on their surface (or basal plane). Upon adsorption, electronic charge is injected from WS_2 towards the gas molecule, which generates a hole accumulation zone that results in a decrease in the resistance of the film. According to previously reported computational chemistry studies in MoS_2, the edges are far more important than the basal plane for the adsorption of NO_2, because the adsorption energy of nitrogen dioxide at S edges is higher (~−0.4 eV) than at the basal plane (~−0.13 eV) and the associated electronic charge transfer is ~0.5e and 0.1e, respectively. [49] These adsorption energies suggest that the interaction between WS_2 and NO_2 would involve the physisorption of nitrogen dioxide. This is supported by the experimental results showing that sensor baseline resistance can be regained when flowing the sensor surface with clean air, even when sensors are operated at room temperature (i.e. 25 °C). It is worth noting that the assembly of WS_2 nanotriangles on 1D nanoneedles or nanorods shows a highly increased porosity and increased number of edges for gas interaction in comparison to the more closely packed nanoflake assembly. This explains the superior gas sensing properties recorded for WS_2 with nanotriangle morphology.

4. Conclusions

We have demonstrated an efficient route to synthesize high quality,

multi-layered WS_2 nanosheets homogeneously assembled in 1D nanoneedles or nanorods. The nanomaterials are directly grown onto standard ceramic application transducers for developing chemoresistive gas sensors, using a double step CVD technique. It can be concluded that the final morphology of WS_2 films heavily depends on that of pre-deposited WO_3 layers, which is easily scalable and controllable, making it possible to meet the demands for different applications. Gas sensing results showed that WS_2 NTs exhibited excellent NO_2 gas sensing characteristics at low operating temperature, even at room temperature. The high sensitivity observed and the unprecedentedly low limit of detection achieved (in the ppt range), were attributed to the porous surface and the increased number of sulfur edges in WS_2 NTs, which were created by the random 3D assembly of WS_2 nanosheets on WS_2 nanoneedles. Furthermore, WS_2 NTs have shown an excellent response stability during long-term stability tests conducted over an 8-month period. Hence, these results shed light on the important role played by the morphology in enhancing sensor performance. Furthermore, good stability and reproducibility of the responses were observed as well and these were related to the direct growth of the material on the sensor transducer. Henceforth this study paves a way to develop WS_2 gas sensors with improved quality for NO_2 detection.

CRediT authorship contribution statement

Aanchal Alagh: Investigation, Formal analysis, Data curation, Writing - original draft. **Fatima Ezahra Annanouch:** Conceptualization, Supervision, Validation, Formal analysis, Writing - review & editing. **Polona Umek:** Investigation, Formal analysis, Writing - review & editing. **Carla Bittencourt:** Investigation, Formal analysis, Writing - review & editing. **Ayrton Sierra-Castillo:** Investigation. **Emile Haye:** Formal analysis, Writing - review & editing. **Jean François Colomer:** Conceptualization, Supervision, Writing - review & editing, Funding acquisition. **Eduard Llobet:** Conceptualization, Supervision, Writing - review & editing, Funding acquisition.

Declaration of Competing Interest

The authors declare that they have no known competing financial interests or personal relationships that could have appeared to influence the work reported in this paper.

Acknowledgements

Funded in part by the Marie Skłodowska-Curie Actions (MSCA) Research and Innovation Staff Exchange (RISE) H2020-MSCA-RISE-2018- 823895 'SENSOFT', by MICINN and FEDER grant no. RTI2018-101580-I00 and AGAUR grant no. 2017 SGR 418.

A.A. is supported by a COFUND project the European Union's Horizon 2020 research and innovation program under the Marie Skłodowska-Curie grant agreement No. 713679 and the Universitat Rovira i Virgili (URV). The technological SIAM (Synthesis, Irradiation and Analysis of Materials) and Morph'IM platforms from the UNamur are acknowledged for XPS and SEM measurements. C.B. and J.F.C. are Research Associates of the National Funds for Scientific Research (FRS-FNRS, Belgium; E.L. is supported by the Catalan Institute for advanced studies (ICREA) via the 2018 Edition of the ICREA Academia Award.

Appendix A. Supplementary data

Supplementary material related to this article can be found, in the online version, at doi:https://doi.org/10.1016/j.snb.2020.128813.

References

[1] WHO, Ambient air pollution: Health impacts.
[2] D. Zhang, Z. Liu, C. Li, T. Tang, X. Liu, S. Han, B. Lei, C. Zhou, Detection of NO_2 down to ppb levels using individual and multiple In_2O_3 nanowire devices, Nano Lett. 4 (2004) 1919–1924.
[3] M.E. Munawer, Human health and environmental impacts of coal combustion and post-combustion wastes, J. Sustain. Min. 17 (2018) 87–96.
[4] S.S. Shendage, V.L. Patil, S.A. Vanalakar, S.P. Patil, N.S. Harale, J.L. Bhosale, J. H. Kim, P.S. Patil, Sensitive and selective NO_2 gas sensor based on WO_3 nanoplates, Sens. Actuators, B-chem. 240 (2017) 426–433.
[5] W. Zheng, Y. Xu, L. Zheng, C. Yang, N. Pinna, X. Liu, J. Zhang, MoS_2 Van Der Waals p–n junctions enabling highly selective room-temperature NO_2 sensor, Adv. Funct. Mater. (2020), 2000435.
[6] Environmental Protection Agency, Primary National Ambient Air Quality Standards (NAAQS) for Nitrogen Dioxide.
[7] S. Zampolli, I. Elmi, F. Mancarella, P. Betti, E. Dalcanale, G.C. Cardinali, M. Severi, Real-time monitoring of sub-ppb concentrations of aromatic volatiles with a MEMS-enabled miniaturized gas-chromatograph, Sens. Actuators, B-chem. 141 (2009) 322–328.
[8] N.G. Cho, D.J. Yang, M.-J. Jin, H.-G. Kim, H.L. Tuller, I.-D. Kim, Highly sensitive SnO_2 hollow nanofiber-based NO_2 gas sensors, Sens. Actuators, B-chem. 160 (2011) 1468–1472.
[9] A. Falak, Y. Tian, L. Yan, M. Zhao, X. Zhang, F. Dong, P. Chen, H. Wang, W. Chu, Room temperature detection of NO_2 at ppb level and full recovery by effective modulation of the barrier height for titanium oxide/graphene schottky heterojunctions, Adv. Funct. Mater. 6 (2019) 1900992.
[10] Z. Song, Z. Wei, B. Wang, Z. Luo, S. Xu, W. Zhang, H. Yu, M. Li, Z. Huang, J. Zang, Sensitive room-temperature H_2S gas sensors employing SnO_2 quantum wire/reduced graphene oxide nanocomposites, Chem. Mater. 28 (2016) 1205–1212.
[11] W. Hyung Cheong, J. Hyeb Song, J. Joon Kim, Wearable, wireless gas sensors using highly stretchable and transparent structures of nanowires and graphene, Nanoscale. 8 (2016) 10591–10597.
[12] S.M. Mortazavi Zanjani, M.M. Sadeghi, M. Holt, S.F. Chowdhury, L. Tao, D. Akinwande, Enhanced sensitivity of graphene ammonia gas sensors using molecular doping, Appl. Phys. Lett. 108 (2016) 033106.
[13] R. Pearce, T. Iakimov, M. Andersson, L. Hultman, A. Lloyd Spetz, R. Yakimova, Epitaxially grown graphene based gas sensors for ultra sensitive NO_2 detection, Sens. Actuators, B-chem. 155 (2011) 451–455.
[14] J. Ping, Z. Fan, M. Sindoro, Y. Ying, H. Zhang, Recent advances in sensing applications of two-dimensional transition metal dichalcogenide nanosheets and their composites, Adv. Funct. Mater. 27 (2017), 1605817.
[15] W.-T. Koo, J.-H. Cha, J.-W. Jung, S.-J. Choi, J.-S. Jang, D.-H. Kim, I.-D. Kim, Few-layered WS_2 nanoplates confined in Co, N-doped hollow carbon nanocages: abundant WS_2 edges for highly sensitive gas sensors, Adv. Funct. Mater. 28 (2018), 1802575.
[16] Z. Qin, K. Xu, H. Yue, H. Wang, J. Zhang, C. Ouyang, C. Xie, D. Zeng, Enhanced room-temperature NH3 gas sensing by 2D SnS2 with sulphur vacancies synthesized by chemical exfoliation, Sens. Actuators, B-chem. 262 (2018) 771–779.
[17] Q. He, Z. Zeng, Z. Yin, H. Li, S. Wu, X. Huang, H. Zhang, Fabrication of flexible MoS2 thin-film transistor arrays for practical gas-sensing applications, Small. 8 (2012) 2994–2999.
[18] X. Li, X. Li, Z. Li, J. Wang, J. Zhang, WS2 nanoflakes based selective ammonia sensors at room temperature, Sens. Actuators, B-chem. 240 (2017) 273–277.
[19] D.J. Late, R.V. Kanawade, P.K. Kannan, C.S. Rout, Atomically thin WS_2 nanosheets based gas sensor, Sens. Lett. 14 (2016) 1249–1254.
[20] C.C. Mayorga-Martinez, A. Ambrosi, A.Y.S. Eng, Z. Sofer, M. Pumera, Metallic 1T-WS2 for selective impedimetric vapor sensing, Adv. Funct. Mater. 25 (2015) 5611–5616.
[21] J.Z. Ou, W. Ge, B. Carey, T. Daeneke, A. Rotbart, W. Shan, Y. Wang, Z. Fu, A. F. Chrimes, W. Wlodarski, Physisorption-based charge transfer in two-dimensional SnS_2 for selective and reversible NO_2 gas sensing, ACS Nano 9 (2015) 10313–10323.
[22] Y.-H. Kim, D.-T. Phan, S. Ahn, K.-H. Nam, C.-M. Park, K.-J. Jeon, Two-dimensional SnS2 materials as high-performance NO_2 sensors with fast response and high sensitivity, Sens. Actuators, B-chem. 255 (2018) 616–621.
[23] D.J. Late, Y.-K. Huang, B. Liu, J. Acharya, S.N. Shirodkar, J. Luo, A. Yan, D. Charles, U.V. Waghmare, V.P. Dravid, Sensing behavior of atomically thin-layered MoS_2 transistors, ACS Nano 7 (2013) 4879–4891.
[24] M. O'Brien, K. Lee, R. Morrish, N.C. Berner, N. McEvoy, C.A. Wolden, G. S. Duesberg, Plasma assisted synthesis of WS_2 for gas sensing applications, Chem. Phys. Lett. 615 (2014) 6–10.
[25] D. Gu, X. Li, H. Wang, M. Li, Y. Xi, Y. Chen, J. Wang, M.N. Rumyntseva, A. M. Gaskov, Light enhanced VOCs sensing of WS_2 microflakes based chemiresistive sensors powered by triboelectronic nangenerators, Sens. Actuators, B-chem. 256 (2018) 992–1000.
[26] K.Y. Ko, J.G. Song, Y. Kim, T. Choi, S. Shin, C.W. Lee, K. Lee, J. Koo, H. Lee, J. Kim, T. Lee, J. Park, H. Kim, Improvement of gas-sensing performance of large-area tungsten disulfide nanosheets by surface functionalization, ACS Nano 10 (2016) 9287–9296.
[27] T. Xu, Y. Liu, Y. Pei, Y. Chen, Z. Jiang, Z. Shi, J. Xu, D. Wu, Y. Tian, X. Li, The ultra-high NO_2 response of ultra-thin WS_2 nanosheets synthesized by hydrothermal and calcination processes, Sens. Actuators, B-chem. 259 (2018) 789–796.
[28] W. Yan, M.A. Worsley, T. Pham, A. Zettl, C. Carraro, R. Maboudian, Effects of ambient humidity and temperature on the NO_2 sensing characteristics of WS_2 /graphene aerogel, Appl. Surf. Sci. 450 (2018) 372–379.
[29] K.M. McCreary, A.T. Hanbicki, G.G. Jernigan, J.C. Culbertson, B.T. Jonker, Synthesis of large-area WS_2 monolayers with exceptional photoluminescence, Sci. Rep. 6 (2016) 19159.

[30] C. Lan, C. Li, Y. Yin, Y. Liu, Large-area synthesis of monolayer WS2 and its ambient-sensitive photo-detecting performance, Nanoscale. 7 (2015) 5974–5980.
[31] S.P. Vattikuti, C. Byon, C.V. Reddy, Synthesis of MoS_2 multi-wall nanotubes using wet chemical method with H_2O_2 as growth promoter, Superlattices Microstruct. 85 (2015) 124–132.
[32] J. Sun, X. Li, W. Guo, M. Zhao, X. Fan, Y. Dong, C. Xu, J. Deng, Y. Fu, Synthesis methods of two-dimensional MoS_2: a brief review, Crystals 7 (2017) 198.
[33] T.A.J. Loh, D.H.C. Chua, A.T.S. Wee, One-step synthesis of few-layer WS2 by pulsed laser deposition, Sci. Rep. 5 (2015) 1–9.
[34] P. Arod, S. Shivashankar, Single-step synthesis of carbon nanotubes/iron/iron oxide composite films through inert-ambient CVD using ferric acetylacetonate as a precursor, RSC Adv. 5 (2015) 59463–59471.
[35] K.M. McCreary, A.T. Hanbicki, G.G. Jernigan, J.C. Culbertson, B.T. Jonker, Synthesis of large-area WS_2 monolayers with exceptional photoluminescence, Sci. Rep. 6 (2016) 1–7.
[36] N.R. Pradhan, D. Rhodes, S. Feng, X. Yan, S. Memaran, M. B.H, H. Terrones, M. Terrones, L. Balicas, Controlled synthesis and transfer of large-area WS_2 sheets: from single layer to few layers, ACS Nano 7 (2013) 5235–5242.
[37] F.E. Annanouch, Z. Haddi, S. Vallejos, P. Umek, P. Guttmann, C. Bittencourt, E. Llobet, Aerosol-assisted CVD-grown WO_3 nanoneedles decorated with copper oxide nanoparticles for the selective and humidity-resilient detection of H_2S, ACS Appl. Mater. Interfaces 7 (2015) 6842–6851.
[38] F.E. Annanouch, Z. Haddi, M. Ling, F. Di Maggio, S. Vallejos, T. Vilic, Y. Zhu, T. Shujah, P. Umek, C. Bittencourt, Aerosol-assisted CVD-grown PdO nanoparticle-decorated tungsten oxide nanoneedles extremely sensitive and selective to hydrogen, ACS Appl. Mater. Interfaces 8 (2016) 10413–10421.
[39] S. Vallejos, P. Umek, T. Stoycheva, F. Annanouch, E. Llobet, X. Correig, P. De Marco, C. Bittencourt, C. Blackman, Single-step deposition of Au- and Pt-Nanoparticle-Functionalized tungsten oxide nanoneedles synthesized via aerosol-assisted CVD, and used for fabrication of selective gas microsensor arrays, Adv. Funct. Mater. 23 (2013) 1313–1322.
[40] Q. Fu, W. Wang, L. Yang, J. Huang, J. Zhang, B. Xiang, Controllable synthesis of high quality monolayer WS 2 on a SiO_2/Si substrate by chemical vapor deposition, RSC Adv. 5 (2015) 15795–15799.
[41] Y. Rong, Y. Fan, A.L. Koh, A.W. Robertson, K. He, S. Wang, H. Tan, R. Sinclair, J. H. Warner, Controlling sulphur precursor addition for large single crystal domains of WS_2, Nanoscale. 6 (2014) 12096–12103.
[42] J. Park, W. Lee, T. Choi, S.-H. Hwang, J.M. Myoung, J.-H. Jung, S.-H. Kim, H. Kim, Layer-modulated synthesis of uniform tungsten disulfide nanosheet using gas-phase precursors, Nanoscale 7 (2015) 1308–1313.
[43] M. Krause, A. Mücklich, A. Zak, G. Seifert, S. Gemming, High resolution TEM study of WS2 nanotubes, Phys. Status Solidi B 248 (2011) 2716–2719.
[44] V. Weiß, S. Seeger, K. Ellmer, R. Mientus, Reactive magnetron sputtering of tungsten disulfide (WS 2− x) films: influence of deposition parameters on texture, microstructure, and stoichiometry, J. Appl. Phys. 101 (2007) 103502.
[45] G. Jimenez-Cadena, J. Riu, F.X. Rius, Gas sensors based on nanostructured materials, Analyst. 132 (2007) 1083–1099.
[46] D. Ovchinnikov, A. Allain, Y.-S. Huang, D. Dumcenco, A. Kis, Electrical transport properties of single-layer WS_2, ACS Nano 8 (2014) 8174–8181.
[47] F. Zhang, Y. Lu, D.S. Schulman, T. Zhang, K. Fujisawa, Z. Lin, Y. Lei, A.L. Elias, S. Das, S.B. Sinnott, Carbon doping of WS_2 monolayers: bandgap reduction and p-type doping transport, Sci. Adv. 5 (2019) eaav5003.
[48] G.A. Asres, J.J. Baldoví, A. Dombovari, T. Järvinen, G.S. Lorite, M. Mohl, A. Shchukarev, A.P. Paz, L. Xian, J.-P. Mikkola, Ultrasensitive H_2S gas sensors based on p-type WS_2 hybrid materials, Nano Res. 11 (2018) 4215–4224.
[49] G. Deokar, P. Vancsó, R. Arenal, F. Ravaux, J. Casanova-Cháfer, E. Llobet, A. Makarova, D. Vyalikh, C. Struzzi, P. Lambin, MoS_2–carbon nanotube hybrid material growth and gas sensing, Adv. Mater. Interfaces 4 (2017) 1700801.
[50] W. Yan, A. Harley-Trochimczyk, H. Long, L. Chan, T. Pham, M. Hu, Y. Qin, A. Zettl, C. Carraro, M.A. Worsley, Conductometric gas sensing behavior of WS_2 aerogel, FlatChem. 5 (2017) 1–8.
[51] D. Liu, Z. Tang, Z. Zhang, Comparative study on NO_2 and H_2S sensing mechanisms of gas sensors based on WS2 nanosheets, Sens. Actuators, B-chem.303 (2020) 127114.

Aanchal Alagh is a MSCA−COFUND PhD fellow at the Universitat Rovira i Virgili. Her research interest are on the synthesis and application of transition metal dichalcogenide materials.

Fatima Ezahra Annanouch is a Post-Doctoral Fellow at the Universitat Rovira i Virgili. Her research interests are on the synthesis and application of metal oxides and transition metal dichalcogenide materials to gas sensing.

Polona Umek is a research Fellow at the Josef Stefan Institute in Ljubljana, Slovenia. She is an expert in the characterization of nanomaterials.

Carla Bittencourt is a research Fellow of the Belgian National Fund for Research at the University of Mons. She is interested in the chemical characterization of nanomaterials.

Ayrton Sierra Castillo is a Post-Doctoral Fellow at the University of Namur. His research interests include the development of 2D nanomaterials

Emile Haye is a researcher at the University of Namur. Among his research interest is the study of 2D nanomaterials.

Jean François Colomer is a research Fellow of the Belgian National Fund for Research at the University of Namur. His research interest are in the synthesis and applications of carbon nanomaterials and of transition metal dichalcogenides.

Eduard Llobet is Professor at the Universitat Rovira i Virgili. His research interests comprise the synthesis of 1D and 2D nanomaterials for gas sensing.

Chapter-3

An ultrasensitive room-temperature H_2S gas sensor based on 3D assembly of Cu_2O decorated WS_2 nanomaterial

An Ultrasensitive Room-Temperature H_2S Gas Sensor Based on 3D Assembly of Cu_2O Decorated WS_2 Nanomaterial

Aanchal Alagh, Fatima Ezahra Annanouch, Polona Umek, Carla Bittencourt, Jean François Colomer, and Eduard Llobet, *Senior Member, IEEE*

Abstract*—Herein, we report for the first time on the fabrication of a hybrid material consisting of Cu_2O nanoparticles-decoratedmultilayeredtungstendisulfidenanostructuresand demonstrate their remarkable gas sensing characteristics towards hydrogen sulfide gas. In the first step, a contin- uous film of WS2 was deposited directly on commercial alumina substrate by adopting a facile route combining aerosol-assisted chemical vapor deposition with H_2 free atmospheric pressure CVD technique. For functionalization an additional step of synthesis was added where copper oxide nanoparticles were grown and deposited directly over as-grown tungsten disulfide at low temperature (i.e., 150 °C) using a simple and cost-effective technique. The morphological, structural and chemical characteristicswere investigatedusing FESEM, TEM, and EDX spectroscopy. The gas-sensing studies performed shows that this hybrid nanomaterial has excellent sensitivity towards hydrogen sulfide (11-times increase in response compared to that of pristine WS_2 sensor) at moderate temperature (150 °C). Additionally, functionalization of pristine WS_2 sensor with Cu_2O nanoparticles further enhances the gas sensing performance towards the targeted gas even at room temperature (13-times increase in response compared with that of pristine WS_2 sensor). Moreover, results obtained from humidity cross-sensitivityof Cu_2O-WS_2 sensor indicates superior gas sensing response (with a negligible decrease in response) as compared to pristine WS_2 sensor, when ambient humidity is increased to 50%, which is rarely found in metal oxide-based sensors. This study could add a significant research value in the gas sensor domain.

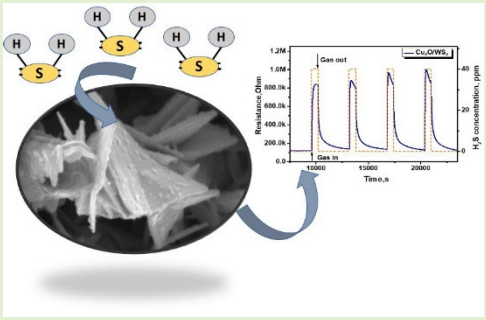

***Index Terms*— 2D, APCVD, gas sensor, H_2S, TMDs, WS_2, Cu_2O.**

I. Introduction

HYDROGEN sulfide (H_2S) appears as a colorless gas having pungent odor of rotten eggs [1]. It is highly toxic and flammable gas [2]. This noxious gas occurs naturally in crude petroleum, natural gas, volcanoes, hot springs [3], [4] and can be released as a by-product from industrial activities including food processing, water treatment, paper mills [4], [5]. Depending on the concentration present, it has a characteristic odor, for instance at concentrations below 5 ppm it has an odor of rotten eggs, whereas at higher concentrations above 100 ppm it deadens the sense of smell, which makes it a silent threat for potential victims [6]. The effect on health of such a poisonous gas depends on its concentration and duration of exposure. For instance, with minimal exposure it causes eye irritation with blurred vision whereas when present in higher concentrations it can lead to corneal ulceration resulting in permanently impaired vision. Moreover, at concentrations above 100 ppm, the gas acts upon the human nervous system, which leads to paralysis and with prolonged exposure, it could even cause immediate death [7]. Aside from the harmful health effects to humans, wet hydrogen sulfide can even corrode steel, carbon and other metallic surfaces bringing out economic losses. Therefore, the acceptable concentration of H_2S (recommended by the Scientific Advisory Board on Toxic Air Pollutants, USA) is set in the range of 20–100 ppb [8]. For this reason, it is necessary to constantly screen H_2S gas levels to forestall spills and limit work related dangers. In this regard semiconducting metal oxide-based gas sensors

Manuscript received February 13, 2021; revised July 24, 2021; accepted July 26, 2021. Date of publication August 11, 2021; date of current version October 1, 2021. This work was supported in part by the European Union's Horizon 2020 Research and Innovation Program through the Marie Sklodowska-Curie Grant 713679 and Grant 823895 and in part by the MININN-FEDER under Grant RTI2018-101580-B-I00. The work of Eduard Llobet was supported by the Catalan Institute for Research and Advanced Studies through the 2018 Edition of the International Consortium of Real Estate Associations (ICREA) Academia Award. This article was presented at the IEEE Sensors 2020 Conference. The associate editor coordinating the review of this article and approving it for publication was Prof. Minhee Yun. *(Corre- sponding author: Fatima Ezahra Annanouch.)*

Aanchal Alagh, Fatima Ezahra Annanouch, and Eduard Llobet are with the Department of Electrical Electronic Engineering and Automation, Universitat Rovira i Virgili, 43007 Tarragona, Spain (e-mail: alagh.aanchal@urv.cat; fatimaezahra.annanouch@urv.cat; eduard.llobet@urv.cat).

Polona Umek is with Josef Stefan Institute in Ljubljana, 1000 Ljubljana, Slovenia (e-mail: polona.umek@ijs.si).

Carla Bittencourt is with the Plasma-Surface Interaction Chemistry, University of Mons, 7000 Mons, Belgium.

Jean François Colomer is with the Belgian National Fund for Research, University of Namur, 5000 Namur, Belgium (e-mail: jean-francois.colomer@unamur.be).

This article has supplementary downloadable material available at https://doi.org/10.1109/JSEN.2021.3103925, provided by the authors.

Digital Object Identifier 10.1109/JSEN.2021.3103925

have been extensively studied for real-time monitoring of numerous hazardous gases at ppb levels as they offer multiple advantages over other sensing materials investigated [4]. The major advantages of these metal-oxide chemoresistive sensors are their small size, easy and simple fabrication, low weight, low cost [9]. Therefore, several metal oxide semiconductors have been investigated as active sensing material for H_2S gas detection. For instance, SnO_2 thin films have shown promising results in detecting H_2S gas in the range 1-15 ppm at room temperature, where the gas sensing properties were enhanced when SnO_2 films were modified with CuO resulting in faster response (20 s) and recovery times (40 s) [10]. Also, ZnO strikes as a most appealing sensing material showing superior detectability with detection limit as low as 20 ppb for H_2S gas [11]. In another work, similar detectability of 20 ppb has been achieved using WO_3 nanoparticle films [12]. However, limited selectivity against other interfering gases, poor long-term stability and high working temperature have hindered the practical applications of metal oxide-based sensors for H_2S gas detection [4]. Accordingly, in line of improving the existing sensing performance of chemiresistive gas sensors, transition metal chalcogenide (TMDs) based gas sensors have attracted much attention to replace oxides of the corresponding metals [13]–[15]. This is due to the much lower operation temperature of TMDs based sensors, which is attributed to their lower bandgap and better conductivity. However, similar to semiconducting metal oxide sensors, the gas selectivity of TMDs is related with the surface affinity for adsorbing different analytes and related surface charging effects [16]. Consequently, decoration of TMDs with certain metal-oxide nanocrystals have proven to improve the functional proper- ties of these materials and achieve sensors with enhanced sensitivity, excellent selectivity, fast response/recovery rate along with room temperature gas sensing performance. For instance, 2D Graphene/MoS_2 heterostructure sensor is able to detect low concentrations of NO_2 (1.2 ppm) and demonstrates excellent stability [17]. WS_2/WO_3 composite exhibits phenomenal gas detection towards H2 and NH3 in the range of 1-10 ppm while operating at moderate temperature of 150 °C [18]. Also, room temperature sensing towards NO_2 gas detection has also been realized using MoS_2/SnO_2 nanohybrids [19]. Moreover, many reports in the literature confirm the suitability of Cu2O nanoparticles as additives to enhance the sensitivity and selectivity of sensors towards H_2S gas [3], [20]–[25]. Accordingly, the gas sensing properties of WS_2 are expected to be improved with the addition of Cu_2O nanostructures.

In this respect, we report here H_2S gas-sensing perfor- mance of Cu_2O functionalized WS_2 nanosheets grown in two-steps. In the first step, a continuous film of WS_2 was deposited directly on commercial alumina substrate by adopt- ing a facile route combining aerosol-assisted chemical vapor deposition (AACVD) with H2 free atmospheric pressure CVD technique. In the second step functionalization was incorpo- rated where copper oxide nanoparticles (NPs) were grown and deposited directly over previously grown tungsten disulfide nanostructures at much lower temperature (i.e., 150 °C) using a simple and cost-effective AACVD technique. Field emission scanning electron microscopy (FESEM), transmission electron microscopy (TEM), Energy-dispersive X-ray analysis (EDX) have been used to determine the morphology, chemical composition, and microstructure of the deposited layers. Subsequently, corresponding gas sensing performance of the functionalized WS2 sensor was studied and compared to that of pristine WS2 sensor. The gas-sensing performance of the fabricated sensor (Cu2O-functionalised WS2 sensor and pristine WS2 sensor) towards hydrogen sulfide (H2S) has been studied under both dry and humid atmospheres. To the best of our knowledge, no previous reports have described the synthesis and gas sensing properties of Cu2O-decorated WS2 nanostructures towards H2S gas. Conclusively, a dis- cussion on the H2S sensing mechanism for the 3D assem- bly Cu2O NPs decorated WS2 nanostructures is discussed as well.

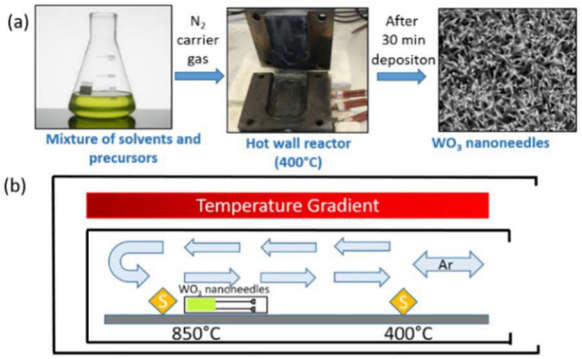

Fig. 1. (a) WO_3 synthesis by AACVD process (b) WS_2 synthesis adopting CVD technique.

II. Experimental Section

A. Material Synthesis

Functionalized and non-functionalized WS_2 sensors were grown directly on commercial alumina substrates using a combination of two techniques namely aerosol-assisted chemical vapor deposition (AACVD) technique and chemical vapor deposition technique (CVD). WS_2 multilayered nanosheets were grown in two-steps following the procedure as reported in our previous work [25]. In brief in the first step, WO_3 nanoneedles (NNs) were grown directly on commercial alumina substrates, via AACVD technique as shown in Fig.1 (a) 50 mg of tungsten hexacarbonyl (W(CO)6) (purity 97%) dissolved in a mixture of 15 mL acetone and 5 mL methanol were first sonicated and then kept in an ultrasonic humidifier to generate vapors from the dissolution. Nitrogen gas with a flow of 1L/min was used as a carrier to transport the aerosol inside the heated deposition chamber, which was kept at a temperature of 400 °C. The duration of the complete growth process was about 45 min. After deposition, the samples were annealed at 400 °C for 3 h under synthetic air in a carbolite CWF 1200 muffle furnace.

In the second step, WS_2 nanosheets were obtained via sulfurization of the as-grown WO_3 nanofilms using an atmospheric pressure CVD technique as shown in Fig.1 (b). In a typical process, 0.44 g sulfur (S) powder (99.5%), purchased from

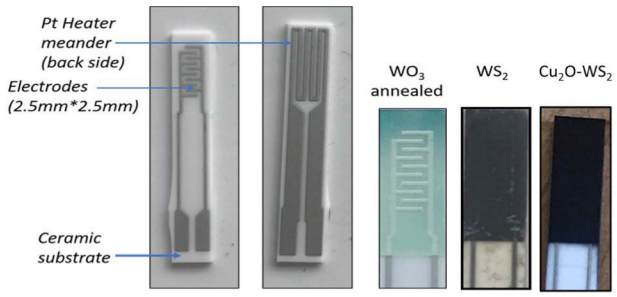

Fig. 2. Alumina transducer substrate used to deposit WO_3 nanomaterial (green color), sulfurized to deposit WS_2 nanomaterial (black color), functionalized with Cu_2O nanoparticles (dark black color).

Alfa Aesar was equally distributed in two ceramic boats and placed at different temperature zones of the furnace such that one was positioned at the 40 °C temperature zone and the other at 850 °C temperature zone. The substrate deposited with WO_3 nanomaterial in the first step was placed at the 850 °C temperature zone in the downstream of argon flow in the quartz tube reactor. Before the sulfurization process, the tube furnace was flushed with 0.725 L/min of argon gas to eliminate any oxygen content in the reactor. The primary step of sulfurization process goes for a period of 30 minutes (mins) during which the S powder set at the 850 °C zone sublimates. The second step of sulfurization was executed by pushing the quartz tube in the hot zone of the furnace, such that the S powder which was initially placed at 40 °C reaches the 400 °C temperature zone. As the quartz tube was pushed over a few centimeters, the WO_3 sample remained at 850 °C. After sulfurization, the furnace was naturally cooled down to room temperature.

Furthermore, Cu_2O-functionalized WS_2 sensor was fabricated by incorporating Cu_2O NPs on the pregrown WS_2 nanosheets via AACVD using copper (II) acetylacetonate [7 mg, Cu(acac)2 Sigma-Aldrich, 99.9%], mixed in chloroform [4mL, Sigma-Aldrich]. The sensor substrate comprising WS_2 nanomaterial is again placed inside the deposition chamber and is heated at 150 °C. The solution containing Cu precursor is placed at the aerosol generator and delivered into the chamber using nitrogen flow of 1L/min. The duration of the complete growth process was not more than 20 min. After deposition, the deposition chamber was naturally cooled down to room temperature and the sensor was taken out.

B. Sensor Fabrication Process and Gas Sensing Measurement System

For sensor processing, commercial alumina substrates which comprises of interdigitated platinum electrodes with 300 μm electrode gap on the front side and a platinum (Pt) resistive heater meander on the backside were used. Fig.2 depicts an image of the commercial alumina substrate used. The gas sensing measurements were performed using a Teflon test chamber of 35 mL in volume, where up to four interdigitated alumina sensors can be placed and measured simultaneously. This chamber was connected to a fully automated, continuous gas flow measurement set-up able to supply diluted gas mixtures. The electrical resistance of sensors was measured using an Agilent-34972A multimeter.

Initially, the sensor was kept in a dry synthetic air flow (Air Premier Purity: 99.995%) at 100 mL/min for 4 h to stabilize its baseline resistance. The Pt heater meander was characterized to set the operating temperature of the sensor depending on the external power supply (Agilent, model 3492A). Dry air was chosen as the carrier and balance gas along all the experiments performed for the gas sensing characterization. Gas cylinders of H_2S (100 ppm in air) were used for the sensing measurements. The concentration of hydrogen sulfide gas was adjusted by controlling the flow rates of the target and balance gases with a total flow rate of 100 mL/min, which was kept constant throughout the measurements. After each sensing measurement the samples were cleaned in dry air for 1 h. Experiments under humid conditions were also conducted. For performing measurements in humid atmospheres, a computer-controlled humidification system was used, which comprises of a liquid mass flow and a mixer, to set the moisture level to 50% at 25 °C. The gas sensing characteristics were examined in terms of response percentage, detection limit and repeatability. The sensor response is defined as percentile change in the baseline resistance of the sensor when exposed to an analyte gas. It can be calculated by using (1), given as:

$$\text{Response } (\%) \quad \frac{Rgas - Rair}{Rair} = 100 \qquad (1)$$

Here Rair and Rgas are respectively, the sensor resistance before and after exposure to H_2S gas. [26]. The response time of the sensor (tres) is defined as the time taken by the sensor to obtain 90% of the total resistance change when exposed to target gas and recovery time (trec) is defined as the time taken by the sensor to retrieve 90% of the total resistance change upon removal of target gas [27].

C. Material Characterization

The crystalline structure of the as-grown WO_3 and WS_2 material was characterized using scanning electron microscope (SEM-FEI Quanta 600) whereas after the sulfurization process the morphology of the material was characterized using a field-emission scanning electron microscope Hitachi 2000 and FEI Helios Nanolab 650. A high-resolution transmission electron microscope (Jeol, JEM-2100) was used for crystal- lographic information at the atomic level. The images were acquired using a Gatan CCD camera ORIUS. For chem- ical phase analysis XRD measurements were made, using a Bruker-AXS D8-Discover diffractometer. Finally, Raman spectroscopy measurements were carried out using Renishaw in Via, laser 514 nm, ion argon-Novatech, 25 mW. The surface morphology of functionalized WS_2 material was investigated using field emission scanning electron microscope (FESEM) from ThermoScientific, model Scios 2 and corresponding energy dispersive spectroscopy (EDX) mapping were done using software pathfinder. Furthermore, TEM analysis was also carried out to analyze the morphology of the grown material.

III. Results and Discussion

A. Material Synthesis and Characterization

1) Pristine WS_2: Extensive material characterizatiosn was performed using SEM, XRD, HRTEM, Raman spectroscopy

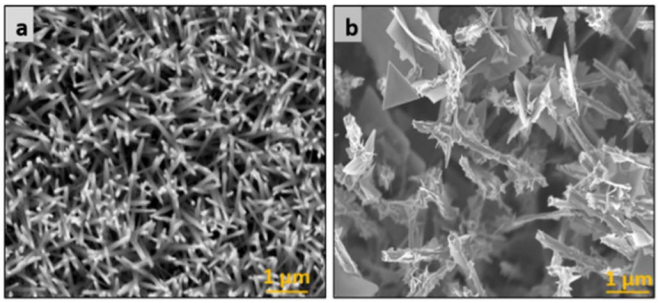

Fig. 3. SEM images of (a) WO_3 NNs, (b) WS_2 NTs/NNs film.

to assess a variety of material properties including morphology, structure and chemical composition. Scanning electron microscopy (SEM) gave an insight into the morphology and arrangement of the as-grown WO3 and WS2 nanomaterial. Fig.3 (a) shows the SEM imaging results of the material prepared during the first step of synthesis.

In view of the results obtained, WO_3 grown by AACVD technique consisted of thin and 6 μm long nanoneedles (Fig.S1(a)) which were haphazardly aligned and evenly distributed on the alumina substrate. After sulfurization, the morphology of these nanoneedles changed completely to form a 31μm thick nanostructured film (Fig. S1(b)) of WS_2 having a mixed morphology of nanotriangles (NTs) and nanoneedles (NNs), as shown in Fig.3 (b). SEM image shows that WS_2 NTs are adhered to the WS_2 NNs and form an integral part of the nanostructured film in accordance with an arrangement that results a 3D architecture. The morphology and other characteristics of the grown WO_3 and WS_2 NTs/NNs hybrid material examined from SEM were identical to those reported in our previous work [28]. Additionally, it was deduced from our previous research work that the ultimate morphology of WS_2 nanofilms is dependent on the assembly of the starting material (WO_3) [28].

The as-grown WO_3 as well as WS_2 nanofilms were further investigated by using X-ray powder diffraction (XRD) to identify their crystallographic phase. Fig.4 displays the XRD pattern (upper spectrum) obtained for the grown WS_2 nanostructured film, which is compared with the spectrum of WO_3 (lower spectrum) to detect the presence of any WO_3 impurities. From the diffractograms obtained, the diffraction peaks were perfectly indexed to the 2H-WS_2 [29]. The presence of sharp peaks in the spectrum further confirms the crystallinity of the grown nanofilms. Also, some peaks belonging to the alumina substrate were present [22] however peaks from any other impurity were not detected, indicating that a well-crystallized single phase WS_2 was obtained.

Raman spectroscopy is a powerful technique to evaluate the crystal quality and film thickness of 2D materials and hence is used to analyze the as-synthesized material [30]. Fig.5 depicts Raman spectra obtained for the as-synthesized WO_3 and WS_2 nanofilms. The lower spectrum depicts peaks at 271 cm-1, 327 cm-1, 715 cm-1 and 805 cm-1, which indicates the formation of monoclinic tungsten trioxide phase, which is in good accordance with our previous results [22]. From the upper spectrum, the two main Raman active modes for 2H-WS_2 were found, E12g at 348.5 cm-1 and A1g at

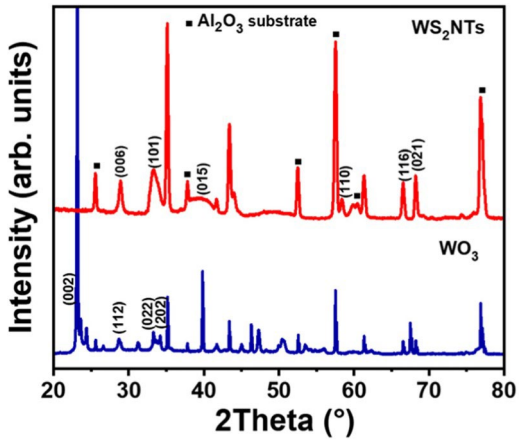

Fig. 4. XRD diffractograms for WO_3 NNs (bottom spectrum) and WS_2 NTs/NNs (upper spectrum).

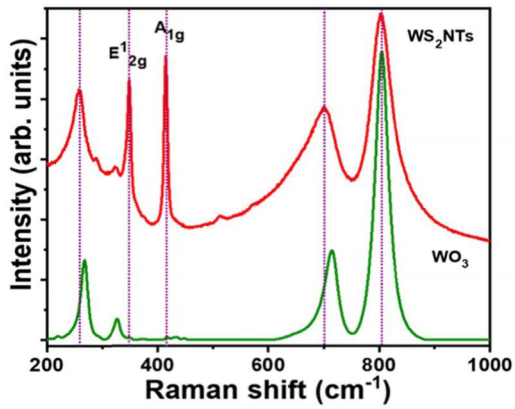

Fig. 5. Raman spectra of WO3 NNs (lower spectrum), WS2 NTs/NNs (upper spectrum).

414.5 cm-1, where A1g and E12g mode indicates in plane and out-of-plane vibrations respectively. The sharp Raman peaks further indicates the crystallinity of the multilayered film, consistent with XRD results. Furthermore, it is possi- ble to evaluate the number of layers present in the grown material by calculating the peak intensity difference between E12g and A1g mode (I E12g/I A1g). The observed dif- ference of 0.89 indicates that the grown nanofilms consist of multilayers of WS_2, stacked together by van der Waals forces of interaction, which suppresses atom vibrations [31]. In addition, two broad peaks at 700 cm-1 and 803 cm-1, were also detected with low intensity compared to WS_2 spectrum, indicating the presence of some WO_3 impurities. Hence it can be concluded that Raman spectroscopy is more sensitive than other characterization techniques at detecting traces of tungsten oxide which could be present within the bulk core of grown WS_2 films. Observations from TEM and HRTEM are presented in Fig.6 wherein (a) shows characteristic WS_2 cluster composed of several 2D nanotriangles with side walls of about 800 nm. It appears that triangles are growing on top of one another. They are crystalline and no amorphous material is observed on their edges (Fig. 6b). Besides 2D nanostructures, also 1D nanostructures, i.e., nanoneedles, are observed. The characteristic interlayer distance of (002) planes

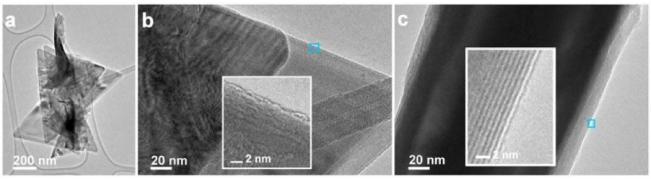

Fig. 6. TEM images of WS_2 cluster composed of nanotriangles with side wall of about 800 nm (a, b) and a middle part of the nanoneedle with diameter of 180 nm (c). Blue frames in images b and c indicate areas where HRTEM insets were taken.

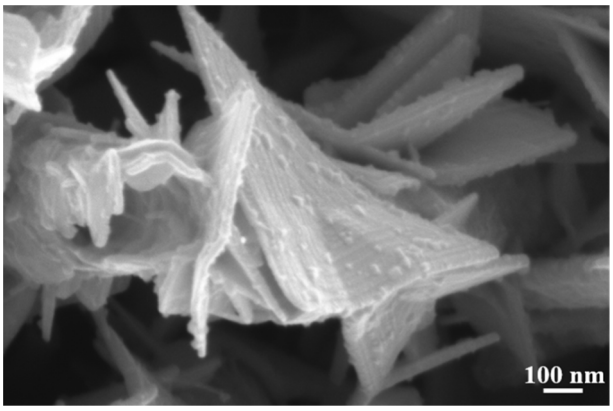

Fig. 7. FESEM image depicting decoration of WS2 NTs/NNs with Cu2O NPs.

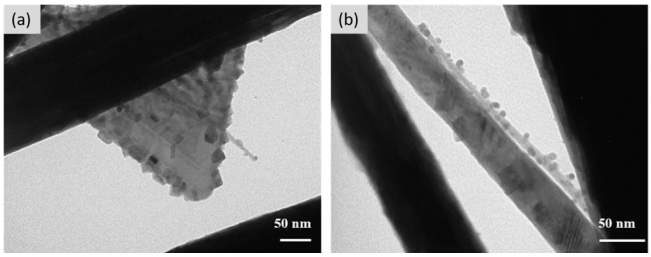

Fig. 8. TEM image depicting Cu_2O NPs functionalized WS_2 (a) nanotriangle (b) nanoneedles.

in the nanoneedle close to the surface is 0.69 nm (Fig. 6c). The planes are expanded compared to the (002) planes in WS_2 single crystal most likely due to crystallographic defects, especially dislocations [32].

Thus, results from different characterization techniques performed, confirm the transformation of WO_3 nanomaterial to WS_2 with small traces of WO_3, which may be present in the bulk of the sulfurized multilayered nanofilms.

2) Functionalized WS2: Details of the morphological and structural features after decoration of WS_2 NTs/NNs with Cu_2O were studied using FESEM, TEM and EDX. The presence of nanoparticles (NPs) can be well observed in Fig. 7. The NPs are deposited on top of the as grown WS_2 nanosheets. Furthermore, Fig. 8 (a) and (b) display low magnification TEM images of Cu_2O NPs decorating WS_2 nanotriangles and nanoneedles respectively. The formation of nanoparticles with an average diameter of about 5-6 nm and the co-existence of a few bigger ones with diameter of about 15-20 nm can be observed.

In addition to this, presence of Cu_2O was also confirmed using EDX. The spectrum is displayed in Fig. 9. From the

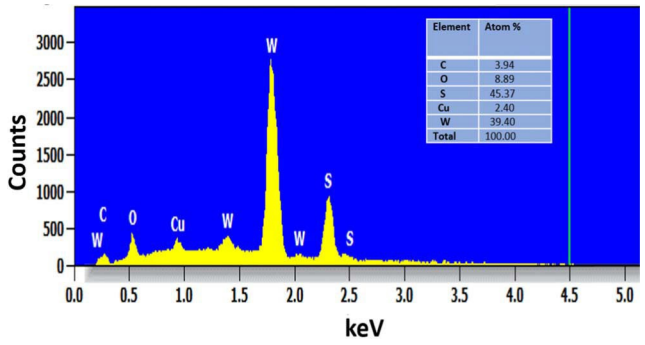

Fig. 9. EDX spectrum of the as prepared Cu_2O functionalized WS_2 hybrid nanomaterial.

EDX analysis, it is detected that the concentration of copper present is less than 3%, hence it can be concluded that the doping concentration is very less. Nevertheless, results from FESEM, TEM and EDX confirms the decoration of WS_2 NTs/NNs with Cu_2O NPs.

IV. Gas Sensing Results and Discussion

The gas sensing properties towards 40 ppm of H_2S gas of pristine WS_2 and Cu_2O-functionalized WS_2 were examined at three different operating temperatures (25 °C, 100 °C and 150 °C). For all measurements, H_2S gas was injected for 10 mins followed by 60 mins purging with dry airflow so that the sensor can recover its initial baseline resistance. Excellent response stability was achieved using 10 min exposure followed by 1 h recovery. As shown in Fig.10 (a) the sensor response increases with increase in operating temperature, which clearly indicates more interactions between the target gas and the WS_2 sensing surface at higher temperature.

This can be attributed to the minimum activation energy required for the adsorption of gas molecules at the sensor surface, which is provided by applying heat, hence results in higher response at an elevated temperature. However, measurements beyond 150 °C were not performed, since at temperatures above 150 °C sulfur could evaporate and could lead to the formation of a composite of tungsten oxide and sulfide. Thus, for subsequent studies with both functionalized and pristine sensor, 150 °C was considered as the optimal working temperature for the two fabricated sensors. Consequently, lower operating temperature is one of the many advantages of using transition metal dichalcogenides based sensors (such as WS_2 nanofilms) for H_2S gas detection in comparison to the higher operating temperatures used for most metal oxide based H_2S gas sensors.

Furthermore, Fig.10 (b) and (c) depicts the dynamic electrical responses for the two sensors towards 40 ppm of H_2S gas at the optimal working temperature (150 °C). The maximum gas response recorded for pristine WS_2 at 150 °C was 54.70% towards 40 ppm H_2S gas, while it reached 610% for Cu_2O/WS_2. Thus, the decoration with Cu_2O NPs on WS_2 NTs/NNs sensor has resulted in 11-fold increase in the sensor response. The response and recovery time for pristine WS_2 sensor towards 40 ppm of H_2S gas were 230 s and 1710 s respectively. With the addition of Cu_2O NPs to WS_2 nanomaterial, the response and recovery time were

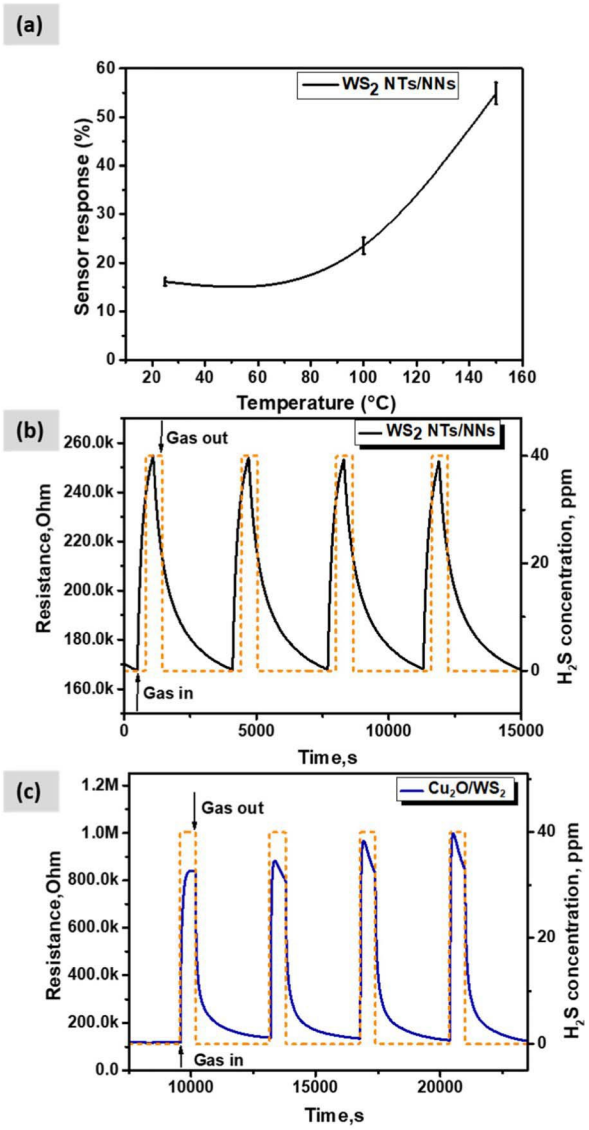

Fig. 10. Response towards 40 ppm H_2S gas (a) for pristine sensor as a function of temperature, (b) depicting change in electrical resistance of pristine sensor (4 replicate response and recovery cycles) when operated at 150 °C (c) depicting change in electrical resistance of functionalized sensor (4 replicate response and recovery cycles) when operated at 150 °C.

reduced to 141 s and 328 s respectively (Fig. S3). To evaluate the long term stability of the sensors, we have monitored them over a period of 7 months towards 40 ppm of H_2S gas. Results demonstrate good stability in terms of sensor response and baseline resistance for both sensors (Fig. S4). H_2S response was decreased compared to the initial values by only 16%. The steady and reproducible gas response in both the sensors is attributed to the direct growth of tungsten disulphide nanomaterial at the electrode surface.

Moreover, it is observed that when the sensor is exposed to a reducing gas, the baseline resistance increases, indicating a p-type semiconducting behaviour for both sensors. This is consistent to the results reported in the literature for WS_2 nanofilms [27], [33]–[36].

Moreover, the two sensors were also tested towards 40 ppm H_2S gas at room temperature and the corresponding responses

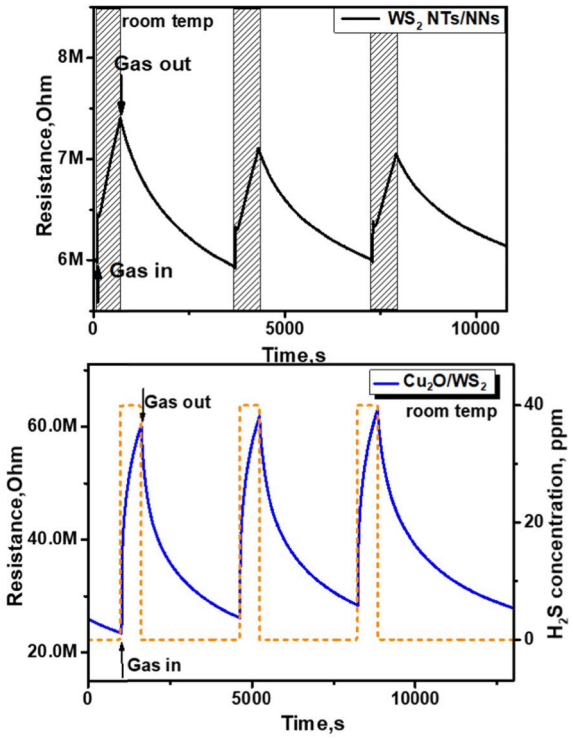

Fig. 11. Response recorded at room temperature towards 40 ppm H_2S gas depicting change in electrical resistance of (top) pristine sensor (down) functionalized sensor.

are presented in Fig. 11. As expected, the sensing response was much lower at room temperature, where the highest response was only 10% for pristine WS_2 sensor whereas the response was much more intensified and rose to 138% from 10% with the addition of Cu_2O NPs to pristine WS_2. Also, a small drift is observed in both the sensors which can be attributed to the slow desorption of gas molecules when operated at room temperature. Nevertheless, a response value of 138% at room temperature is significantly higher for Cu_2O/WS_2 nanofilms that is ever reported in literature.

Additionally, sensing characteristics of bare WS_2 sensor for H_2S gas in humid environment were also tested and the corresponding results are shown in Fig.12 (a). The sensor was tested for 3 replicates towards 40 ppm of H_2S, operated at 150 °C in humid backgrounds with 50% RH. It was observed that the sensor response for pristine sample dropped down from 54.7% to 20% with the adsorption of water vapor on the WS_2 sensor surface which apart from changing the baseline resistance, blocks the reaction sites, also reported in literature [35]. The sensing characteristics of the Cu_2O functionalized WS_2 sensor for H_2S gas in humid environment were also tested and the corresponding results are shown in Fig.12 panel (b) and (c). This sensor was also tested for 3 replicates towards 40 ppm of H_2S, operated at 150 °C and room temperature in humid backgrounds with 50% RH. Surprisingly, even after humidity exposure there was not much change in sensor response as the response dropped down by only 14% from 610% to 596% when operated at 150 °C. At room temperature, there is a drop of 41% in gas response from 138% to 97% in the similar humidity

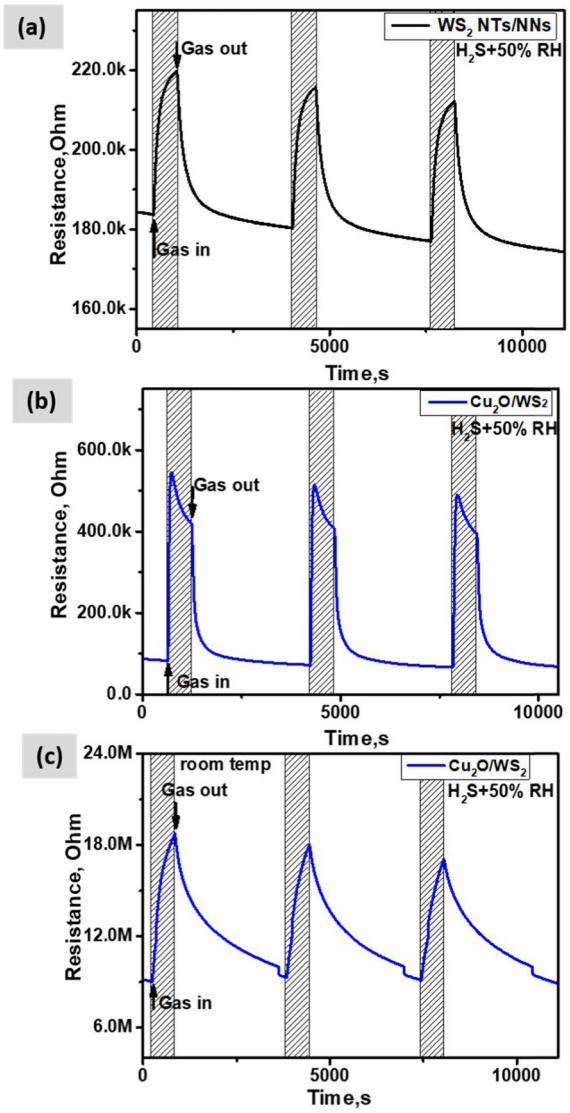

Fig. 12. Electrical resistance towards 40 ppm H_2S in 50% RH background recorded for (a) pristine sensor at 150 °C (b) functionalized sensor at 150 °C (c) functionalized sensor at room temperature.

conditions. It is very important to note here, that most of the reported studies on layered WS_2 gas sensors have not studied the effect of ambient humidity on sensing performance, which is an essential parameter for the practical application of gas sensors. Therefore, the addition of Cu_2O to pristine WS_2 sensor for H_2S detection, would enable suppression of the moisture cross-sensitivity. These results highlight the superior gas sensing performance of Cu2O functionalized WS2 sensor towards H_2S gas sensing.

A selectivity study was performed by exposing the sen- sors towards other interfering gases such as NO_2 and NH_3. The results are depicted in Fig. S5 which demonstrates the important role played by Cu_2O in enhancing the sensitivity and selectivity of WS_2 towards H_2S gas detection.

In this respect, Table I gives more insights by comparing the performance in the detection of H_2S reported in this paper with those found in the literature. From the results obtained, the fabricated Cu_2O functionalized WS_2 sensor shows outstanding gas responses with high sensitivity towards H_2S gas and a

TABLE I
COMPARISON OF THE SENSING PROPERTIES OF H_2S RESISTIVE AND FET TYPE GAS SENSORS BASED ON DIFFERENT WS_2 SENSING MATERIAL STRUCTURES IN THE LITERATURE AND THE TWO WS_2 SENSORS IN THIS STUDY

Material structure	Concentration (ppm)	Operating temp.(°C)	Response (%)	Sensitivity (Response /ppm)	Detection limit	References
Cu20/ WS2	40	150	610	0.152	0.5 (exper)	This work
Cu20/ WS2	40	25	138	0.034	NA	This work
NTs/NNs	40	150	54.7	0.013	0.2 (exper)	This work
NTs/NNs	40	25	10.0	0.002	N/A	This work
NS	5	160	14.0	N/A	N/A	[33]
NW-NF hybrid	1	200	N/A	0.023	0.02 (exper)	[35]
NW-NF hybrid	0.02	200	N/A	0.043	0.02 (exper)	[35]
NS 0	50	120	1.3 (Ra/Rg)	N/A	N/A	[36]
NP	10	100	7.2	0.007	N/A	[27]

N/A: Not available; experimentally measured; NTs/NNs; NTs/NNs: nanotriangles-nanoneedles; NS: nanosheets; NW-NF: nanowire-nanoflake; NP: nanoparticles

detection limit below 500 ppb when operated at 150 °C. Besides that, the sensor remains functional and demonstrates good sensitivity towards the targeted gas (H_2S) even at room temperature.

V. H_2S Gas Sensing Mechanism

The It is evident from the gas sensing measurements the addition of Cu_2O NPs significantly enhances the sensing response of the WS_2 nanomaterial towards H_2S gas. The sensing mechanism (Fig. S6) of WS_2 nanosheets is based on charge transfer process. When the sensor is exposed to a reducing gas such as H_2S in our case, the gas molecules get physiosorbed on the sensing layer resulting in change of electrical resistance of the material. H_2S being an electron donor, upon adsorption the molecule donates electrons to the multi-layered WS_2, thereby decreasing the concentration of charge carriers (holes), which in turn increases the overall resistance of the material. The reaction equations are provided in SI. This indicates a p-type semiconducting behavior for the fabricated tungsten disulfide sensor. In this regard, many reports have revealed a similar behavior. Additionally, according to previous research findings in literature, the adsorption energy for a monolayer WS_2 nanofilm for H_2S gas molecule is slightly lower than that for bilayer WS_2 nanofilms which is 246.2 meV [35]. This suggests that as the number of layers increases from mono to multi layered WS_2, their corresponding adsorption energy towards H_2S increases resulting in a qualitatively higher sensitivity towards H_2S, which is in accordance with our experimental results for multilayered WS_2. In the case of Cu_2O decoration, with addition of p-type Cu_2O NPs to the p-type WS_2 NTs/NNs there is a formation of a p-p junction

between the two materials. Considering the fact that the band gap of bulk WS_2 is 1.4 eV and that of Cu_2O is 2.2 eV [16], from a thermodynamic view, the electrons from the conduction band or donor level of Cu_2O will jump to the conduction band of WS_2 nanomaterial. This transfer of electrons towards WS_2 diminishes the number of majority carriers (holes), which results in an increase in the baseline resistance of the material (Fig. 11). According to our previous findings supported by XPS studies, when Cu_2O nanoparticles are exposed to H_2S there is a transition from oxide (Cu_2O) to sulfide (Cu_2S), which results in the injection of electronic charge from Cu_2S towards WS_2, thereby decreasing the concentration of charge carriers (holes) of the WS_2 host matrix. This transition is reversible, namely Cu_2S is oxidized back to Cu_2O when H_2S is removed from the sensor environment [27]. Furthermore, the synergistic effect between Cu_2O and WS_2 surface resulting from remarkable increase in surface area and exposed active sites further increases the sensor response. In addition to the high surface to volume ratio of nanoneedles-nanotriangle nanostructure, the nanoparticles offer more interspace, as a result, the assembly shows an increased porosity with a greater number of edges, resulting in availability of abundant active sites for gas interaction [36]. Moreover, multilayered nanofilms offer more electron transfer channels for improved reaction between the material and target gas, in comparison to the more closely packed nanoflake assembly. This may explain the supe- rior gas sensing properties recorded for Cu_2O nanoparticles decorated WS_2 with nanotriangle and nanoneedle morphology. Additionally, a significant change in resistance is observed at room temperature, which is attributed to the formation of metallic Cu_2S [27] when the sensor surface is exposed to H_2S.

VI. Conclusion

A We have investigated the H_2S gas sensing performance of Cu_2O decorated WS_2 sensor fabricated directly on commercial sensor transducer via a combination of AACVD and CVD technique and compared its sensing performance with pristine WS2 sensor. The sensor is composed of a hybrid structure of nanoneedles and nanotriangles of WS_2 with high quality and crystallinity as confirmed by XRD, Raman, TEM characterization techniques and Cu_2O nanoparticles attached on top of its surface confirmed by FESEM, TEM and EDX spectroscopy. The gas-sensing results have revealed that the decoration of WS2 nanoneedles/nanotriangles with Cu_2O nanoparticles dramatically increases their response to H_2S (i.e., 11-times increase in response compared to that of pristine WS_2 sensor from 54% to 610%. Additionally, this hybrid nanomaterial shows negligible moisture cross-sensitivity with a small drop in sensing response from 610% to 596%, which is rarely found in metal oxides. Moreover, the fabricated sensor shows excellent stability over a period of 7 months with only 16% fall off in its sensing response from 610% to 510%. Also, room temperature measurements show interesting results where the Cu_2O decorated WS_2 sensor shows significantly high gas sensing response of 138% as compared to that of pristine sensor with only 10% sensing response towards hydrogen sulphide detection. Furthermore, the direct growth of Cu_2O-functionalised WS_2 nanofilms on the sensor transducer with high degree of scalability and controllability makes the production of these nanofilms much more feasible. In this regard, our results provide new insights and paves a way to improve the gas sensing performance for next-generation materials with commercial potential due to the stable and high responses attained at much lower operating temperatures (even room temperature) than those of metal oxides.

Appendix

Supplementary material related to this article.

Acknowledgment

Fatima Ezahra Annanouch is a JdC Fellow. Carla Bittencourt and Jean Francois Colomer are research associates of FNRS (Belgium).

References

[1] J. Miao, C. Chen, and J. Y. S. Lin, "Humidity independent hydrogen sulfide sensing response achieved with monolayer film of CuO nanosheets," *Sens. Actuators B, Chem.*, vol. 309, Apr. 2020, Art. no. 127785, doi: 10.1016/j.snb.2020.127785.

[2] H. Sulfide, "Hydrogen sulfide (H_2S)," *Heal. San Fr.*, vol. 19, no. 7, p. 2, 2005. [Online]. Available: http://www.osha.gov/OshDoc/data_Hurricane_Facts/hydrogen_sulfide_fact.pdf

[3] S. K. Pandey, K.-H. Kim, and K.-T. Tang, "A review of sensor-based methods for monitoring hydrogen sulfide," *TrAC Trends Anal. Chem.*, vol. 32, pp. 87–99, Feb. 2012, doi: 10.1016/j.trac.2011.08.008.

[4] A. Mirzaei, S. S. Kim, and H. W. Kim, "Resistance-based H_2S gas sensors using metal oxide nanostructures: A review of recent advances," *J. Hazardous Mater.*, vol. 357, pp. 314–331, Sep. 2018, doi: 10.1016/j.jhazmat.2018.06.015.

[5] C. H. Moon, M. Zhang, N. V. Myung, and E. D. Haberer, "Highly sensitive hydrogen sulfide (H_2S) gas sensors from viral-templated nanocrystalline gold nanowires," *Nanotechnology*, vol. 25, no. 13, Apr. 2014, Art. no. 135205, doi: 10.1088/0957-4484/25/13/135205.

[6] A. Mortezaali and R. Moradi, "The correlation between the substrate temperature and morphological ZnO nanostructures for H_2S gas sensors," *Sens. Actuators A, Phys.*, vol. 206, pp. 30–34, Feb. 2014, doi: 10.1016/j.sna.2013.11.027.

[7] C. International and C. Assessment, "H2S human health aspects," World Health Org., Geneva, Switzerland, 2003.

[8] Y. Guo, M. Gong, Y. Li, Y. Liu, and X. Dou, "Sensitive, selective, and fast detection of ppb-level H_2S gas boosted by ZnO-CuO mesocrys- tal," *Nanosc. Res. Lett.*, vol. 11, no. 1, Dec. 2016, Art. no. 475, doi: 10.1186/s11671-016-1688-y.

[9] T. Xu *et al.*, "The ultra-high NO_2 response of ultra-thin WS_2 nanosheets synthesized by hydrothermal and calcination processes," *Sens. Actuators B, Chem.*, vol. 259, pp. 789–796, Apr. 2018, doi: 10.1016/j.snb.2017.12.070.

[10] N. S. A. Eom, H.-B. Cho, Y. Song, G. M. Go, J. Lee, and Y.-H. Choa, "Room-temperature H_2S gas sensing by selectively synthesized $Cu_{x(x=1,2)}O$:SnO_2 thin film nanocomposites with oblique & vertically assembled SnO_2 ceramic nanorods," *Sens. Actuators B, Chem.*, vol. 273, pp. 1054–1061, Nov. 2018, doi: 10.1016/j.snb.2018.06.098.

[11] Z. S. Hosseini, A. I. Zad, and A. Mortezaali, "Room temperature H_2S gas sensor based on rather aligned ZnO nanorods with flower-like structures," *Sens. Actuators B, Chem.*, vol. 207, pp. 865–871, Feb. 2015, doi: 10.1016/j.snb.2014.10.085.

[12] W. Yu-De, C. Zhan-Xian, L. Yan-Feng, Z. Zhen-Lai, and W. Xing-Hui, "Electrical and gas-sensing properties of WO_3 semiconductor material," *Solid. State. Electron.*, vol. 45, no. 5, pp. 639–644, 2001, doi: 10.1016/S0038-1101(01)00126-5.

[13] C. Cong *et al.*, "Synthesis and optical properties of large-area single-crystalline 2D semiconductor WS_2 monolayer from chemical vapor deposition," *Adv. Opt. Mater.*, vol. 2, no. 2, pp. 131–136, Feb. 2014, doi: 10.1002/adom.201300428.

[14] J. Yu, J. Li, W. Zhang, and H. Chang, "Synthesis of high quality two-dimensional materials via chemical vapor deposition," *Chem. Sci.*, vol. 6, no. 12, pp. 6705–6716, 2015, doi: 10.1039/c5sc01941a.

[15] W. Choi, N. Choudhary, G. H. Han, J. Park, D. Akinwande, and Y. H. Lee, "Recent development of two-dimensional transition metal dichalcogenides and their applications," *Mater. Today*, vol. 20, no. 3, pp. 116–130, 2017, doi: 10.1016/j.mattod.2016.10.002.

[16] T. Järvinen *et al.*, "WS_2 and MoS_2 thin film gas sensors with high response to NH_3 in air at low temperature," *Nanotechnology*, vol. 30, no. 40, Oct. 2019, Art. no. 405501, doi: 10.1088/1361-6528/ab2d48.
[17] B. Cho *et al.*, "Chemical sensing of 2D Graphene/MoS_2 heterostructure device," *ACS Appl. Mater. Interface*, vol. 7, no. 30, pp. 16775–16780, Aug. 2015, doi: 10.1021/acsami.5b04541.
[18] F. Perrozzi, S. M. Emamjomeh, V. Paolucci, G. Taglieri, L. Ottaviano, and C. Cantalini, "Thermal stability of WS_2 flakes and gas sensing properties of WS_2/WO_3 composite to H_2, NH_3 and NO_2," *Sens. Actuators B, Chem.*, vol. 243, pp. 812–822, May 2017, doi: 10.1016/j.snb.2016.12.069.
[19] S. Cui, Z. Wen, X. Huang, J. Chang, and J. Chen, "Stabilizing MoS_2 nanosheets through SnO_2 nanocrystal decoration for high-performance gas sensing in air," *Small*, vol. 11, no. 19, pp. 2305–2313, May 2015, doi: 10.1002/smll.201402923.
[20] D. Zhang, J. Wu, and Y. Cao, "Ultrasensitive H_2S gas detection at room temperature based on copper oxide/molybdenum disulfide nanocomposite with synergistic effect," *Sens. Actuators B, Chem.*, vol. 287, pp. 346–355, May 2019, doi: 10.1016/j.snb.2019.02.008.
[21] J. A. Rodriguez, S. Chaturvedi, M. Kuhn, and J. Hrbek, "Reaction of H_2S and S_2 with metal/oxide surfaces: Band-gap size and chemical reactivity," *J. Phys. Chem. B*, vol. 102, no. 28, pp. 5511–5519, Jul. 1998, doi: 10.1021/jp9815208.
[22] Z. U. Abideen, J.-H. Kim, A. Mirzaei, H. W. Kim, and S. S. Kim, "Sensing behavior to ppm-level gases and synergistic sensing mechanism in metal-functionalized rGO-loaded ZnO nanofibers," *Sens. Actuators B, Chem.*, vol. 255, pp. 1884–1896, Feb. 2018, doi: 10.1016/j.snb.2017.08.210.
[23] F. Wang *et al.*, "A highly sensitive gas sensor based on CuO nanoparticles synthetized via a sol–gel method," *RSC Adv.*, vol. 6, no. 83, pp. 79343–79349, 2016, doi: 10.1039/c6ra13876d.
[24] A. Alagh *et al.*, "CVD growth of self-assembled 2D and 1D WS_2 nanomaterials for the ultrasensitive detection of NO_2," *Sens. Actuators B, Chem.*, vol. 326, Jan. 2021, Art. no. 128813, doi: 10.1016/j.snb.2020.128813.
[25] T. A. J. Loh, D. H. C. Chua, and A. T. S. Wee, "One-step synthesis of few-layer WS_2 by pulsed laser deposition," *Sci. Rep.*, vol. 5, no. 1, Nov. 2016, Art. no. 18116, doi: 10.1038/srep18116.
[26] Y. Wu, Y. Hao, M. Fu, W. Jiang, and Q. Wu, "Effects of thermally-induced changes of Cu grains on domain structure and electrical performance of CVD-grown graphene," *Nanoscale*, vol. 8, pp. 930–937, 2016, doi: 10.1039/c5nr06195d.
[27] F. E. Annanouch *et al.*, "Aerosol-assisted CVD-grown WO_3 nanoneedles decorated with copper oxide nanoparticles for the selective and humidity-resilient detection of H_2S," *ACS Appl. Mater. Interface*, vol. 7, no. 12, pp. 6842–6851, Apr. 2015, doi: 10.1021/acsami.5b00411.
[28] F. Lan *et al.*, "Synthesis of large-scale single-crystalline monolayer WS_2 using a semi-sealed method," *Nanomaterials*, vol. 8, no. 2, p. 100, Feb. 2018, doi: 10.3390/nano8020100.
[29] V. Weiß, S. Seeger, K. Ellmer, and R. Mientus, "Reactive magnetron sputtering of tungsten disulfide (WS_{2_x}) films: Influence of deposition parameters on texture, microstructure, and stoichiometry," *J. Appl. Phys.*, vol. 101, no. 10, May 2007, Art. no. 103502, doi: 10.1063/1.2716395.
[30] D. Liu, Z. Tang, and Z. Zhang, "Comparative study on NO_2 and H_2S sensing mechanisms of gas sensors based on WS_2 nanosheets," *Sens. Actuators B, Chem.*, vol. 303, Jan. 2020, Art. no. 127114, doi: 10.1016/j.snb.2019.127114.
[31] E. Lee, Y. S. Yoon, and D.-J. Kim, "Two-dimensional transition metal dichalcogenides and metal oxide hybrids for gas sensing," *ACS Sensors*, vol. 3, no. 10, pp. 2045–2060, Oct. 2018, doi: 10.1021/acssensors.8b01077.
[32] G. A. Asres *et al.*, "Ultrasensitive H_2S gas sensors based on P-type WS_2 hybrid materials," *Nano Res.*, vol. 11, no. 8, pp. 4215–4224, Aug. 2009.
[33] J.-H. Kim, A. Mirzaei, H. W. Kim, and S. S. Kim, "Realization of au-decorated WS_2 nanosheets as low power-consumption and selec- tive gas sensors," *Sens. Actuators B, Chem.*, vol. 296, Oct. 2019, Art. no. 126659, doi: 10.1016/j.snb.2019.126659.
[34] Y. Jeong *et al.*, "Gas sensing characteristics of the FET-type gas sensor having inkjet-printed WS_2 sensing layer," *Solid-State Electron.*, vol. 153, pp. 27–32, Mar. 2019, doi: 10.1016/j.sse.2018.12.009.
[35] W. T. Koo *et al.*, "Few-layered WS_2 nanoplates confined in Co, N-doped hollow carbon nanocages: Abundant WS_2 edges for highly sensitive gas sensors," *Adv. Funct. Mater.*, vol. 28, no. 36, pp. 1–11, 2018, doi: 10.1002/adfm.201802575.
[36] T.-T. Li, N. Bao, A.-F. Geng, H. Yu, Y. Yang, and X.-T. Dong, "Study on room temperature gas-sensing performance of CuO film-decorated ordered porous ZnO composite by In_2O_3 sensitization," *Roy. Soc. Open Sci.*, vol. 5, no. 2, Feb. 2018, Art. no. 171788, doi: 10.1098/rsos.171788.

Aanchal Alagh received the bachelor's and master's dual degrees in nanotechnology from the Amity Institute of Nanotechnology, Amity University, Noida, India, in 2016. She is currently pursuing the Ph.D. degree with the Department of Electrical, Electronic Engineering and Automation, Universitat Rovira i Virgili, Tarragona, Spain. She has undertaken research projects and internships at prestigious organizations in India and abroad, such as the Indian Institute of Technology, Bombay (IIT-B), CSIR-Central Scientific Instruments Organization (CSIO). She worked on development of icephobic coatings for aerospace applications (project funded by BOEING). She is working on the synthesis of mono and multilayers dichalcogenides using chemical vapor deposition technique for gas sensing applications. Her research interests include scalable synthesis of these 2D nanomaterials, either directly or by transferring them later, to different application substrates including flexible substrates.

Fatima Ezahra Annanouch received the master's degree in electronic of autonomous system from the Faculty of Sciences, University Moulay Ismail Meknes, Morocco, in 2010, and the Ph.D. degree in the fabrication and characterization of metal oxide nanowires gas sensors from the Department of Electrical Electronic Engineering and Automation, Rovira i Virgili University, Tarragona, Spain, in 2015. She started her first postdoctoral position (two years) at IM2NP, Aix-Marseille Université, France, in 2016. During this period, she was working on the transdermal detection of alcohol using metal oxides gas sensors. Since 2018, she has been holding a postdoctoral position with the Minos Group, Rovira i Virgili University. Her research interests include fabrication and characterization of metal oxide nanostructures, material characterization (SEM, TEM, XRD, XPS, and RAMAN spectroscopy), nanomaterial synthesis (aerosol assisted CVD, CVD, Sputtering), 1D metal oxide nanostructures (WO_3, SnO_2, ZnO), 2D transition metals dichalcogenides (WS_2 and MoS_2).

Polona Umek received the Ph.D. degree in materials chemistry from the University of Ljubljana. She is currently working as a Higher Associate Researcher with Jožef Stefan Institute. Her research interest includes synthesis and morphology control of semiconducting nanomaterials for water remediation and catalysis.

Carla Bittencourt received the Ph.D. degree in chemistry from UMONS, Belgium. She worked as a Postdoctoral Researcher with the University of Warwick, U.K. She is currently a Research Associate with the Fonds de la Recherche Scientifique (FRS-FNRS) and a Professor with the University of Mons, Belgium. Her research interests include surface analysis and surface modification by low-energy ion irradiation.

Jean François Colomer is a Senior Research Associate with the National Funds for Scientific Research (FRS-FNRS, Belgium), working with the University of Namur, Belgium. His research interests include synthesis using atmospheric chemical vapor deposition (CVD) method and characterization of low-dimensional materials covering carbon materials as graphene to other 2D materials such as transition metal dichalcogenides.

Eduard Llobet (Senior Member, IEEE) received the Ph.D. degree from UPC in 1997. He completed a one-year postdoctor with the University of Warwick, U.K. He is a Full Professor of Electronics with the Universitat Rovira i Virgili, Tarragona, Spain. He is also the President of the Spanish Network of Microsystems and Nanotechnology (IBERNAM). He is gaining insight in the surface chemistry, nature of defects and the specific mechanisms of interaction with target gases, unveiling gas-sensing mechanisms, structure-performance relationships, and functionalization of carbon nanomaterials employing cold plasmas, for grafting metal nanoparticles or complex molecules, achieving highly sensitive and selective sensors. He is also working towards the realization of nanomaterial-based flexible gas sensors and sensor systems with a performance that matches the one of conventional rigid devices. His research interests include growth of single crystalline metal oxide nanomaterials employing bottom-up approaches and the CVD growth of transition metal dichalcogenides.

Chapter-4

PdO and PtO loaded WS_2 boosts NO2 gas sensing characteristics at room temperature

Sensors & Actuators: B. Chemical 364 (2022) 131905

Contents lists available at ScienceDirect

Sensors and Actuators: B. Chemical

journal homepage: www.elsevier.com/locate/snb

PdO and PtO loaded WS_2 boosts NO_2 gas sensing characteristics at room temperature

Aanchal Alagh [a], Fatima Ezahra Annanouch [a,*], Khaled Al Youssef [b], Carla Bittencourt [b], Frank Güell [c], Paulina R. Martínez-Alanis [c], Marc Reguant [c], Eduard Llobet [a]

[a] Departament d'Enginyeria Electronica, Universitat Rovira i Virgili, avenida Països Catalans 26, 43007 Tarragona, Spain
[b] Laboratory of Plasma-Surface Interaction Chemistry (PSI Chem), University of Mons, Av. Nicolas Copernic 1, 7000 Mons, Belgium
[c] ENFOCAT-IN2UB, Universitat de Barcelona, C/Martí i Franquès 1, 08028 Barcelona, Catalunya, Spain

ARTICLE INFO

Keywords:
TMDs
Functionalization
Gas sensors
CVD
AACVD
Tungsten disulphide

ABSTRACT

In this work tungsten disulphide nanostructures loaded with platinum-oxide (PtO), or palladium-oxide (PdO) were grown directly onto alumina substrates. This was achieved using a combination of aerosol-assisted chemical vapour deposition (AA-CVD) method with atmospheric pressure CVD technique. At first, tungsten oxide nanowires loaded with either PtO or PdO nanoparticles were successfully co-deposited via AA-CVD followed by sulfurization at 900 °C in the next step. The morphological, structural, and chemical characteristics were investigated using FESEM, TEM, XRD, XPS and Raman spectroscopy. The results confirm the presence of PdO and PtO in the WS_2 host matrix. Gas sensing attributes of loaded and pristine WS_2 sensors were investigated, at room temperature, towards different analytes (NO_2, NH_3, H_2 etc.). Both pristine and metal-oxide loaded WS_2 gas sensors show remarkable responses at room temperature towards NO_2 detection. Further, the loaded sensors demonstrated stable, reproducible, ultrasensitive, and enhanced gas sensing response, with a detection limit below 25 ppb. Additionally, the effect of ambient humidity on the sensing response of both loaded and pristine sensors was investigated for NO_2 gas. The response of PtO loaded sensor considerably decreased in humid environments, while the response for pristine and PdO loaded sensors increased. However, slightly heating (at 100 °C) the sensors, suppresses the influence of humidity. Finally, the long-term stability of different sensors is investigated, and the results demonstrate high stability with repeatable results after 6 weeks of gas sensing tests. This work exploits an attractive pathway to add functionality in the transition metal dichalcogenide host matrix.

1. Introduction

While technological advancements have improved an individual's lifestyle, they have also contributed to the emergence of environmental issues, such as global warming and pollution. In particular, the number of pollutant emissions in the atmosphere has increased dramatically, leading to air pollution [1]. This phenomenon is caused by particulate matter and several harmful gases, including nitrogen dioxide (NO_2), ammonia (NH_3), carbon monoxide (CO), sulphur dioxide (SO_2), hydrogen sulphide (H_2S), carbon monoxide (CO), and ozone (O_3) [2]. These gases not only pose a threat to the environment but are also detrimental to human health, as they are a leading cause of ailments such as respiratory irritation syndrome, lung diseases, and bronchitis, only to name a few. According to research, air pollution is responsible for one out of every nine deaths each year, making it the leading cause of death. Besides, around 92% of the world's population lives in areas with poor air quality, putting them at significant risk of premature death [3]. Furthermore, among all, NO_2 is one of the life-threatening contaminants. Therefore, the legitimate airborne permissible exposure limit of NO_2, as stipulated by the Occupational Safety and Health Administration (OSHA) is 5 ppm, which cannot be surpassed [4]. Also, the American Industrial Hygiene Association has set a 5-minute emergency exposure limit for NO_2 at 35 parts per million (ppm) as exposure above this concentration can cause skin damage and respiratory issues [5]. Therefore, it is now more important than ever to regularly monitor and evaluate the air quality.

In this respect, gas sensing devices play an essential role in the detection and monitoring of poisonous pollutants like NO_2 to reduce their damaging effects. Based on their working mechanism, these devices are categorised into chemoresistive, optical, electrochemical, and

* Corresponding author.
E-mail address: fatimaezahra.annanouch@urv.cat (F.E. Annanouch).

https://doi.org/10.1016/j.snb.2022.131905
Received 31 January 2022; Received in revised form 2 April 2022; Accepted 13 April 2022
Available online 16 April 2022

gravimetric (e.g., micro-cantilever) sensors. Among them, the chemoresistive type gas sensors have obtained broad consideration as they offer significant advantages over other sensors in terms of their simple fabrication, ease of operation and affordable cost. In general, these sensors are based on metal oxide semiconductors (MOX), thanks to their excellent gas-sensing performance towards harmful gases, such as NH_3, H_2S and CO [6]. However, conventional MOX chemoresistive sensors typically work at elevated temperatures above 200 ºC, which along with high power consumption brings a huge hindrance to their portability and long-run reliability [7]. As a result, in the last few years, considerable efforts have been directed towards the development of room temperature gas sensors for application in consumer electronics, wearables and wireless sensing networks.

Consequently, 2D materials like inorganic analogues of graphene (GR), such as transition-metal dichalcogenides (TMDs), have emerged as a viable material for gas sensing applications. Similar to GR, this class of materials have a layered structure. They have X-M-X architecture, where M is a transition metal atom and X is a chalcogen atom, however, unlike GR, they do not have a single layer of atoms. The chalcogen atoms are arranged in two hexagonal planes separated by a plane of metal atoms, forming sandwich structures. The atoms in these three layers are bonded together by strong covalent connections, whereas each three-layer sheet is attached to its neighbouring atoms by weak Van der Waals forces of attraction. Moreover, TMDs, unlike other carbon-based 2D structures (such as GR), have an inherent energy bandgap, which gives them remarkable chemical and electrical characteristics [8]. As a result, these materials are extremely useful in a variety of sectors including aerospace, military, semiconductor, automotive, and medicine. For instance, they are utilized as a photovoltaic material for solar cell application [9], light-emitting devices [10], transistors [11], diodes and many more.

While there has been a recent spike in interest in the synthesis and study of TMDs thin films, most of these studies have focused on MoS_2 and WS_2. 2D layered tungsten disulphide, on the other hand, has fascinated the gas sensing community with its remarkable electrical and optoelectronic capabilities. A two-dimensional layer of WS_2 is made up of covalently bound W-S atoms that are stacked together by a weak Van der Waals interaction [13], which permits gases to diffuse smoothly in between the layers. Furthermore, because of its large surface area and active gas adsorption sites (edges, vacancies, and surface defects), its 2D structure outperforms conventional MOX-based gas sensors at significantly lower operating temperatures [3,6,12]. It is not only due to its unique features, but also to the ease with which these properties may be tuned through dimension control, surface design, and doping.

However, despite all the above-stated properties, pristine WS_2 shows poor gas sensing response at room temperature, this is due to the strong adsorption of gas molecules on the WS_2 surface which leads to partial desorption of these molecules during the recovery cycle, resulting in much longer response time with low sensing response. Hence, limiting the practical applications of pristine WS_2 based gas sensors in the real environment [12,13].

In MOX chemoresistors, loading the active layer with noble metals is a successful way to enhance the gas sensing performance, as these noble metals can induce electronic and chemical sensitization effects at the surface of the host matrix. Catalytic metal particles increase the number of active sites and lower the activation energy for gas adsorption, resulting in higher adsorption rates and lower operating temperatures. Subsequently, improved sensing response, better recovery characteristics and enhanced selectivity are achieved [14–16]. A similar approach has also been reported for enhancing the sensing response of TMDs. The dispersion of noble metal particles on the surface of TMDs creates spill-over effects that aid to increase the rate of surface reactions, resulting in faster response and recovery times [17]. For instance, it has been reported that loading WS_2 nanosheets with Ag nanowires dramatically improves the sensing response with a 12-fold increase (667%) towards NO_2 exposure via a spillover effect [18]. Similarly, a study of Au decorated WS_2 nanosheets reported enhanced sensing response towards CO using very low power consumption (28.6 μW), which is attributed to the spillover effect brought about by Au NPs. Moreover, the sensor showed enhanced selectivity towards CO owing to the catalytic effect of Au NPs [13]. Decoration of WS_2 with WO_3 NPs via layer-by-layer self-assembly technique displayed enhanced gas sensing results. The response values of WS_2, WO_3, and WS_2/WO_3-LbL sensors toward 10 ppm of ethanol gas were 37.82%, 14.88%, and 74.50%, respectively. The enhanced sensing performance towards ethanol detection is attributed to the WS_2/WO_3 heterojunction unique charge-transfer properties as well as the synergistic effects of the two materials [19]. Moreover, our recent study on Cu_2O doped WS_2 also revealed enhanced gas sensing properties (11-fold increase in the sensor response) towards H_2S gas detection. Herein, the proposed gas sensing mechanism is based on the p-p heterojunction formed between the two materials. [20]. Even though the literature reviewed above indicates that the modification of TMDs results in enhanced gas sensing properties, there is a need for sensors that work at room temperature and are simple to fabricate.

To date, a variety of methods have been explored to graft functional groups or complex molecules onto pristine TMDs, such as plasma treatment [22], [23], low-energy ion implantation/substitutional doping [24], [25], and covalent or non-covalent functionalization [26]. However, each method has its limitations. For instance, substitutional doping causes defects in the TMD structure [27], [28]. Another study suggests functionalisation of TMDs flakes with different solutions to achieve the effect of doping, nevertheless, the procedure is often difficult and time-consuming [29], [30]. Moreover, doping with plasma has also been reported in previous studies, resulting in defect formation along with a considerable reduction in charge mobility [22], [23]. Sputtering is another technique that is widely used for depositing metal/metal oxide NPs. Besides, the use of sputtering equipment is involved, and the overall operating cost is high. As a result, it is necessary to investigate efficient loading strategies that are stable, simple to perform, and do not result in severe defects appearing in the TMD material.

Alternatively, inspired by our previous research works [31,32], deposition via aerosol-assisted chemical vapour deposition (AACVD) is an excellent choice to incorporate metal additives on the TMD host matrix. Indeed, it allows us to simultaneously incorporate two or more materials along the host matrix, using one step deposition. It is easy and practical compared to the above-mentioned techniques. Moreover, by combining CVD with AACVD, we can directly grow the sensing material onto the sensor transducer, resulting in a high growth yield, uniform coverage and stable gas sensing responses. Besides, the direct growth of these films, which has a high degree of scalability and controllability, makes nanostructure production considerably closer to mass production.

In this regard, we propose for the first time, the successful growth of tungsten disulphide nanosheets loaded with PdO and PtO materials, using the combination of AACVD and CVD methods for the fabrication of room temperature NO_2 gas sensor. Throughout the paper, loaded sensors are either denoted by WS_2/PtO (platinum-oxide) or WS_2/PdO (palladium-oxide) whereas pristine sensors are denoted by WS_2. Tungsten oxide nanowires loaded with PtO and/or PdO nanoparticles were co-deposited via aerosol-assisted chemical vapour deposition, followed by sulfurization at 900 °C in the corresponding step. The sensing films were then characterised by FESEM, TEM, XRD, Raman spectroscopy, PL spectroscopy and X-ray photoelectron spectroscopy (XPS) to verify the material characteristics of pristine and loaded nanostructures. Moreover, the gas sensing properties of pristine and loaded WS_2 sensors were investigated and compared towards NO_2 detection under both dry and humid atmospheres. Additionally, the selectivity of the fabricated sensors was also studied by exposing them to different analytes such as NH_3, H_2S, CO and H_2. To the best of our knowledge, no previous reports have described the synthesis of platinum (PtO), or palladium (PdO) loaded WS_2 adopting the methodology we exploited in our study. Finally, the underlying gas sensing mechanism for the loaded WS_2 nanostructures is

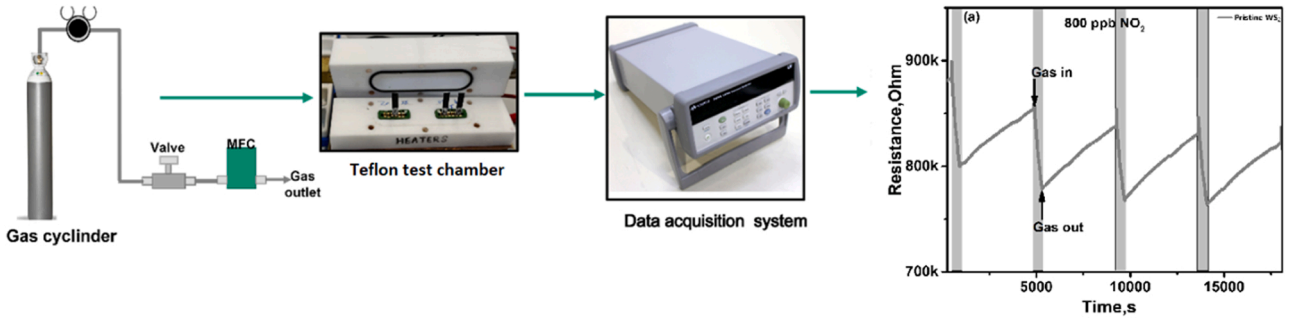

Fig. 1. Gas sensing measurement system setup.

also discussed in detail.

2. Experimental section

2.1. Material synthesis

Multi-layered nanosheets of pristine and/or loaded WS_2 films were grown in two steps.

2.1.1. First step deposition using aerosol-assisted chemical vapour deposition technique (AACVD)

In the first step, either pristine or metal-oxide NPs loaded nanowires of WO_3 were grown, directly on a commercial alumina substrate, with screen-printed, interdigitated platinum electrodes on one side and a platinum resistor heater on the backside. It is a one-step growth process achieved via AACVD method. This technique is widely used to deposit nano and microstructures of metal oxides (Fig. S1 gives a pictorial description of the complete process). Pristine nanowires of WO_3 were grown using 50 mg of tungsten hexacarbonyl (WCO_6) dissolved in a solution of 15 mL acetone (CAS: 67–64–1) and 5 mL methanol (CAS: 67–56–1). The solution was kept in an ultrasonic bath for 20 min. After the solution was fully solubilised, it was placed in an ultrasonic bath to convert the solution to an aerosol. Nitrogen (N_2) was used as a carrier gas and the flow rate was set to 0.5 L/min to transport the aerosol to the deposition chamber, where the alumina substrate was kept. Before this, the deposition chamber was heated to a temperature of 400 °C. The growth process took approximately 30 min to complete. Afterwards, the chamber was allowed to naturally cool down and later the substrate with WO_3 nanowires was annealed at 500 °C for 2 h using a carbolite CWF 1200 muffle furnace. Annealing was done to remove any carbon residual left from the precursor, resulting in fully oxidised WO_3 nanowires.

Metal-oxide NPs loaded nanowires were fabricated adopting the same procedure and equipment as described for the deposition of pristine WO_3 nanowires. However, the solution containing precursors and the amount of organic solvent used varied. For instance, in the case of PdO/WO_3, 25 mg of $W(CO)_6$ was dissolved in 9 mL acetone and 5 mg of palladium acetylacetonate ($Pd(C_5H_7O_2)_2$) was dissolved in 3 mL methanol separately. The solutions were then mixed and sonicated for 15–20 mins, whereas for PtO/WO_3, 25 mg of $W(CO)_6$ was dissolved in 9 mL acetone and 36 mg platinum acetylacetonate $Pt(O_2C_5H_7)_2$ was dissolved in 3 mL methanol separately. Again, the two solutions were then mixed and sonicated for 15–20 mins. After this, the same procedure was followed as described previously for growing pristine WO_3 nanowires. However, for growing metal-oxide loaded nanowires the deposition chamber was heated to a temperature of 350 °C only instead of 400 °C.

2.1.2. Second step deposition using atmospheric pressure chemical vapour deposition technique (CVD)

In the second step of the synthesis, the as-grown WO_3 nanowires are sulfurized to form WS_2 nanomaterial using a quartz tube furnace via atmospheric pressure chemical vapour deposition technique (CVD). This experiment is performed inside an in-house custom built CVD reactor under hydrogen-free conditions (Fig. S2). Preceding the sulfurization process, the quartz tube is flushed with 0.5 L/min of argon gas to remove any oxygen content present in the reactor. Two ceramic boats containing an equal amount of sulphur (S) powder each (>99.95%, Sigma Aldrich, CAS: 7704–34–9) are placed at different temperature zones of the deposition furnace. One of which is placed inside a secondary semi-sealed quartz tube next to the WO_3 nanowires and the other sulphur boat is placed outside the secondary quartz tube. The boat outside the secondary quartz tube is placed upstream of the argon flow inside the bigger quartz tube. This promotes the double sulfurization of the as-grown WO_3 nanowires. The furnace is then heated from room temperature to 900 °C with a heating rate of 40 °C/min to remove contaminants such as water or residual organics. This is done to obtain the nucleation of WS_2. The growth of WS_2 is achieved by allowing the reaction to proceed at 900 °C for 60 min under a constant flow of argon. It is vital to control all the growth parameters including the gas flow rate, heating rate and the quantity of sulphur powder used to obtain homogeneously sulfurized multi-layered films of WS_2. After the growth phase, the furnace is cooled naturally to room temperature.

Metal-oxide loaded nanowires were sulfurized adopting the same procedure and equipment as described for the sulfurization of pristine WO_3 nanowires.

2.2. Material characterization techniques

The morphology of the as-grown WO_3 nanowires loaded with PtO or PdO NPs were examined using a transmission electron microscope (JEOL 1011) and a field-emission scanning electron microscope (FESEM) Hitachi 2000 and FEI Helios Nanolab 650. Furthermore, once the films were sulfurized, they were again examined using FESEM. For crystalline phase analysis, XRD measurements were made, using a Bruker-AXS D8-Discover diffractometer equipped with a parallel incident beam (Gober mirror), vertical XYZ motorized stage and with a GADDS (General Area Diffraction System). The elemental and chemical composition was studied via X-ray photoelectron spectroscopy (XPS) using a versaprobe PHI5000 spectrometer (equipped with a monochromatic Al Kα X-ray source). For spectrum analysis, the CASA XPS software was used. The Raman spectroscopy measurements were obtained using a Renishaw in Via, laser 514 nm, ion argon-Novatech, 25 mW. Moreover, Photoluminescence measurements at room temperature were also made using a chopped Kimmon IK Series He-Cd laser (325 nm and 40 mW). Fluorescence was dispersed with an Oriel Corner Stone 1/8 74000 monochromator, detected using a Hamamatsu H8259–02 with a socket assembly E717–500 photomultiplier, and amplified through a Stanford Research Systems SR830 DSP. A filter in 360 nm was used to stray light. All spectra were corrected for the response function of the setups.

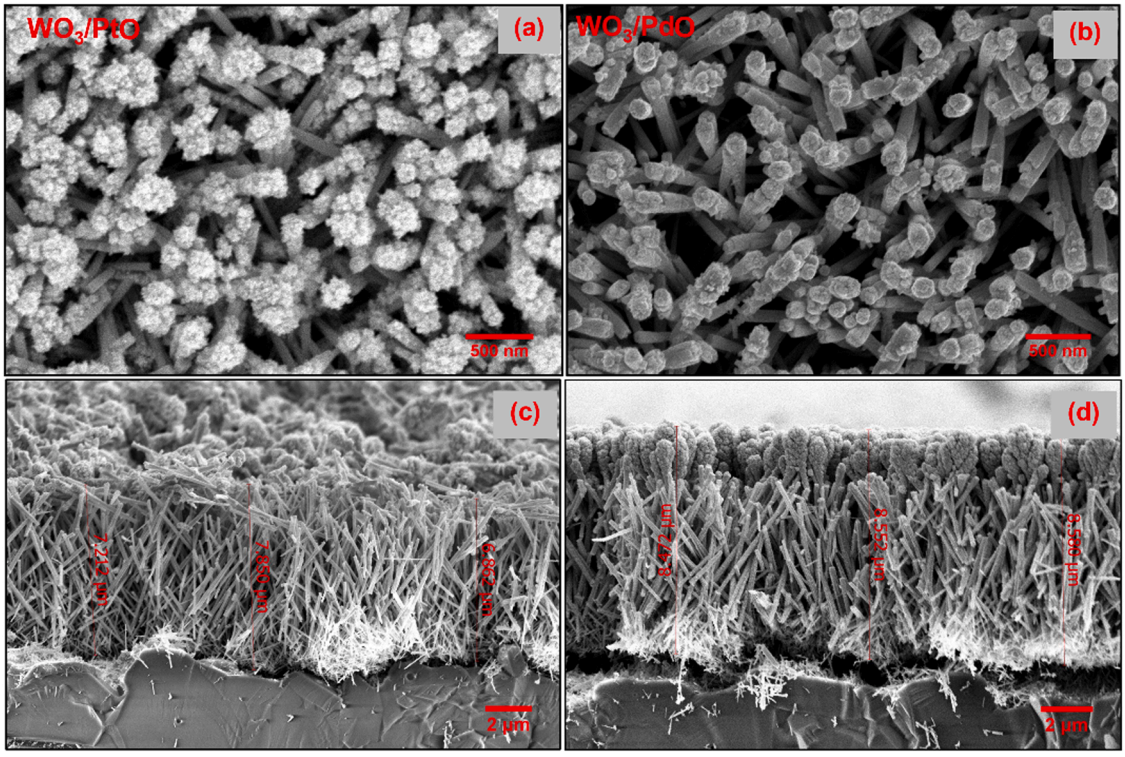

Fig. 2. FESEM images of WO_3 nanoneedles decorated with (a) PtO, (b) PdO nanoparticles. Cross-section image depicting vertically aligned (c) pristine (d) metal-oxide NPs loaded on WO_3.

2.3. Gas sensing tests

The gas sensing characteristics of the as-fabricated loaded and pristine WS_2 sensors were measured using a homemade detection system. Commercial alumina substrates with interdigitated platinum electrodes (with 300 µm electrode gap) on the front side and a platinum resistive heater meander on the backside were used to grow either PtO or PdO loaded WO_3 nanowires which were later sulfurized to grow pristine or loaded films of WS_2. The as-fabricated sensors were then tested under a continuous gas flow (100 sccm) in a Teflon test chamber (35 mL in volume) that can accommodate four sensors simultaneously. This testing chamber was connected to a fully automated, continuous gas flow measurement set-up, able to supply diluted gas mixtures as well as humidified gas mixtures using mass flow controllers. An illustration of a typical gas measurement setup is shown in Fig. 1. The gases employed for testing were used from calibrated gas cylinders balanced in dry synthetic air. Unless otherwise specified, all the gas sensing measurements were performed at room temperature.

The sensing measurements consisted of monitoring the change in electrical resistance of the sensor upon exposure to different concentrations of various analytes (such as NO_2, NH_3, H_2, CO, H_2S) performing up to four replicates for each analyte concentration. The electrical resistance was measured by using an Agilent-34972A multimeter. The sensors were exposed to a given analyte for 10 min and subsequently, the chamber was purged with dry air for 110 min to recover initial baseline resistance. The time left to recover the initial baseline resistance was kept longer purposely since gas sensing measurements were done at room temperature, and desorption of gas molecules takes generally longer than when sensors are operated at elevated temperatures. Sensors were kept overnight in a dry air flow to better stabilise their baseline resistance every time they had to be exposed to a new target gas. The total flow rate was kept constant at a value of 100 mL/min throughout the measurements. Some experiments were also conducted under a humid background (e.g., 50% RH at room temperature, i.e., 21°C) to investigate the humidity interference. This humidity level was kept constant while exposing the sensor to different concentrations of NO_2 gas.

3. Results and discussion

3.1. Structural and morphological characteristics

AACVD of pure $W(CO)_6$ and/or a mixture of $W(CO)_6$ with Pd $(C_5H_7O_2)_2$ and/or Pt $(O_2C_5H_7)_2$ resulted in the formation of adherent uniform films of tungsten trioxide nanoneedles and/or tungsten trioxide nanoneedles loaded with PdO and/or PtO nanoparticles, grown directly onto commercial alumina sensor substrates. The as-grown films were initially dark blue while after annealing, they change to pale green for tungsten oxide, brown for tungsten trioxide decorated with palladium-oxide nanoparticles, and off-white for the tungsten trioxide decorated with platinum-oxide nanoparticles. Once these films have been sulfurized the colour for all the samples changes to dark black confirming the formation of WS_2.

A field-emission scanning electron microscope (FESEM) was used to characterise the as-deposited films before and after sulfurization. Fig. 2a and b show the FESEM imaging results of the as-synthesised material loaded with either PtO or PdO NPs. It was observed that loading the material with different nanoparticles did not affect the morphology resulting in 60–120 nm thick nanoneedles with similar structures. Moreover, a cross-section of the loaded and pristine films was obtained using an ETD detector installed in the FESEM. The results (Fig. 2c-d) show a small difference in morphology and film thickness between loaded and pristine materials. As depicted in Fig. 2c, pristine nanomaterial consists of 60–120 nm thick nanoneedles with a film thickness of roughly 6–7 µm. After decorating, the nanoneedles are loaded with nanoparticles along with their bodies, as well as an accumulation of these nanoparticles at their tips, resulting in an 8–9 µm film thickness, as seen in Fig. 2d. Furthermore, the nanoneedles were found to be vertically aligned, slanted, and dispersed equally across the entire substrate.

The as-grown films containing WO_3 nanoneedles were also analysed

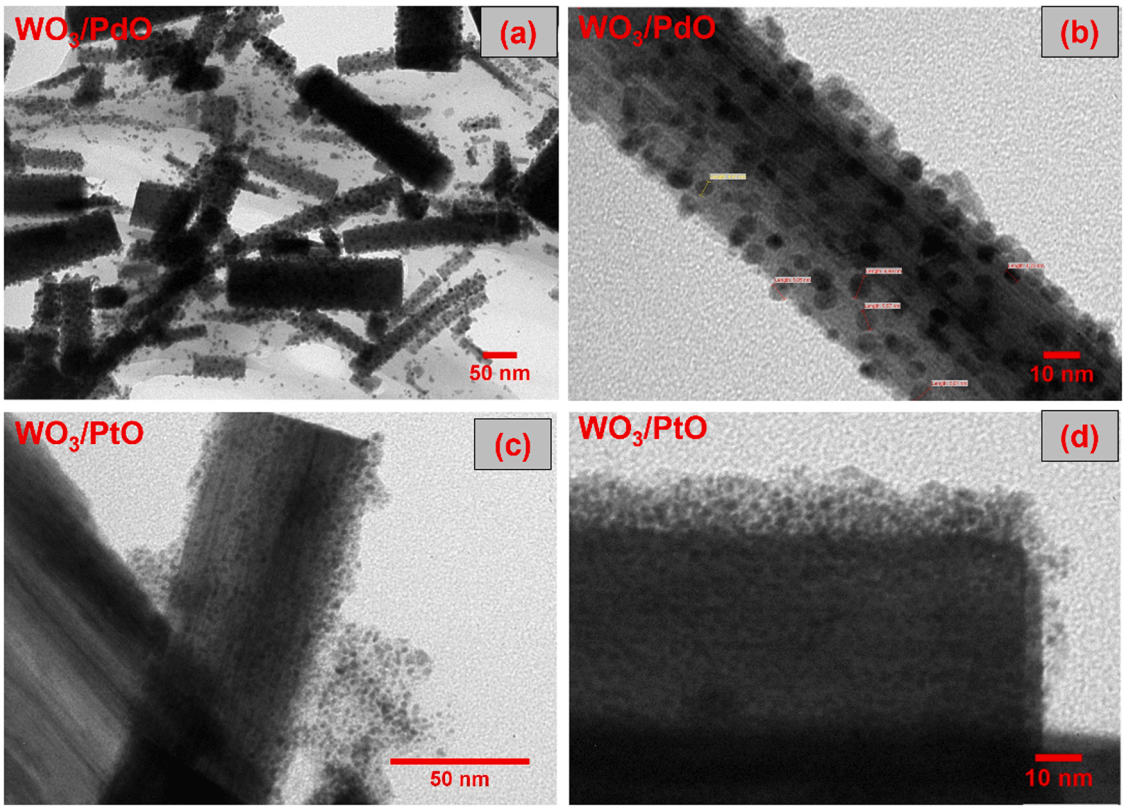

Fig. 3. TEM imaging results depicting WO_3 nanoneedles (NNs) decorated with nanoparticles of (a and b) palladium oxide, having a particle size in the range of 4–6 nm and (c and d) platinum oxide with significantly smaller size in the range of 1–2 nm.

using TEM before sulfurization. The films were scraped from the alumina substrate and deposited over carbon-coated copper grids for analysis. As shown in Fig. 3, the nanoneedles were randomly aligned and uniformly decorated with PdO and/or PtO NPs, indicating that the tungsten oxide nanoneedles had been loaded with well-dispersed metal-oxide NPs. The diameter of the NPs was between 4 and 6 nm in the case of PdO decorated nanoneedles, as shown in Fig. 3a and b, but significantly smaller (1–2 nm) in the case of PtO NP decoration, as shown in Fig. 3c and d.

Following that, the annealed films were sulfurized in a CVD chamber using the methodology described earlier. The films were then examined using FESEM, revealing a change in surface morphology from nanoneedles to nano triangles (in pristine WS_2), nanoflakes (in WS_2/PtO), and nanoplatelets (in WS_2/PdO). The NPs were not visible at the surface after sulfurization, as they had been before. The arrangement of nanomaterial that forms nanotriangles in pristine WS_2 is depicted in Fig. 4a and b, whereas the morphology obtained in loaded films differ slightly, as shown in Fig. 4b-f.

The sensor substrate is uniformly covered with nanoflakes that seem considerably thinner with defined shape and sharp edges with PtO loading, whereas the shape of these nanosheets changes to hexagonal nanoplatelets that are randomly oriented covering the entire substrate with PdO loaded WS_2. As a result, the differences in the two morphologies could be linked to differences in the initial morphology of WO_3 nanocomposite (nanoparticles size) as well as the film composition (different functionalization sources). A cross-section of the sulfurized films was also obtained, revealing film thickness in the 30–32 μm range, as shown in Fig. 4g.

The structural and chemical characteristics of the loaded and pristine films were also evaluated using Raman spectroscopy. In all three samples, Raman features confirm the formation of WS_2. Fig. 5a corresponds to the Raman spectra obtained for pristine and loaded WS_2, using a 514 nm excitation wavelength laser. $E^1_{2\,g}$ and $A_{1\,g}$ are the two typical Raman modes, with the former representing in-plane vibrations of S and W atoms and the latter representing out-of-plane vibrations of S atoms. These two typical Raman modes of pristine WS_2, $E^1_{2\,g}$ and $A_{1\,g}$ appear at 349 and 415 cm^{-1} respectively [13,32]. The loaded samples, on the other hand, show a small upshift in both modes, with the $E^1_{2\,g}$ of WS_2/PtO and WS_2/PdO samples shifting by 1 cm^{-1} (from 349 to 350 cm^{-1}) and 6 cm^{-1} (from 349 to 355 cm^{-1}) respectively, which can be attributed to the effect of adding functionality [3]. Likewise, an upshift of $A_{1\,g}$ band by 1 cm^{-1} (i.e., from 415 to 416 cm^{-1}) and 4 cm^{-1} (i.e. from 415 to 419 cm^{-1}) was also observed for PtO and PdO loaded WS_2 films, respectively. In contrast, two broad peaks with very low intensity were observed at 693 cm^{-1} and 806 cm^{-1} for pristine WS_2 film, and at 696 cm^{-1} and 800 cm^{-1} for WS_2 /PtO film. These peaks are indicative of the presence of some WO_3 impurities, as previously reported [11,13]. Whereas, in the WS_2 /PdO material, no such peaks were discovered. However, additional characterisation results discussed below also confirm the presence of tungsten oxide in WS_2 /PdO. In our previous results [33], we have observed such impurities (WO_3) in the WS_2 samples. They can be originated from the uncompleted sulfurization process as well as the presence of some oxygen traces inside the CVD tube since the growth occurs at atmospheric pressure.

For both pristine and loaded WS_2 films, the ratio of $A_{1\,g}$ to $E^1_{2\,g}$ peaks remains constant at 0.84, suggesting the formation of multi-layered WS_2. The crystallinity of the multi-layered film is further shown by the strong Raman peaks. Also, the Raman analysis results are consistent with those found in prior studies [17,19].

Furthermore, X-ray powder diffraction was used to detect the crystallographic phase of the films. The XRD diffractograms of a pristine WS_2 sample (upper panel) was compared to those of WS_2/PtO (middle panel) and WS_2/PdO (lower panel) nanostructured films in view of checking for the presence of additional peaks in loaded samples and the results are depicted in Fig. 5b. The three diffractograms obtained were perfectly indexed to the 3R-WS_2 (JCPDOS card no. 01–084–1399). In the WS_2/

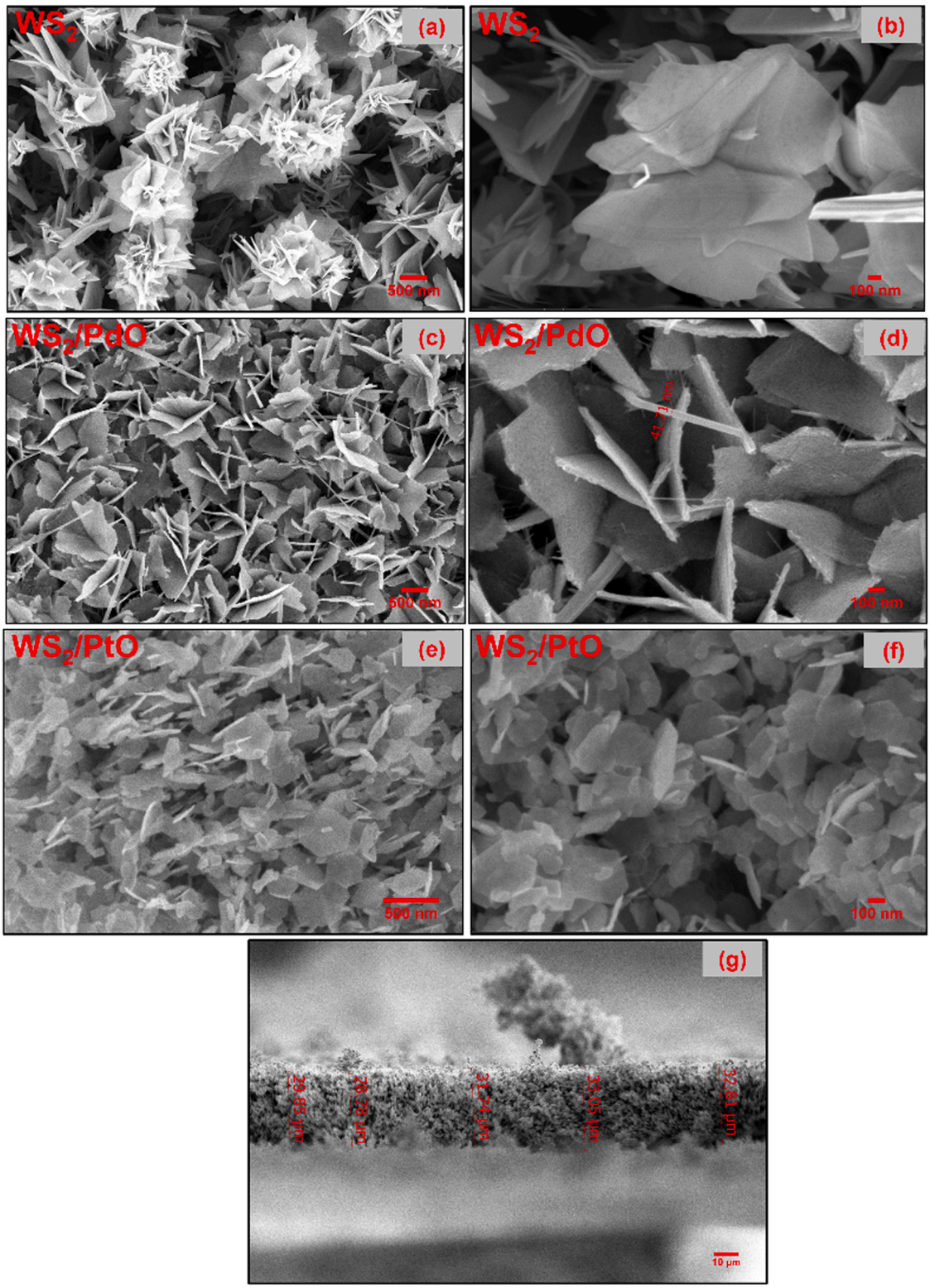

Fig. 4. FESEM images (a and b) pristine WS_2 (c and d) WS_2/PdO, (e and f) WS_2/PtO NPs. Cross-section image depicting WS_2 film thickness (g).

PdO sample, some additional low-intensity diffraction peaks suggesting the presence of PdO were also discovered. These peaks indicate the presence of tetragonal PdO (002) at 2θ of 33.54 (JCPDOS card no. 41–1107). Additionally, a small peak at 2θ of 23.1(002) was also found in this sample, indicating the presence of WO_3 impurities. For the WS_2/PtO sample, peaks at 2θ of 33.5 (002) and 41.4 (110) indicate the presence of tetragonal PtO (JCPDOS card no. 43–1100). Whereas some additional peaks with low intensity indicating the presence of PtS in low quantity were also observed at 2θ of 29.59 (101) and 47.52 (112) (JCPDOS card no. 26–1302) in PtO decorated WS_2. Furthermore, some peaks corresponding to the alumina substrate were present in all three samples, however, peaks from any other impurity were not detected, indicating that a well crystallised single-phase WS_2 was obtained.

The room-temperature photoluminescence (PL) spectra for WO_3

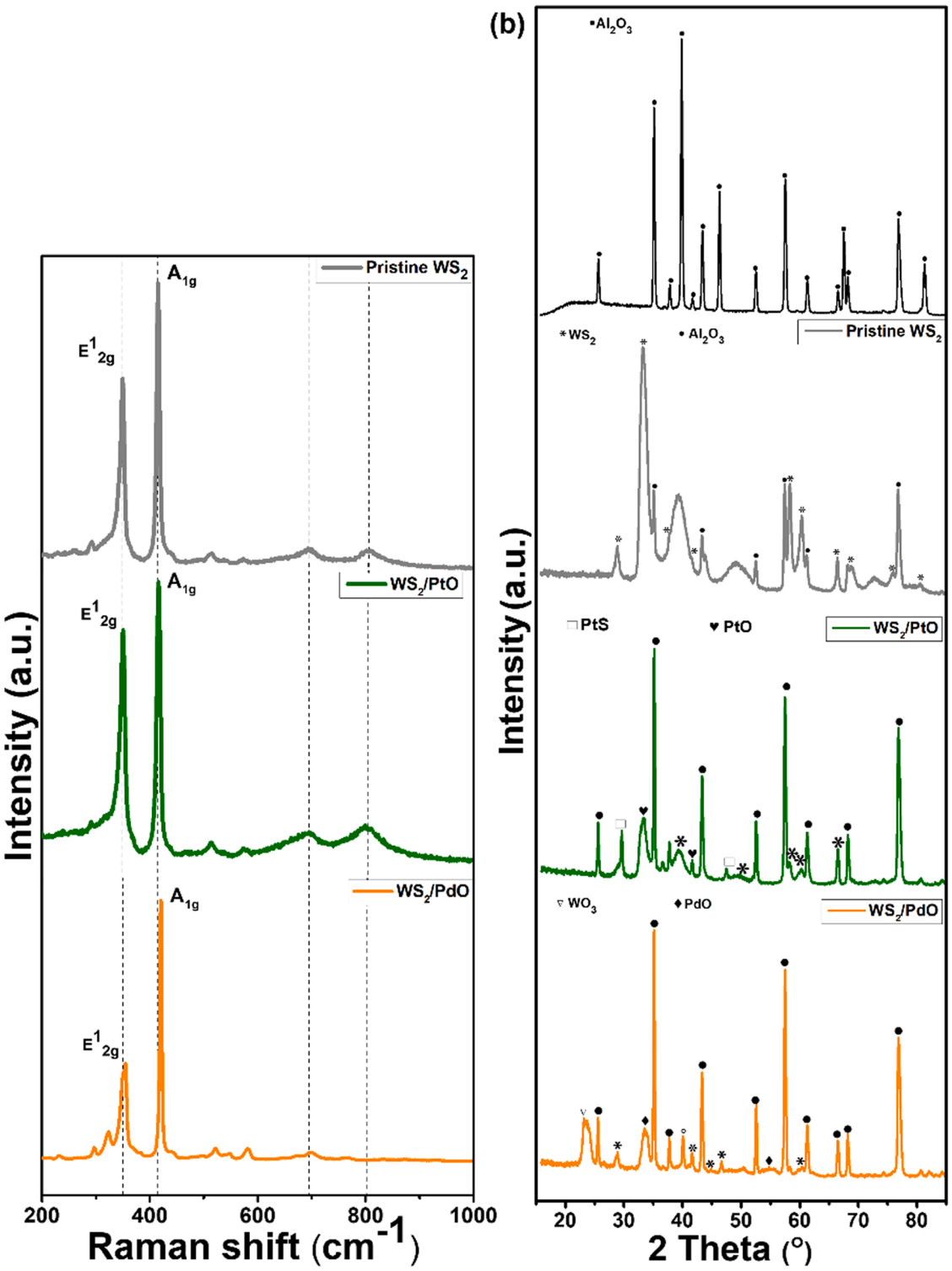

Fig. 5. (a) Raman spectra and (b) XRD diffractograms of pristine WS_2, WS_2/PtO and WS_2/PdO NPs.

decorated either with PtO or PdO NPs and WS_2 loaded either with PtO or PdO are presented in Fig. 6a and b respectively. The intensity of each spectrum was normalized to the maximum emission intensity for relative comparison. By pumping at 325 nm, we observed an emission peak of WO_3 nanoneedles at around 450 nm (2.75 eV) with a full width at half maximum (FWHM) of 370 meV (Fig. 7a). When loading the WO_3 nanoneedles with the PdO or PtO NPs, the emission peak is shifted to 490 nm (2,53 eV) and 530 nm (2,34 eV) and the FWHM are around 540 and 660 meV, respectively. This broadening observed on the FWHM indicates that the quantity of intrinsic defects is higher when loading the WO_3 NWs with the PdO or PtO NPs. On the other hand, by pumping at 325 nm, we observed an emission peak of WS_2 nanostructures at around 393 nm (3.16 eV) with a full width at half maximum (FWHM) of 440 meV (Fig. 6b). When loading the WS_2 nanostructures with the PdO or PtO NPs, the emission peak is shifted to 430 nm (2,88 eV) and 461 nm (2,69 eV) and the FWHM are around 540 and 480 meV, respectively. This broadening observed on the FWHM indicates that the quantity of intrinsic defects is higher when loading the WS_2 nanostructures with the

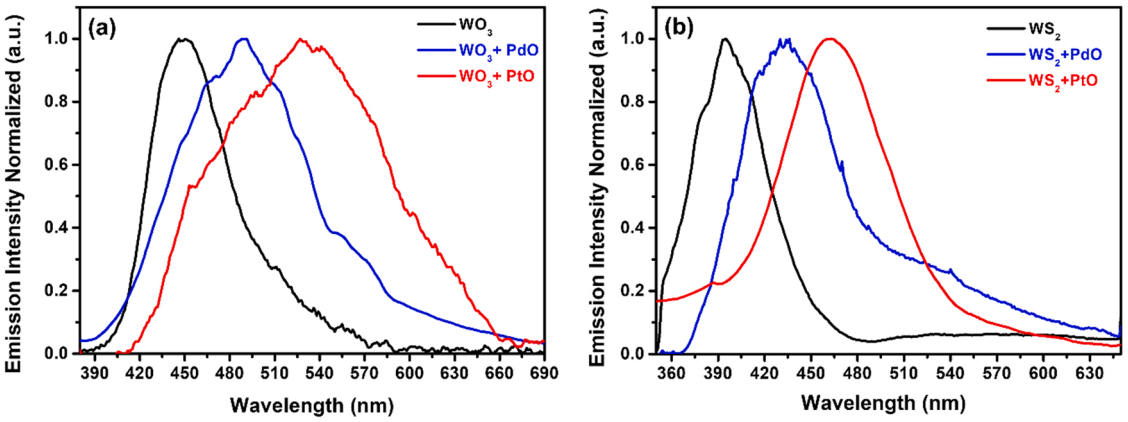

Fig. 6. PL spectra of (a) pure WO_3, WO_3/PdO and WO_3/PtO, (b) pristine WS_2, WS_2/PdO and WS_2/PtO.

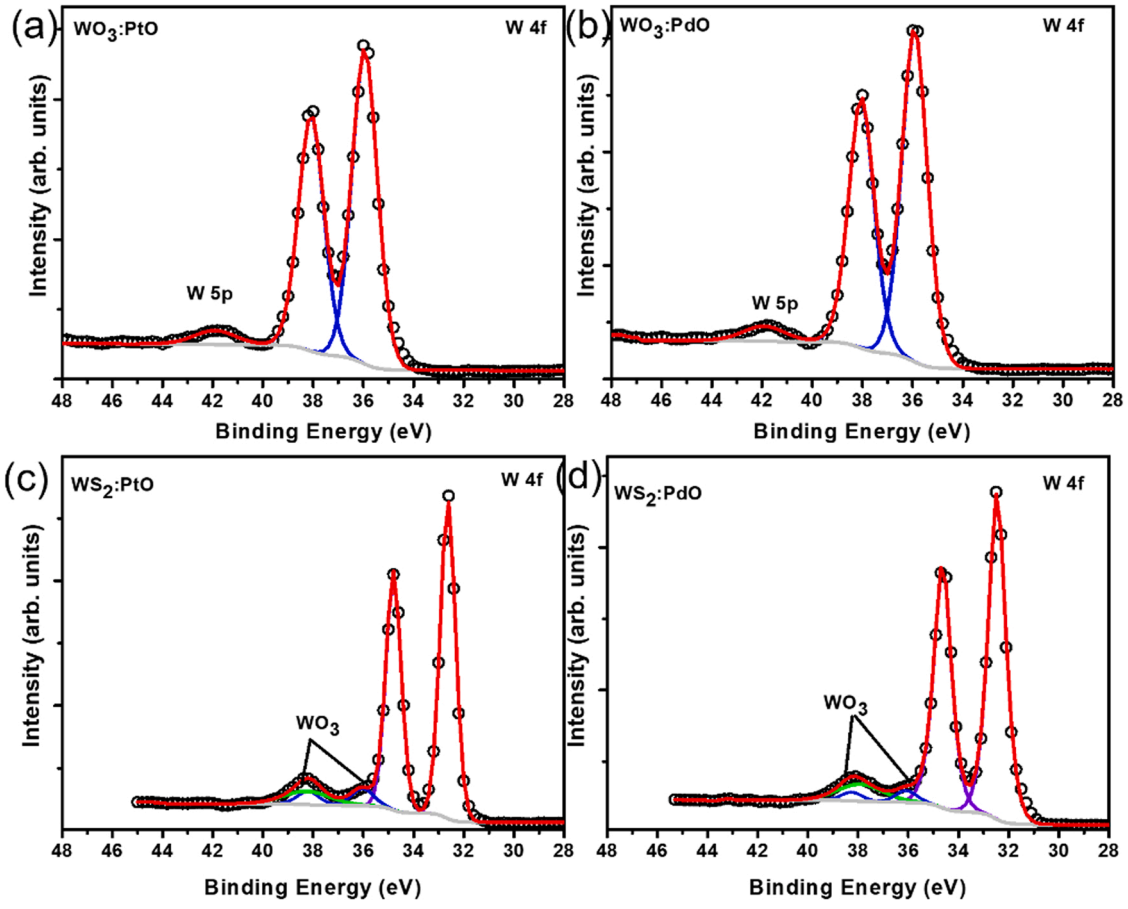

Fig. 7. XPS W 4 f core level (a) WO_3: PtO (b) WO_3: PdO (c) WS_2: PtO (d) WS_2: PdO.

PdO or PtO NPs. Emission peaks at around 393 nm (3.16 eV), 420 nm (2,95 eV) and 461 nm (2,69 eV) were previously observed in WS_2 quantum dots [1] and are assigned to the direct gap (~3.16 eV) of monolayered WS_2 quantum dots and to defect levels, respectively. Then, the shift observed in the emission peaks is due to the additional emission contributions originated from new defect levels, which generates the main emissions at around 430 and 461 nm in the WS_2 nanostructures loaded with PdO or PtO NPs, respectively. It was reported that presence of PdO or PtO NPs changes the electronic band structure of WS_2 monolayers [34].

X-ray photoelectron spectroscopy was used to explore the chemical composition of the sample surface. Herein, pristine, and loaded samples were analysed and compared with the sulfurized samples. The XPS survey spectra show the presence of W, C and O in WO_3 while for WS_2, an additional signal associated with the presence of sulphur atoms is observed [Fig. S3]. The core-level regions recorded with higher energy resolution allow determining the oxidation state of the elements. The spectrum recorded in the W*4 f* binding energy region of WO_3 samples is well reproduced by three components centred at binding energies 35.9 eV, 38.0 eV and 41.8 eV corresponding to W*4* $f_{7/2}$, W*4* $f_{5/2}$ and W*5*$p_{3/2}$ core energy levels, respectively (Fig. 7a, b). These binding energy values indicate the (6 +) valence state, in both WO_3: PtO and WO_3: PdO samples [35].

To reproduce the W *4 f* peak of the WS_2 samples an additional

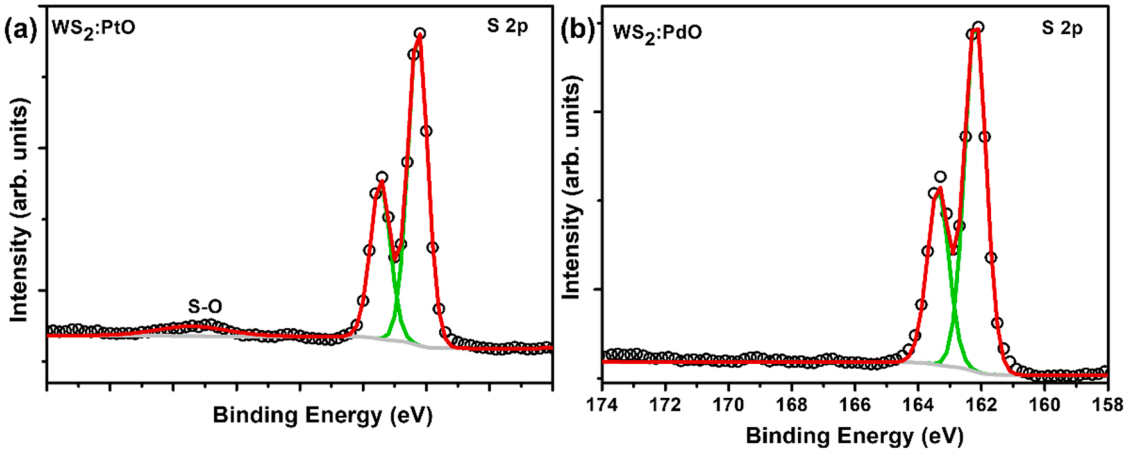

Fig. 8. XPS S 2p core level (a) WS_2: PtO (b) WS_2: PdO.

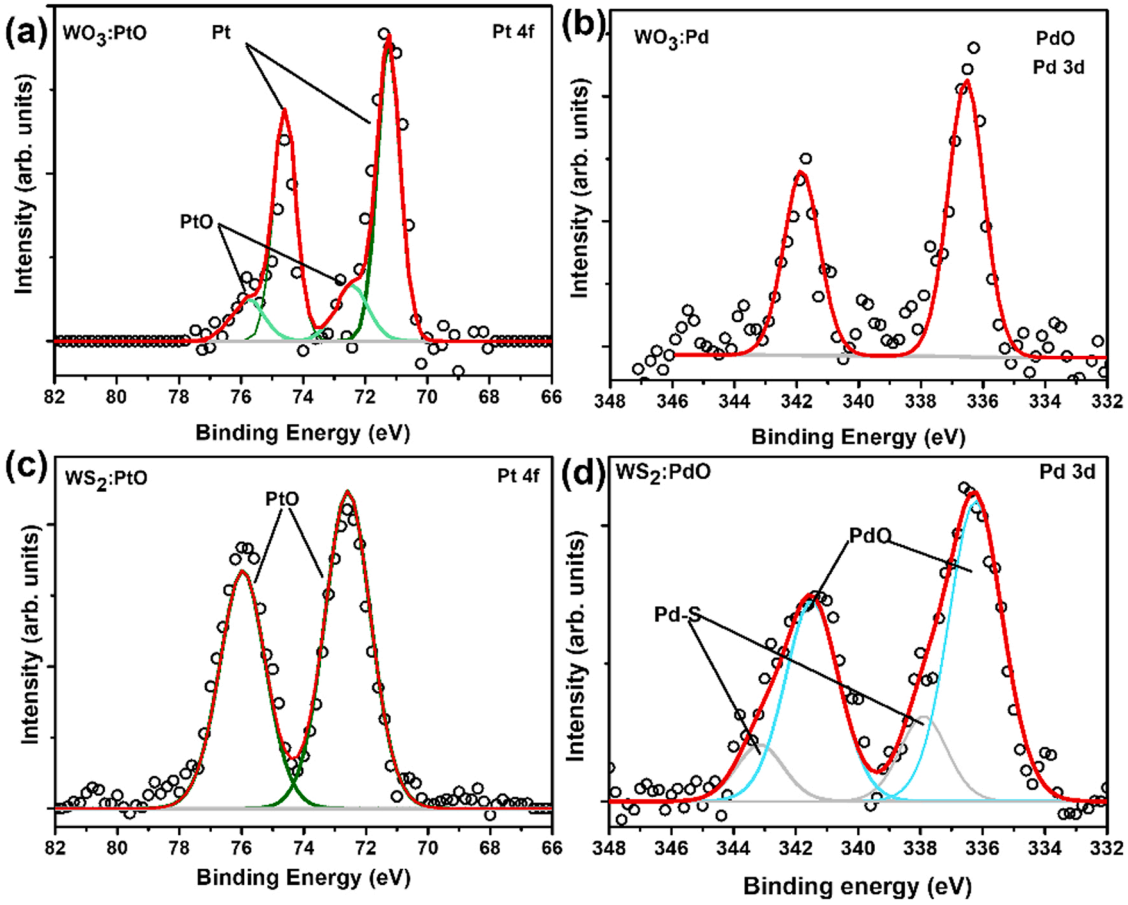

Fig. 9. XPS core level spectra: (a) PtO 4 f region in WO_3: PtO (b) 3d PdO region in WO_3: PdO (c) PtO 4 f region in WS_2: PtO and (d) 3d PdO region in WS_2: PdO.

doublet with components centred at 32.4 eV (W4 $f_{7/2}$) and 34.6 eV (W4 $f_{5/2}$) was used, this high-intensity doublet demonstrates the presence of tungsten atoms in the (4 +) valence state in WS_2 (Fig. 7c,d) [36]. The low-intensity doublet indicates the presence of WO_3 in a very small quantity which is sometimes present as an impurity, also observed in our [33] previous research work. The S 2p spectra show the presence of S-O bonds (S2p at 168.8 eV) [36] in the WS_2:PtO, though S-W (S2p1/2 and S2p3/2, respectively at 163.3 eV and 162.) [33] is most of the bonding confirming the formation of WS_2 in both samples (Fig. 8a, b). Fig. 9 shows the Pd and Pt XPS core level spectra of the WO_3 samples. The Pd *3d* doublet peak with components centred at 336.5 eV ($3d_{5/2}$) and 341.8 eV ($3d_{3/2}$) suggests the formation of PdO [37]. The Pt *4 f* peak is reproduced by two doublets, one with components at 71.2 eV ($4f_{7/2}$) and 74.5 eV ($4f_{5/2}$) indicating the presence of metallic Pt and the other with components at 72.5 eV ($4f_{7/2}$) and 75.8 eV ($4f_{5/2}$) associated with the formation of PtO and PtS [37]. Indeed, these two materials have narrow binding energies [37,38] and by considering the synthesis method and the FWHM of the Pt 4 F we suggest that both materials coexist. The Pd and Pt core level XPS spectra recorded on WS_2 samples are shown in Fig. 9c and d. The Pd 3d spectrum is reproduced by two doublets related to the presence of PdO (336.5 eV ($3d_{5/2}$) and 341.8 eV ($3d_{3/2}$)) and the formation of Pd-S bonding (337.0 eV ($3d_{5/2}$) and

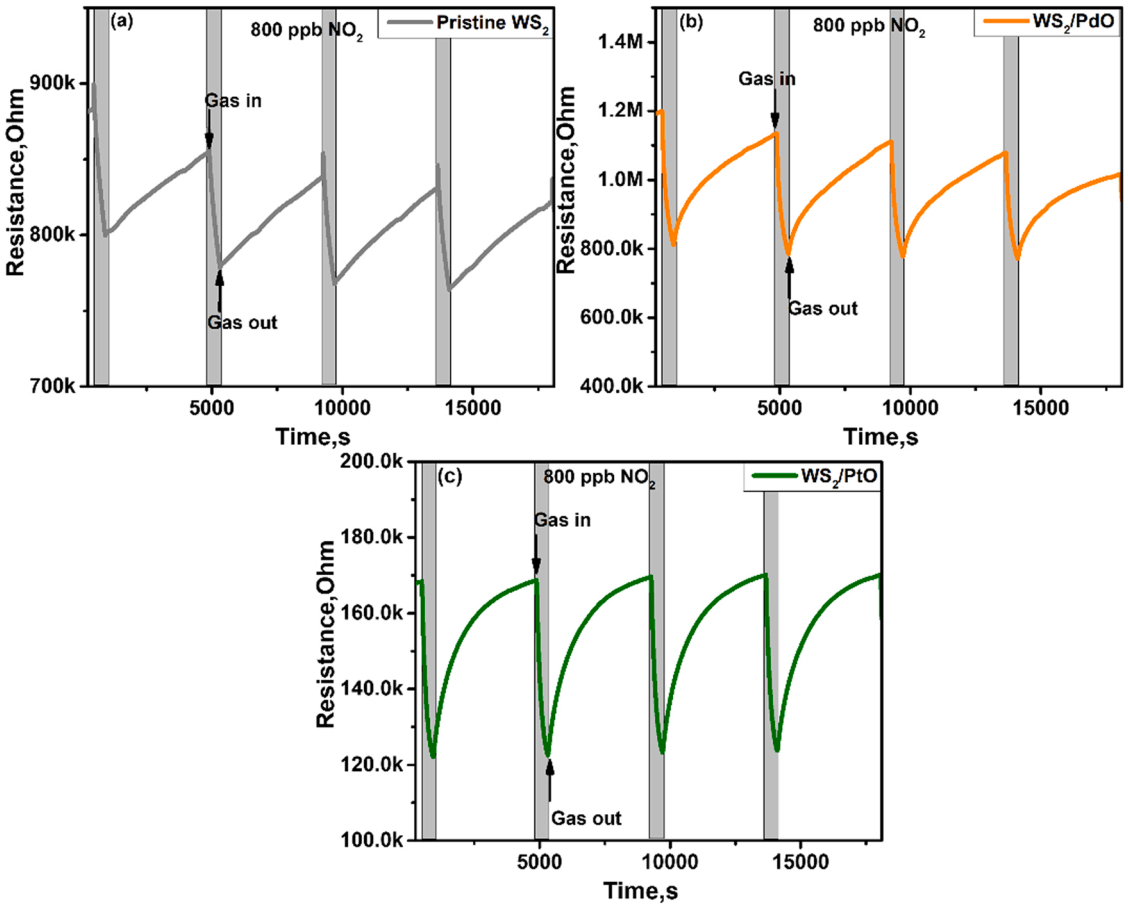

Fig. 10. Pristine WS_2 (grey), WS_2/PdO (orange), WS_2/PtO (olive), 4 replicate response and recovery cycles towards 800 ppb of NO_2 at room temperature.

343.6 eV ($3d_{3/2}$)) [39].

Thus, Raman, PL, XRD, XPS, TEM and FESEM results show good accordance between them and confirm the formation of WS_2, WS_2/PdO and WS_2/PtO with the presence of some WO_3 impurities produced by the uncompleted sulfurization of the initial WO_3 nanomaterial as well as the presence of a small quantity of oxygen within the quartz tube where the experiment is conducted.

3.2. Gas sensing results

NO_2 Gas

The gas sensing characteristics of loaded and pristine sensing films (WS_2, WS_2/PtO, WS_2/PdO) to both oxidising (NO_2), as well as reducing (NH_3, H_2, CO, H_2S) gases, has been analysed using a homemade gas-sensing detection system as described above (Fig. 1). The performances of the as-fabricated sensors were determined at room temperature utilising dry air balance. To calculate the sensor response towards oxidising gas, we have used equation-1 whereas in the case of reducing gases the sensor response is calculated using equation-2, given as:

$$R = \frac{(Rair - Rgas)}{Rair} * 100 \quad (1)$$

$$R = \frac{(Rgas - Rair)}{Rair} * 100 \quad (2)$$

Accordingly, as shown in Fig. 10 we exposed both loaded and pristine WS_2 films towards 800 ppb of NO_2. It is worth noting that this is the highest gas concentration tested, and it is still well below the NO_2 exposure limit recommended by the American Conference of Government Industrial Hygienists [6]. For the three different materials operated at room temperature, Fig. 10a-c displays the dynamic film resistance change towards 800 ppb NO_2 gas. The figure clearly shows that when exposed to an oxidising type of gas, such as NO_2, sensors exhibit a decrease in their electrical resistance, thereby indicating a p-type semiconducting behaviour for all of them. This is in good accordance with the findings of our previous study, in which pristine WS_2 sensors exhibited similar p-type behaviour [33]. While the response of the pure WS_2 sensor is 10.68%, one of the loaded sensors, WS_2/PdO and WS_2/PtO, is much greater, reaching 26.5% and 27.5%, respectively.

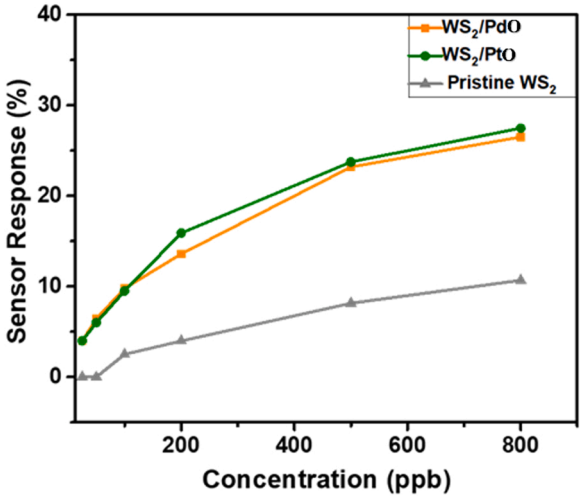

Fig. 11. Gas sensing response of pristine WS_2 (grey) WS_2/Pd (orange), WS_2/Pt (olive) as a function of NO_2 gas concentration at room temperature.

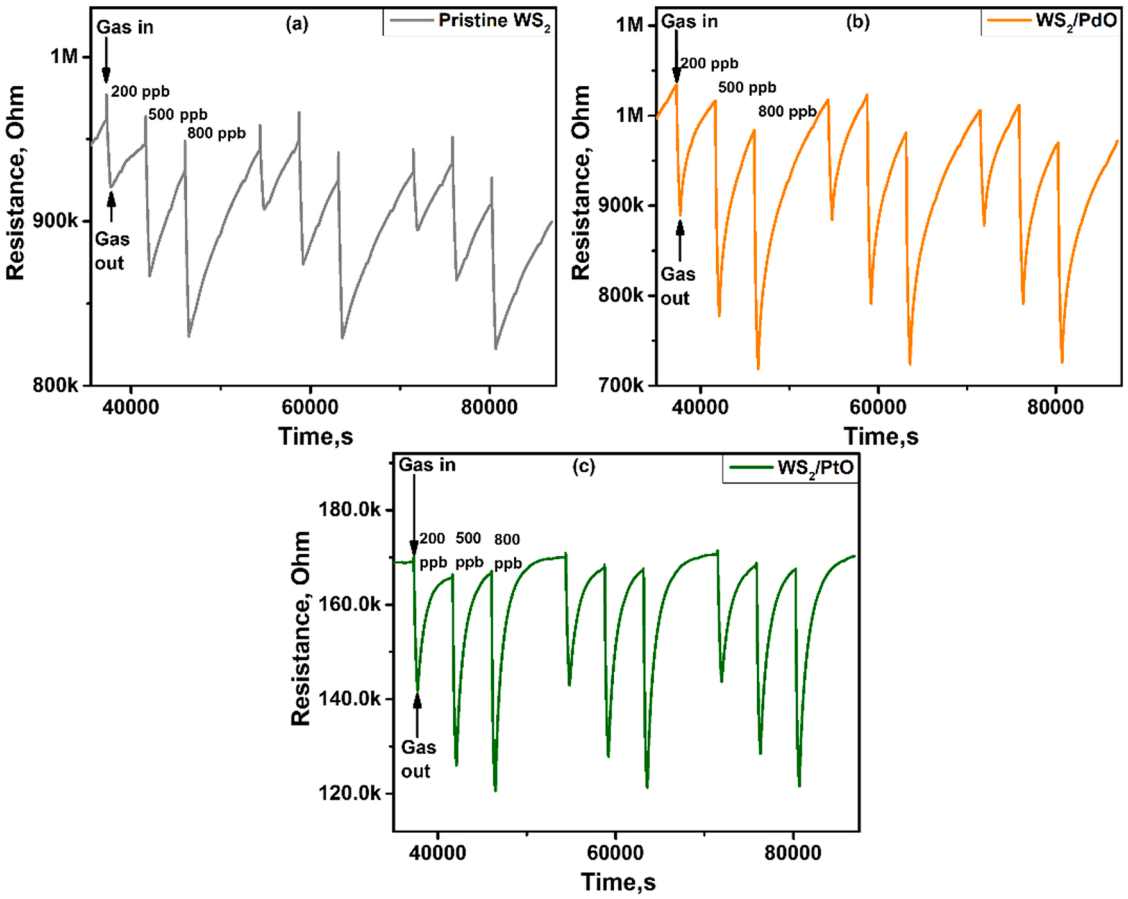

Fig. 12. Electrical resistance change of (a) pristine WS_2 (grey), (b) WS_2/PdO (orange) and (c) WS_2/PtO (olive) towards pulses of increasing concentrations of NO_2 gas (from 200 to 800 ppb), operated at room temperature.

At this concentration, all three sensors showed consistent and replicable responses where the maximum response was recorded from the loaded ones. Furthermore, during the recovery cycle, when the target gas is removed and the sensors are only exposed to dry air, they return completely to their baseline resistance, which is shown in Fig. 10. We also exposed pristine and loaded WS_2 sensors to various NO_2 gas concentrations. Fig. 11 displays the sensor response as a function of NO_2 concentrations. The experimental results for pristine WS_2 are equivalent to those obtained in our previous study for WS_2 NT sensors [33]. In contrast, both loaded sensors (PdO and PtO) perform similarly and display an enhanced sensing response towards NO_2 gas detection when compared to pristine WS_2.

Furthermore, Fig. 12a-c shows three replicate measurements cycles to increasing concentration pulses of NO_2 ranging from 200 to 800 ppb in a background of dry air. During each cycle, sensors were exposed to three different concentrations of NO_2 while operated at room temperature. The results show an increase in sensing response with each increment in analyte concentration. The sensing response for pristine WS_2 was calculated to be 4%, 8.1%, 10.7% towards 200, 500 and 800 ppb of nitrogen dioxide, respectively. Again, responses for WS_2/PdO and WS_2/PtO were very similar. These were calculated to be 15.9%, 23.8% and 27.5% for WS_2/PtO and 13.6%, 23% and 27% for WS_2/PdO towards 200, 500 and 800 ppb of nitrogen dioxide, respectively. It can be observed from Fig. 12 that the response for WS_2/PtO is significantly more stable because this sensor completely regains its initial baseline resistance after each cycle of measurement. These results encouraged us to explore the NO_2 gas sensing characteristics towards NO_2 at the much lower concentrations of 50 and 25 ppb. The responses of the three sensors to very low NO_2 gas concentrations (25 and 50 ppb) at room temperature are shown in Fig. 13a-c and Fig. S4. To test repeatability, four consecutive replicate measurements and recovery sequences were performed. The results demonstrate that both PdO and PtO loaded WS_2 sensors have an adequate response to NO_2 for a concentration as low as 25 ppb, whereas the pristine sensor stays unresponsive until the gas concentration is increased to 100 ppb. At such a low concentration, the sensing response of the loaded sensors was reproducible and was reported to be practically equal with a value of 4%. However, at such low response signals and because the desorption of the gas molecules at room temperature is difficult, considerable drift in the response was detected for the loaded sensors.

Hence, it is observed that loading improves (i.e. lowers) the detection limit (LoD) of pristine WS_2 sensors. While the NO_2 LoD for pristine WS_2 sensors is 100 ppb, the LoD is lower than 25 ppb for the loaded sensors. To the best of our knowledge, such a low detection limit under 25 ppb of NO_2 had never been reported before using either loaded or pristine WS_2 nanomaterials operated at room temperature.

Selectivity test

In addition to NO_2 gas sensing studies, the performance of pristine WS_2, WS_2/PtO and WS_2/PdO sensors were investigated for reducing gases such as, H_2, CO, NH_3, H_2S to determine the potential selectivity of each sensor towards NO_2 gas detection. Fig. S5 illustrates typical response and recovery cycles for each gas.

The histogram in Fig. 14 summarises the results obtained from the selectivity measurements for each material. MOX loading clearly enhances the response towards NO_2 and diminishes the cross-sensitivity towards ammonia and hydrogen sulphide observed in pristine WS_2. WS_2/PtO shows some cross-sensitivity towards H_2 and CO. However, considering that possible interfering species were measured at significantly higher concentrations than that of NO_2, it can be derived that the loading has improved selectivity towards nitrogen dioxide.

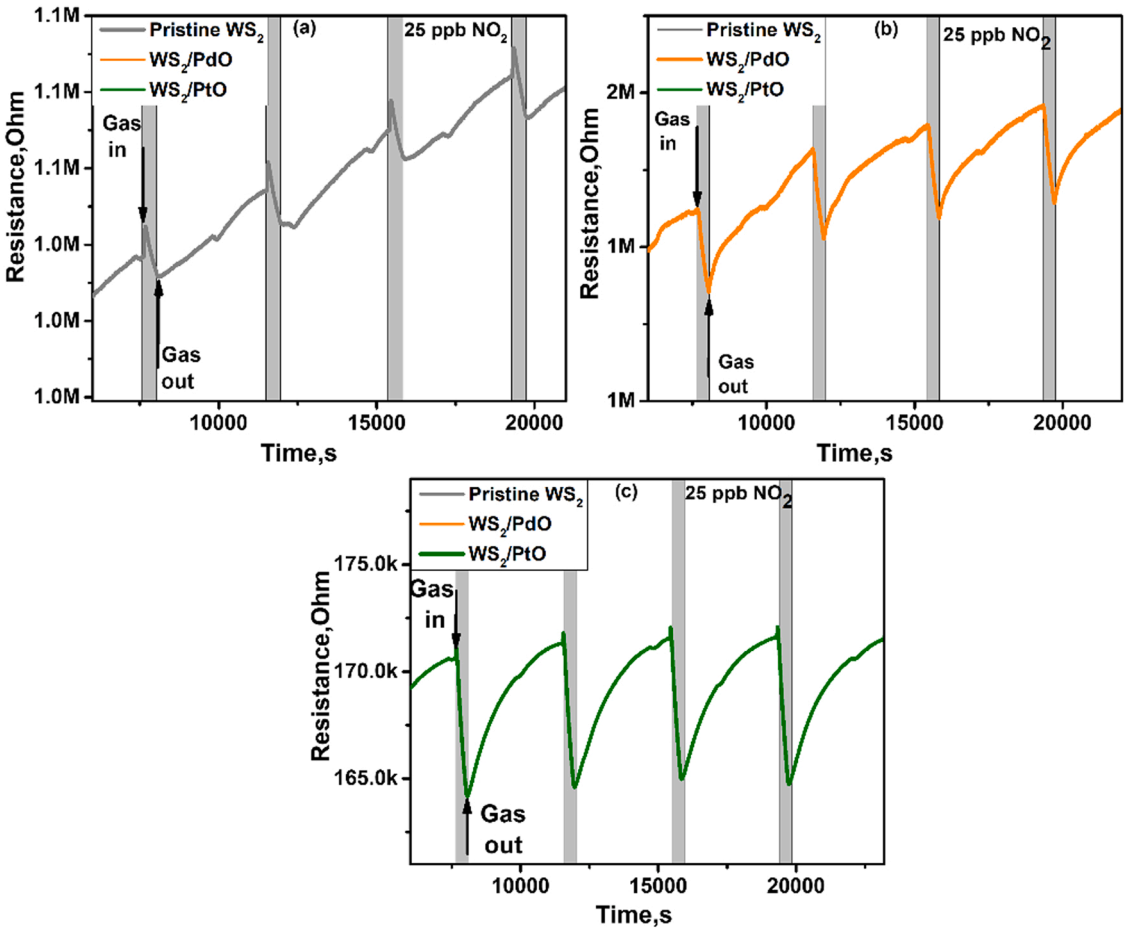

Fig. 13. Electrical resistance change of (a) pristine WS_2 (grey), (b) WS_2/PdO (orange) and (c) WS_2/PtO (olive) towards NO_2 at 25 ppb, operated at room temperature.

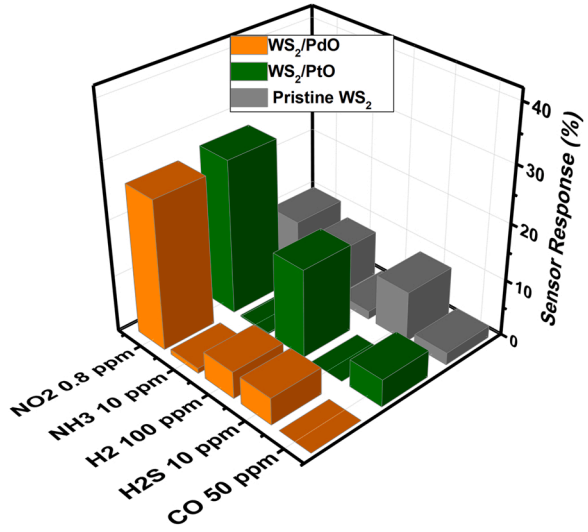

Fig. 14. Response histogram of pristine WS_2, WS_2/PdO and WS_2/PtO sensors towards NO_2 (0.8 ppm), NH_3 (10 ppm), H_2 (100 ppm), H_2S (10 ppm) and CO (50 ppm) gas, at room temperature.

Humidity.

The influence of humidity on the sensor response towards NO_2 has also been studied. The sensors were tested towards 0.8 ppm NO_2 at room temperature in a 50% humidified background (@ 21°C), and the results are presented in Fig. 15. According to the findings, all three sensors have different responses to humidity. For example, the pristine WS_2 sensor, as well as the PdO/WS_2 sensor, showed enhanced gas sensing response, with the PdO/WS_2 sensor response increasing from 26.5% to 54% and the pristine WS_2 sensor response increasing from 10.68% to 53%. However, the PtO/WS_2 sensor, on the other hand, exhibited a completely different behaviour, with sensor response dropping from 27.5% to only 3%. Based on the literature, it is suggested that when PtO/WS_2 sensor is exposed to humidity, the OH- occupy most of the active sites that were previously available for the interaction with NO_2 gas molecules. As a result, the access of NO_2 gas molecules to the surface-active sites is reduced [40]. Thereby resulting in negligible sensing response (3%) under a humid atmosphere. Regarding pristine as well as PdO/WS_2 sensor, the effect of humidity is quite different, as both sensors showed enhanced gas sensing responses towards NO_2. This behaviour has been reported earlier for WS_2 nanoflakes based gas sensor towards NH_3 detection [42]. They suggested that the enhancement observed in the sensor response is due to the sulphides-ions assisted hydroxylation of the co-adsorbed water molecules and due to the oxidation of the solvated ammonia with adsorbed oxygen ions on the surface of WS_2 nanoflakes . Another study reports WS_2/graphene aerogel-based sensor, where the sensor response towards NO_2 increases when humidity imncreases [41]. They interpret this behaviour by Grotthus transport mechanism where the resistance change is related to the movement of protons H+ or H_3O+ within the physisorbed water molecules. Since all the measurements were done at room temperature, the migration of protons becomes much easier, which results in a further decrease in film resistance, thereby increasing sensor response towards NO_2 detection .

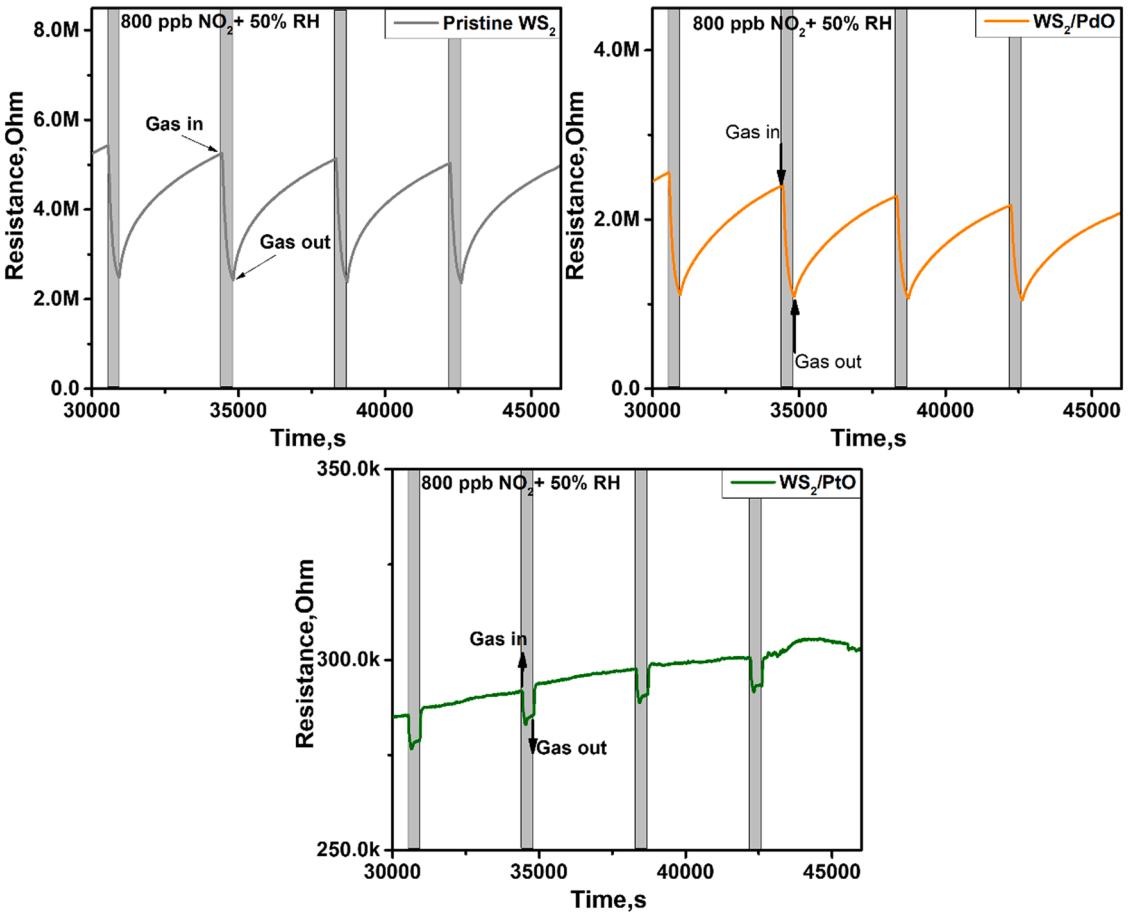

Fig. 15. Relative humidity (50%) cross-sensitivity of pristine WS_2, WS_2/PdO and WS_2/PtO sensors towards 0.8 ppm NO_2, at room temperature.

The behaviour of TMD gas sensors under humid conditions is not deeply studied and needs to be further explored.

After the humidity was removed from the background, all sensors regained their original sensing response after applying mild heating (100 °C) for 4–5 h and the corresponding results are presented in Fig. S6. These results also indicate that PdO/WS_2 shows the best NO_2 sensing characteristics among the different materials tested. This difference observed in the gas sensing properties between the loaded sensors can be attributed to the metal used as well as the size of the nanoparticles. Additionally, a stability study was performed by exposing the sensors towards 0.8 ppm NO_2 at room temperature for 6 weeks (Fig. S6) and all three materials showed good stability.

4. Gas sensing mechanisms

4.1. Detection of nitrogen dioxide

NO_2 molecules are electron acceptors and H_2S, H_2, CO or NH_3 are electron donors. The resistance of the different WS_2 devices decreases in the presence of NO_2 and increases in the presence of the above-mentioned electron donor species. This is indicative that our pure or loaded tungsten disulphide samples behave as p-type semiconducting materials. The n-type or p-type nature of WS_2 depends on its morphology, nanostructure alignment on the substrate or even on the presence of few carbon atoms substituting sulfur atoms [29,30]. The p-type behaviour of WS_2 achieved via the sulfurization of WO_3 has been reported previously [33,45]. The nitrogen dioxide sensing mechanism in WS_2 involves the adsorption of NO_2 molecules both on the edges of flakes and on their surface (or basal plane). Upon adsorption, an electronic charge is injected from WS_2 towards the gas molecule, which generates a hole accumulation zone that results in a decrease in the resistance of the film. According to previously reported computational chemistry studies in MoS_2, the edges are far more important than the basal plane for the adsorption of NO_2, because the adsorption energy of nitrogen dioxide at S edges is about 4 times higher than at the basal plane and so is the associated electronic charge transfer [46]. The computed adsorption energies suggest that the interaction between WS_2 and NO_2 involves the physisorption of nitrogen dioxide. This is supported by the experimental results showing that sensor baseline resistance can be regained when flowing the sensor surface with clean air when sensors are operated at room temperature.

PL analysis conducted on pure WO_3 and PtO or PdO loaded WO_3 indicates that PtO or PdO loaded tungsten oxide have an increased number of defects in comparison to pure tungsten oxide. Since WS_2 is achieved via the sulfurization of tungsten oxide samples, these additional defects translate into an increased number of S edges in PtO or PdO loaded WS_2. Indeed, the PL studies have shown that PtO and PdO loaded WS_2 samples are characterized by a redshift of the PL maximum and by a higher FWHM in comparison to the one for pure WS_2 samples, which can be associated with a higher number of defects being present in loaded samples. This explains why PtO and PdO loaded WS_2 show significantly higher responses to NO_2 than pure WS_2.

Some authors have reported that platinum and palladium oxide nanoparticles supported on a semiconducting nanomaterial play a role in the sensitization of this nanomaterial to NO_2. These authors described both electronic and chemical sensitization effects for explaining the increased responses towards nitrogen dioxide observed [47,48]. PtO and PdO were found on the surface of loaded WS_2 samples by XPS (also detected by XRD). Therefore, the presence of such oxides could also contribute to the enhanced NO_2 response shown by PtO or PdO loaded

WS_2.

4.2. Response to hydrogen

Besides the significant improvement in the response towards nitrogen oxide observed for PtO or PdO loaded WS_2 samples, a small increase in response towards hydrogen was observed too. Platinum and palladium oxides are p-type materials well known for acting as chemical and/or electronic sensitizers towards hydrogen when dispersed in n-type metal oxides [30] and this may be the reason why PtO or PdO loaded WS_2 samples show an increased response towards hydrogen in comparison to the one of pure WS_2. However, as already stated, this response increase is rather moderate. The sulfurization of PtO and PdO oxides results in PtS and PdS, which hinders the above-described hydrogen sensitization effect. While the presence of PdS was confirmed both by XPS and XRD, PtS could be confirmed by XRD only. These results indicate that PtS is found in lower quantities than PdS, which explains why PtO loaded WS_2 is slightly more sensitive to hydrogen than PdO loaded WS_2.

5. Conclusion

We have been able to develop a unique method to fabricate loaded WS_2 directly on commercial sensor substrate via a combination of AACVD and CVD techniques. This co-deposition approach demonstrates an effective route to bring functionality in metal sulphides. Metal-oxide loaded sensors are composed of a hybrid structure of nanoneedles and nanosheets of WS_2 with high quality and crystallinity, as determined by Raman, XRD, and FESEM characterization techniques, and either a combination of PtO and PtS or PdO and PdS NPs are present between its surface, as determined by TEM, XRD and XPS spectroscopy. Moreover, we have investigated the gas sensing performance of both loaded sensors and unloaded sensor. The electrical characteristics of pristine WS_2 were tuned through loading with metal-oxide ions. It is fascinating to know that all the gas sensing measurements were carried out at room temperature and the WS_2-based gas sensors exhibited stable, reproducible, and ultrasensitive responses towards NO_2 at ppb concentration levels. The sensing results revealed that loading of WS_2 nanosheets with either PtO or PdO ions significantly increases their gas response towards NO_2 (i.e., double the response as compared to pristine WS_2 sensor from 10% to 26.5%, thereby lowering the detection limit of the sensor (lower than 25 ppb after loading, which is far lower than that of pristine WS_2 gas sensor). To our knowledge, no previous research has used a loaded or pristine WS_2 nanomaterial to obtain such a low detection limit of 25 ppb of NO_2 at room temperature. Even though the sensor displayed considerable humidity cross-sensitivity at room temperature, once the moisture was removed with mild heating, it regained its original sensing response, demonstrating its outstanding NO_2 gas detection properties. Moreover, when compared to the WS_2/PtO sensor, the WS_2/PdO sensor is extremely selective for NO_2, exhibiting little or no response to other gases. In the end, the synthesis methodology adopted during this study is promising to incorporate metal-oxide ions on transition metal dichalcogenides. Henceforth, we believe, the results obtained in this study at room temperature are intriguing and encouraging in terms of developing a sensitive, cost-effective, and energy-efficient NO_2 gas sensor.

Credit authorship contribution statement

Aanchal Alagh: Investigation, Formal analysis, Data curation, Writing – original draft. **Fatima Ezahra Annanouch:** Conceptualization, Supervision, Writing – review & editing. **Khaled Al Youssef:** Investigation and Data curation. **Carla Bittencourt:** Investigation and Data curation. **Frank Güell:** Investigation and Data curation. **Paulina R. Martínez-Alanis:** Investigation and Data curation. **Marc Reguant:** Investigation and Data curation. **Eduard Llobet:** Conceptualization, Supervision, Writing – review & editing, Funding acquisition.

Declaration of Competing Interest

The authors declare that they have no known competing financial interests or personal relationships that could have appeared to influence the work reported in this paper.

Acknowledgements

Funded in part by the Marie Skłodowska-Curie Actions (MSCA) Research and Innovation Staff Exchange (RISE) H2020-MSCA-RISE-2018- 823895 'SENSOFT', by MICINN and FEDER grant no. RTI2018-101580-I00 and AGAUR grant no. 2017 SGR 418. A.A. is supported by a COFUND project the European Union's Horizon 2020 research and innovation program under the Marie Skło- dowska-Curie grant agreement No. 713679 and the Universitat Rovira i Virgili (URV). C.B. is a Research Associate of the National Funds for Scientific Research (FRS-FNRS, Belgium; E.L. is supported by the Catalan Institute for advanced studies (ICREA) via the 2018 Edition of the ICREA Academia Award.

Appendix A. Supporting information

Supplementary data associated with this article can be found in the online version at doi:10.1016/j.snb.2022.131905.

References

[1] D.Galán Madruga, Importance of air quality networks in controlling exposure to air pollution, Environ. Emiss. (2021) 1–15, https://doi.org/10.5772/intechopen.92335.
[2] S.J. Jung, J.S. Mehta, L. Tong, Effects of environment pollution on the ocular surface, Ocul. Surf. 16 (2) (2018) 198–205, https://doi.org/10.1016/j.jtos.2018.03.001.
[3] J.H. Kim, A. Mirzaei, H.W. Kim, S.S. Kim, Flexible and low power CO gas sensor with Au-functionalized 2D WS2 nanoflakes (December), Sens. Actuators, B Chem. 313 (no) (2019), 128040, https://doi.org/10.1016/j.snb.2020.128040.
[4] New Jersey Department of Health and Senior Sevices, "Hazardous Substance Fact Sheet, Nitrogen Dioxide," 1989, [Online]. Available: https://nj.gov/health/eoh/rtkweb/documents/fs/1376.pdf.
[5] J.P. Frawley, Emergency exposure limits American industrial hygiene association, toxicology committee, Am. Ind. Hyg. Assoc. J. 25 (6) (1964) 578–586, https://doi.org/10.1080/00028896409342646.
[6] A. Moumen, et al., Robust room-temperature No2sensors from exfoliated 2D few-layered CVD-grown bulk tungsten Di-selenide (2H-WSe2), ACS Appl. Mater. Interfaces 13 (3) (2021) 4316–4329, https://doi.org/10.1021/acsami.0c17924.
[7] H. Luo, et al., Design of p–p heterojunctions based on CuO decorated WS 2 nanosheets for sensitive NH 3 gas sensing at room temperature, Nanotechnology 32 (44) (2021), 445502, https://doi.org/10.1088/1361-6528/ac1800.
[8] J. Sun, et al., Synthesis methods of two-dimensional MoS2: a brief review, Crystals 7 (7) (2017) 1–11, https://doi.org/10.3390/cryst7070198.
[9] S. Vallejos, et al., Single-step deposition of au- and pt-nanoparticle-functionalized tungsten oxide nanoneedles synthesized via aerosol-assisted CVD, and used for fabrication of selective gas microsensor arrays, Adv. Funct. Mater. 23 (10) (2013) 1313–1322, https://doi.org/10.1002/adfm.201201871.
[10] D. Andrzejewski, et al., Flexible large-area light-emitting devices based on WS2 monolayers,", Adv. Opt. Mater. 8 (20) (2020) 5–9, https://doi.org/10.1002/adom.202000694.
[11] R. Levi, O. Bitton, G. Leitus, R. Tenne, E. Joselevich, Field-effect transistors based on ws2 nanotubes with high current-carrying capacity, Nano Lett. 13 (8) (2013) 3736–3741, https://doi.org/10.1021/nl401675k.
[12] M. Ikram, et al., Fabrication and characterization of a high-surface area MoS2@WS2 heterojunction for the ultra-sensitive NO2 detection at room temperature, J. Mater. Chem. A 7 (24) (2019) 14602–14612, https://doi.org/10.1039/c9ta03452h.
[13] J.H. Kim, A. Mirzaei, H.W. Kim, S.S. Kim, Realization of Au-decorated WS2 nanosheets as low power-consumption and selective gas sensors," Sensors Actuators, B Chem. 296 (June) (2019), 126659, https://doi.org/10.1016/j.snb.2019.126659.
[14] Y. Ren, et al., Noble metal nanoparticles decorated metal oxide semiconducting nanowire arrays interwoven into 3D mesoporous superstructures for low-temperature gas sensing, ACS Cent. Sci. 7 (11) (2021) 1885–1897, https://doi.org/10.1021/acscentsci.1c00912.
[15] S. Park, P.M. Bulemo, W.T. Koo, J. Ko, I.D. Kim, "Chemiresistive acetylene sensor fabricated from Ga-doped ZnO nanofibers functionalized with Pt catalysts (May), in: Sensors Actuators, B Chem, vol. 343, 2021, 130137, https://doi.org/10.1016/j.snb.2021.130137 (May).
[16] J. Guo, S. Wang, Z. Lin, L. Liu, Y. Hui, Ultrasensitive acetone sensor based on holey zinc oxide nanosheets doped by gold nanoparticles (July), Mater. Lett. 302 (no) (2021), 130443, https://doi.org/10.1016/j.matlet.2021.130443.

[17] A. Hermawan, N.L.W. Septiani, A. Taufik, B. Yuliarto, Suyatman, S. Yin, Advanced Strategies to Improve Performances of Molybdenum-Based Gas Sensors, vol. 13, Springer,, Singapore, 2021.
[18] K.Y. Ko, et al., "Improvement Gas. -Sens. Perform. Large-Area Tungsten Disul fi De. Nanosheets Surf. Funct.," (2016), https://doi.org/10.1021/acsnano.6b03631.
[19] D. Zhang, Y. Cao, J. Wu, X. Zhang, Tungsten trioxide nanoparticles decorated tungsten disulfide nanoheterojunction for highly sensitive ethanol gas sensing application (August), Appl. Surf. Sci. 503 (no) (2019), 144063, https://doi.org/10.1016/j.apsusc.2019.144063.
[20] A. Alagh, F.E. Annanouch, P. Umek, C. Bittencourt, J.F. Colomer, E. Llobet, An ultrasensitive room-temperature HS gas sensor based on 3D assembly of CuO decorated WS nanomaterial, IEEE Sens. J. 21 (19) (2021) 21212–21220, https://doi.org/10.1109/JSEN.2021.3103925.
[22] M. Chen, et al., Stable few-layer MoS2 rectifying diodes formed by plasma-assisted doping, Appl. Phys. Lett. 103 (14) (2013), https://doi.org/10.1063/1.4824205.
[23] M.R. Laskar, et al., P-type doping of MoS2 thin films using Nb, Appl. Phys. Lett. 104 (9) (2014), https://doi.org/10.1063/1.4867197.
[24] V.E. Fedorov, et al., Tuning electronic properties of molybdenum disulfide by a substitution in metal sublattice," 2013 36th Int. Conv. Inf. Commun. Technol. Electron, Microelectron. MIPRO 2013 - Proc. 2 (2013) 11–14.
[25] A. Alagh, et al., CVD growth of self-assembled 2D and 1D WS2 nanomaterials for the ultrasensitive detection of NO2 (April), Sens. Actuators, B Chem. 326 (2020), 128813, https://doi.org/10.1016/j.snb.2020.128813.
[26] H. Fang, S. Chuang, T.C. Chang, K. Takei, T. Takahashi, A. Javey, High-performance single layered WSe 2 p-FETs with chemically doped contacts, Nano Lett. 12 (7) (2012) 3788–3792, https://doi.org/10.1021/nl301702r.
[27] S. Tongay, et al., Broad-range modulation of light emission in two-dimensional semiconductors by molecular physisorption gating, Nano Lett. 13 (6) (2013) 2831–2836, https://doi.org/10.1021/nl4011172.
[28] Y. Li, C. Xu, P. Hu, L. Zhen, Carrier control of MoS 2 nanoflakes by, ACS Nano 7 (9) (2013) 7795–7804.
[29] S. Mouri, Y. Miyauchi, K. Matsuda, Tunable photoluminescence of monolayer MoS2 via chemical doping, Nano Lett. 13 (12) (2013) 5944–5948, https://doi.org/10.1021/nl403036h.
[30] F.E. Annanouch, et al., Aerosol-assisted CVD-grown PdO nanoparticle-decorated tungsten oxide nanoneedles extremely sensitive and selective to hydrogen, ACS Appl. Mater. Interfaces 8 (16) (2016) 10413–10421, https://doi.org/10.1021/acsami.6b00773.
[31] F.E. Annanouch, et al., Aerosol-assisted CVD-grown WO3 nanoneedles decorated with copper oxide nanoparticles for the selective and humidity-resilient detection of H2S, ACS Appl. Mater. Interfaces 7 (12) (2015) 6842–6851, https://doi.org/10.1021/acsami.5b00411.
[32] W.S. Nanomaterials, et al., Use Pulse UV Or. Visible Light Act. Gas. Sens. Reducing Oxid. Species WO 3 (2021).
[33] A. Alagh, et al., CVD growth of self-assembled 2D and 1D WS2 nanomaterials for the ultrasensitive detection of NO2 (August), Sens. Actuators, B Chem. vol. 326 (no) (2020), 128813, https://doi.org/10.1016/j.snb.2020.128813.
[34] X. Zhao, C. Xia, X. Dai, T. Wang, P. Chen, L. Tian, Electronic and magnetic properties of X-doped (X⎯Ni, Pd, Pt) WS2 monolayer, J. Magn. Magn. Mater. 414 (2016) 45–48, https://doi.org/10.1016/j.jmmm.2016.04.050.
[35] C. Navío, et al., Gold clusters on WO 3 nanoneedles grown via AACVD: XPS and TEM studies, Mater. Chem. Phys. 134 (2–3) (2012) 809–813, https://doi.org/10.1016/j.matchemphys.2012.03.073.
[36] K.M. McCreary, A.T. Hanbicki, G.G. Jernigan, J.C. Culbertson, B.T. Jonker, Synthesis of large-area WS 2 monolayers with exceptional photoluminescence, Sci. Rep. 6 (2015) (2016) 1–7, https://doi.org/10.1038/srep19159.
[37] G.K. Reddy, T.C. Peck, C.A. Roberts, 'PdO vs. PtO'—The influence of PGM oxide promotion of Co3O4 spinel on direct NO decomposition activity, Catalysts vol. 9 (1) (2019), https://doi.org/10.3390/catal9010062.
[38] "Dembowski, Pdf. " (1993), https://doi.org/10.1116/1.1247716.
[39] D. Zhao, et al., Synthesis of large-scale few-layer PtS 2 films by chemical vapor deposition, AIP Adv. 9 (2) (2019), https://doi.org/10.1063/1.5086447.
[40] Y. Han, et al., Interface engineered WS2/ZnS heterostructures for sensitive and reversible NO2 room temperature sensing, Sens. Actuators, B Chem. 296 (April) (2019), 126666, https://doi.org/10.1016/j.snb.2019.126666.
[41] W. Yan, M.A. Worsley, T. Pham, A. Zettl, C. Carraro, R. Maboudian, Effects of ambient humidity and temperature on the NO 2 sensing characteristics of WS 2 /graphene aerogel, Appl. Surf. Sci. 450 (2018) 372–379, https://doi.org/10.1016/j.apsusc.2018.04.185.
[42] X. Li, X. Li, Z. Li, J. Wang, J. Zhang, WS2 nanoflakes based selective ammonia sensors at room temperature," Sensors Actuators, B Chem. 240 (2017) 273–277, https://doi.org/10.1016/j.snb.2016.08.163.
[45] G.A. Asres, et al., "Ultrasensitive H. 2 S Gas. Sens. Based p-Type WS 2 Hybrid. Mater.," (2009) 1–10.
[46] G. Deokar, et al., MoS2–carbon nanotube hybrid material growth and gas sensing, Adv. Mater. Interfaces 4 (24) (2017), https://doi.org/10.1002/admi.201700801.
[47] S.W. Choi, J. Kim, Y.T. Byun, Highly sensitive and selective NO2 detection by Pt nanoparticles-decorated single-walled carbon nanotubes and the underlying sensing mechanism, Sens. Actuators, B Chem. 238 (2) (2017) 1032–1042, https://doi.org/10.1016/j.snb.2016.07.153.
[48] X. Chen, et al., NO2 sensing properties of one-pot-synthesized ZnO nanowires with Pd functionalization, Sens. Actuators, B Chem. 280 (2) (2019) 151–161, https://doi.org/10.1016/j.snb.2018.10.063.

Aanchal Alagh is a MSCA– COFUND PhD fellow at the Universitat Rovira i Virgili. Her research interest are on the synthesis and application of transition metal dichalcogenide materials.

Fatima Ezahra Annanouch is a Juan de la Cierva Post-Doctoral Fellow at the Universitat Rovira i Virgili. She obtained her PhD degree (2015) on the fabrication and characterization of metal oxide nanowires gas sensors, from the department of electrical electronic engineering and automation, Rovira i Virgili university (Tarragona), Spain. On 2016, she started her first postdoctoral position (2 years) at IM2NP, university of Aix-Marseille, France. Her research interests are on the synthesis and application of metal oxides and transition metal dichalcogenide materials to gas sensing.

Khaled Al Youssef is research within the Department of Chemistry at the University of Mons-Hainaut, Belgium. He is working on low kinetic energy irradiation of thin films prepared by various methods (CVD - Wet Chemistry procedure - mechanical exfoliation.).

Carla Bittencourt is Research Professor within the Department of Chemistry at the University of Mons-Hainaut, Belgium. One of her research interest is in the development of carbon based, hybrid nanomaterials for sensing gases at low operating temperatures.

Frank Güell received in 2005 the Ph.D. degree in Physics from Universitat de Barcelona (UB), and currently is Associate Professor at the Electronics Department of UB. During his Ph.D. and afterwards he joined several times the Max-Born-Institute for Nonlinear Optics and Ultrafast Spectroscopy in Berlin, Germany. His general area of research is in the growth and study of semiconductor nanomaterials such as ZnO nanowires. His research interests also include laser physics, optical sensors and solar cells based on nanostructures.

Paulina R. Martínez-Alanis obtained her Ph.D. in Science working on the field of bio-inorganic chemistry from Universidad Nacional Autónoma de México in 2012. Currently she is working on the vapor–liquid–solid growth of ZnO nanostructures at Universitat de Barcelona. She is also interested in the conversion of CO2, H2, O2, N2 in to feedstock products

Marc Reguant is a master student at the Electronics Department of Universitat de Barcelona.

Eduard Llobet Eduard Llobet is a full professor at the Department of Electronic Engineering of the Universitat Rovira i Virgili in Tarragona (Spain). He was awarded a Ph.D. in 1997 from the Technical University of Catalonia (Barcelona) and then joined the Gas Sensor Lab (UWarwick, UK)for a one-year postdoc. From2010 to 2014 he was Director of the Research Centre on Engineering of Materials and micro/nano Systems. He is currently addressing the fabrication of sensor arrays employing low-dimensional metal oxides and carbon nanomaterials. Cost-effective and industrially scalable methods are considered for bottom-up integration in MEMS or flexible platforms. The applications sought are (i) sensitive and selective gas microsensors for environmental monitoring, medicine or safety and (ii) heterogeneous catalysis. He got the ICREA Academia Award in the 2018 Edition.

Chapter-5

A robust gas sensor with bifunctional sensitivity and reliable anti-humidity ability based on WSe_2 nanoflower

A robust gas sensor with bifunctional sensitivity and reliable anti-humidity ability based on WSe_2 nanoflower

Aanchal Alagh[a], Fatima Ezahra Annanouch[a], Ayrton Sierra-Castillo[b], Emile HAYE[c]

Jean-François Colomer[b], Eduard Llobet[a]

[b]: Department d'Enginyeria Electronica, Universitat Rovira I Virgili, Avenida Paisos Catalans 26,43007, Tarragona, Spain.

[b]: Research Group on Carbon Nanostructures (CARBONNAGe), University of Namur, Rue de Bruxelles 61, 5000 Namur.

[c]: Laboratoire d'Analyse par Réactions Nucléaires (LARN), Namur Insitute of Structured Matter (NISM), Université de Namur, Rue de Bruxelles 61, 5000 Namur.

Abstract

Herein, we present for the first time, a chemoresistive-type gas sensor composed of two-dimensional WSe_2, fabricated by a simple selenization of tungsten trioxide (WO_3) nanowires at atmospheric pressure. The morphological, structural, and chemical composition investigation shows the growth of vertically oriented 3D assemblies of WSe_2 nanoplatelets arrayed in nanoflower's shape. The gas sensing attributes of flowered nanosheets (2H-WSe_2) are investigated thoroughly towards the specific gases (NH_3 and NO_2) at different operating temperatures. The integration of 3D WSe_2 with unique structural arrangements resulted in exceptional gas sensing characteristics with dual selectivity towards NH_3 and NO_2 gas. Additionally, the selectivity of the sensor can be tuned by selecting its operating temperature (150°C for NH_3 and 100°C for NO_2). For instance, the sensor has shown stable, reproducible, and ultrasensitive responses (24.5 %) towards 40 ppm NH_3 gas detection with an experimental LoD < 2 ppm at moderate temperatures. The gas detecting capabilities of CO, H_2, C_6H_6 and NO_2 gas were also investigated to better comprehend the selectivity of the nanoflower sensor. The sensor showed repeatable responses with high sensitivity to NO_2 molecules at a substantially lower operating temperature (100° C) (even at room temperature) and LoD < 0.1ppm. However, the gas sensing attributes reveal high selectivity towards NH_3 gas at moderate operating temperature. Moreover, the sensor demonstrated great resilience against high levels of ambient humidity (Rh = 50%), demonstrating its remarkable stability towards

NH_3 gas detection. While for NO_2 detection in humid ambient there was a modest increase in sensor response (5.5%). Furthermore, four-month long-term stability assessments were also taken towards NH_3 gas detection, and the sensor showed good stability. Therefore, this study highlights the practical application of the 2H variant of WSe_2 nanoflower gas sensor for NH_3 gas detection.

1. Introduction

Year by year, gas sensors have known tremendous developments in term of size, sensing material, heater power consumption, fabrication cost, etc. They become indispensable items in the monitoring of indoor and outdoor toxic gases, to ensure the safety, the air quality, or the environmental monitoring. [1–4] Among the main toxic and air pollutant gases, we find nitrogen dioxide (NO_2) and ammonia (NH_3), which are generated from motor vehicle exhaust, refineries, power plants, etc. They have a direct contribution in the formation of ground level ozone in the stratosphere, acid rain and inorganic ambient particulate matter. [5–7]For instance, exposure to nitrogen dioxide and ammonia may cause chronic bronchitis, respiratory irritation, mucous membrane inflammation syndrome and asthma. The odor thresholds of NO_2 and NH_3, in the air, are around 400 ppb and 40 ppb, respectively, while the thresholds limit values (TLV) were set by the Occupational Safety and Health Administration (OSHA) to 5 ppm and 25 ppm respectively. Exposure to high concentrations of these gases is a serious health threat. Hence, developing new generation of gas sensor that can monitor such pollutant gases in a real time and can detect concentrations from as low as a few parts per billion to the several hundred parts per million in the air is of a strong industry demand. In this context, chemiresistive sensors based on nanostructured metal oxide semiconductors, such as WO_3, ZnO, SnO_2 and In_2O_3, etc. [5,8–10]have been extensively used for detecting pollutant gases, owing to their advantages of low cost, simple fabrication process, reliability etc. They were launched as new building blocks material for gas sensors, owing to their high surface-to- volume ratio, low number of defects, electron confinement effect etc. [11–13]Yet, the lack of selectivity and humidity cross-sensitivity remain the major drawbacks to overcome. Additionally, these sensors are normally operated at 100–400 °C, leading to high power consumption and reduced sensor stability and lifetime owing to an induced growth of metal oxide grains. Thus, it limits the achievement of wider real-time applications.

Inspiring by these drawbacks, researchers and scientists have recently drawn towards atomically layered two-dimensional (2D) transition metal dichalcogenides (TMDs)

nanomaterials, thanks to their unique properties such as direct band gap, large specific surface area due to sheet-like structures, semiconducting properties etc. [14,15] They are consisted of metal atomic layer (such as Mo, W, Hf, Ti, Zr, V, Nb, Ta, Re, etc) collocated between two chalcogen atomic layers (S, Se or Te) and then these multiple trilayers are stacked on top of another one by van der Waals interactions.[16] Among the TMDs nanomaterials that have proven its feasibility as a gas-sensing element, we cite tungsten diselenide (WSe_2), which has ultimately sparked the interest of many researchers especially in the detection of NO_2 and ammonia. Guo and co-workers[17] have reported ultrasensitive room temperature NO_2 sensors based on liquid phase exfoliated WSe_2 nanosheets. Medina and co-workers[18] synthesized a wafer-scale of WSe_2 monolayers toward phase-engineered hybrid WOx/WSe_2 films with Sub-ppb NOx gas sensing by a low-temperature plasma-assisted selenization process. Ko and co-workers[19] developed high-performances NO_2 and NH_3 gas sensor based on three-layer WS_2 nanomaterial. Up to now, most of the reported works have synthesized WSe_2 in a two-dimensional direction, in the form of mono or multilayer nanosheets. However, it has been reported that vertical orientation (3D) of these nanomaterials is very suitable for gas sensing application. [20–22] It offers a large surface area to volume ratio with enriched exposed edge sites, has many defects that make it highly reactive with gas molecules and has plenty of voids for gas diffusion. Indeed, the gas adsorption at the edge sites of the TMDs is more important compared to their basal plan which has minimal dangling bonds and with the effect of thermodynamic forces it is very challenging to expose their edges to the environment.

In this respect, there are two techniques that are mostly used for the growth of 3D assemblies of edge enriched WSe_2 nanosheets: hydrothermal and atmospheric pressure chemical vapor deposition methods. [23–25] Hydrothermal synthesis has the advantage of low cost; however, it is a time-consuming technique (multistep fabrication) and sometimes it needs hazardous precursors that hinders its development. In contrast, atmospheric pressure CVD has a large yield deposition with the control of the layer number. Moreover, it is a catalyst free technique, and it allows as the direct deposition of the material on the alumina sensor transducer.

Herein, we report for the first time, on the successful synthesis of 3D assemblies of edge enriched tungsten diselenide nanoflowers, using a combination of aerosol assisted CVD and atmospheric pressure CVD techniques, for the development of bifunctional NO_2 and NH_3 gas sensor. The films were directly synthesized on alumina substrate, at atmospheric pressure without the need of any catalyst seeding. It is worth noting that very few papers have succeeded

to synthesis and use 3D assemblies of edge enriched WSe_2 nanoflowers for gas sensing application. Moreover, the grown films were highly investigated by using SEM, FESEM and HRTEM to analyze their morphology, XRD to determine their structure and Raman and XPS to define their composition. Additionally, the films were studied against small concentrations of NH_3 and NO_2 at very low operating temperatures ranging from 25 ºC to 150 ºC. Besides, the sensors were examined in the presence of moisture. Finally, a comparison study between this work and the literature has been performed and the gas sensing mechanism for both gases has been illustrated and discussed.

2. Experimental details

2.1 Synthesis of WSe_2 nanosheets

The gas-sensitive nanomaterial was synthesized in two steps. In the first step, WO_3 nanowires were grown on commercial alumina substrate (Ceram Tech GmBH, Germany). The front side of this substrate consists of interdigitated platinum electrodes (having a gap of 300 μm), while the backside comprises a heater (having a resistance of 8 Ω) to modify the operating temperature of the sensor.

The WO_3 nanofilms were grown using the aerosol-assisted chemical vapour deposition method, following a protocol discussed in detail in our previous reports [1][2]. Afterwards, the as-grown nanowires were selenised to grow WSe_2 nanomaterial via double selenization of WO_3 nanofilm using an ambient-pressure Chemical Vapor Deposition (CVD) technique. The quartz tube was flushed for one hour to remove (reduce) oxygen, using a 0.475 L min^{-1} argon flow outside of the furnace, prior to the selenization process. The growth conditions were taken from the previously reported vertically aligned WSe_2 nanosheets synthesis method [3]. As in a typical selenization process, the Se powder (purity 99%) was placed into two temperature zones, one part at 40 °C and the other at 850 °C (in total 0.700 g), along with the WO_3 nanofilm sample, which was placed at 850 °C with the argon flow, into the reactor. A 0.150 L-min^{-1} H_2 flow was inserted. In the first step of 30 min, the Se powder was placed at the 850 °C zone. The optimized second selenization step was performed by inserting the quartz tube in the hot zone of the furnace, such that the Se powder placed at 40 °C reaches the 400 °C temperature zone. The sample remained at 850 °C as the quartz reactor was moved over a few centimetres. After the reaction, the H_2 flow was stopped, and the quartz tube was removed from the reactor (quartz tube) and was cooled with the argon flow for 1 h.

2.2 Characterization Techniques

The morphology of the as-grown WO_3 nanowires was examined using a scanning electron microscope (JEOL 7500F microscope operating at 15 kV) whereas, after the selenization of WO_3 nanowires, the as-grown WSe_2 nanosheets were analyzed using a field-emission scanning electron microscope Hitachi 2000 and FEI Helios Nanolab 650. Transmission Electron Microscopy (TEM) studies were carried out on a TECNAI T20 microscope working under 200 kV. To prepare a sample, the material was scratched from the surface of an electrode, dispersed in ethanol using sonication and a droplet was put on the holey-carbon copper grid. For chemical phase analysis, XRD measurements were made, using a Bruker-AXS D8-Discover diffractometer. The chemical composition of the WO_3 nanowires and WSe_2 nanosheets was studied by X-ray photoelectron spectroscopy (XPS) using an Escalab 250i Thermo Fisher spectrometer (Al Kα 1486.68 eV). The O 1s, Se 3d and W 4f core levels have been recorded at pass energy of 20eV, with 20 scans, on a spot size of 250x250µm. A flood gun has been used for charge compensation and no additional energy shifting is applied to the spectra. The authors are aware of the recent warnings about XPS analysis on insulating samples [4][5][6]. The spectra are analysed with Thermo Avantage® software, considering a shirley background. The Raman spectra were obtained using a Renishaw in Via, laser 514 nm, ion argon-Novatech, 25 mW.

2.3 Gas Sensing Device Fabrication and Gas-Sensing Measurements.

The gas sensing characteristics of the fabricated WSe_2 nanoflower sensor were measured by using a homemade gas-sensing detection system. A schematic diagram of the home-made gas sensing detection system is shown in Fig.1. The as-fabricated sensor was placed inside a teflon test chamber of 35 mL in volume. This testing chamber was connected to a fully automated, continuous gas flow measurement set-up able to supply diluted gas mixtures as well as humidified gas mixtures using a mass flow controller (Bronkhorst High-Tech B.V.) and electro valves. The gases employed for testing were used from calibrated gas cylinders balanced in dry synthetic air (Air Premier purity: 99.999%). The operating temperature of the sensor was controlled by connecting its heater to an external power supply (Agilent, model 3492A).

The sensing measurements were done by recording the change in electrical resistance of the sensor upon exposure to several different concentrations of target gases such as NO_2, NH_3, H_2, CO, and C_6H_6 at different operating temperatures (100 °C and 150 °C). The sensor

was kept in a dry airflow for a period of 2 h before gas sensing measurements to stabilise its baseline resistance. Then the sensor was exposed to a given concentration of gaseous species for 10 mins followed by 50 min exposure to dry air to stabilise. The electrical resistance of the sensor was measured by using an Agilent-34972A multimeter. The gas flow and humidity were controlled using mass-flow controllers (MFC). Throughout the tests, the overall flow rate was maintained at 100 mL/min. To evaluate humidity interference, certain tests were done in a humid environment (e.g., 50 % RH at 23 °C). While the sensor was exposed to varying concentrations of NO_2 and NH_3, the humidity level was kept constant. For an oxidising gas, such as NO_2, the sensor response was calculated by using equation 1 while in the case of a reducing gas (such as NH_3) the gas sensing response value was calculated using equation 2.

$$Response = \frac{Rair-Rgas}{Rair} * 100 \quad (1)$$

$$Response = \frac{Rgas-Rair}{Rair} * 100 \quad (2)$$

Here Rair and Rgas are respectively the real-time resistances of the sensor exposed to air-condition and target gas, respectively. For practical applications, the response and recovery times are very important paramEters. In this work, the response time of the sensor (tres) is defined as the time taken by the sensor to obtain 90% of the total resistance change when exposed to the target gas and recovery time (trec) is defined as the time required to recover to within 10% of the total resistance change when the flow of analyte gas is removed.

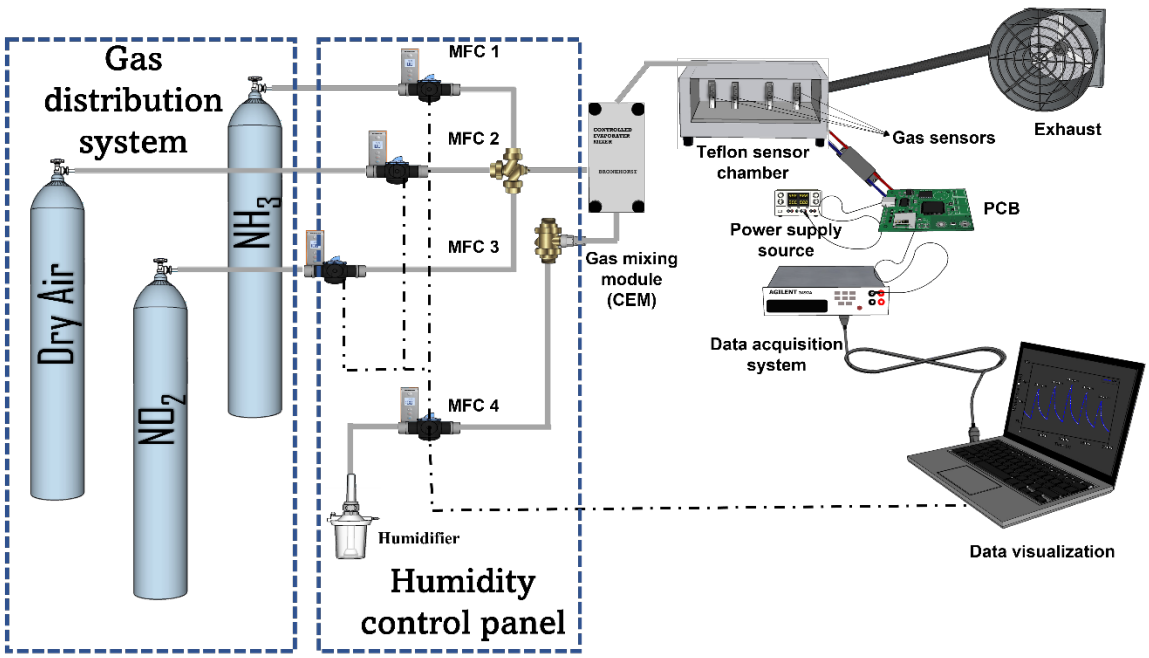

Fig. 1 Schematic demonstrating home-made gas sensing detection system.

3. Results and discussion

3.1 Material Characterization

The morphological and chemical characteristics of as-fabricated tungsten diselenide nanomaterial were assessed through various techniques, discussed in detail in this section.

3.1.1 SEM and FESEM characterisation

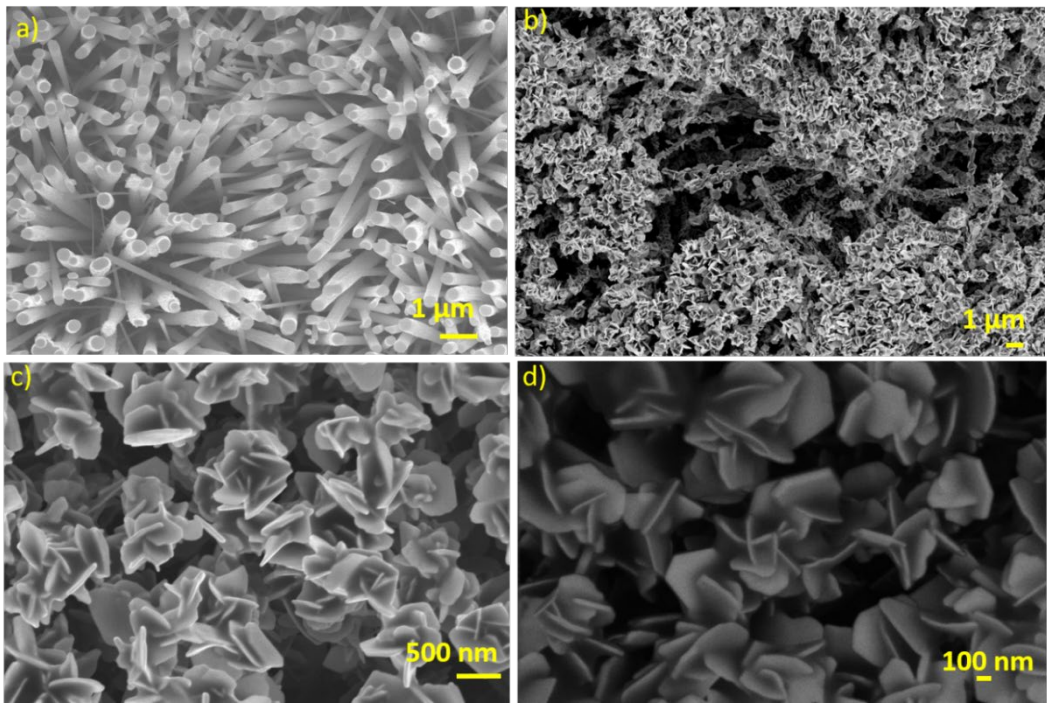

Fig. 2 SEM and FESEM images depicting the growth of vertically aligned (a) WO_3 nanowires (b) WSe_2 nanosheets (c) (d) WSe_2 nanoflowers.

The AACVD method was employed to grow adherent uniform films of tungsten trioxide nanowires on alumina substrates. A scanning electron microscope was used to analyze the morphology and microstructure of these nanowires, as presented in Fig. 2a. The result demonstrates that the sensor substrate is homogeneously covered with vertically aligned thin nanowires of WO_3. The length of as-grown nanowires is in the range of 6-7 µm since these films are obtained using the same procedure as reported in our previous works [1][7]. Afterwards, the as-grown WO_3 films were selenized to produce WSe_2 nanofilms, which were subsequently examined using a high-resolution scanning electron microscope (Fig. 2b-d). It is evident from the results obtained that after undergoing the selenization process the morphology of these nanowires changes completely resulting in platelets with well-defined shapes and sharp edges. Moreover, the layer-stacked bulk platelets grow vertically, similar to WO_3

nanowires, as illustrated in Fig. 2b. The results highlight that these platelets are evenly distributed and piled on top of one another, resulting in WSe_2 nanowires with platelet attachments covering the entire length of the nanowires, as seen in Fig. 2b. Furthermore, SEM pictures reveal nanoplatelets assembled in the form of nanoflowers at the tips of these nanowires (Fig 2c). Also, the higher magnification image presented in Fig. 2d reveals the thickness of these platelets which is in the range of 40-50 nm.

3.1.2 TEM characterization

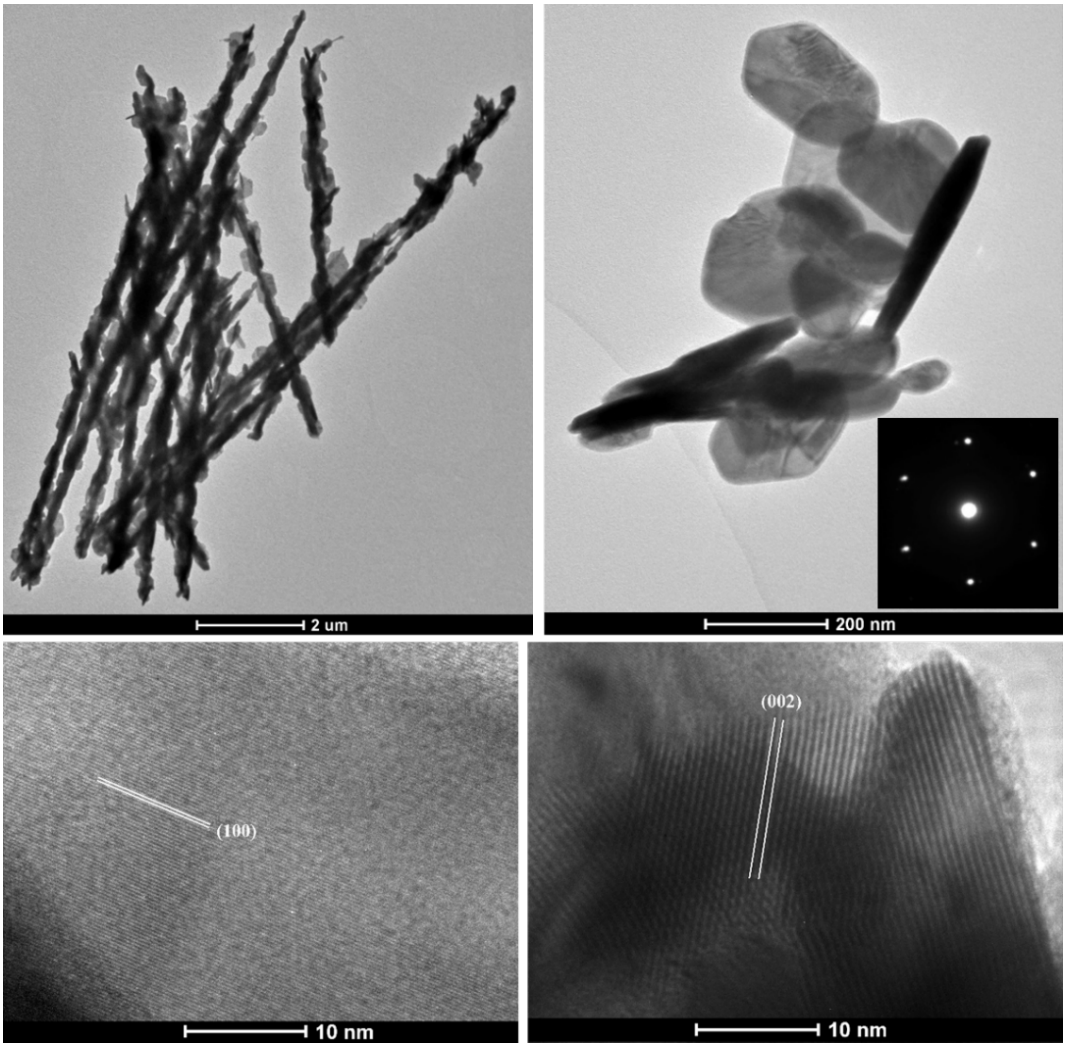

Fig. 3 Low magnification TEM images of (a) WSe_2 nanowires and (b) WSe_2 nanoflower petals with an inset of the SAED pattern along the [100] axis and high-resolution images of (c) a petal showing the (001) crystal planes and (d) the layered structures of WSe_2 nanosheets composing of the petals with the (002) interlayer spacing.

The morphology, structure, and crystallinity of the as-prepared nanoflowered material were further investigated using TEM (Fig. 3). It can be observed in Fig. 3a that WO_3 nanowires completely transform into WSe_2 nanowires after undergoing the selenization process. These

WSe_2 nanowires, which are about 10 µm in length contain WSe_2 nanosheets along their entire length. These nanosheets arrange themselves in nanoflowers at the ends of the nanoneedles, as shown in SEM, but not in Fig. 3a, certainly due to the TEM preparation. However, these nanosheets composing the petals of these nanoflowers are found dispersed on the grid as shown in Fig. 3b. In the inset of Fig. 3b, the selected area electron diffraction (SAED) pattern of a single petal was acquired along the [100] axis and reveals only a single set of diffraction points arranged in a hexagonal symmetry, demonstrating its high crystallinity. The (001) planes in Fig. 3c have a lattice spacing of about 0.29 nm, which is consistent with the 2H-phase of WSe_2. Furthermore, Fig. 3d displays an interlayer spacing of roughly 0.66 nm, corresponding to the (002) plane of the hexagonal WSe_2.

3.1.3 Raman characterization

Raman spectroscopy is a powerful and non-destructive tool for assessing nanomaterial quality and device feasibility. It is also very useful to determine the number of layers that contribute to the film thickness of a sample. In this respect, Raman spectroscopy was used to further examine the grown sample. To check for the presence of tungsten oxide in the selenized samples, the Raman spectra of the starting material (WO_3 nanowires) were compared to the films formed after the selenization process. Two spectra were obtained using a laser with an excitation wavelength of 532 nm, where the upper spectrum (Fig. 4a) corresponds to the nanoflowers film obtained after selenization of WO_3 nanowires and the lower spectrum corresponds to the WO_3 nanowires (Fig. 4b). As presented in Fig. 4a, two main peaks were obtained, the peak at 251 cm^{-1} corresponds to the E^1_{2g} (in-plane vibration of the Se and W atoms) while a small shoulder peak at 257.6 cm^{-1} corresponds to the A_{1g} (out-of-plane vibration) modes, respectively. These are the two characteristic peaks associated with the presence of 2H-phase WSe_2. An additional peak was observed at 306 cm^{-1} (B_{2g}^1 mode) which has been linked to interlayer interaction.The absence of this peak is associated with the growth of monolayers, which is not the case here. [7][8]. The Raman analysis results are consistent with prior publications, demonstrating that the as-grown WSe_2 nanoflowers films are multilayered structures [9][10]. Moreover, there was no other peak that indicated the presence of WO_3 impurities or any other impurity. Furthermore, to compare, the Raman spectra of WO_3 NWs are shown in Fig. 4b. All of the peaks (271 cm^{-1}, 327 cm^{-1}, 715 $cm^{-1}$and 805 cm^{-1}) are

indicative of the monoclinic tungsten trioxide phase, which is consistent with our previous reported works [2], [11]

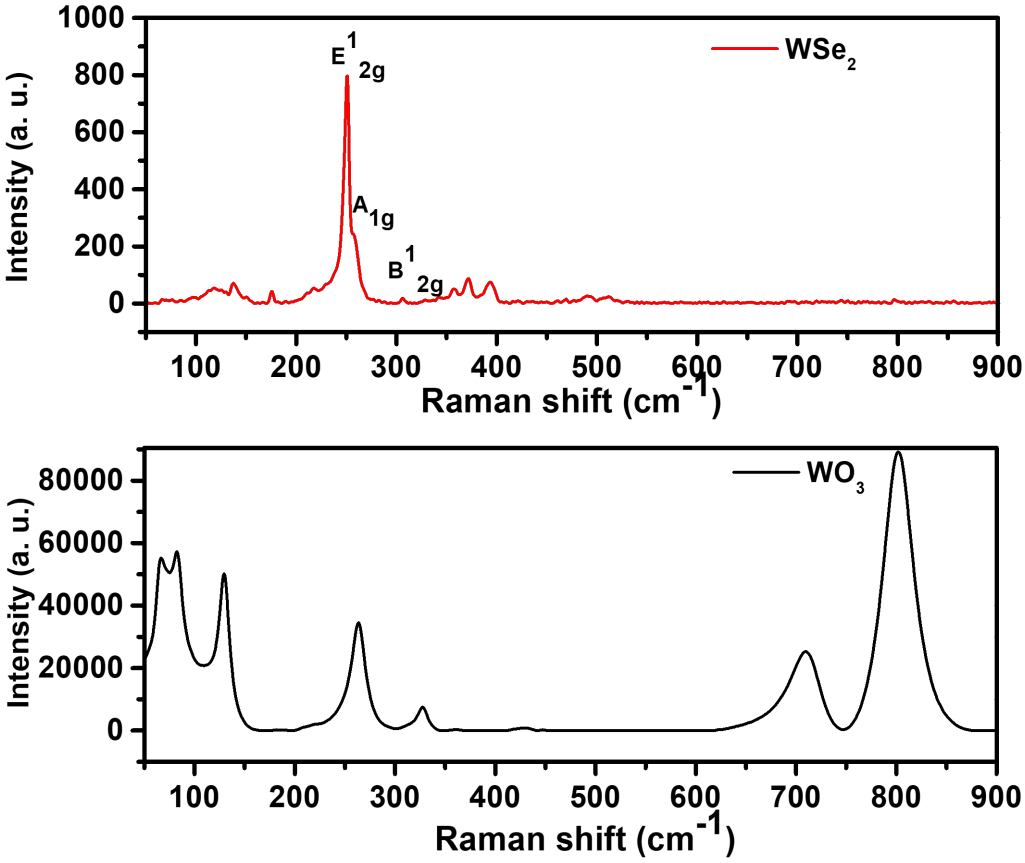

Fig. 4 Raman spectrum of (a) as-grown WSe_2 nano-flowered film (b) WO_3 nanowires.

3.1.4 XRD analysis

The crystallographic structure, as well as the purity of the WSe_2 nanoflowers film, are evaluated by the X-ray diffraction technique. The XRD pattern obtained (Fig. 5) reveals the presence of intense peaks at 13.65°, 27.50°, 31.44°, 37.86°, 41.78°, 47.43°, 55.99°, and 57.92°, in agreement with the (002), (004), (100), (103), (006), (105), (110), (112) crystal planes of the hexagonal WSe_2, respectively. All the diffraction peaks are indexed to the ICDD no: 01-071-0600 confirming the presence of 2H phase WSe_2, marked with black colour in the spectra. The high-intensity peaks imply a highly crystalline material, having a crystallite size above 400 nm, also reported earlier [3]. Additionally, peaks corresponding to alumina substrate were also detected and their lattice planes are highlighted in red. It was found that the peaks at 32.9°, 45.3°, 49.0°, and 60.3° can be indexed to the (011), (012), (110), (021) crystal planes indicating the presence of platinum selenide sulfide, Pt(SSe). These diffraction peaks are coloured blue

in the spectra and are referenced to the ICDD number 01-078-9794. Moreover, the absence of a diffraction peak towards the impurity phase indicates that a single-phase WSe_2 is formed. As a result, the XRD analysis confirms the presence of 2H-phase WSe_2 in the grown material along with the presence of some small impurity of Pt(SSe).

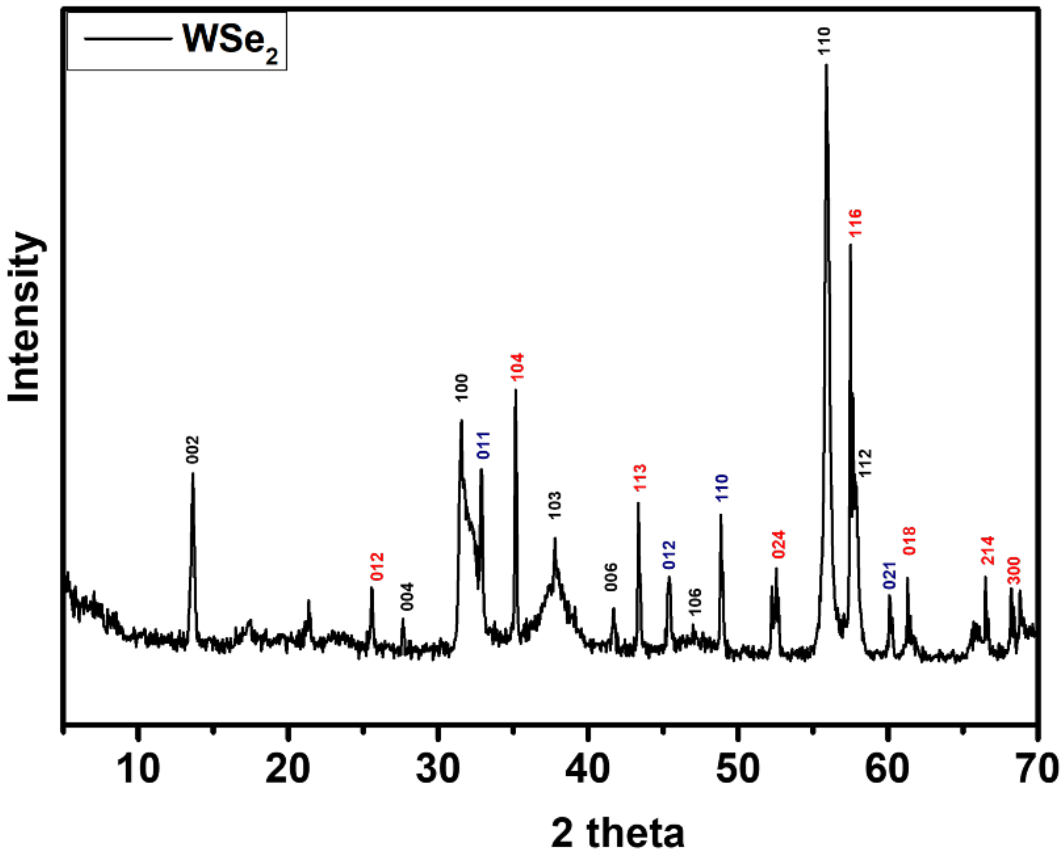

Fig. 5 XRD pattern of as-grown WSe_2 nano-flowered film.

3.1.5 XPS analysis

To further investigate the chemical composition of the as-prepared material, an XPS analysis was performed. The analysis of the sample before and after selenization is shown in Fig. 6, confirming that the tungsten oxide nanomaterial has been completely transformed. Before selenization, the W4f signal (Fig. 6a) is composed of a doublet centred at 35.5 and 37.7eV, corresponding to W 4f7/2 and W4 f5/2 and an additional contribution at 41.2eV, attributed to W 5p3/2 level. These positions are in agreement with WO_3 formation [12]. On the O 1s level (Fig. 5b), an intense contribution at 530.3eV, corresponding to WO_3, confirms the oxide production. Two additional peaks are observed at 531.9 and 533.5 eV, attributed to organic oxygen (C-O, C=O), which are most likely from synthesis. As expected, no selenium

is present before the selenization steps (Fig. 6c). However, after selenization, the W 4f signal shifts to lower binding energy, and exhibits a unique doublet contribution centred at 32.2 and 34.3 eV, which is consistent with WSe_2 2H phase formation, where literature reports binding energy in the range 32.0 to 32.4 eV [13][14] and up to 32.7eV [15] for large oxygen-free tungsten diselenide flakes. Following WSe_2 2H phase creation, the Se 3d signal is composed of a unique doublet contribution centred at 54.4 and 55.26 eV due to the Se 3d5/2 and Se 3d3/2 levels, respectively. After selenization, there is no evidence of significant oxygen presence. As a result, the presence of the 2H phase is confirmed by XPS, XRD, and RAMAN analysis, as the 1T (or 1T') phase exhibits W 4f and Se 3d signals that are slightly shifted to lower binding energy (≈ 31.9 eV for W 4f signal and 53.6-54.1 eV for Se 3d) [13][14][16].

In summary, the results of SEM and TEM demonstrate the growth of vertically aligned WSe_2 nanoflowers. Furthermore, the results from the XRD analysis reveal that the as-grown WSe_2 nanoflowers exhibit excellent crystallinity. The lack of a diffraction peak towards the impurity phase also suggests that WSe_2 is formed as a single phase. We may also conclude, that the WSe_2 nanoflowers have a multilayered structure based on the Raman and XRD findings.

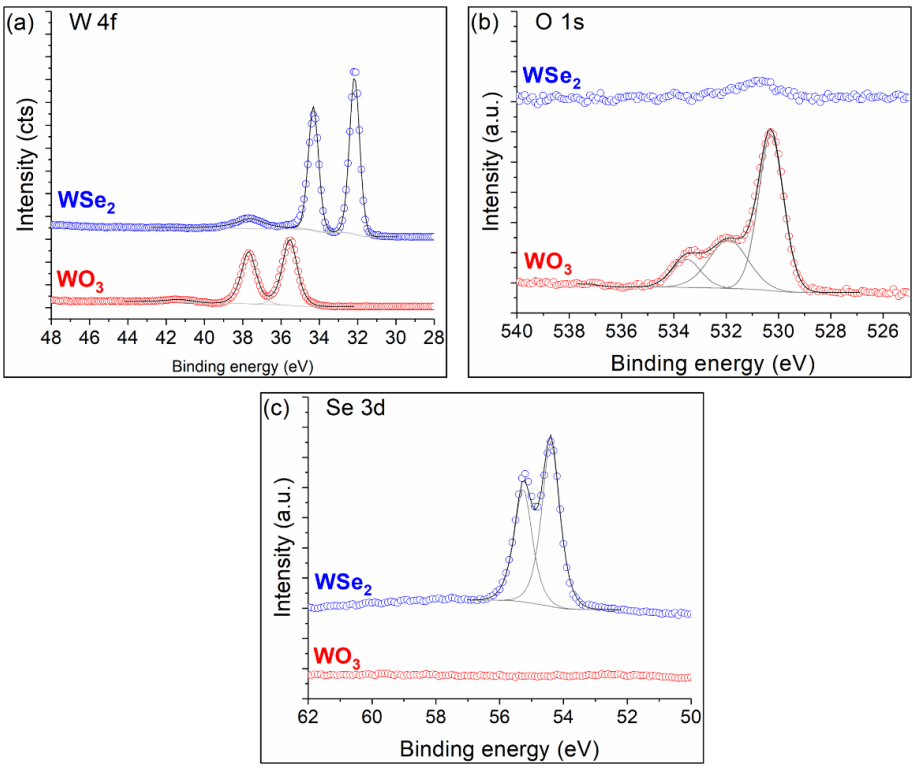

Fig. 6 (a) W 4f, (b) O 1s and (c) Se 3d XPS core levels spectra, of WO_3 nanowires and WSe_2 nanoflowers.

3.2 Gas sensing results

3.2.1 NO_2 detection

The gas sensing properties of the as-fabricated WSe_2 nanoflower sensor were evaluated using a homemade gas monitoring system (described in detail in the previous section). Choosing the optimal working temperature for a gas sensor is crucial for evaluating its performance. The temperature-dependent responses of the sensor to 800 ppb NO_2 were initially investigated to determine the ideal working temperature because the sensitivity, selectivity, and response/recovery speed of gas-sensitive materials are all heavily dependent on the operating temperature. As a consequence, we subjected our sensor to 800 ppb NO_2 in dry air balance and measured the resulting responses at various operating temperatures below 150 °C. This is due to the thermal instability of 2H-WSe_2 at high temperatures as well as to prevent ambient oxidation of 2H-WSe_2 which is also beneficial for developing low-power devices [17].

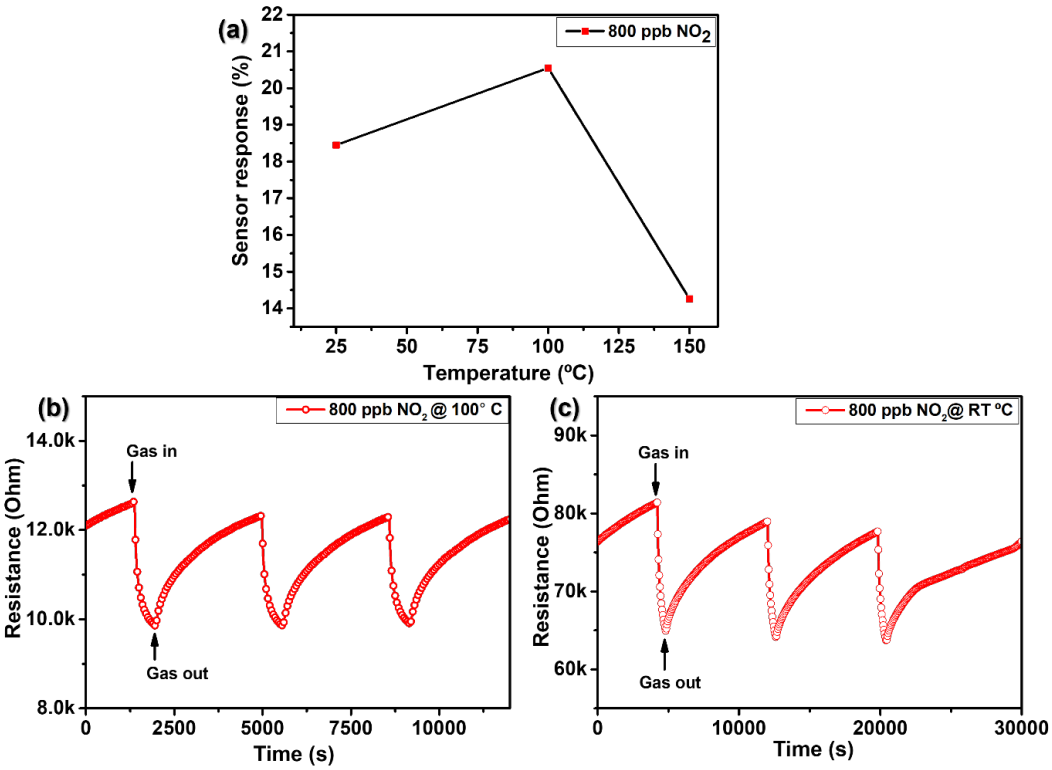

Fig. 7 (a) WSe_2 sensor response as a function of temperature towards NO_2 gas (b) Film resistance change as a function of time, towards 800 ppb of NO_2 at 100 °C (c) Film resistance change as a function of time, towards 800 ppb of NO_2 at 25 °C.

The sensor response to 800 ppb NO_2 gas is shown in Fig. 7a at varying operating temperatures ranging from 25°C to 150°C. As demonstrated, the sensor response increases with an increase in operating temperature from 25°C to 100°C, then gradually decreases as the

temperature climbs more. The presence of potential selenium vacancies is attributed for the increased response at 100°C. For instance, it has been reported in the literature that these vacancies promote NO_2 molecule adsorption at the WSe_2 surface, thereby increasing the interaction with the target gas molecules[18].

Furthermore, the sensor response is calculated to be 18.5 % at room temperature (25 ºC), rising to more than 20.5 % at an operating temperature of 100°C before dropping down to only 14.2 % at 150°C. Consequently, 100°C has been determined to be the optimal operating temperature for the fabricated WSe_2 nanoflowered sensor for NO_2 gas detection. It is worthy to mention that when compared to various metal oxides and other TMDs materials, this temperature is relatively low [19][20].

Fig. 7 (b) and (c) show an example of dynamic film resistance change in response to 800 ppb NO_2 gas, at 100 °C and 25 °C respectively. When exposed to an oxidising gas, such as NO_2, the WSe_2 sensor responds as a p-type semiconductor with decreasing resistance. The electron-acceptor characteristics of oxidizing gases like NO_2 can elucidate this behaviour. When a p-type material is exposed to an oxidizing atmosphere, electrons are removed from the conduction band, increasing the hole density and decreasing the material's electrical resistance, and vice versa when exposed to a reducing atmosphere [1]. Besides, it is observed that the sensor does not completely return to its baseline resistance when the target gas is withdrawn and the sensor is exposed to only dry air, however, the baseline resistance is recovered when the temperature is raised to 100 °C. This is due to the fact that higher temperature promotes faster desorption of gas molecules, resulting in a faster recovery cycle. In addition, the sensor's response and recovery time for 800 ppb NO_2 varied considerably with temperature. For instance, at room temperature, the response and recovery times towards 800 ppb of NO_2 gas are computed to be 411 s and 5446 s (Fig S1a), respectively, while at 100°C, they fall to 196 s and 2218 s (Fig. S1b). This decrease in response, as well as recovery times, is attributed to the much faster adsorption and desorption of NO_2 gas molecules at an elevated temperature.

Furthermore, at an operating temperature of 100 °C, the sensor was tested against a wide range of NO_2 gas concentrations ranging from 0.1 to 0.8 ppm. As expected, increasing NO_2 concentrations lead to higher resistance changes, resulting in an enlarged sensing response. Fig. 8 depicts the observed data, which indicate a superlinear increase in sensing response with each increase in gas concentration (Fig. 8a).

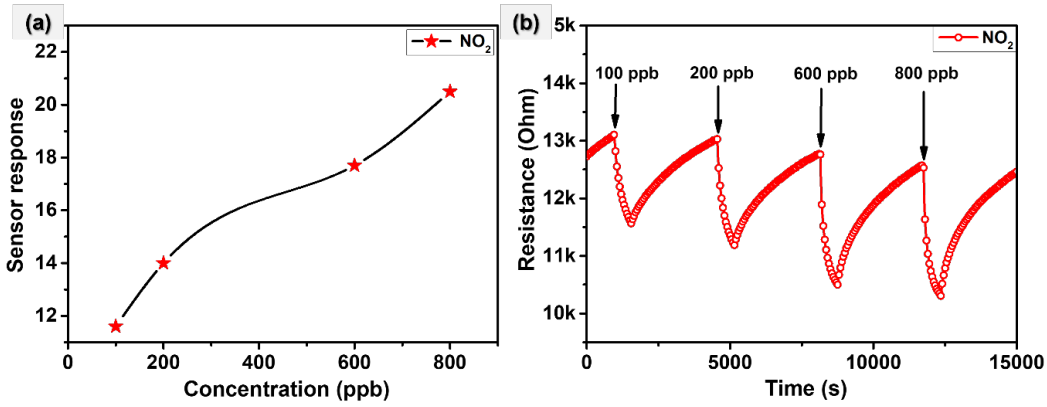

Fig. 8 (a) WSe_2 sensor response as a function of different NO_2 concentrations (b) Film resistance change as a function of time, towards different NO_2 concentrations, at 100 °C.

An example of the dynamic film resistance change over time in response to various NO_2 gas concentrations is presented in Fig. 8b. The responses towards 0.1 ppm, 0.2 ppm, 0.6 ppm, and 0.8 ppm NO_2 were calculated to be 111.5%, 14%, 17.6% and 20.4%, respectively. It is worth mentioning that the sensor demonstrated a remarkable sensitivity and high stability when detecting lower concentrations. The WSe_2 sensor, as shown in Fig. 8b, can detect NO_2 gas concentrations as low as 0.1 ppm, which is substantially lower than the threshold exposure limit of NO_2 as recommended by the American Conference of Government Industrial Hygienists [21]. Henceforth, it can be deduced that the sensor exhibited exceptionally low LoD which is below 100 ppb at moderate temperature (100 ˚C).

Moreover, Table 1 gives more insights by comparing the performance in the detection of NO_2 gas reported in this paper with those found in the literature. From the results obtained, the fabricated WSe_2 sensor shows outstanding gas responses with high sensitivity towards NO_2 detection and with LoD < 0.1 ppm when operated at 100 ºC. Besides that, the sensor remains functional and demonstrates acceptable sensitivity towards the targeted gas (NO_2) even at room temperature.

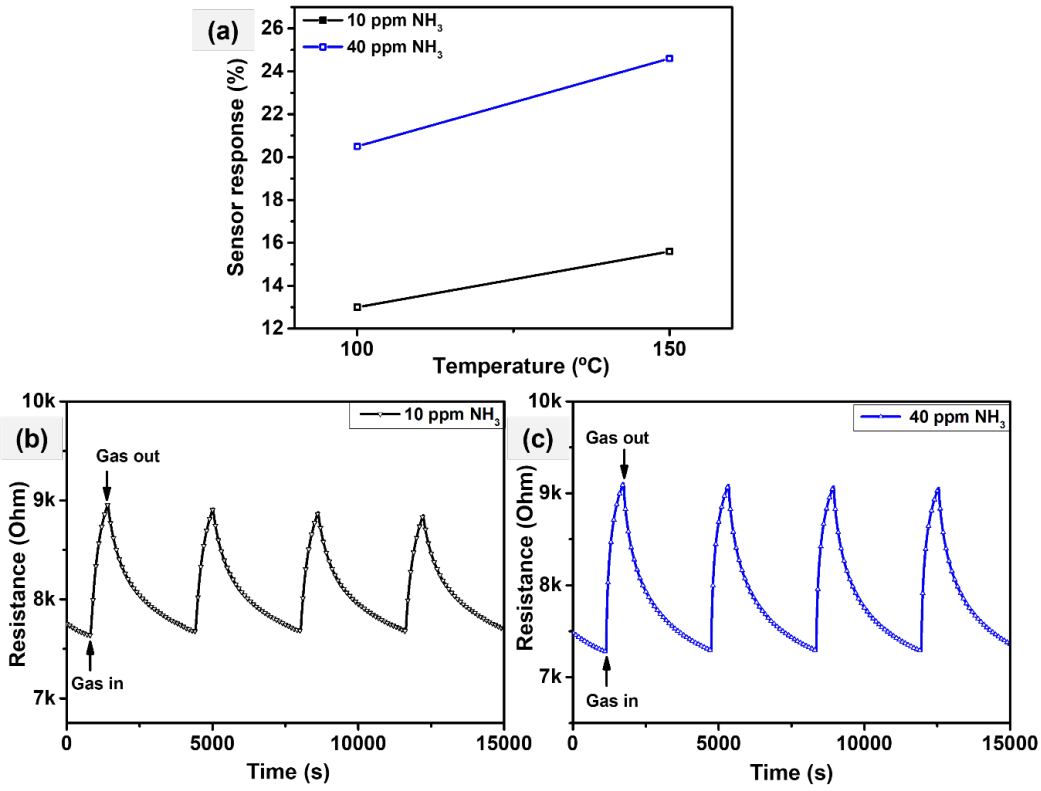

Fig. 9 (a) WSe_2 sensor response as a function of temperature towards NH_3 gas (b) Film resistance change as a function of time, towards (b) 10 ppm of NH_3 (c) 40 ppm of NH_3, at 150 °C.

3.2.2 NH_3 sensing

Aside from NO_2 gas sensing, the performance of the WSe_2 nanoflower sensor against NH_3 gas is also investigated. Ammonia is most widely used in livestock, food manufacturing and textile industries. This gas is of particular interest due to its adverse effects on human health and the environment at higher concentrations. Nevertheless, the exposure to even low levels of ammonia can cause irritation of nose and throat [22]. We investigated the optimal working temperature for the WSe_2 nanoflower sensor in the presence of NH_3 gas once more. As shown in Fig. 9a, sensor response increases linearly with temperature, with practically little response at room temperature, which can be expected due to rapid reaction rates at elevated temperatures. This behaviour is more prominent when the concentration of the target gas is increased from 10 ppm to 40 ppm. For instance, the gas response at 100 °C and 150 °C is 13% and 15.5% respectively, towards 10 ppm of NH_3 gas. Furthermore, as the NH_3 gas concentration is further increased to 40 ppm the calculated response climbs up to a value of 20.5% and 24.5% at 100 °C and 150 °C respectively. This can be attributed to the hierarchical nanoflowered structure resulting in a high surface area which in turn enhances the active sites for NH_3 gas adsorption and surface reactions. Considering a higher sensing response at 150 °C

it has been considered the optimal working temperature for subsequent measurements with NH_3 gas.

Fig. 9(b) and (c) show typical repeated response and recovery cycles for the WSe_2 sensor towards 10 and 40 ppm of NH_3 respectively. As mentioned earlier, the sensor shows p-type semiconducting properties resulting in increased electrical resistance upon exposure to NH_3 molecules (i.e., a reducing gas). Furthermore, the sensor exhibits a repeatable response at each concentration, with the response and recovery time being substantially shorter for the higher NH_3 concentration (40 ppm) (Fig. S2). For instance, for 10 ppm of NH_3, the WSe_2 sensor has a response time of 460 s and a recovery time of 2282 seconds, respectively (Fig. S2a). For 40 ppm, the sensor has a response time of 396 s and a recovery time of 1917 s (Fig. S2b). The lengthy recovery time is associated to the strong adhesion of NH_3 molecules to the sensing material's surface, which promotes high sensitivity for analyte detection at the cost of difficulties in removing these molecules.

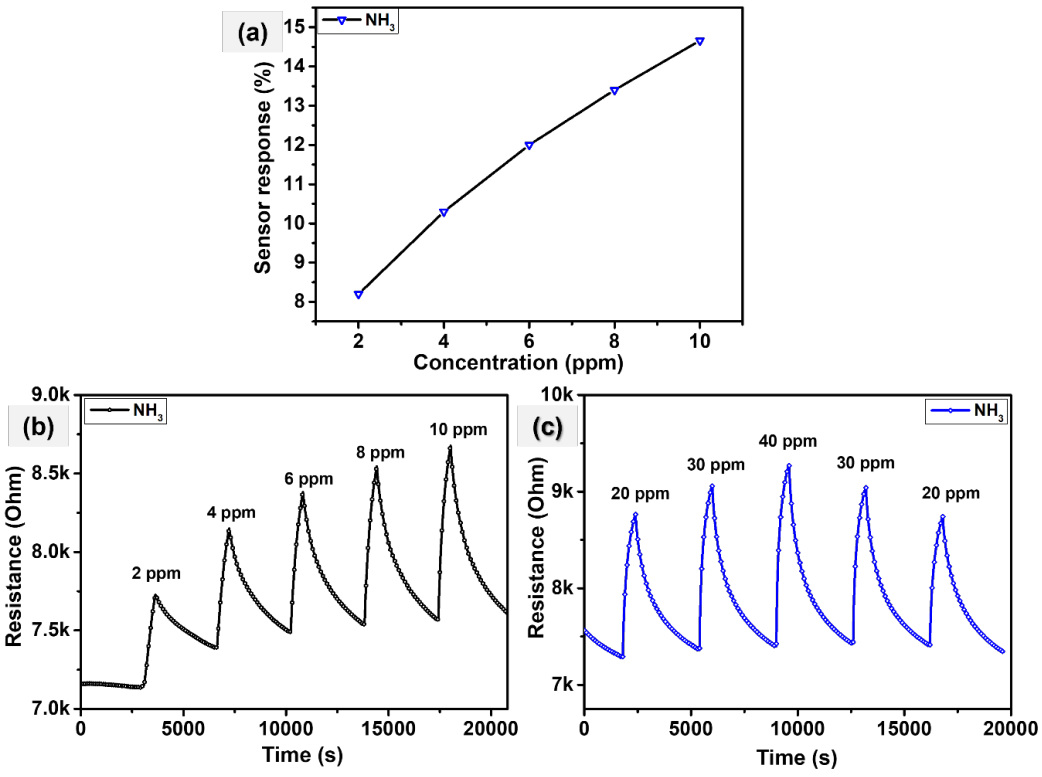

Fig. 10 (a) WSe_2 sensor response as a function of NH_3 concentrations, (b-c) Film resistance change as a function of time, towards different concentrations of NH3 at 150 °C.

Fig. 10a demonstrates the response to varied NH_3 concentrations at a constant operating temperature of 150 °C. The results reveal that as the concentration of analyte rises, so does the

sensing response. During this measurement, the sensor was exposed to five successive NH_3 concentration pulses ranging from 2 to 10 ppm, as illustrated in Fig. 10b. For 10 minutes, a diluted mixture of NH_3 in dry air was injected at concentrations of 2, 4, 6, 8, and 10 ppm. The WSe_2 sensor response was calculated to be 8.2%, 10.3%, 12%, 13.4% and 14.5% towards 2, 4, 6, 8, and 10 ppm of NH_3, respectively. In addition, as shown in Fig. 9c, the sensor was evaluated for increasing and decreasing NH_3 gas pulses from 20 to 40 ppm and vice versa. During this measurement, the sensor was exposed to 20, 30, 40, 30, and 20 ppm of NH_3 pulses. As expected, the sensing response increases manifolds with an increase in analyte concentration. For instance, the sensor response rose from 15.6% to 24.6% towards 10 and 40 ppm NH_3 respectively. It is evident from the results obtained that the sensor shows reproducible and repeatable responses.

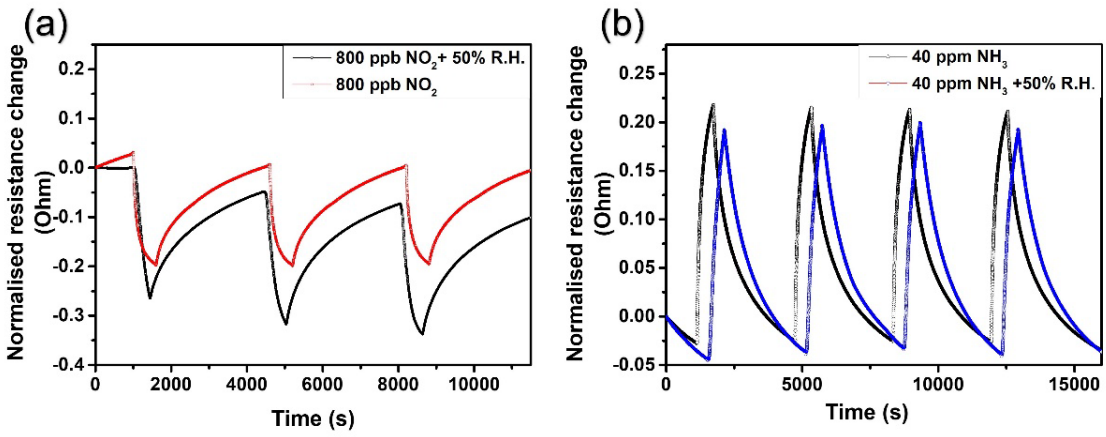

Fig. 11 Relative humidity cross-sensitivity to (a) 0.8 ppm NO_2 at 100 °C (b) 40 ppm NH_3 at 150 °C.

3.2.3 Humidity

To verify the practicability of the WSe_2 sensor, the influence of relative humidity on the sensor response towards NO_2 and NH_3 gas were also investigated. The results are presented in Fig. 11(a) and (b), where the sensor was tested at 100°C for 0.8 ppm NO_2 gas and 150°C for 40 ppm NH_3 gas in a 50% humidified background. It was observed that the sensor response was increased from 20.5% to 26% when the sensor was subjected to 0.8 ppm NO_2 gas in the presence of ambient moisture (50% R.H). This slight increase in response could be assigned to the ionization of NO_2 molecules in presence of water molecules. Similar results regarding water-enhanced sensor response have previously been reported in the literature [23].

However, no apparent decrease in sensor response is observed when exposed to NH_3 gas in presence of water vapour. The sensor response to 40 ppm NH_3 is calculated to be 24.1

% in the presence of 50 % RH, indicating a negligible change in its sensing response. This is owing to our sensor's high resistance to the presence of the hydroxyl group. Moreover, water vapour is widely recognized for interfering with gas detection by changing a sensor's electrical resistance in a similar way to reducing gas. The great resilience of the sensor films, on the other hand, illustrates the WSe_2 nanoflower sensor's strong reproducibility and stability towards NH_3 gas, especially in humid conditions [23]. Also, it's worth mentioning that only a few studies, particularly for WSe_2 based gas sensors, have documented its anti-humidity characteristics.

In this respect, when compared to prior research works using WSe_2 and other TMDs material, the WSe_2 sensor fabricated in this work, possess relatively high performance (Table 2), with high sensitivity, low LoD, and outstanding tolerance to humidity cross-sensitivity.

Table 1. Comparison of the NO_2, NO, and NOx sensing performance of WSe_2 nanosheets with other sensing materials

2D material	Studied conc.	Working temp. (°C)	Response	LoD (ppm)	Gas detected	Response time	Recovery time	Ref.
WSe_2 NFs	**0.8 ppm**	**100**	**20.5%**	**0.1 (exper.)**	**NO_2**	**196 s**	**2218 s**	**This work**
WSe_2 vertical structure	500 ppm	RT	4.5%	not available	NO	not available	not available	[24]
hybrid WOx/WSe_2	25 ppm	RT	~13%	0.3 (theor.)	NOx	250 s	not available	[25]
WSe_2 nanoscrews	1 ppm	RT	~350%	0.072 (theor.)	NOx	120 s	not available	[26]
WS_2 nanosheets	5 ppm	160	121 %	0.2 (exp.)	NO_2	not available	not available	[27]
WS_2 aerogel	3 ppm	250	0.36 ($\Delta R/R_0$)	8 ppb (theoret.)	NO_2	2 min	14 min	[28]
MoS_2/ graphene	5 ppm	150	1.08/5 ppm	1200 ppb	NO_2	not available	not available	[29]
MoS_2 /rGO hybrid	3 ppm	160	1.29 R_a/R_g	100 ppb	NO_2	8 s	32 s	[30]
WS_2 graphene aerogel	2 ppm	180	3 %	10 ppb (theoret.)	NO_2	100 s	300 s	[31]

NFs: nanoflowers; 5L: 5 layers; ns: nanosheets; conc.: concentration; exper.: experimental; theoret.: theoretical; LoD: limit of detection

Table 2 Ammonia gas sensing characteristics reported in this work are compared with various TMDs materials.

2D material	Studied conc. (ppm)	Working temp. (°C)	Response	LoD (ppm)	Selectivity study	Response time	Recovery time	Ref.
WSe_2 NFs	**40**	**150**	**24.65%**	**2 ppm**	**NO_2, C_6H_6, CO and H_2**	**396 s**	**1917 s**	**This work**
3D WSe_2 on 5L Al_2O_3	50	150	1.3 (Rg/Ra)	not available	NO_2, CO, C_3H_6O	not available	not available	[32]
2D WSe_2 on 5L Al_2O_3	50	150	1.1 (Rg/Ra)	not available	NO_2, CO, C_3H_6O	not available	not available	[32]
MoS_2 ns	10	25	11%	2 ppm	CO and H_2			
WS_2 aerogel	800	250	-0.8 ($\Delta R/R_0$)	13 ppm (theoret.)	H_2 and NO_2	3 min	5 min	[28]
Cu_2S thin films	500	25	19.78 %	Not available	Not available	60 s	90 s	[33]
SnS_2	100	200	7.4%	0.5 ppm	CO_2, H_2, CH_4, ethanol, acetone	40.6	624 s	[34]
Mixed-phase WS_2	100	150	4.72	1 ppm	C_3H_8O, C_6H_5Cl, $C_6H_{12}O_2$, C_2H_5OH, C_7H_8,	19 s	33 s	[35]
WS_2 thin films	5	25	-0.019 % ($\Delta R/ R_0$)	1.2 ppm (theoret.)	Not available	Not available	In-complete	[36]

NFs: nanoflowers; 5L: 5 layers; ns: nanosheets; conc.: concentration exper.: experimental; theoret.: theoretical

3.2.4 Selectivity

One of the most essential criteria in determining a sensor's performance is selectivity. At 150°C, we tested our sensor's selectivity by exposing it to fixed concentrations of various gases such as benzene, carbon monoxide, and hydrogen gas. These gases are also of particular importance since they represent substantial health risks; for example, exposure to 5 ppm of benzene vapours for more than 15 minutes has been linked to the development of cancer [37].

The results in Fig. 12 reveal the WSe_2 nanoflower sensor's selectivity for NH_3 gas, with a maximum response of 24.65 % and minimal responses to benzene and carbon monoxide. In addition to NH_3, the sensor exhibits some small reactivity to hydrogen gas (5%). However, it must be noticed that the hydrogen concentration tested was 20 times higher than the NH_3 concentration. The sensor also responds moderately (14 %) to 0.8 ppm NO_2 gas at 150 °C which could be ascribed to the dual selective nature of the WSe_2 sensor. Although the sensor shows dual selectivity towards NH_3 and NO_2 gas detection, it cannot be denied that the sensor is significantly more sensitive to NH_3 than NO_2 at 150 ºC. In the line of research, functionalization with various nanomaterials can be considered to overcome the existing cross-sensitivity issues and increase the sensor selectivity towards NH_3 gas detection. Moreover, the sensor's high resilience towards humidity cross-sensitivity cannot be neglected. In this respect, these findings could pave a way for the development of WSe_2-based sensors that can operate at lower temperatures with ambient moisture in comparison to traditional metal oxide-based gas sensors.

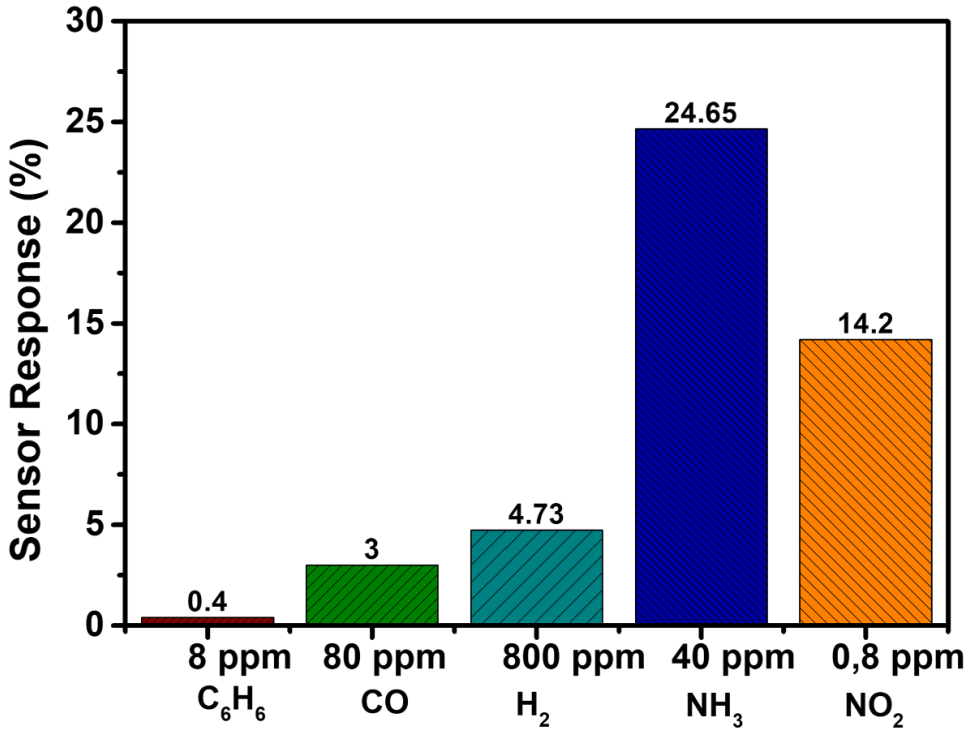

Fig. 12 WSe_2 nanoflower sensor response based on exposure to 8 ppm C_6H_6, 80 ppm CO, 800 ppm H_2, 40 ppm NH_3, and 0.8 ppm NO_2 gas at an operating temperature of 150 °C.

Furthermore, the sensor's stability has been investigated, with the results shown in Fig. 13. The evolution of the baseline resistance and sensor response was studied when NH_3 measurements (40 ppm) were repeated at regular intervals over a prolonged period (4 months).

While the baseline resistance remains stable, the WSe_2 sensor exhibits a substantial downward trajectory with time but also recovered back the original sensing response. The sensor response towards 40 ppm NH_3 gives consistent values for the first 4 months after the initial measurement, but gradually starts decreasing, eventually falling to 16% after four months. However, the baseline resistance of the sensor shows insignificant change and remains stable over the 4 months duration.

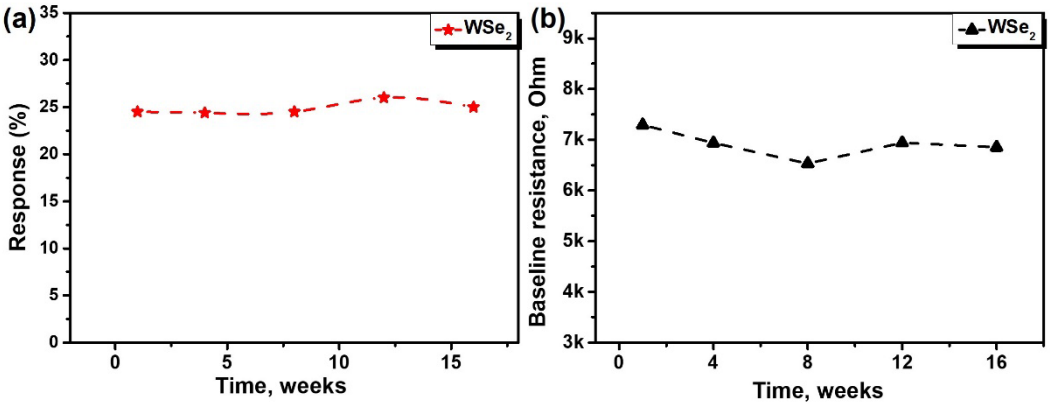

Fig. 13 Long-term stability study. (a) Stability study for WSe_2 sensor towards NH_3 gas over time, (b) evolution of the baseline resistance with time.

4. Gas Sensing Mechanism

A gas sensor´s performance is linked to its sensing mechanism. While in traditional metal oxide-based sensors, their gas sensing mechanism is based on a surface reaction between the analyte gas molecules and pre-adsorbed oxygen ions on the metal-oxide surface. TMD-based gas sensors, on the other hand, depend completely on the adsorption/desorption and charge transfer processes between the target gas and the reactive sites in these materials [36].

The NH_3 gas sensing mechanism of 2D WSe_2 nanoflowers could be illustrated as the physisorption of the NH_3 gas molecules and charge transfer between WSe_2 nanoflowers and NH_3 [9]. As a result of the induced charge transfer the conductance of the material changes. To better understand the sensing mechanism, a concise schematic is illustrated in Fig. 14.

Meanwhile, to fully comprehend the gas sensing mechanism, the presence of oxygen in ambient air cannot be neglected, as it is one of the prominent absorbates during the gas sensing measurements [18] [38]Therefore, the gas sensing mechanism of a 2H variant of WSe_2 is based on two consecutive reactions occurring at the WSe_2 surface. Initially, when the sensor is exposed to dry synthetic air, oxygen molecules are adsorbed on the exposed surface [18]. From literature, it is well known that the adsorbed oxygen species exists as O_2^- (<150 ºC), O^-

(150-400 ºC) and O^{2-} (>400 ºC) [39]. Since all the gas sensing measurements are performed at and below 150 ºC (owing to the thermal degradation of WSe_2 material at temperature above 200 ºC) the adsorbed oxygen molecule is equivalent to O_2^-. The as-adsorbed oxygen molecule results into extraction of electrons from the valence band of WSe_2 which results in the formation of a hole accumulation region (HAR) near the valence band, as shown in Fig. 15a. The reaction can be represented by the following equation.

$$O_2^- \rightarrow O_2^- + h^+ \quad (1)$$

Afterwards, when the sensor is exposed to NH_3 gas, the spontaneously adsorbed nucleophilic molecules donate electrons to the WSe_2 surface as well as it may react to the pre-adsorbed oxygen species present at the surface, resulting in the formation of free electrons. The free electrons that are released during the reaction combine with holes present in the valence band thereby reducing the concentration of holes and subsequently increasing the resistivity of the sensor (as shown in Fig. 8). As, a result, the concentration of holes in the HAR region is reduced (Fig. 15b). The p-type semiconductor behaviour of WSe_2 nanoflowers could be described by the following equation [40]:

$$4NH_{3(ads)} + 3O_2^- \rightarrow N_2 + 6H_2O + 3e^- \quad (2)$$

As the NH_3 gas concentration is further increased, the electron density increases leading to the high resistivity of the sensor, resulting in much higher sensitivity of the sensor towards increasing gas concentrations (as shown in Fig. 10b and c). Furthermore, when the gas is removed and the sensor is exposed only to dry air at room temperature, there is an inadequate recovery of the WSe_2 sensor due to the difficulties in desorption of these gas molecules at room temperature. However, mild heating of the sensor at 150°C resulted in complete baseline recovery while the recovery time was larger.

Contrary to this, when the sensor is exposed to NO_2 molecules, an opposite behaviour is seen owing to the oxidising nature of NO_2 gas. Because NO_2 molecules are electrophilic, they extract electrons from the valence band of 2D WSe_2 nanoflowers, causing electron deficit and a rise in hole concentration (Fig. 15c). Consequently, the electrical conductance of the material increases, thereby resulting in a decrease in the sensor´s resistance, as shown in Fig. 6 (where the baseline resistance of the WSe_2 nanoflower decreases when exposed to NO_2 gas). Similar to NH_3, NO_2 gas molecules might as well interact with the preabsorbed oxygen species at the WSe_2 surface resulting in the formation of NO_3^-. The reactions occurring at the surface of WSe_2 can be described by the following equations [18] :

$$O_2^- \rightarrow O_2^- + h^+ \quad (1)$$

$$NO_2 \rightarrow NO_2^- + h^+ \quad (2)$$

$$NO_2 + O_2^- \rightarrow NO_3^- + 2O^- + h^+ \quad (3)$$

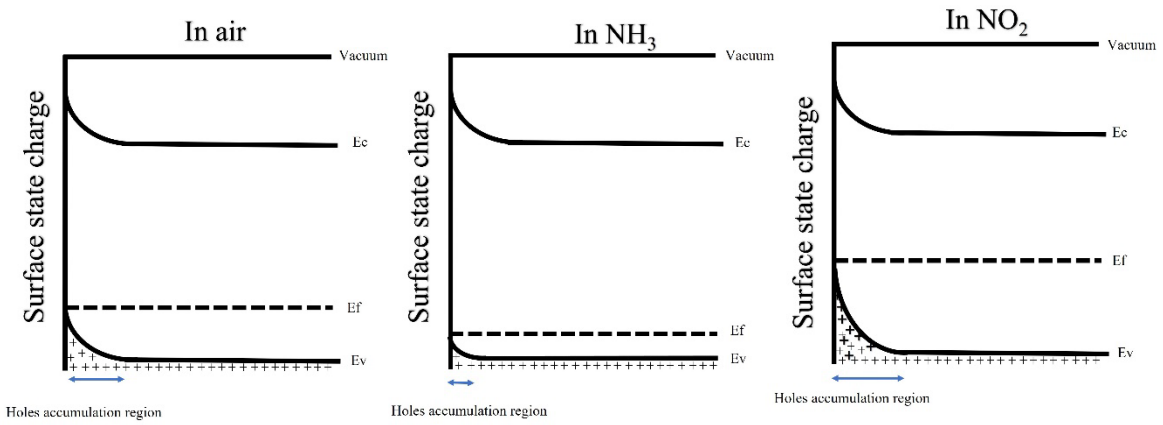

Fig. 15 Energy band diagram of 2H WSe_2 demonstration (a) reaction in air, (b) on reaction with NH_3 gas, (c) on reaction with NO_2 gas, where Ec is the conduction band, Ef is the fermi level and Ev is the valence band.

Furthermore, both edge atoms and in-plane defects of WSe_2 have previously been demonstrated to be active sites for molecule adsorption, resulting in providing additional surface area for gas adsorption, thereby enhancing the overall gas sensing. Moreover, these reactions are particularly prevalent at the 2H defect sites, mainly at the Se vacancies. These vacancies contribute to the carrier charge transfer on the TMDs surface and play a crucial role in the gas sensing mechanism since prior research has shown that adsorption of NO_2 molecules is impossible without Se vacancies[41]. This is further supported by the DFT theories, which demonstrated that in the absence of disulphide vacancies, the adsorption of N_2 molecules on MoS_2 is low [42]. Despite the lack of research in the case of WSe_2, current studies on MoS_2 suggest that sulphur vacancies are one of the major defects in MoS_2 due to their low formation energy.

Gas sensing might also benefit from the active sites on the edges of these 2D materials. The 2D morphology of the WSe_2 nanoflowers that are attached to the 1D WSe_2 nanowires plays a significant role in providing a high surface area for the adsorption of these gaseous molecules (NO_2 and NH_3). Similar reports in the literature have revealed enhanced gas sensing characteristics of vertically distributed MoS_2 nanostructures supported by vertically arranged carbon nanotubes in comparison to horizontally arranged MoS_2 [43] . Moreover, in our previous studies, we have reported enhanced gas sensing properties of 2D assemblies of WS_2

nanoflowers on 1D nanowires in comparison to the more closely packed nanoflake assembly [1]

Conclusions

We used an atmospheric pressure CVD approach to demonstrate a simple, effective, and high-yield synthesis process to obtain WSe_2 films. The morphology of as-grown WSe_2 is nanoflowers, which are composed of highly crystalline vertically aligned nanoplatelets. Furthermore, the synthesis approach is scalable and enables the direct growth of nanostructured material over functional substrates. The as-grown material is used to develop a chemoresistive type gas sensor having dual sensitivity towards NH_3 and NO_2 gas detection, depending on the operating temperature used. To the best of our knowledge, no previous research on WSe_2-based gas sensors has yielded such intriguing results. Moreover, the cross-sensitivity test revealed that H_2, C_6H_6, and CO have a negligible effect on NH_3 gas detection while the presence of NO_2 molecules shows some cross-sensitivity which could be assigned to the dual sensitive nature of the WSe_2 films. Moreover, water vapour at 50% relative humidity also resulted in having no interference to the measure of NH_3 gas, attesting to promising characteristics of WSe_2 for gas sensing applications. Henceforth, we believe the results obtained in this study at moderate temperature are intriguing and can provide a useful conceptual framework for detecting low concentrations of NH_3 in the real environment.

Acknowledgements

Funded in part by the Marie Skłodowska-Curie Actions (MSCA) Research and Innovation Staff Exchange (RISE) H2020-MSCA-RISE- 2018- 823895 ‘SENSOFT’, by MICINN and FEDER grant no. RTI2018- 101580-I00 and AGAUR grant no. 2017 SGR 418. A.A. is supported by a COFUND project the European Union’s Horizon 2020 research and innovation program under the Marie Skłodowska Curie grant agreement No. 713679 and the Universitat Rovira I Virgili (URV). JFC is Senior Research Associate of the national funds for Scientific Research (FRS-FNRS, Belgium). E.L. is supported by the Catalan Institute for advanced studies (ICREA) via the 2018 Edition of the ICREA Academia Award. The technological SIAM (Synthesis, Irradiation and Analysis of Materials) and Morph-IM platforms from the UNamur are acknowledged for XPS and electron microscopy analysis.

References

[1] A. Alagh *et al.*, "CVD growth of self-assembled 2D and 1D WS2 nanomaterials for the ultrasensitive detection of NO2," *Sensors and Actuators, B: Chemical*, vol. 326, no. April 2020, p. 128813, 2021, doi: 10.1016/j.snb.2020.128813.

[2] A. Alagh, F. E. Annanouch, J. F. Colomer, and E. Llobet, "3D assembly of WS 2 nanomaterial for H 2 S gas sensing application," vol. 6, pp. 2–5.

[3] A. Sierra-Castillo, E. Haye, S. Acosta, C. Bittencourt, and J. F. Colomer, "Synthesis and characterization of highly crystalline vertically aligned WSe2 nanosheets," *Applied Sciences (Switzerland)*, vol. 10, no. 3, 2020, doi: 10.3390/app10030874.

[4] G. Greczynski and L. Hultman, "X-ray photoelectron spectroscopy: Towards reliable binding energy referencing," *Progress in Materials Science*, vol. 107, no. April 2019, p. 100591, 2020, doi: 10.1016/j.pmatsci.2019.100591.

[5] G. Greczynski and L. Hultman, "Compromising Science by Ignorant Instrument Calibration—Need to Revisit Half a Century of Published XPS Data," *Angewandte Chemie - International Edition*, vol. 59, no. 13, pp. 5002–5006, 2020, doi: 10.1002/anie.201916000.

[6] M. R. Linford *et al.*, "Proliferation of Faulty Materials Data Analysis in the Literature," *Microscopy and Microanalysis*, no. May, pp. 1–2, 2019, doi: 10.1017/S1431927619015332.

[7] J.-K. Huang *et al.*, "Large-Area Synthesis of Highly," *ACS Nano*, vol. 8, no. 1, pp. 923–930, 2014.

[8] B. Liu, M. Fathi, L. Chen, A. Abbas, Y. Ma, and C. Zhou, "Chemical Vapor Deposition Growth of Monolayer WSe2 with Tunable Device Characteristics and Growth Mechanism Study," *ACS Nano*, vol. 9, no. 6, pp. 6119–6127, 2015, doi: 10.1021/acsnano.5b01301.

[9] B. Li *et al.*, "Enhanced dimethyl methylphosphonate detection based on two-dimensional WSe2nanosheets at room temperature," *Analyst*, vol. 145, no. 24, pp. 8059–8067, 2020, doi: 10.1039/d0an01671c.

[10] P. Tonndorf *et al.*, "Photoluminescence emission and Raman response of monolayer MoS_2, MoSe_2, and WSe_2," *Optics Express*, vol. 21, no. 4, p. 4908, 2013, doi: 10.1364/oe.21.004908.

[11] A. Alagh, F. E. Annanouch, and E. Llobet, "Enhanced gas sensing characteristics of metal doped WS 2 nanoflowers," no. Cvd, pp. 21–24, 2021.

[12] D. Barreca, G. Carta, A. Gasparotto, G. Rossetto, E. Tondello, and P. Zanella, "A Study of Nanophase Tungsten Oxides Thin Films by XPS," *Surface Science Spectra*, vol. 8, no. 4, pp. 258–267, 2001, doi: 10.1116/11.20020801.

[13] M. S. Sokolikova, P. C. Sherrell, P. Palczynski, V. L. Bemmer, and C. Mattevi, "Direct solution-phase synthesis of 1T' WSe 2 nanosheets," *Nature Communications*, vol. 10, no. 1, 2019, doi: 10.1038/s41467-019-08594-3.

[14] P. C. Wu, C. L. Yang, Y. Du, and C. H. Lai, "Scalable Epitaxial Growth of WSe2 Thin Films on SiO2/Si via a Self-Assembled PtSe2 Buffer Layer," *Scientific Reports*, vol. 9, no. 1, pp. 1–10, 2019, doi: 10.1038/s41598-019-44518-3.

[15] J. R. Shallenberger, "2D tungsten diselenide analyzed by XPS," *Surface Science Spectra*, vol. 25, no. 1, p. 014001, 2018, doi: 10.1116/1.5016189.

[16] A. Sierra-Castillo, E. Haye, S. Acosta, C. Bittencourt, and J. F. Colomer, "Synthesis and characterization of highly crystalline vertically aligned WSe2 nanosheets," *Applied Sciences (Switzerland)*, vol. 10, no. 3, 2020, doi: 10.3390/app10030874.

[17] A. Alagh *et al.*, "CVD growth of self-assembled 2D and 1D WS2 nanomaterials for the ultrasensitive detection of NO2," *Sensors and Actuators, B: Chemical*, vol. 326, no. August 2020, p. 128813, 2021, doi: 10.1016/j.snb.2020.128813.

[18] A. Moumen *et al.*, "Robust Room-Temperature NO2Sensors from Exfoliated 2D Few-Layered CVD-Grown Bulk Tungsten Di-selenide (2H-WSe2)," *ACS Applied Materials and Interfaces*, vol. 13, no. 3, pp. 4316–4329, 2021, doi: 10.1021/acsami.0c17924.

[19] V. Paolucci, S. M. Emamjomeh, M. Nardone, L. Ottaviano, and C. Cantalini, "Two-step exfoliation of WS2 for NO2, H2 and humidity sensing applications," *Nanomaterials*, vol. 9, no. 10, pp. 1–17, 2019, doi: 10.3390/nano9101363.

[20] D. Liu, Z. Tang, and Z. Zhang, "Comparative study on NO2 and H2S sensing mechanisms of gas sensors based on WS2 nanosheets," *Sensors and Actuators, B: Chemical*, vol. 303, no. 2, p. 127114, 2020, doi: 10.1016/j.snb.2019.127114.

[21] A. Moumen *et al.*, "Robust Room-Temperature NO2Sensors from Exfoliated 2D Few-Layered CVD-Grown Bulk Tungsten Di-selenide (2H-WSe2)," *ACS Applied Materials and Interfaces*, vol. 13, no. 3, pp. 4316–4329, 2021, doi: 10.1021/acsami.0c17924.

[22] B. Timmer, W. Olthuis, and A. van den Berg, "Ammonia sensors and their applications - A review," *Sensors and Actuators, B: Chemical*, vol. 107, no. 2, pp. 666–677, 2005, doi: 10.1016/j.snb.2004.11.054.

[23] X. Li, X. Li, Z. Li, J. Wang, and J. Zhang, "WS2 nanoflakes based selective ammonia sensors at room temperature," *Sensors and Actuators, B: Chemical*, vol. 240, pp. 273–277, 2017, doi: 10.1016/j.snb.2016.08.163.

[24] Y. Z. Chen *et al.*, "Low-Temperature and Ultrafast Synthesis of Patternable Few-Layer Transition Metal Dichacogenides with Controllable Stacking Alignment by a Microwave-Assisted Selenization Process," *Chemistry of Materials*, vol. 28, no. 4, pp. 1147–1154, 2016, doi: 10.1021/acs.chemmater.5b04579.

[25] H. Medina *et al.*, "Wafer-Scale Growth of WSe2 Monolayers Toward Phase-Engineered Hybrid WOx/WSe2 Films with Sub-ppb NOx Gas Sensing by a Low-Temperature Plasma-Assisted Selenization Process," *Chemistry of Materials*, vol. 29, no. 4, pp. 1587–1598, 2017, doi: 10.1021/acs.chemmater.6b04467.

[26] Y. Z. Chen, S. H. Lee, T. Y. Su, S. C. Wu, P. J. Chen, and Y. L. Chueh, "Phase-modulated 3D-hierarchical 1T/2H WSe2 nanoscrews by a plasma-assisted selenization process as high performance NO gas sensors with a ppb-level detection limit," *Journal of Materials Chemistry A*, vol. 7, no. 39, pp. 22314–22322, 2019, doi: 10.1039/c9ta05348d.

[27] D. Liu, Z. Tang, and Z. Zhang, "Comparative study on NO2 and H2S sensing mechanisms of gas sensors based on WS2 nanosheets," *Sensors and Actuators, B: Chemical*, vol. 303, no. 2, p. 127114, 2020, doi: 10.1016/j.snb.2019.127114.

[28] W. Yan *et al.*, "Conductometric gas sensing behavior of WS2 aerogel," *FlatChem*, vol. 5, pp. 1–8, 2017, doi: 10.1016/j.flatc.2017.08.003.

[29] B. Cho *et al.*, "Chemical Sensing of 2D Graphene/MoS2 Heterostructure device," *ACS Applied Materials and Interfaces*, vol. 7, no. 30, pp. 16775–16780, 2015, doi: 10.1021/acsami.5b04541.

[30] Z. Wang *et al.*, "Rational synthesis of molybdenum disulfide nanoparticles decorated reduced graphene oxide hybrids and their application for high-performance NO2 sensing," *Sensors and Actuators, B: Chemical*, vol. 260, no. 2, pp. 508–518, 2018, doi: 10.1016/j.snb.2017.12.181.

[31] W. Yan, M. A. Worsley, T. Pham, A. Zettl, C. Carraro, and R. Maboudian, "Effects of ambient humidity and temperature on the NO 2 sensing characteristics of WS 2 /graphene aerogel," *Applied Surface Science*, vol. 450, pp. 372–379, 2018, doi: 10.1016/j.apsusc.2018.04.185.

[32] M. J. Kang *et al.*, "Atomic-Layered Tungsten Diselenide-Based Porous 3D Architecturing for Highly Sensitive Chemical Sensors," *Physica Status Solidi - Rapid Research Letters*, vol. 13, no. 12. 2019. doi: 10.1002/pssr.201900340.

[33] M. S. Shinde, D. R. Patil, and R. S. Patil, "Ammonia gas sensing property of nanocrystalline Cu2S thin films," *Indian Journal of Pure and Applied Physics*, vol. 51, no. 10, pp. 713–716, 2013.

[34] Y. Xiong *et al.*, "Ultra-sensitive NH3 sensor based on flower-shaped SnS2 nanostructures with sub-ppm detection ability," *Journal of Hazardous Materials*, vol. 341, pp. 159–167, 2018, doi: 10.1016/j.jhazmat.2017.07.060.

[35] F. Meng, T. Zhu, Z. Yuan, W. Qin, H. Gao, and H. Zhang, "Investigation of Mixed-Phase WS2Nanomaterials for Ammonia Gas Sensing," *IEEE Sensors Journal*, vol. 21, no. 6, pp. 7268–7274, 2021, doi: 10.1109/JSEN.2021.3050145.

[36] M. O'Brien *et al.*, "Plasma assisted synthesis of WS2 for gas sensing applications," *Chemical Physics Letters*, vol. 615, pp. 6–10, 2014, doi: 10.1016/j.cplett.2014.09.051.

[37] P. F. Infante, "Benzene: A historical perspective on the American and European occupational setting," *The Precautionary Principle in the 20th Century: Late Lessons from Early Warnings*, pp. 35–48, 2013.

[38] D. Burman, H. Raha, B. Manna, P. Pramanik, and P. K. Guha, "Substitutional Doping of MoS2for Superior Gas-Sensing Applications: A Proof of Concept," *ACS Sensors*, vol. 6, no. 9, pp. 3398–3408, 2021, doi: 10.1021/acssensors.1c01258.

[39] F. E. Annanouch *et al.*, "Aerosol-assisted CVD-grown WO3 nanoneedles decorated with copper oxide nanoparticles for the selective and humidity-resilient detection of H2S," *ACS Applied Materials and Interfaces*, vol. 7, no. 12, pp. 6842–6851, 2015, doi: 10.1021/acsami.5b00411.

[40] A. Moumen, G. C. W. Kumarage, and E. Comini, "P-Type Metal Oxide Semiconductor Thin Films: Synthesis and Chemical Sensor Applications," *Sensors*, vol. 22, no. 4, 2022, doi: 10.3390/s22041359.

[41] P. Zhao *et al.*, "Air Stable p - Doping of WSe 2 by," *ACS Applied Materials and Interfaces*, no. 10, pp. 10808–10814, 2014.

[42] S. Tongay *et al.*, "Defects activated photoluminescence in two-dimensional semiconductors: Interplay between bound, charged, and free excitons," *Scientific Reports*, vol. 3, pp. 1–5, 2013, doi: 10.1038/srep02657.

[43] S. Y. Cho *et al.*, "Highly Enhanced Gas Adsorption Properties in Vertically Aligned MoS2 Layers," *ACS Nano*, vol. 9, no. 9, pp. 9314–9321, 2015, doi: 10.1021/acsnano.5b04504.

Chapter-6

Controlled Growth of 3D Assemblies of Edge Enriched Multilayer MoS_2 Nanosheets for dually selective NH_3 and NO_2 gas sensors

Controlled Growth of 3D Assemblies of Edge Enriched Multilayer MoS_2 Nanosheets for Dually Selective NH_3 and NO_2 Gas Sensors

Fatima Ezahra Annanouch [1*], Aanchal Alagh [1], Polona Umek [2], Juan Casanova-Chafer [1], Carla Bittencourt [3] and Eduard Llobet [1]

[1] Departament d'Enginyeria Electronica, Universitat Rovira i Virgili, avenida Països Catalans 26, 43007 Tarragona, Spain.

[2] Department of Solid-State Physics, Jozef Stefan Institute, Jamova cesta 39, 1000 Ljubljana, Slovenia.

[3] Laboratory of Plasma-Surface Interaction Chemistry (PSI Chem), University of Mons, Av. Nicolas Copernic 1, 7000 Mons, Belgium.

Corresponding author

*Fatima Ezahra Annanouch: fatimaezahra.annanouch@urv.cat

Abstract

Herein, we report on the successful controlled growth of edge enriched 3D assemblies of MoS_2 nanosheets by adjusting the gas flow rate, during atmospheric pressure CVD deposition. The results revealed that 30 ml/min was the optimal flow rate, in which the growth direction shifts from in-plane nanosheets to out-of-plane 3D assemblies of MoS_2 nanosheets. It is suggested that at this flow rate, we have an ideal tradeoff between the surface interaction and the mass transport of precursor molecules. Morphological, structural and chemical composition analysis showed the formation of vertically oriented MoS_2 nanosheets with MoO_{3-x} impurities, resulting from the incomplete sulfurization during the synthesis. Based on the morphological evolution of the studied material, the growth mechanism was explored. Gas sensing properties of the as grown films were tested against NH_3 and NO_2. They exhibited stable and reproducible responses with excellent sensitivity to ppm-level NH_3 (20 % response to 2 ppm) and to ppb-level NO_2 (11% response to 20 ppb). Additionally, this nanomaterial showed dual selectivity towards NH_3 at room temperature and NO_2 at 100 ºC. To the best of our knowledge, none of the reported works on MoS_2 based gas sensor have described this dual selectivity. The experimental detection limit for NH_3 was below 2 ppm while it was lower than 20 ppb for NO_2. Besides, the vertical growth of edge enriched MoS_2 bestows sensors with notable resilience against high levels of ambient humidity. Sensor response was only slightly increased (R=70 %) in a humid ambient compared to a dry background (R= 65 %) when measuring 800 ppb of NO_2. Therefore, this paper shows for the first time that by adjusting flow rate it is possible to tune the morphology of AP-CVD grown

MoS_2 for achieving a 3D sponge-like assembly of nanoflakes, showing high sensitivity to NO_2 and NH_3, and low humidity cross-sensitivity. In addition, the nanomaterial can be made quite specific for detecting NO_2 or NH_3 by selecting its operating temperature.

Keywords: TMDs; gas sensors; MoS_2; APCVD; 3D assemblies; dual selectivity.

Introduction

Graphene with its hexagonal lattice structure was the first two dimensional (2D) material that fascinated researchers and scientists, thanks to its unique properties and broad relevant applications.[1,2] In contrast to conventional gas sensors based on MOX nanostructures,[3,4] graphene offers some advantages as large specific surface area (i.e., atomically 2D form), high conductivity, moderate operating temperatures, and low electrical noise.[5,6] Its lack of band gap, however, prevents this material from showing semiconducting properties.[3,7] This shortcoming is relevant for developing chemoresistive gas sensors and has inspired researchers to move towards others atomically layered 2D semiconductor materials with assigned band gap. Among the 2D materials which have been identified and investigated for gas sensing application, we find tin sulfide (SnS_2), molybdenum selenide ($MoSe_2$), tungsten disulfide (WS_2), molybdenum disulfide (MoS_2), phosphorene and tellurene, only to cite a few.[8–15]

Molybdenum disulfide belongs to the family of transition metal dichalcogenide materials (TMDs) in which molecular layers are stacked together by van der wall forces. It is an *n-type* semiconductor with a band gap ranging from 1.2 eV for bulk MoS_2 (indirect band gap) to 1.83 eV for monolayer MoS_2 (direct and wider band gap).[16] Indeed, the bandgap of TMDs materials depends on the number of their atomic layers, which opens different possibilities for their application in various fields such as optoelectronics[17], solar cells[18], photocatalysis and gas sensors. [19] It was reported that high quality monolayer fit well with FET devices, whereas few layer TMDs are suitable for gas sensing applications. Babar and co-workers found that bilayer and hetero-bilayer MoS_2 and WS_2 showed improved gas sensing performances compared to their monolayers.[20] Late and co-workers showed that few layer MoS_2 exhibited excellent sensing performances towards NO_2, NH_3 and humidity, compared to MoS_2 single layer.[21] Additionally, obtaining a continuous monolayer is very challenging, most reports describe the synthesis of discontinue monolayer domains dispersed on top of the substrate.[22–24] This non-continuity is a drawback for their use in chemoresitive transduction schemes in gas sensing applications.

Recently, the three-dimensional (3D) assembly of multilayer TMDs nanosheets has attracted the attention of many researchers, since the gas adsorption at the edge sites of the TMDs nanosheets is more significant than at their basal plane, thus enhancing sensitivity as well as selectivity. [25–27] In the case of MoS_2, its basal plane is most of the times used as chemical receptor,

because it is easy to expose and to produce using exfoliation or chemical vapor deposition techniques. However, this basal plane surface has minimal dangling bonds, and due to thermodynamic forces, it is difficult to expose their edge sites to the environment [28,29]. In contrast, in 3D MoS_2 nanosheets, the edge sites have a local stoichiometry with physical and electronic properties that make them more exposed. Moreover, the vertical nanosheets are formed by the (002) plane, which usually ends with the predominance of either exposed molybdenum atoms or exposed sulfur atoms.[30,31] Cho and coworkers reported highly enhanced gas adsorption properties in vertically aligned MoS_2 layers.[28] They found about 5-fold enhanced sensitivity to NO_2 gas molecules compared to horizontally aligned MoS_2 films. This finding was corroborated by density functional theory (DFT) calculations. Lee and co-workers showed that the addition of active edge sites enhances the surface-to-mass ratio and the resulting gas-sensing properties.[25] Agrawal and co-workers reported that the total surface free energy of MoS_2 rises by increasing the density of the edge sites, which enhances the catalytic activity of MoS_2 material.[26] Therefore, it is essential to develop 3D assemblies of edge enriched MoS_2 networks rather than in-plane MoS_2 lattice geometries for the fabrication of highly sensitive gas sensors. The most reported techniques that are used for such growth are: hydrothermal and atmospheric pressure CVD (APCVD).[32–36] Using hydrothermal method to synthesize MoS_2 nanosheets needs hazardous precursors such as molybdenum chloride, which can release harmful chloride vapors. Moreover, it involves a many step fabrication process and thus, is a time- consuming technique. Conversely, in APCVD technique, we need sulfur and molybdenum precursor sources. The deposition occurs in a single step, at atmospheric pressure without the assistance of hydrogen, in a self-catalyzed process. It has a large yield with a direct deposition onto the sensor substrate. Additionally, it is a catalyst free technique.

In the literature, there are few reports on 3D assemblies of edge enriched MoS_2 nanosheets for gas sensing applications. For instance, Agrawal and co-workers presented photoactivated mixed in-plane and edge-enriched p-type MoS_2 flake-based NO_2 sensor working at room temperature.[33] There, the vertical flakes were not interconnected between them, there were more in-plane flakes rather than edge enriched vertical ones. Moreover, the sensors were assisted by UV light and the NO_2 concentrations tested were very high, ranging from 10 to 500 ppm. Jaiswal and co-workers reported vertically aligned edge-oriented MoS_2 nanostructured thin films functionalized by Pd nanoparticles for gas sensing applications.[37] These films were deposited via a single step dc-magnetron sputtering technique. Their morphology was characterized by a continuous porous film with dispersed grains and absence of a multilayer MoS_2 nanosheet network. Besides, the fabricated sensor showed low sensitivity against very high concentrations of NH_3 and NO_2 gases, at room temperature. The responses were 2.5 % and 5 % against 500 ppm of NH_3 and NO_2 respectively. Hang and coworkers studied the controlled growth of vertically

oriented three-layer MoS_2 nanoflakes for room-temperature NO_2 gas sensor applications.[38] The density and the thickness of MoS_2 nanosheets were controlled by varying the heating rate of a CVD process conducted under vacuum. The fabricated sensors displayed a good sensitivity and selectivity towards NO_2. The response towards 0.5 ppm NO_2 at room temperature was 20.1%. However, the effect of ambient humidity cross-sensitivity was not studied.

In this paper we report for the first time a successful controlled growth of, large scale, 3D assemblies of edge enriched MoS_2 nanosheets using a single step atmospheric pressure CVD method for the fabrication of dually selective NH_3 and NO_2 gas sensors. During the depositions, no hydrogen assistance was used. The films were obtained by controlling the argon gas flow rate during the APCVD process. In addition, they were directly grown on the sensor substrate without the need of further fabrication steps or seeding with noble metals. Moreover, an extensive material characterization study of the as grown nanostructured films was performed by using FE-SEM to analyze the morphology, XRD and Raman spectroscopy to verify the structure, and XPS and HRTEM to identify the chemical composition. Besides to this, the growth mechanism was thoroughly studied by analyzing the morphology evolution of the 3D assembly of MoS_2 nanosheets, which is not often reported in the literature. The gas sensing performance of the synthesized films were tested against low concentrations of NH_3 and NO_2 (at concentrations under the threshold limits defined for health safety standards). Sensors were operated at room temperature and at 100 ºC and tested under dry and humid (50% R.H.) conditions. Sensors showed high sensitivity with dual selectivity behavior. Namely they were selective to NH_3 when operated at room temperature and to NO_2 when operated at 100 ºC. It is worth noting that reports on MoS_2 based gas sensor have never reported such advantageous dual selectivity towards two different pollutant gases.

Experimental section

Material synthesis:

The atmospheric pressure CVD (APCVD) method was employed to grow edge enriched 3D assemblies of MoS_2 nanosheets. As it is shown in Fig. S1. a, the system was composed of a quartz tube-in-tube growth chamber, a heating belt and a CVD furnace. The small quartz tube has a diameter of 15 mm while the large tube is 38 mm in diameter. Before starting the synthesis, the substrate (SiO_2, 300 nm) was cleaned with acetone (30 min), isopropanol (30 min) and distilled water. Then, it was dried with air, placed vertically in a homemade ceramic support and then pushed inside the CVD furnace. MoO_3 powder (25 mg, 99.97 %, Sigma-Aldrich) and sulfur powder (700 mg, 99.97 %, Sigma-Aldrich) were loaded separately in two ceramic boats and located in distinct zones (heating belt and CVD furnace) in order to provide independent temperature control. The distance between MoO_3 and the S was 25 cm while the distance between MoO_3 and the substrate was 5 cm. The APCVD synthesis procedure was composed of five steps:

1) the growth chamber (tube-in-tube) was flushed with argon (500 ml/ min) during 30 min in order to remove oxygen molecules; 2) the furnace was ramped to 850 ºC with an Ar flow of 100 ml/ min; 3) once the furnace reached 500 ºC, the heating belt (200 ºC) was powered on, and the sulfur began to evaporate (Fig. S1.b); 4) when the temperature of the furnace reached 850 ºC, the Ar flow was modified and set according to the different growth conditions (10, 30 or 70 ml/ min) during 60 min; 5) the furnace was left to cool down while the heating belt was kept ON, to provide a sufficiently sulfur rich atmosphere, thus avoiding the oxidation of the film deposited.

Material characterization techniques:

The morphology of the prepared samples was analyzed by scanning electron microscopy (SEM-FET quanta 600) coupled with a field-emission scanning electron microscope (FESEM) Hitachi 2000 and FEI Helios Nanolab 650. The crystal structure at the atomic level was studied by high-resolution transmission electron microscopy (HRTEM) (Jeol, JEM-2100) and X-ray diffraction using a Bruker-AXS D8-Discover diffractometer equipped with a parallel incident beam (Gober mirror), vertical XYZ motorized stage and with a GADDS (General Area Diffraction System). The elemental and chemical analysis have been performed via X-ray photoelectron spectroscopy (XPS) using a versaprobe PHI5000 spectrometer (equipped with a monochromatic Al Kα X-ray source). For data analysis, the CASA XPS software was used. The Raman spectra were obtained using a Renishaw in Via, laser 514 nm, ion argon-Novatech, 25 mW.

Gas sensing measurements

Gas sensing measurements were performed in a Teflon chamber with a volume of 35 ml. The test chamber has an inlet and an outlet, and connectors for housing up to four sensors at the same time. The inlet was connected to the gas delivery system and the outlet was connected to the exhaust. Regarding the sensors, they were fabricated in our lab by connecting two platinum wires to the growth substrate using silver paste as depicted in Fig.S2. Besides to this, the substrate was glued to a ceramic hotplate that comprised a platinum resistive heater, using a conductive epoxy. This allowed raising the operating temperature above room temperature when needed. Finally, the whole device was wire-bonded to a PCB that could be plugged inside the test chamber. The sensor responses were obtained by monitoring the sensing film resistance using an Agilent-34972A multimeter. To acquire the target concentration, calibrated cylinders of either nitrogen dioxide (total concentration, 1 ppm), Ammonia (total concentration, 100 ppm), hydrogen (total concentration, 1000 ppm) and carbon monoxide (total concentration, 100 ppm) were mixed with pure synthetic air by means of Bronkhorst mass-flow controllers and associated software. The total flow rate was kept constant at 100 ml/ min during all the experiments. The exposure time to the target gas was fixed to 10 min, while duration of the cleaning phase (dry air) was adapted to the sensor operating temperature. It was 50 min for measurements performed at 100 ºC and 120

min for the ones realized at room temperature. For calibrating the sensors, we expose them to dry air during 4 hours before each cycling measurements and during 1 night before measuring a new gas. This calibration is needed in order to reach the initial baseline resistance and to clean the sensor surface as well as the chamber. Moreover, humidity measurements were conducted by introducing 50 % of relative humidity during the hole gas cycling measurements. The sensor response was calculated by using (Eq.1) for reducing species and by (Eq. 2) for oxidizing ones. Additionally, the response and recovery time are defined as the time required to reach 90% of the total changes in resistance in the case of detection and recovery phases, respectively.

$$\frac{(Rair-Rgas)*100}{Rair} \quad \text{(Eq. 1)}$$

$$\frac{(Rgas-Rair)*100}{Rair} \quad \text{(Eq. 2)}$$

Results and discussion

Material characterization

MoS_2 nanostructured thin films were synthesized at 850 °C using a tube-in-tube, hydrogen free APCVD method. Samples were directly grown on a 300 nm thick SiO_2 on Si substrates (1 × 2 cm^2) without any further fabrication step. This configuration (tube-in-tube) leads to stable provision of both gaseous precursors to the reaction area, near the substrate, during the whole deposition. Additionally, it allowed us to avoid the quenching and gradual sulfurization of MoO_3 caused by sublimated sulfur. The films were grown under three different carrier gas (Ar) flow rate conditions: 10, 30 and 70 ml/min and were labelled as: MoS_2-10, MoS_2-30 and MoS_2-70, respectively. Fig. 1 depicts the FE-SEM images obtained from the three samples. It is clear that the flow rate significantly affected the obtained morphologies. At 10 ml/min of argon gas, we achieved sparse multilayer MoS_2 nanotriangles dispersed all over the substrate (Fig. 1.a). Each one, consisted of several nanotriangles deposited on top of each other, forming a pyramidal shape. More images are provided in the SI Fig.S3. When the argon gas flow rate was increased to 30 ml/min, the morphology was changed from in plane MoS_2 nanotriangles to out-of-plane, edge enriched 3D assemblies of MoS_2 nanosheets (Fig.1.b). The film was continuous (Fig.S4), completely coating the substrate area. The size of the nanosheets was not completely homogeneous, they were longer in the center of the substrate while they grew shorter at the borders. A further increase in the argon gas flow rate, (70 ml/ min) generated another change in the morphology of the samples. From Fig. 1.c we can observe a continuous layer of 2D quadrilateral nanostructures with different size, deposited randomly over the substrate. Based on the literature, at low gas flow rate (10 ml/ min), the mass transport of the precursor species limits the amount of the deposited nuclei onto the substrate active sites. In this reaction, the crystals growth is carried out by thermodynamics regime where the surface chemical reaction rate is proportional to the carrier gas flow rate and the deposited nuclei are grown laterally to form

nanotriangles. At 30 ml/ min, the direction growth becomes out-plan and the crystal growth changes from thermodynamics regime to kinetics one. This case of growth is further studied and illustrated in growth mechanism section.

At high gas flow rate (70 ml/ min), an overdose of the precursors species arrived to the substrate active sites, outperforming the rate-ability of the surface reaction that could occur at the deposition temperature (850 °C), leading in gas phase reactions before reaching the substrate sites and depositing nanoflakes at the surface of the substrate. Herein, the CVD deposition is controlled by a surface reaction. [39–41]

Therefore, at 30 ml/ min of argon, we have a perfect fit between the surface interaction and the mass transport of precursor molecules, resulting in a suitable morphology for gas sensor fabrication. In fact, it offers a large surface area to volume ratio with enriched exposed edge sites, has plenty of voids for gas diffusion, and has many defects that make it highly reactive with gas molecules.

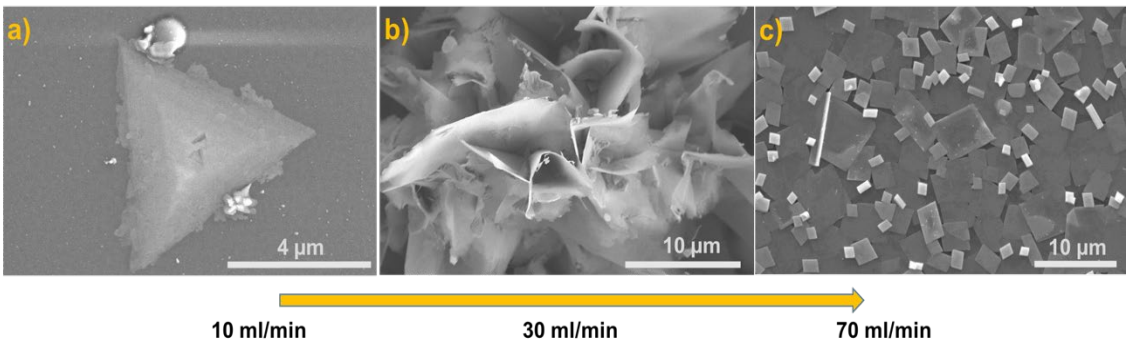

Fig.1. FE-SEM images of the grown films using (a) 10 ml/min (b) 30 ml/min and (c) 70 ml/min of argon flow rate.

The crystal structure of the films was analyzed by X-ray diffraction (XRD) method. Fig. 2 shows the XRD patterns recorded from MoS_2-30 and MoS_2-70 films, in the range of 20° to 80°. It can be deduced that the analyzed samples have a polycrystalline structure. For MoS_2-30 we detected peaks at 33.4°, 34.1°, 40.9°, 44.2°, 58°, 60° and 69°, which are attributed to (101), (012), (015), (009), (110), (113) and (202) planes of MoS_2, respectively, according to JCPDS card number (77-0341). Also, we noticed peaks at 25.7°, 36.7°, 37.34°, 53.15° and 66.4°, which belong to (-111), (200), (-202), (220) and (202) planes of MoO_2, respectively, in accordance to JCPDS card number (32-0671), and peaks located at 23.3°, 27.3°, 38.9° and 49.2° which correspond respectively to (100), (011), (102) and (020) planes of MoO_3 (JCPDS card number: 47-1320). Regarding MoS_2-70, we found peaks at 25.9°, 37.4° and 57.4° indicative of (-111), (-202) and (-303) planes of MoO_2 (JCPDS card number: 32-0671), respectively, and two peaks at 44.2° and 60° assigned to (009) and (113) planes of MoS_2, respectively (JCPDS card number: 77-0341). The peaks indexed by black arrows in Fig. 2 are enlarged and clearly displayed in Fig.S5. It is

worth noting that we could not analyze MoS_2-10 samples, since the nanotriangles were very small and sparsely dispersed over the substrate, thus it was difficult to localize them. Therefore, the presence of intermediate MoO_{3-x} in both samples can be associated to the insufficient sulfurization (i.e. incomplete CVD reaction) of MoO_3 as well as the presence of some oxygen molecules inside the CVD tube during the APCVD deposition. Many works in the literature reported the presence of these intermediate phase when MoO_3 precursor is used and this is an issue that should be addressed in the future. Based on the literature,[42] MoO_3 is first reduced to MoO_{3-x} and with further sulfur it is converted to MoS_2. Equations (Eq. 3) and (Eq. 4) describe the conceivable chemical reaction that can occur during the synthesis.

$$2MoO_3 + xS \rightarrow 2MoO_{3-x} + xSO_2 \qquad \text{(Eq. 3)}$$

$$2MoO_{3-x} + (7-x)S \rightarrow 2MoS_2 + (3-x)SO_2 \qquad \text{(Eq. 4)}$$

Additionally, from the XRD patterns, MoS_2-30 samples contain more MoS_2 peaks that those observed in MoS_2-70 samples. This can be related to the CVD reaction time as well as the amount of sulfur that reaches the substrate. These two parameters are strongly influenced by the gas flow rate used during the deposition.

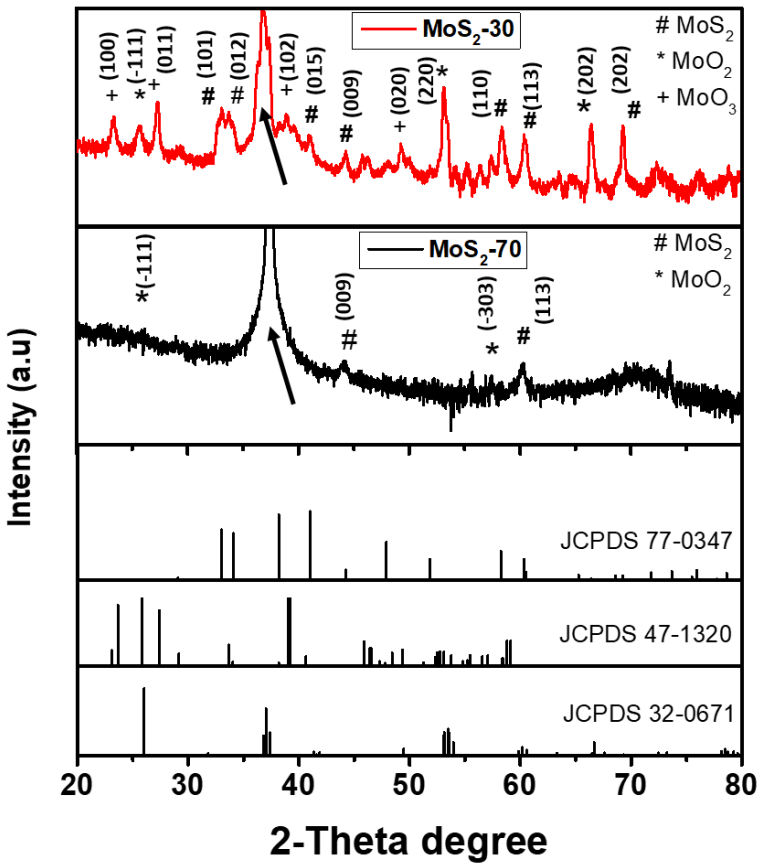

Fig.2. XRD patterns recorded from MoS_2-30 and MoS_2-70 films.

Fig. 3 displays Raman spectra recorded from MoS_2-10, MoS_2-30 and MoS_2-70 samples. The results showed the presence of two common peaks in all the samples near 400 cm^{-1}. They belong to the two vibration modes of MoS_2: in-plane vibration of molybdenum and sulfur atoms E^1_{2g} and out-of-plane vibration of sulfur atoms A_{1g}. [26,41] Besides, in MoS_2-70 samples, we observed other obvious peaks at 283, 336, 663, 818 and 992 cm^{-1}, which are assigned to MoO_2 phase.[43–45] Additionally, in MoS_2-30 we noticed three of these peaks, located at 283, 818 and 992 cm^{-1}, but with very low intensity. Regarding the MoS_2-10 spectrum, we did not detect further peaks rather than the ones of MoS_2. Consequently, these Raman results confirm the formation of MoS_2 with intermediate MoO_{3-x} products in samples prepared by using 30 ml/ min and 70 ml/ min, which is in line with XRD results.

Table 1 summarizes for all samples, the position of E^1_{2g} and A_{1g} MoS_2 vibration modes, difference between them (Δ) and their intensity ratio (I_{ratio}). In fact, using Δ information, helps to infer the number of MoS_2 layers that compose the film. As we can see from table 1, $\Delta \geq 26$, indicating the formation of multilayer MoS_2 material in all the grown films. Moreover, the intensity ratio I_{ratio} provides more information about the vertical orientation of the MoS_2 nanosheets grown by APCVD technique. Indeed, E^1_{2g} peak resulted from the vibration of Mo atom in the in-plane and opposite to two S atom, whereas in A_{1g} peak the Mo atom is immobile and the two S atoms vibrate in opposite directions in the out-of-plane direction. Hence, E^1_{2g} is in preference to be emitted from the in plane oriented MoS_2 nanosheets, while A_{1g} is preferred by the edge sites of vertically oriented MoS_2 nanosheets.[41] Therefore, a decrease in the intensity ratio, is correlated with an increase in the vertical orientation of the MoS_2 nanosheets. Based on the calculated intensity ratio of all the samples, the lowest ratio was observed for MoS_2-30 which exhibits vertically oriented MoS_2 nanosheets while the highest one was recorded from the sample composed of 2D nanotriangles. These observations are in line with FE-SEM results.

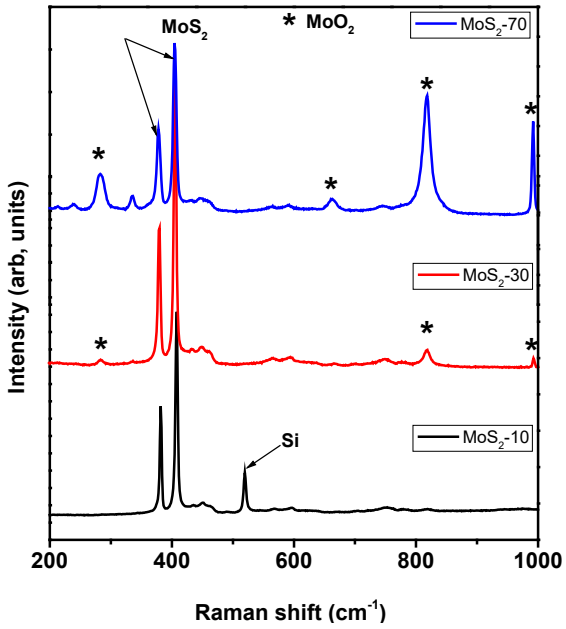

Fig.3. Raman spectra of MoS_2-10, MoS_2-30 and MoS_2-70 films.

Table 1: summary of Raman data for the as grown samples

Sample name	E^1_{2g}	A_{1g}	$\Delta = (A_{1g} - E^1_{2g})$	$I_{ratio} = (E^1_{2g}/A_{1g})$
MoS_2-10	381	408	27	0.55
MoS_2-30	379	405	26	0.49
MoS_2-70	378	404	26	0.52

As we have mentioned in the introduction, samples enriched with edge sites are more suitable for gas sensing applications. Consequently, we have further studied the chemical composition as well as the morphology and the structure of MoS_2-30 films by using XPS and HRTEM analysis. Fig.4.a displays the core level spectra of Mo (3d) obtained from MoS_2-30 sample. The molybdenum spectrum exhibits four peaks which were reproduced by three separate doublets. The first one with components, located at 229.5 eV ($3d_{5/2}$) and 232.8 eV ($3d_{3/2}$) which correspond to MoS_2.[26] The second doublet composed of two small peaks at 229,8 eV ($3d_{5/2}$) and 232.9 eV ($3d_{3/2}$), which are attributed to MoO_2.[26] The last doublet with components at 232.8 eV and 236 eV, which are assigned to MoO_3.[46] A long with Mo doublets, we have observed a peak at 226.8 which correspond to S (2s). Fig.4.b illustrate the S (2p) spectrum of MoS_2-30 sample. It is composed of a S(2p) doublet positioned at 162.6 eV and 163,8 eV, which correspond to S ($2p_{3/2}$) and S ($2p_{1/2}$) spectral lines of S^{2-} in MoS_2 and a peak at 168.5 eV. This later can be ascribed to MoO_xS_y. Thus, XPS results are in line with the ones obtained from XRD and Raman spectroscopy.[46,47]

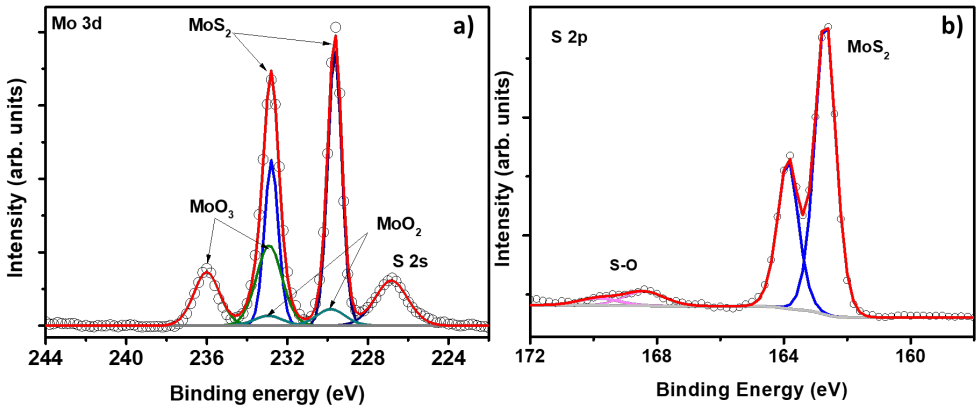

Fig. 4. XPS spectra (a) Mo 3d and (b) S 2p core-levels of MoS_2-30 sample.

TEM and HRTEM were employed to investigate in detail the morphology and the composition of MoS_2-30 samples. Fig.5.a shows multilayer nanosheets with size ranging from 400 nm up to 1.5 µm in one dimension. The layers were crystalline, their surface was very clean without any amorphous material. In addition, in some regions we detected nanosheets with randomly deposited layers while in other regions the layers were arranged in a stepwise manner. On sheet 1, indexed by orange arrow in Fig.5.b, we verified the average interlayer distance measured on 10 fringes, the calculated value was 0.615 nm, which corresponds to (002) plane of MoS_2 (phase 2H) (JCPDS card number 00-037-1492). In the second sheet (Fig.5.c) the measured d-spacing was 0.63 nm (only 6 layers). This distance coincides with (002) plane of MoS_2 (phase 2H) (JCPDS card number 75-1539). In the third sheet (Fig.5.d), the d-spacing was 0.27 nm which is assigned to the (100) plane of MoS_2.[48] In the last sheet (sheet 4, Fig.5.d) the d-spacing was 0.68 nm, it was measured on 6 fringes. This value is ascribed to the expanded interlayer MoS_2.[49] According to the literature,[50] the difference observed in the (002) d-spacing can be explained by the presence of sulfur vacancy defects that produce an expansion at the level of the lattice. In addition to nanosheets, we observed quadrilateral structures (Fig.5.e) in which the core level is assigned to (200) planes of MoO_2 (JCPDS card number 32-0671). The d-spacing from FFT pattern was 0.245 nm. It agrees with the most intense peak observed in the XRD pattern. Regarding the shell of this nanostructure, the measured d-spacing varied between 0.61 nm and 0.56 nm, which indicates the presence of MoS_2/MoO_xS_y. This was observed before in the XPS results and it results from the incomplete sulfurization process of MoO_3. In sum, the results obtained from all the material characterization techniques are in good agreement, while HRTEM has clarified and shed light on the morphological composition of MoS_2-30 samples. Indeed, it has demonstrated that vertical nanosheets consist of pure MoS_2 while the remnant MoO_{3-x} appears in the quadrilateral nanostructures observed. In the next section, more details are given about the morphology and the growth mechanism of this sample.

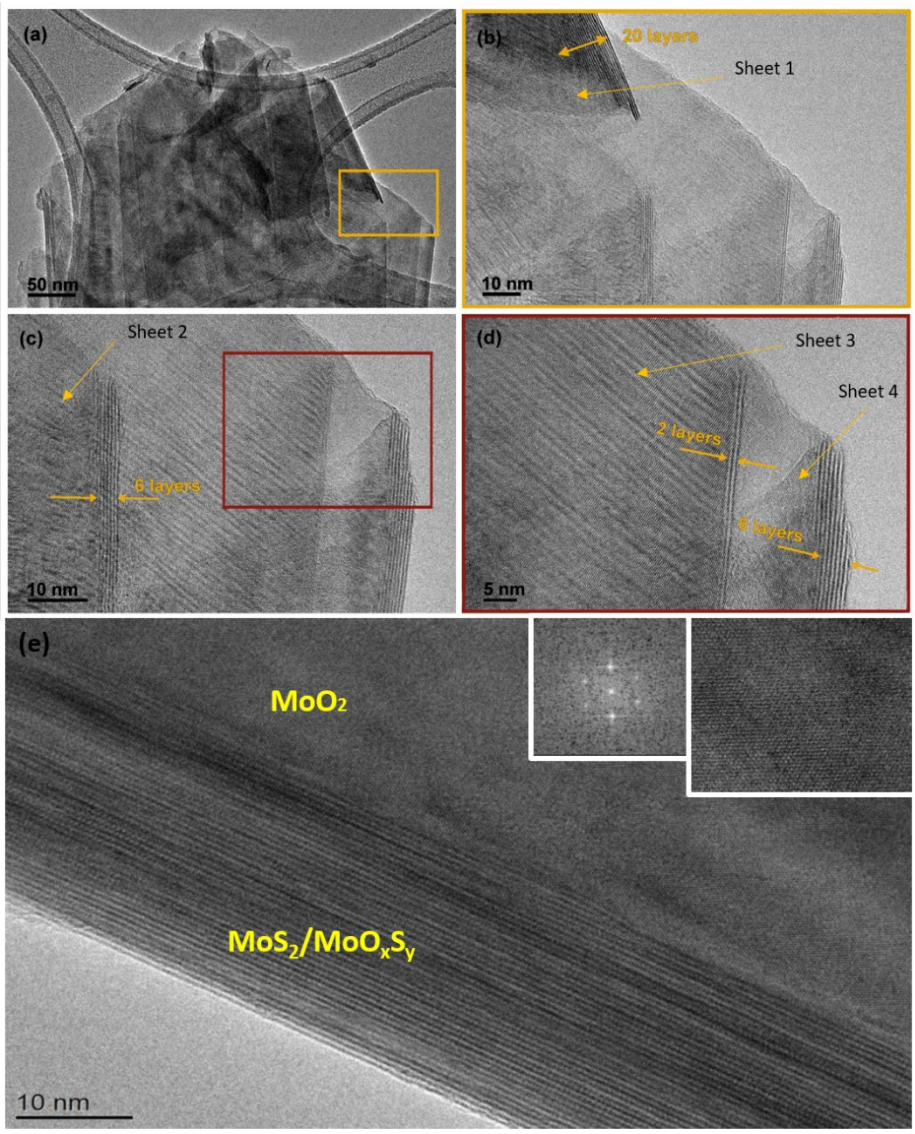

Fig.5. HRTEM images of MoS_2-30 sample: (a) TEM images of multilayer MoS_2 nanosheets and HRTEM of (b) sheet 1 with d-spacing of 0.615 nm, (c) sheet 2 with d-spacing of 0.63nm, (d) sheet 3 with d-spacing of 0.27 nm and (e) quadrilateral nanostructure.

APCVD Growth mechanism of edge enriched 3D assemblies of MoS_2 nanosheets.

Based on the morphological transformation during the growth of edge enriched MoS_2 nanosheets, we have proposed the following growth mechanism, illustrated in Fig. S6. As a first step, MoO_3 vapors get reduced to MoO_{3-x} via sulfur vapors. This step is well known and is reported by many works in the literature.[51,52] At this level, two different pathway reactions can occur during the deposition:

Reaction (1): solid phase reaction, in which the intermediate MoO_{3-x} get adsorbed and diffused onto the substrate forming MoO_{3-x} crystals (mainly MoO_2). These later serve as a seeding platform for the growth of MoO_{3-x} particles to eventually create quadrilateral nanostructures (Fig.6.a). Next, sulfur vapor will penetrate to the first top layers of MoO_{3-x} quadrilaterals and will change them from MoO_{3-x} to MoS_2.[52,42,26] This reaction pathway is supported by Fig. 6.e. It should be noted that XRD, Raman, XPS techniques used in this work revealed the presence of intermediate MoO_{3-x}, which could belong to the quadrilateral nanostructures that remain underneath the layer of MoS_2 nanosheets. This solid phase reaction can be corroborated by Eq. 3 and Eq. 4, mentioned above.

Reaction (2): vapor-phase reaction, in which the reduced MoO_{3-x} interacts directly with the sulfur at the gas phase and form MoS_2 vapor. Based on standard Stranski−Krastanov (SK) growth model, [26,52] when MoS_2 vapor diffuses to the substrate and finds one or many MoS_2 monolayers, the in-plane growth will be unfavorable and the MoS_2 will nucleate vertically (Fig.6.b) and will change to vertically oriented MoS_2 nanosheets, as it is illustrated in Fig 6. c and d. The suggested vapor-phase reaction can be assisted by Eq. 5.

$$2MoO_{3\,(g)} + 7S_{(g)} \rightarrow 2MoS_{2\,(s)} + 3SO_{2\,(g)} \qquad \text{(Eq. 5)}$$

Hence, from FE-SEM results (Fig.6), both suggested reaction pathways can happen together during the APCVD growth, since we have the growth of an in-plane layer in close contact to the substrate (bottom layer) and of edge enriched 3D nanosheets on top of the in-plane layer (upper layer). Moreover, based on the growth mechanism and the material characterization results we can conclude that the MoO_{3-x} impurities appear in the quadrilateral nanostructures located at the bottom layer of samples. They were resulting from the insufficient sulfurization process of the quadrilateral nanostructures as well as the presence of some oxygen molecules inside the CVD tube. In contrast, vertical nanosheets were mainly composed from pure MoS_2 material.

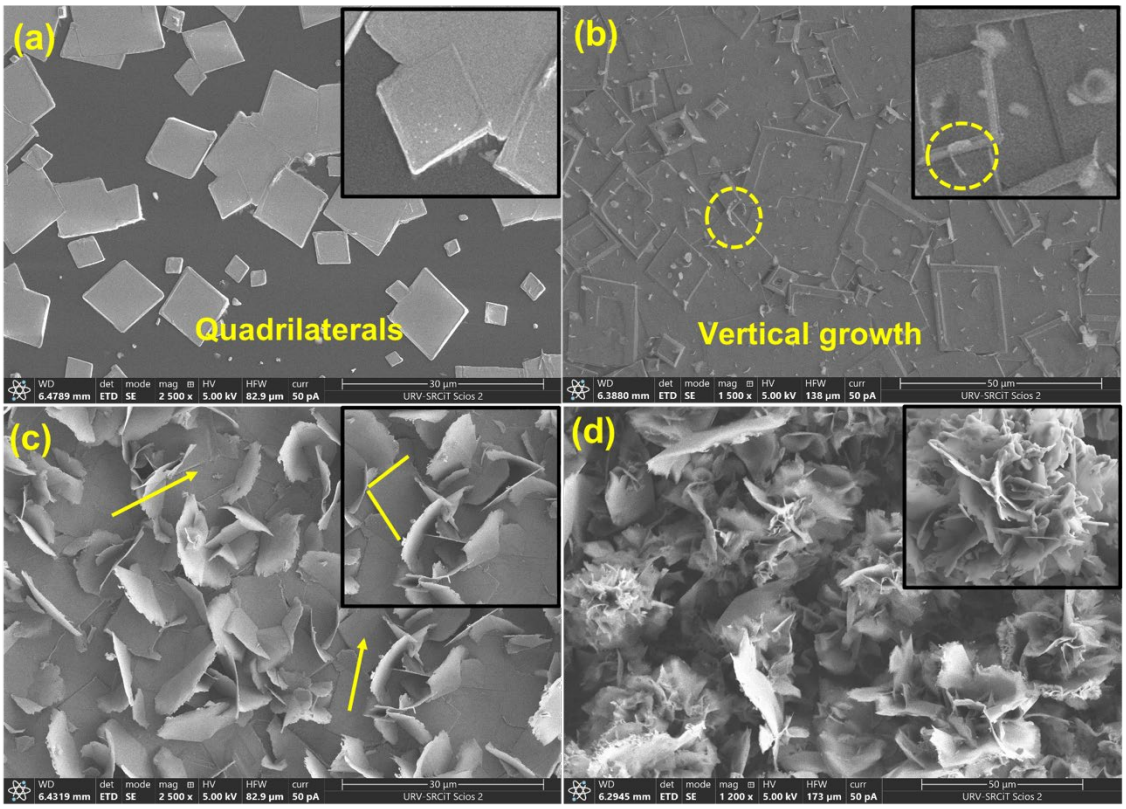

Fig.6. morphological evolution during the growth of edge-enriched 3D assemblies of MoS_2 nanosheets.

Gas sensing results

Nitrogen dioxide (NO_2) and ammonia (NH_3) are among the most important air pollutant gases that thread the human health as well as the environment. Herein, the electrical properties of MoS_2-30 based gas sensors (Fig. S2) were studied towards the above-mentioned gases. The optimal working temperature is an essential parameter that must be defined in order to thermally activate the reactions between the adsorbed oxygen ionic species and the target gas molecules. For this reason, we exposed our sensors towards four replicates of 10 ppm of NH_3, at temperatures ranging from 25 °C to 150 °C. From Fig.7, the sensors responses increased with increasing the temperature, reaching the maximum at 100 °C and then started to decrease by increasing the temperature. Similar behavior was observed for 800 ppb of NO_2. Therefore, the optimal working temperature for detecting ammonia was 100 °C. This temperature it is quite low compared to the operating temperatures of metal oxides and of many TMDs based gas sensors, which is advantageous for the long term stability of gas sensitive nanomaterials. [53–56]

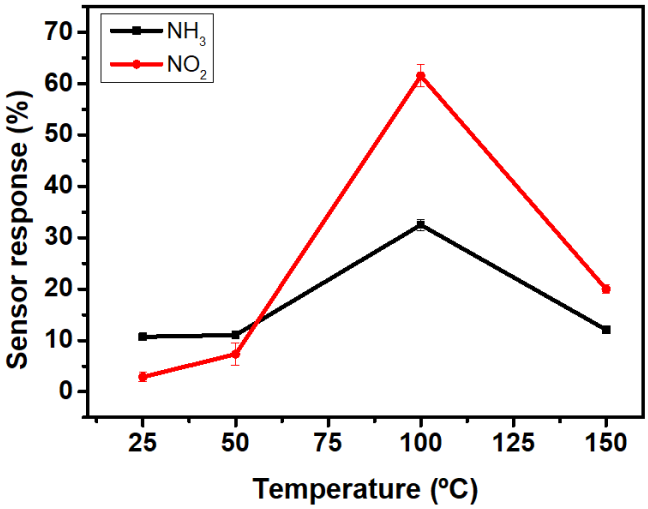

Fig.7. Gas sensor response as a function of temperature.

Fig.8 displays sensors resistance changes as a function of time, towards four replicates of 10 ppm of ammonia (Fig. 8. a) and 800 ppb of NO_2 (Fig.10. b) at an operating temperature of 100 °C. Overall, NH_3 is an electron donor that releases electrons to the conduction band of MoS_2. In contrast NO_2 is an electron acceptor that extracts electrons from the conduction band of MoS_2. Since the exposure to NH_3 decreases the resistance of MoS_2 sensors whereas NO_2 increases this resistance, these results confirm the *n-type* semiconductor behavior of the edge enriched 3D assemblies of MoS_2 nanosheets. It is clearly noticed that the sensors exhibit stable and reproducible responses versus the target gases. A slight drift in the baseline resistance was registered. Besides, the sensors response and recovery times towards NO_2 were much faster compared to NH_3 measurements. They were respectively equal to 60 s and 400 s in the case of NO_2 and they become 193 s and 965 s in the case of NH_3.

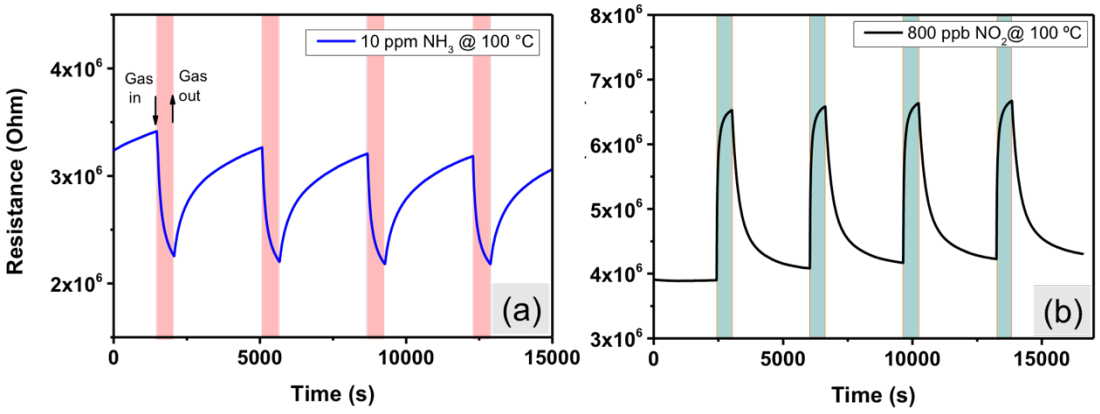

Fig.8. sensor resistance changes as a function of time against (a) 10 ppm of NH_3 and (b) 800 ppb of NO_2, at 100 °C.

Fig. S7 shows the sensors resistance changes towards the same concentrations tested in the previous study, but this time under room temperature operation. Herein, the duration of the

recovery phase was twice that used in the measurements performed at 100 °C. This can be attributed to the difficulty of desorbing gas molecules from the surface of the material (i.e. cleaning of the surface in dry air) when the sensors work at room temperature. From Fig. S7.a, it can be derived that sensors responses to NH_3, were very stable and reproducible, especially if compared to those recorded for NO_2, where the sensors were not able to return to their initial baseline resistance (Fig.S7.b).The responses to repeated exposures were decreasing significantly as a function of time, which can be associated to the lack of complete desorption of NO_2 molecules during the cleaning phases due to strong adsorption energy of NO_2 onto the MoS_2 material.[20]

To further investigate the enhanced gas sensing properties of edge enriched 3D assemblies of MoS_2 nanosheets, we exposed our sensors against a wide range of concentrations, going from 2 ppm to 10 ppm for NH_3, and from 20 ppb to 800 ppb for NO_2. The obtained results are displayed in Fig. 9. For NH_3, we measured the above-mentioned concentration at 25 °C and 100 °C. From Fig.9. a and b, the sensors were able to detect ammonia with an excellent sensitivity for the measured concentration range. Additionally, from both insets in Fig. 9. a and b, the relationship between the sensor response and the gas concentrations was quite linear. The calculated responses at 100 °C ranged from 19.5 % to30 % when NH_3 concentration varied from 2, to 10 ppm of, while at room temperature, the responses to the same range of ammonia concentrations varied from 6 %to 11 %. Besides, we can conclude that the experimental detection limit of the sensors at both operating temperatures was lower than 2 ppm, which is 12 times lower than the exposure limit set by the Occupational Safety and Health Administration (OSHA) (25 ppm). Regarding NO_2, the sensors were not able to detect the tested concentrations when operated at room temperature. This is why all the measurements were conducted at the optimal working temperature (100 °C) (Fig.9.c). Interestingly, the sensors showed two distinct behaviors: at low concentrations (from 20 ppb to 100 ppb) the responses correlated linearly with the NO_2 concentrations, however at elevated concentrations (200 ppb to 800 ppb) the sensors start to show response saturation. It is worth noting that the sensors exhibited remarkable responses towards NO_2 with very good stability. From Fig.9. d, it is clearly seen that the detection limit was below 20 ppb, which is significantly lower than the permissible exposure limit of NO_2 defined by the OSHA (5 ppm). The sensors signal at this low concentration was very clear and highly above the noise level.

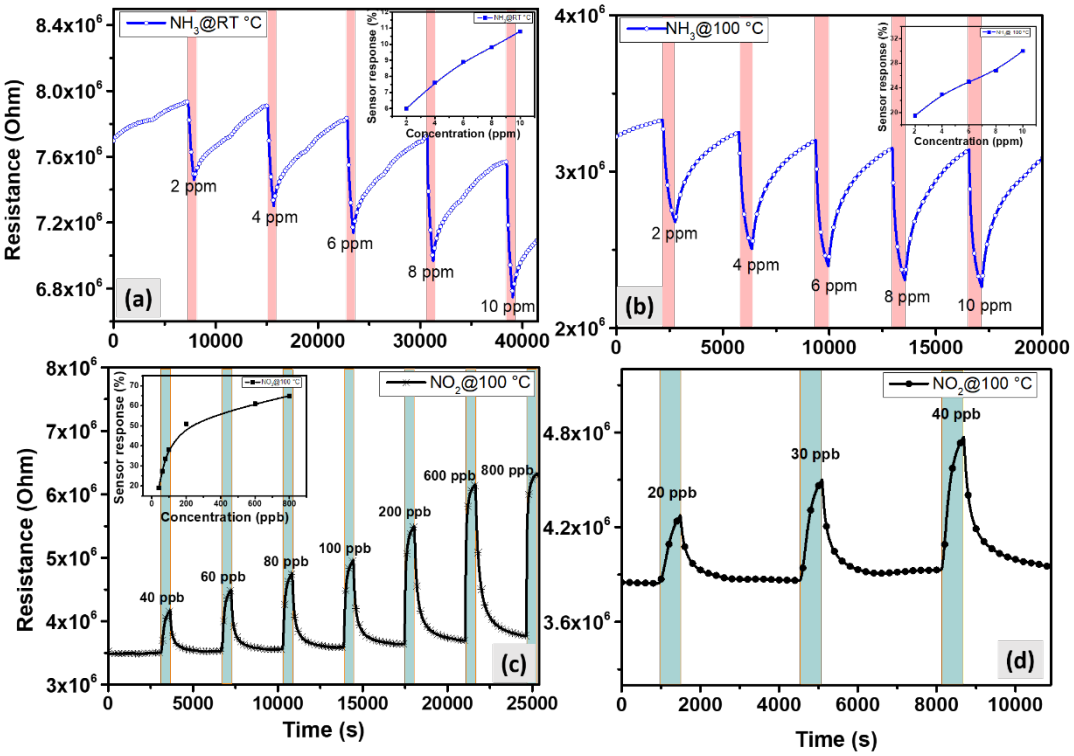

Fig.9. sensors resistance changes as a function of time against different concentration of (a) NH_3 at room temperature (b) NH_3 at 100 °C (c) NO_2 at 100 °C and (d) experimental detection limit of NO_2 at 100 °C.

Selectivity test

In a first approach for assessing the selectivity of our nanomaterial, the responses towards carbon monoxide (CO- 80 ppm) and hydrogen (H_2-500 ppm) were investigated. Fig.10 displays the response histograms for the two different operating temperatures used. It is clear that at room temperature (Fig.10.a), the sensors exhibit high response towards 10 ppm of NH_3, a response that is much higher than the one recorded for the other reducing species (CO and H_2). Ammonia response was 4-times higher than of the one recorded for NO_2. It is worth stressing that NO_2 800 ppb is a very high concentration (e.g. the EPA has set the annual average NO_2 standard of 53 ppb). When the sensors were heated at 100 ºC, the selectivity of the sensors is reversed, as it appears in Fig. 10. b. The sensors showed good response towards 800 ppb of NO_2, higher than the response recorded for any of the other species tested. Indeed, the response towards 800 ppb of NO_2 was 2-times higher than that of NH_3, 30 times higher than that of H_2, whereas for CO, the sensor displayed similar behavior as at room temperature. Therefore, by selecting their operating temperature (R.T. or 100ºC), edge enriched 3D assemblies of MoS_2 present a dually selective behavior towards NH_3 or NO_2. This dual selectivity has been reported before for some metal oxide

gas sensors,[57–59] whereas this behavior has never been reported before for MoS_2 nanomaterials.

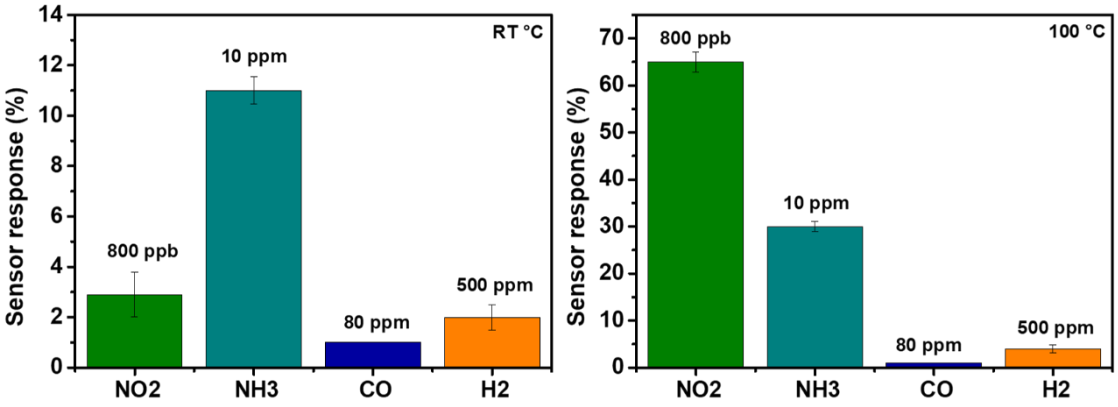

Fig.10. Comparison of the responses towards different gaseous species when the operating temperature is set to R.T (left panel) or to 100ºC (right panel).

Table 2 and 3 compare the gas sensing performances of edge enriched 3D assemblies of MoS_2 nanosheets and other TMDs nanomaterials, towards NH_3 and NO_2. Obviously, our sensors exhibit high sensitivity towards the target gases, with small experimental detection limit (below 2 ppm for NH_3 and below 20 ppb for NO_2), at a lower operating temperature. Moreover, none of the reported TMDs materials have the advantage of a dual selectivity against two different toxic gases.

Table 2. A comparison of NH_3 sensing performance of different TMDs-based gas sensors.

2D material	method	conc. (ppm)	Working temp. (°C)	Resp	LOD	Dual selectivity test	Ref
MoS_2	**APCVD**	**10**	**100**	**30 %**	**below 2 ppm**	**Yes**	**This work**
MoS_2	**APCVD**	**10**	**25**	**11 %**	**below 2 ppm**	**Yes**	**This work**
WS_2 aerogel	Multistep chemical synthesis	800	250	0.8 %	13 ppm (theoret.)	NO	60
Cu_2S	Multistep chemical synthesis	500	25	19.78 %	N.A	NO	61
SnS_2	solvothermal reaction	100	200	7.4%	0.5 ppm	No	62
WS_2	AACVD+APCVD	5	150	16 %	2 ppm	No	9
$MoSe_2$	Mechanical exfoliation	50	25	N.A	50 ppm	No	63

Table 3. A comparison of NO_2 sensing performance of different TMDs-based gas sensors.

2D material	method	Studied conc.	Working temp. (°C)	Resp	LOD	Dual selectivity test	Ref
MoS_2	**APCVD**	**800 ppb**	**100**	**65 %**	**20 ppb**	**Yes**	**This work**
WS_2	Hydrothermal+CVD	5 ppm	160	121 %	200 ppb (exp.)	NO	[64]
WS_2	Multistep chemical synthesis	3 ppm	250	36	8 ppb (theoret.)	NO	[60]
MoS_2	CVD	1.2 ppm	100	5 %	1.2 ppm	NO	[65]
SnS_2/ rGO	Drop-casting	12 ppm	80	54 %	0.6 ppm	NO	[66]
WS_2/ graphene	Multistep chemical synthesis	2 ppm	180	3 %	10 ppb (theoret.)	NO	[67]

Humidity measurements:

As we known, ambient moisture can dramatically affect the electrical properties of gas sensors and heavily impact sensitivity. Consequently, it is necessary to evaluate the behavior of gas sensors in the presence of humidity. Fig.11 illustrates the sensor response against 800 ppb of NO_2 under dry and humid background. From the results, we observed a decrease in the baseline resistance of the sensor from 3.9 MΩ in dry background to 1.5 MΩ in humid one. This behavior has been reported before for metal oxide semi-conducting materials.[68] Moreover, we noticed a slight difference between the sensor responses; it was 65% in dry ambient and it becomes 70% in humid background. Overall, during the gas detection at a humid ambient, the target gas molecules and the water vapor (hydroxyl group) enter in a competition at the level of the active sites. When the relative surface distribution of the hydroxyl group is much higher than that of the oxygen species, the performance of the sensor decreases and the effect of humidity is significantly more noticeable. In contrast, when the sensor exhibits high moisture immunity, most of the active sites consist of absorbed oxygen species and the sensor performance remains unchanged. Therefore, the obtained results indicate the high immunity of edge enriched 3D assemblies MoS_2 nanosheets against a high level of moisture background. [68–71]

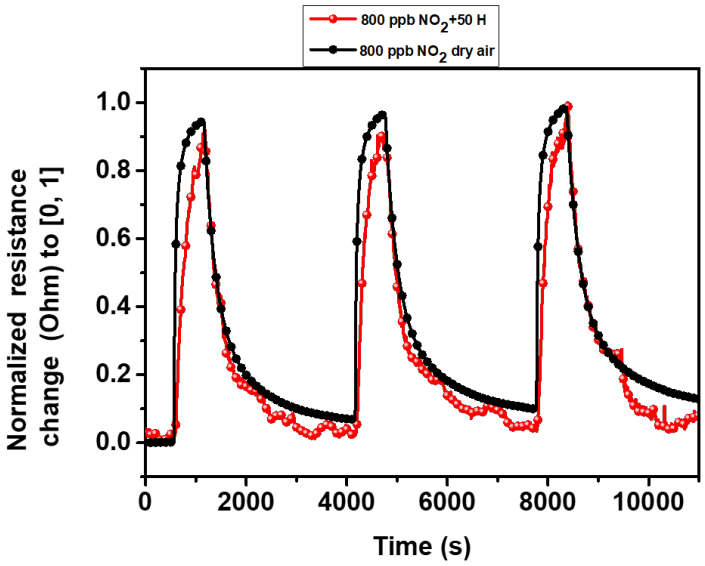

Fig.11. Normalized sensor resistance change as a function of time, in dry (black) and 50 % of relative humidity (red) atmospheres, at 100 °C.

Gas sensing mechanism

It has been shown that the vertical orientation of MoS_2 nanosheets helps the sensor to be more exposed to the target gas and exhibits high gas sensing performances. Indeed, the edge sites of the MoS_2 nanosheets boundaries are thoroughly chemically reactive as compared to the basal plane. According to the literature,[72] the adsorption energy of NO_2 at S edges is higher (~ -0.4 eV) than at the basal plane (~ -0.13 eV) of MoS_2 material and the associated electronic charge transfer is ~ 0.5 e and 0.1 e, respectively. Herein, the proposed gas sensing mechanism is based on the adsorption/desorption of the gas molecules at the active sites of MoS_2 nanosheets and it is illustrated by the schematic sketch in Fig.12. When the sensor is exposed to the air, oxygen molecules get adsorbed at the MoS_2 surface through extracting free electrons from the conduction band and forming an electron-depletion layer with a partial oxidation MoS_2 top layer.[73–75] It is worth noting that the nature of the adsorbed oxygen species depends on the sensor working temperature as shown by Eq.6 to Eq. 9.[53] Thereby, at low temperature, O_2^- are the predominant adsorbed species.

$$O_{2(g)} \rightarrow O_{2(ads)} \qquad \text{(Eq. 6)}$$

$$O_{2(ads)} + e^- \rightarrow O_{2(ads)}^- \qquad \leq 100\,°C \qquad \text{(Eq. 7)}$$

$$O_{2(ads)}^- + e^- \rightarrow 2O_{(ads)}^- \qquad 100 < T < 300\,°C \qquad \text{(Eq. 8)}$$

$$O_{(ads)}^- + e^- \rightarrow O_{(lattice)}^{2-} \qquad > 300\,°C \qquad \text{(Eq. 9)}$$

Next, when the sensor is exposed to an oxidizing gas such as NO_2, this later not only capture electrons from the accepter level of the material but also react with the O_2^- adsorbed species as well as S vacancies (Eq. 10, 11 and 12) leading to the formation of more holes at the valence band and an increase in the sensor resistance.[38,76,77]

$$NO_2 + e^- \rightarrow NO_2^- \quad \text{(Eq. 10)}$$

$$NO_2 + O_2^- + 2e^- \rightarrow NO_2^- + 2O^- \quad \text{(Eq. 11)}$$

$$NO_2^- + Vs^{++} \rightarrow NO_2 + h^+ \quad \text{(Eq. 12)}$$

In the case of a reducing gas such as NH_3, the chemisorbed oxygen species interact with NH_3 molecules and release electrons to the conduction band, which dramatically decrease the thickness of the depletion layer and decrease the sensor resistance. Eq. 13 and describe the reaction between NH_3 and the chemisorbed oxygen species.[78,79]

$$4NH_3 + 3O_2^- \rightarrow 2N_2 + 6H_2O + 3e^- \quad \text{(Eq. 13)}$$

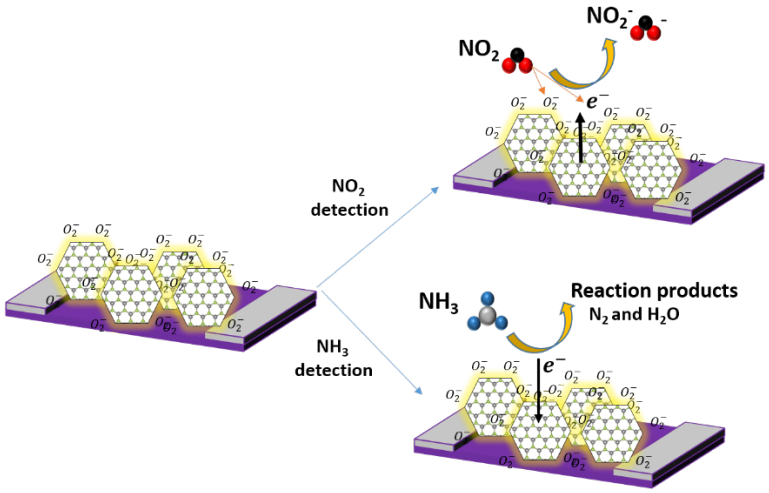

Fig.12. schematic sketch of the proposed NO_2 and NH_3 sensing mechanism.

Conclusion

This paper explores for the first time how a simple approach such as optimizing flow rate in an atmospheric pressure CVD system enables achieving the self-organized, bottom up growth of sponge-like, 3D assemblies of MoS_2 nanosheets. These 3D assemblies are porous (i.e. possess high surface for interacting with gases) and their edges are highly reactive, which results in highly enhanced sensing properties. This single step atmospheric pressure CVD method approach is used for the first time in the fabrication of dually selective NH_3 and NO_2 gas sensors. The gas flow rate

was found to have a strong influence in the morphology of the MoS_2 grown. When the growth was conducted at 10 ml/min Ar flow, a discontinuous layer of sparsely dispersed MoS_2 nanotriangles was obtained.When the flow was set to 70 ml/min, quadrilateral MoS_2 nanostructures were synthesized. Finally, at 30 ml/min, a thick layer of edge-enriched 3D assemblies of MoS_2 nanosheets was achieved. In contrast to the other two flow rates tested, at 30 ml/min the growth of MoS_2 nanosheets changes from in-plane to out-plane, which is advantageous for achieving 3D, sponge structures with higher surface. In fact, 30 ml/min represents an ideal compromise between the surface interaction and the mass transport of precursor molecules. Moreover, material characterization results revealed the formation of edge enriched 3D assemblies of MoS_2 nanosheets with the presence of some MoO_{3-x} impurities. Based on the growth mechanism, these impurities were coming from the bottom layer of the grown film, where quadrilateral nanostructures were not completely sulfurized. The gas sensing performances of edge enriched 3D assemblies of MoS_2 were tested against NH_3, NO_2 and humidity. At the optimal working temperature, sensors exhibit an *n-type* semiconducting behavior towards the studied gases. The responses were stable and reproducible, with high sensitivity. Specificity towards NH_3 or NO_2 could be tuned by operating the sensors at R.T. or at 100ºC, respectively. Regarding the experimental detection limit, it was below 2 ppm for NH_3 and below 20 ppb for NO_2. Finally, the sensor displayed high resilience against moisture interference, since sensor response towards NO_2 barely changed when sensors were operated under dry or humid (50% R.H) conditions. All these results compare favorably to those previously reported for MoS_2 based sensors.

Conflicts of interest

There are no conflicts to declare.

Acknowledgements

Funded in part by the Marie Skłodowska-Curie Actions (MSCA) Research and Innovation Staff Exchange (RISE) H2020-MSCA-RISE-2018-823895 ‘SENSOFT’ and by MICINN and FEDER grant no. RTI2018-101580-I00. A.A. is supported by a COFUND project the European Union’s Horizon 2020 research and innovation program under the Marie Skłodowska-Curie grant agreement No. 713679 and the Universitat Rovira i Virgili (URV). F.E.A. is a *Juan de la Cierva* Post-doctoral Fellow, C.B. is a Research Associate of the National Funds for Scientific Research (FRS-FNRS, Belgium; E.L. is supported by the Catalan Institute for advanced studies (ICREA) via the 2018 Edition of the ICREA Academia Award.

References

1 K. S. Novoselov, A. K. Geim, S. V. Morozov, D. Jiang, M. I. Katsnelson, Iv. Grigorieva, Sv. Dubonos and and A. A. Firsov, *Nature*, 2005, **438**, 197–200.

2 H.-Y. Kim, K. Lee, N. McEvoy, C. Yim and G. S. Duesberg, *Nano Lett.*, 2013, **13**, 2182–2188.

3 N. Joshi, T. Hayasaka, Y. Liu, H. Liu, O. N. Oliveira and L. Lin, *Microchim. Acta*, 2018, **185**, 1–16.

4 Z. Meng, A. Fujii, T. Hashishin, N. Wada, T. Sanada, J. Tamaki, K. Kojima, H. Haneoka and T. Suzuki, *J. Mater. Chem. C*, 2015, **3**, 1134–1141.

5 B. Cho, J. Yoon, M. G. Hahm, D.-H. Kim, A. R. Kim, Y. H. Kahng, S.-W. Park, Y.-J. Lee, S.-G. Park and J.-D. Kwon, *J. Mater. Chem. C*, 2014, **2**, 5280–5285.

6 Y. Wang, M. Yang, W. Liu, L. Dong, D. Chen and C. Peng, *J. Mater. Chem. C*, 2019, **7**, 9248–9256.

7 S. G. Chatterjee, S. Chatterjee, A. K. Ray and A. K. Chakraborty, *Sensors Actuators B Chem.*, 2015, **221**, 1170–1181.

8 A. Alagh, F. E. Annanouch, P. Umek, C. Bittencourt, J. F. Colomer and E. Llobet, *IEEE Sens. J.*, 2021, **21**, 21212–21220.

9 A. Alagh, F. E. Annanouch, P. Umek, C. Bittencourt, A. Sierra-Castillo, E. Haye, J. F. Colomer and E. Llobet, *Sensors Actuators B Chem.*, 2021, **326**, 128813.

10 M. Donarelli and L. Ottaviano, *Sensors*, 2018, **18**, 3638.

11 Y. Ding, X. Guo, B. Du, X. Hu, X. Yang, Y. He, Y. Zhou and Z. Zang, *J. Mater. Chem. C*, 2021, **9**, 4838–4846.

12 M. Peng, X. Zheng, C. Shen, Y. He, H. Wei, P. Qiu, Y. Song, F. Tian, Y. Li and S. Wei, *J. Mater. Chem. C*, 2021, **9**, 7982–7990.

13 H. Hashtroudi, I. D. R. Mackinnon and M. Shafiei, *J. Mater. Chem. C*, 2020, **8**, 13108–13126.

14 F.-F. Hu, H.-Y. Tang, C.-J. Tan, H.-Y. Ye, X.-P. Chen and G.-Q. Zhang, *IEEE Electron Device Lett.*, 2017, **38**, 983–986.

15 X. Chen, X. Chen, Y. Han, C. Su, M. Zeng, N. Hu, Y. Su, Z. Zhou, H. Wei and Z. Yang, *Nanotechnology*, 2019, **30**, 445503.

16 I. Shlyakhov, K. Iakoubovskii, S. Banerjee, A. Gaur, D. Lin, I. Asselberghs, I. Radu, J. Chai, M. Yang and S. J. Wang, *J. Appl. Phys.*, 2021, **129**, 155302.

17 F. Li, B. Xu, W. Yang, Z. Qi, C. Ma, Y. Wang, X. Zhang, Z. Luo, D. Liang and D. Li, *Nano Res.*, 2020, **13**, 1053–1059.

18 S. Rashidi, S. Rashidi, R. K. Heydari, S. Esmaeili, N. Tran, D. Thangi and W. Wei, *Prog. Photovoltaics Res. Appl.*, 2021, **29**, 238–261.

19 W. Zheng, Y. Xu, L. Zheng, C. Yang, N. Pinna, X. Liu and J. Zhang, *Adv. Funct. Mater.*, 2020, **30**, 2000435.

20 V. Babar, H. Vovusha and U. Schwingenschlögl, *ACS Appl. Nano Mater.*, 2019, **2**, 6076–6080.

21 D. J. Late, Y.-K. Huang, B. Liu, J. Acharya, S. N. Shirodkar, J. Luo, A. Yan, D. Charles, U. V Waghmare and V. P. Dravid, *ACS Nano*, 2013, **7**, 4879–4891.

22 T. Shen, F. Li, L. Xu, Z. Zhang, F. Qiu, Z. Li and J. Qi, *J. Mater. Sci.*, 2020, **55**, 14315–14325.

23 J.-H. Ahn, W. M. Parkin, C. H. Naylor, A. T. C. Johnson and M. Drndić, *Sci. Rep.*, 2017, **7**, 1–9.

24 J. Chen, W. Tang, B. Tian, B. Liu, X. Zhao, Y. Liu, T. Ren, W. Liu, D. Geng and H. Y. Jeong, *Adv. Sci.*, 2016, **3**, 1500033.

25 C. M. Lee, C. H. Jin, C. H. Ahn, H. K. Cho, J. H. Lim, S. M. Hwang and J. Joo, *Phys. status solidi*, 2019, **216**, 1800999.

26 A. V Agrawal, N. Kumar, S. Venkatesan, A. Zakhidov, C. Manspeaker, Z. Zhu, F. C. Robles Hernandez, J. Bao and M. Kumar, *ACS Appl. Nano Mater.*, 2018, **1**, 2356–2367.

27 Y. Duan, S. Feng, K. Zhang, J. Qiu and S. Zhang, *ACS Appl. Nano Mater.*, 2021, **4**, 12043–12050.

28 S.-Y. Cho, S. J. Kim, Y. Lee, J.-S. Kim, W.-B. Jung, H.-W. Yoo, J. Kim and H.-T. Jung, *ACS Nano*, 2015, **9**, 9314–9321.

29 J. Kibsgaard, Z. Chen, B. N. Reinecke and T. F. Jaramillo, *Nat. Mater.*, 2012, **11**, 963–969.

30 M. Remškar, I. Iskra, J. Jelenc, S. D. Škapin, B. Višić, A. Varlec and A. Kržan, *Soft Matter*, 2013, **9**, 8647–8653.

31 B. Lei, G. R. Li and X. P. Gao, *J. Mater. Chem. A*, 2014, **2**, 3919–3925.

32 W. Wang, S. Zhu, Y. Cao, Y. Tao, X. Li, D. Pan, D. L. Phillips, D. Zhang, M. Chen and G. Li, *Adv. Funct. Mater.*, 2019, **29**, 1901958.

33 A. V Agrawal, R. Kumar, S. Venkatesan, A. Zakhidov, G. Yang, J. Bao, M. Kumar and M. Kumar, *ACS sensors*, 2018, **3**, 998–1004.

34 X. Lu, Y. Lin, H. Dong, W. Dai, X. Chen, X. Qu and X. Zhang, *Sci. Rep.*, 2017, **7**, 1–8.

35 S. Li, J. K. Lee, S. Zhou, M. Pasta and J. H. Warner, *Chem. Mater.*, 2019, **31**, 387–397.

36 X. Li, S. Guo, W. Li, X. Ren, J. Su, Q. Song, A. J. Sobrido and B. Wei, *Nano Energy*, 2019, **57**, 388–397.

37 J. Jaiswal, P. Tiwari, P. Singh and R. Chandra, *Sensors Actuators B Chem.*, 2020, **325**, 128800.

38 C. M. Hung, V. A. Vuong, N. Van Duy, D. Van An, N. Van Hieu, M. Kashif and N. D. Hoa, *Phys. status solidi*, 2020, **217**, 2000004.

39 S. Wang, Y. Rong, Y. Fan, M. Pacios, H. Bhaskaran, K. He and J. H. Warner, *Chem. Mater.*, 2014, **26**, 6371–6379.

40 T. Chiawchan, H. Ramamoorthy, K. Buapan and R. Somphonsane, *Nanomaterials*, 2021, **11**, 2642.

41 S. Li, S. Wang, M. M. Salamone, A. W. Robertson, S. Nayak, H. Kim, S. C. E. Tsang, M. Pasta and J. H. Warner, *ACS Catal.*, 2017, **7**, 877–886.

42 R. Guan, J. Duan, A. Yuan, Z. Wang, S. Yang, L. Han, B. Zhang, D. Li and B. Luo, *CrystEngComm*, 2021, **23**, 146–152.

43 V. Ramakrishnan, C. Alex, A. N. Nair and N. S. John, *Chem. Eur. J.*, 2018, **24**, 18003–18011.

44 K. Shomalian, M.-M. Bagheri-Mohagheghi and M. Ardyanian, *Appl. Phys. A*, 2017, **123**, 1–9.

45 Q. Tang, Z. Shan, L. Wang and X. Qin, *Electrochim. Acta*, 2012, **79**, 148–153.

46 X. Wang, Y. P. Zhang and Z. Q. Chen, *Mater. Res. Express*, 2016, **3**, 65014.

47 P. Kumar, M. Singh and G. B. Reddy, *Mater. Res. Express*, 2017, **4**, 36405.

48 C. P. Veeramalai, F. Li, Y. Liu, Z. Xu, T. Guo and T. W. Kim, *Appl. Surf. Sci.*, 2016, **389**, 1017–1022.

49 S. Luo, J. Ruan, Y. Wang, J. Hu, Y. Song, M. Chen and L. Wu, *Small*, 2021, **17**, 2101879.

50 Y. Xia, C. Hu, S. Guo, L. Zhang, M. Wang, J. Peng, L. Xu and J. Wang, *ACS Appl. Nano Mater.*, 2019, **3**, 665–673.

51 T. Park, M. Leem, H. Lee, W. Ahn, H. Kim, J. Kim, E. Lee, Y.-H. Kim and H. Kim, *J. Phys. Chem. C*, 2017, **121**, 27693–27699.

52 T. N. Trung and F. Z. Kamand, *Appl. Surf. Sci.*, 2020, **505**, 144551.

53 F. E. Annanouch, Z. Haddi, S. Vallejos, P. Umek, P. Guttmann, C. Bittencourt and E. Llobet, *ACS Appl. Mater. Interfaces*, , DOI:10.1021/acsami.5b00411.

54 S. Vallejos, S. Selina, F. E. Annanouch, I. Gràcia, E. Llobet and C. Blackman, in *Procedia Engineering*, 2016, vol. 168.

55 F. E. Annanouch, I. Gràcia, E. Figueras, E. Llobet, C. Cané and S. Vallejos, *Sensors Actuators, B Chem.*, , DOI:10.1016/j.snb.2015.03.076.

56 A. Alagh, F. E. Annanouch, P. Umek, C. Bittencourt, A. Sierra-Castillo, E. Haye, J. F. Colomer and E. Llobet, *Sensors Actuators, B Chem.*, , DOI:10.1016/j.snb.2020.128813.

57 J. Wang, S. Fan, Y. Xia, C. Yang and S. Komarneni, *J. Hazard. Mater.*, 2020, **381**, 120919.

58 Y. Wang, Y. Cui, X. Meng, Z. Zhang and J. Cao, *Surfaces and Interfaces*, 2021, **24**, 101110.

59 G. Li, Z. Cheng, Q. Xiang, L. Yan, X. Wang and J. Xu, *Sensors Actuators B Chem.*, 2019, **283**, 590–601.

60 W. Yan, A. Harley-Trochimczyk, H. Long, L. Chan, T. Pham, M. Hu, Y. Qin, A. Zettl, C. Carraro and M. A. Worsley, *FlatChem*, 2017, **5**, 1–8.

61 M. S. Shinde, D. R. Patil and R. S. Patil, .

62 Y. Xiong, W. Xu, D. Ding, W. Lu, L. Zhu, Z. Zhu, Y. Wang and Q. Xue, *J. Hazard. Mater.*, 2018, **341**, 159–167.

63 D. J. Late, T. Doneux and M. Bougouma, *Appl. Phys. Lett.*, 2014, **105**, 233103.

64 D. Liu, Z. Tang and Z. Zhang, *Sensors Actuators B Chem.*, 2020, **303**, 127114.

65 B. Cho, J. Yoon, S. K. Lim, A. R. Kim, D.-H. Kim, S.-G. Park, J.-D. Kwon, Y.-J. Lee, K.-H. Lee and B. H. Lee, *ACS Appl. Mater. Interfaces*, 2015, **7**, 16775–16780.

66 M. Shafiei, J. Bradford, H. Khan, C. Piloto, W. Wlodarski, Y. Li and N. Motta, *Appl. Surf. Sci.*, 2018, **462**, 330–336.

67 W. Yan, M. A. Worsley, T. Pham, A. Zettl, C. Carraro and R. Maboudian, *Appl. Surf. Sci.*, 2018, **450**, 372–379.

68 N. Barsan and U. Weimar, *J. Phys. Condens. Matter*, 2003, **15**, R813.

69 K.-I. Choi, H.-J. Kim, Y. C. Kang and J.-H. Lee, *Sensors Actuators B Chem.*, 2014, **194**, 371–376.

70 Z. Bai, C. Xie, M. Hu, S. Zhang and D. Zeng, *Mater. Sci. Eng. B*, 2008, **149**, 12–17.

71 O. Merdrignac-Conanec, Y. Bernicot and J. Guyader, *Sensors Actuators B Chem.*, 2000, **63**, 86–90.

72 G. Deokar, P. Vancsó, R. Arenal, F. Ravaux, J. Casanova-Cháfer, E. Llobet, A. Makarova, D. Vyalikh, C. Struzzi, P. Lambin, M. Jouiad and J. F. Colomer, *Adv. Mater. Interfaces*, , DOI:10.1002/admi.201700801.

73 A. Kumar, R. Chandra and V. K. Malik, *Thin Solid Films*, 2021, **725**, 138625.

74 S. Sharma, A. Kumar, N. Singh and D. Kaur, *Sensors Actuators B Chem.*, 2018, **275**, 499–507.

75 J. Wang, Y. Shen, X. Li, Y. Xia and C. Yang, *Sensors Actuators B Chem.*, 2019, **298**, 126858.

76 R. Kumar, N. Goel and M. Kumar, *ACS sensors*, 2017, **2**, 1744–1752.

77 M. Ikram, L. Liu, Y. Liu, L. Ma, H. Lv, M. Ullah, L. He, H. Wu, R. Wang and K. Shi, *J. Mater. Chem. A*, 2019, **7**, 14602–14612.

78 J. Bai, Y. Shen, S. Zhao, Y. Chen, G. Li, C. Han, D. Wei, Z. Yuan and F. Meng, *Sensors Actuators B Chem.*, 2022, **353**, 131191.

79 Z. Li, H. Li, Z. Wu, M. Wang, J. Luo, H. Torun, P. Hu, C. Yang, M. Grundmann and X. Liu, *Mater.*

Horizons, 2019, **6**, 470–506.

Conclusions and Future Perspectives

This chapter summarises the important accomplishments of this research work, highlighting the advantages of the growth process as well as the enhancement of gas sensing properties resulting from adding functionality with different nanomaterials.

In this thesis, the developed CVD growth process outlined demonstrates a simple and efficient route to synthesize large-area multi-layered TMDs materials, which have strong prospects for scalable production. Moreover, direct growth of these layered materials is achieved on a variety of substrates (such as Si/SiO_2 and alumina substrates with interdigitated platinum electrodes). For instance, the combination of aerosol-assisted CVD with atmospheric pressure CVD technique resulted in the 3D assembly of WS_2 nanosheets on WS_2 nanoneedles. It is worth noting that the assembly of WS2 nano triangles on 1D nanoneedles or nanorods shows a highly increased porosity and increased number of edges for gas interaction in comparison to the more closely packed nanoflake assembly.

Moreover, a unique and efficient route to add functionality to the metal sulphides is also explored. For instance, we have been able to synthesise WS_2 loaded with different metal oxides (PtO/PdO). This method is not limited to only these materials and other materials can be incorporated into the host matrix by adopting this 2-step growth process which takes advantage of a combination of AACVD with the CVD technique.

In an attempt to study the gas sensing properties of other TMDs materials, WSe_2 based gas sensor was developed. This material was grown in the Namur Institute of Structured Matter (NISM), University of Namur, in the lab of Prof. Jean François Colomer (collaborator). It was found that for growing selenium based TMDs, it is necessary to incorporate H_2 in the CVD chamber for the reaction to take place. This is because, unlike Sulfur, Selenium is not a very strong reductant. Therefore, WSe_2 nanomaterial was grown via selenization of WO_3 nanomaterial in the presence of H_2 and Ar gas during the growth process. It was found that using this technique vertically aligned 2H-WSe_2 nanosheets assembled on nanowires were obtained.

Moreover, the growth of 2D layered materials in a single step was also explored during this research work. For instance, optimising the gas flow rate in an atmospheric pressure CVD system enables achieving the self-organized, bottom-up growth of sponge-like, 3D assemblies of MoS_2 nanosheets. The gas flow rate was found to have a strong influence on the morphology of the MoS_2 grown. When the growth was conducted at 10 ml/min Ar flow, a discontinuous layer of sparsely dispersed MoS_2 nanotriangles was obtained. When the flow was set to 70 ml/min, quadrilateral MoS_2 nanostructures were synthesized. Finally, at 30 ml/min, a thick layer of edge-enriched 3D assemblies of MoS_2 nanosheets was achieved. In contrast to the other two flow rates tested, at 30 ml/min the growth of MoS_2 nanosheets changes from in-plane

to out-plane, which is advantageous for achieving 3D, sponge structures with a higher surface. 30 ml/min represents an ideal compromise between the surface interaction and the mass transport of precursor molecules. Moreover, material characterization results revealed the formation of edge enriched 3D assemblies of MoS_2 nanosheets with the presence of some MoO_{3-x} impurities. Based on the growth mechanism, these impurities were coming from the bottom layer of the grown film, where quadrilateral nanostructures were not completely sulfurized.

Furthermore, all these grown materials indicate their potential for next-generation gas sensors. The ability to manipulate the electrical structure of TMD semiconductors is a fundamental key aspect to their practical use in electronics and semiconductors. In particular, our results indicate that multi-layered transition metal dichalcogenides have high sensitivity towards NO_2 molecule detection due to the enhanced charge transfer.

Gas sensing results showed that WS_2 NTs exhibited excellent NO_2 gas sensing characteristics at low operating temperatures, even at room temperature. The high sensitivity observed and the unprecedentedly low limit of detection achieved (in the ppt range), were attributed to the porous surface and the increased number of sulfur edges in WS_2 nano triangles (NTs), which were created by the random 3D assembly of WS_2 nanosheets on WS_2 nanoneedles. Furthermore, WS_2 NTs have shown excellent response stability during long-term stability tests conducted over 8 months. Hence, these results shed light on the important role played by the morphology in enhancing sensor performance.

Moreover, decoration of WS_2 nanoneedles/nanotriangles with Cu_2O nanoparticles dramatically increases their sensitivity and selectivity towards H_2S (i.e., 11-times increase in response compared to that of pristine WS_2 sensor from 54% to 610%. Additionally, this hybrid nanomaterial shows negligible moisture cross-sensitivity with a small drop in sensing response from 610% to 596%, which is rarely found in metal oxides. Moreover, the fabricated sensor shows excellent stability over 7 months with only 16% fall-off in its sensing response from 610% to 510%.

To further improve the sensitivity at room temperature loading with different metal oxides, such as loading WS_2 with palladium oxide and platinum oxide resulted in enhanced gas sensing results towards low concentrations of NO_2 detection. The sensing results revealed that loading of WS_2 nanosheets with either PtO or PdO ions significantly increases their gas response towards NO_2 (i.e., double the response as compared to pristine WS_2 sensor from 10%

to 26.5%, thereby lowering the detection limit of the sensor (lower than 25 ppb after loading, which is far lower than that of pristine WS_2 gas sensor). Moreover, when compared to the WS_2/PtO sensor, the WS_2/PdO sensor is extremely selective for NO_2, exhibiting little or no response to other gases.

The as-grown WSe_2 material is used to develop a chemoresistive type gas sensor having dual sensitivity towards NH_3 and NO_2 gas detection, depending on the operating temperature used. To our knowledge, no previous research on WSe_2-based gas sensors has yielded such intriguing results. The cross-sensitivity test revealed that NO_2, H_2, C_6H_6, and CO have a negligible effect on NH_3 gas detection. Moreover, water vapour at 50% relative humidity also resulted in having no interference to the measure of NH_3 gas, attesting promising characteristics of WSe_2 for gas sensing applications.

These 3D assemblies are porous (i.e. possess a high surface for interacting with gases) and their edges are highly reactive, which results in highly enhanced sensing properties. Gas sensing performances of edge enriched 3D assemblies of MoS2 were tested against NH_3, NO_2 and humidity. At the optimal working temperature, the fabricated sensor exhibited an n-type semiconducting behaviour towards the studied gases. The sensor was selective to NH_3 at room temperature and towards NO_2 at 100 ºC. To the best of our knowledge, none of the reported works on MoS_2-based gas sensors has shown such interesting results. Regarding the experimental detection limit, it was below 2 ppm for NH_3 and below 20 ppb for NO_2. Finally, the sensor displayed high resistivity against water molecules since the sensor response towards 800 ppb of NO2 has been slightly increased (R=70 %) compared to dry background (R= 65 %).

Future Work

We may anticipate 2D TMDs to find practical applications in electronics, optoelectronics, and energy technologies while new synthesis methods are developed in the research laboratories.

This thesis provides the groundwork for (1) direct synthesis of large area 2D TMDs on commercial substrates thereby avoiding the transfer steps required, (2) simple and efficient route to add functionality to TMDs host matrix, (3) design of chemoresistive sensors for gas sensing applications.

Undoubtedly, TMDs materials have shown great potential in gas sensing applications. Despite this, there are a few limitations of the use of these materials that might be addressed in the future to be commercialised for real-world applications. Furthermore, the gas sensing mechanism is still poorly understood.

These limitations can be overcome in the near future by using heterostructures and hybridization with a variety of materials to achieve structural alterations and add functionality, resulting in innovative functional composites for gas sensing applications. In intralayer bonding, these 2D TMDs composites refer to more than one type of transition metal or more than one type of chalcogenide while, in interlayer bonding these 2D layered materials bond with another element. For instance, functionalization of MoS_2, WS_2, and WSe_2, with other nanomaterials like ZnO, CeO_2, and several other metal oxides. Moreover, heterostructures can be fabricated by incorporating two or more TMDs materials such as WS_2/MoS_2, $MoS_2/MoTe_2$ and so on.

Moreover, the widespread use of 2D TMDs has been aided by advancements in synthesis and modification methods. During the manufacture or disposal of 2D TMDs-based products, two-dimensional TMDs may reach the human respiratory system as airborne particles. As a result, 2D TMDs' biosafety must be evaluated.

Annex I

Supporting Information

Supporting Information for:

CVD growth of self-assembled 2D and 1D WS_2 nanomaterials for the ultrasensitive detection of NO_2

Aanchal Alagh,[+a] Fatima Ezahra Annanouch,[+a] Polona Umek,[b] Carla Bittencourt,[c] Ayrton Sierra-Castillo,[d] Emile Haye,[d,e] Jean François Colomer*[d] and Eduard Llobet*[a]

[a.] Departament d'Enginyeria Electrònica, Universitat Rovira i Virgili, Països Catalans 26, 43007 Tarragona, Spain.

[b.] Condensed Matter Physics Department, Jožef Stefan Institute, Jamova cesta 39, 1000 Ljubljana, Slovenia.

[c.] Laboratory of Plasma-Surface Interaction Chemistry (PSI Chem), University of Mons, Av. Nicolas Copernic 1, 7000 Mons, Belgium.

[d.] Research Group on Carbon Nanostructures (CARBONNAGe), Namur Institute of Structured Matter (NISM), University of Namur, 61 Rue de Bruxelles, 5000 Namur, Belgium.

[e.] Laboratoire d'Analyse par Réaction Nucléaires (LARN), Namur Institute of Structured Matter (NISM), University of Namur, 61 Rue de Bruxelles, 5000 Namur, Belgium.

+ Authors with equal contributions to this work.

Corresponding Author

*Eduard Llobet, E-mail: eduard.llobet@urv.cat

*Jean-François Colomer: jean-francois.colomer@unamur.be

Figure S1 shows typical pictures of the sensors fabricated after the growth of tungsten oxide nanomaterials and thermal annealing (left) and after the final sulfurization step performed for the synthesis of WS_2 nanomaterial films (right).

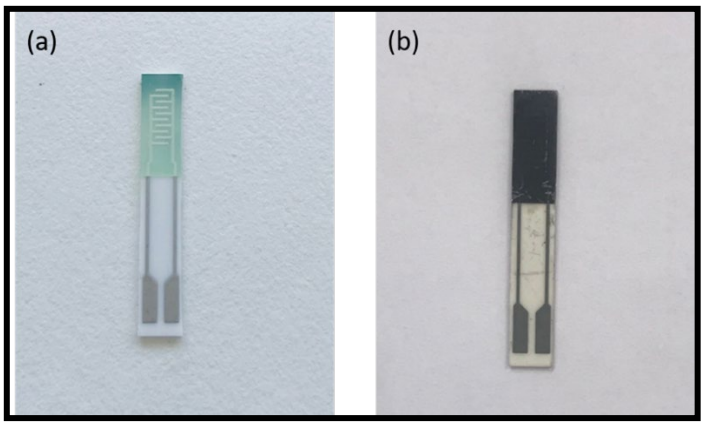

Figure S1. Alumina transducer employed to obtain chemoresistive sensors (a) WO_3 film after the annealing step, (b) WS_2 film obtained after the sulfurization of WO_3.

Figure S2 shows an XRD spectrum obtained from a WS_2 NTs sample. The peaks in the spectrum can be indexed to the hexagonal P63/*mmc* space group, indicating that the structure of the WS_2 phase is 2H-WS_2. Some of the peaks belong also to alumina, which is the substrate onto which the WS_2 NT sample was grown. This is in perfect agreement with what was observed for WS_2 NF samples.

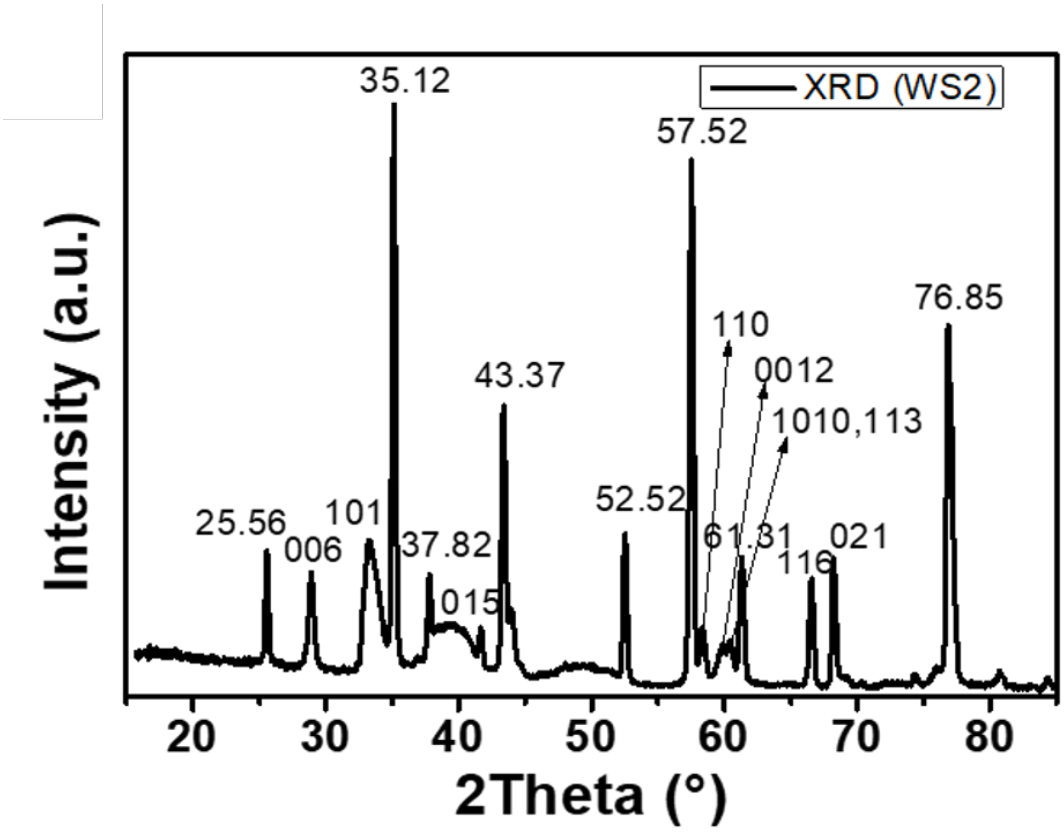

Figure S2. XRD diffractogram for a WS_2 NT sample.

The TEM analysis revealed the formation of WS_2 nanotubes at the tips of WS_2 nanoneedles. **Figure S3** shows a low magnification image (a) and a HRTEM image (b) of one of such nanotubes.

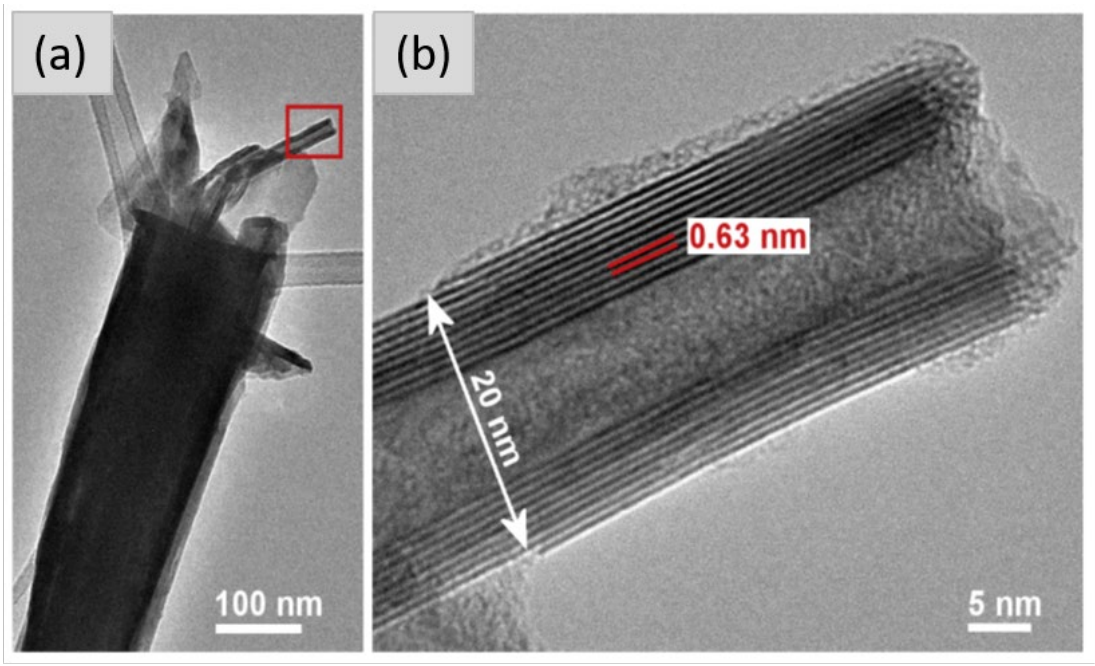

Figure S3. TEM image of WS_2 nanoneedle tip (a). HRTEM image of WS_2 nanotube with an outer diameter of 20 nm, growing from WS_2 nanoneedle. The measured interlayer distance of the nanotubes walls is 0.63 nm (b). The red frame in image (a) indicates an area of image (b).

Figure S4 displays the sensor responses toward reducing gases. The responses were calculated by using the following equation:

$$R = \frac{(R_{gas} - R_{air})}{R_{air}} * 100 \qquad (1)$$

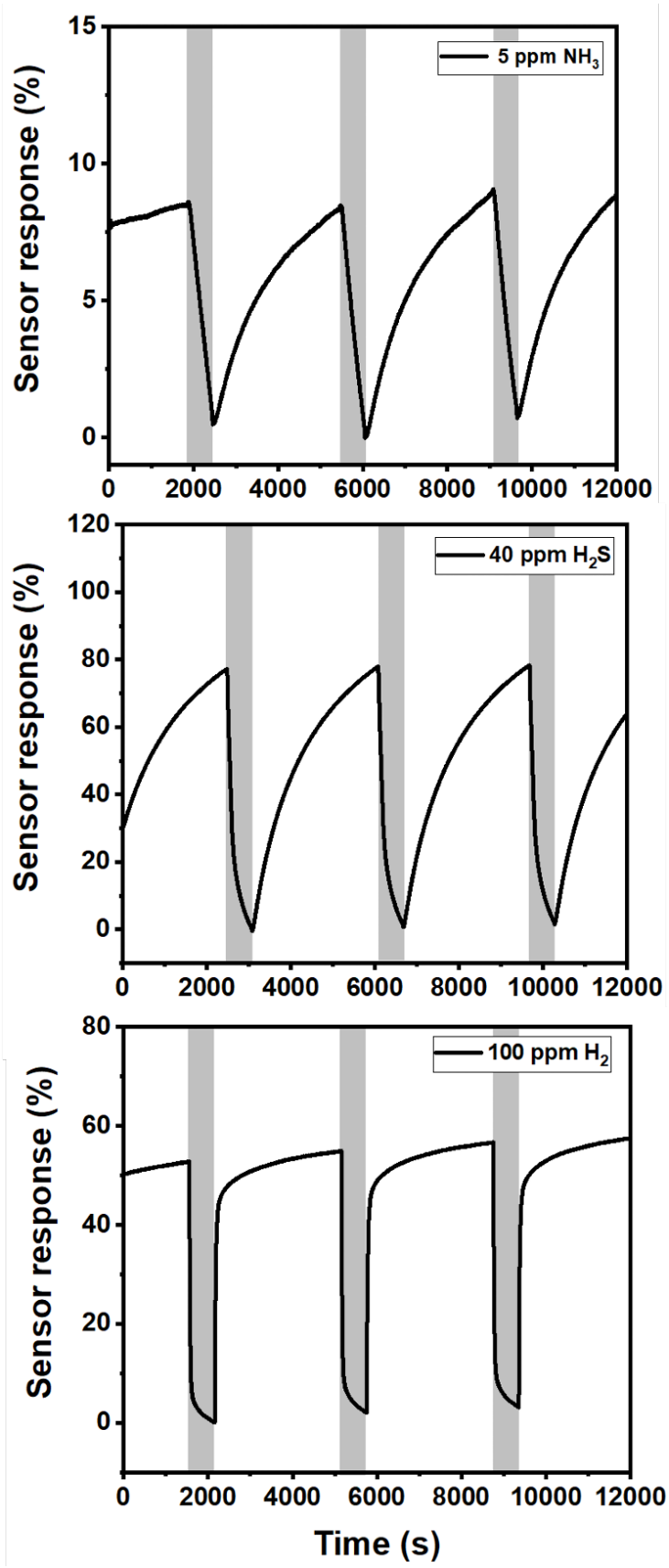

Figure S4. Typical sensor responses towards 5 ppm of NH_3, 40 ppm of H_2S and 100 ppm of H_2, recorded at 150 °C.

Long-term stability study

The long-term stability of the sensors was studied. NO_2 measurements were repeated at regular intervals over a long period and the evolution of the baseline resistance and sensor response was monitored. For WS_2 NFs, both baseline resistance and NO_2 response show a significant decreasing trend over time. The response towards 800 ppb of NO_2 diminishes from 26.65% to 19.45% over a period of 19 weeks. The behavior for WS_2 NTs is different. While the baseline resistance shows a clear decreasing trend, sensor response towards NO_2 shows remarkable stability, as it varies from 55.95 % to 54.15% over a period of 35 weeks.

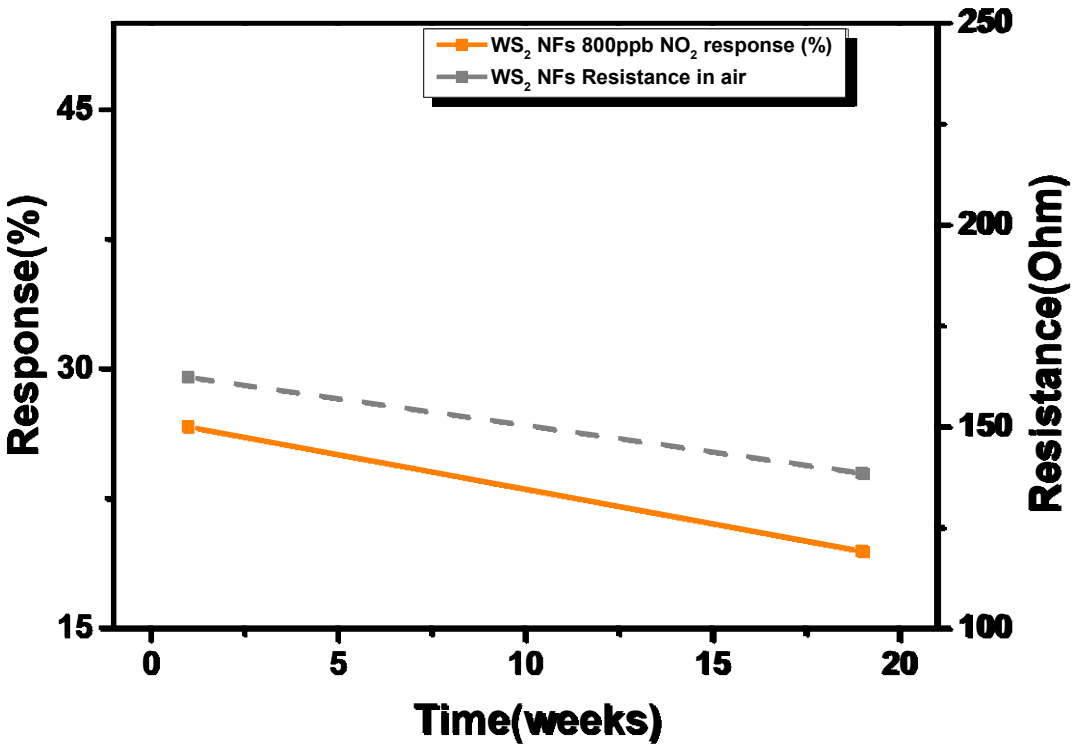

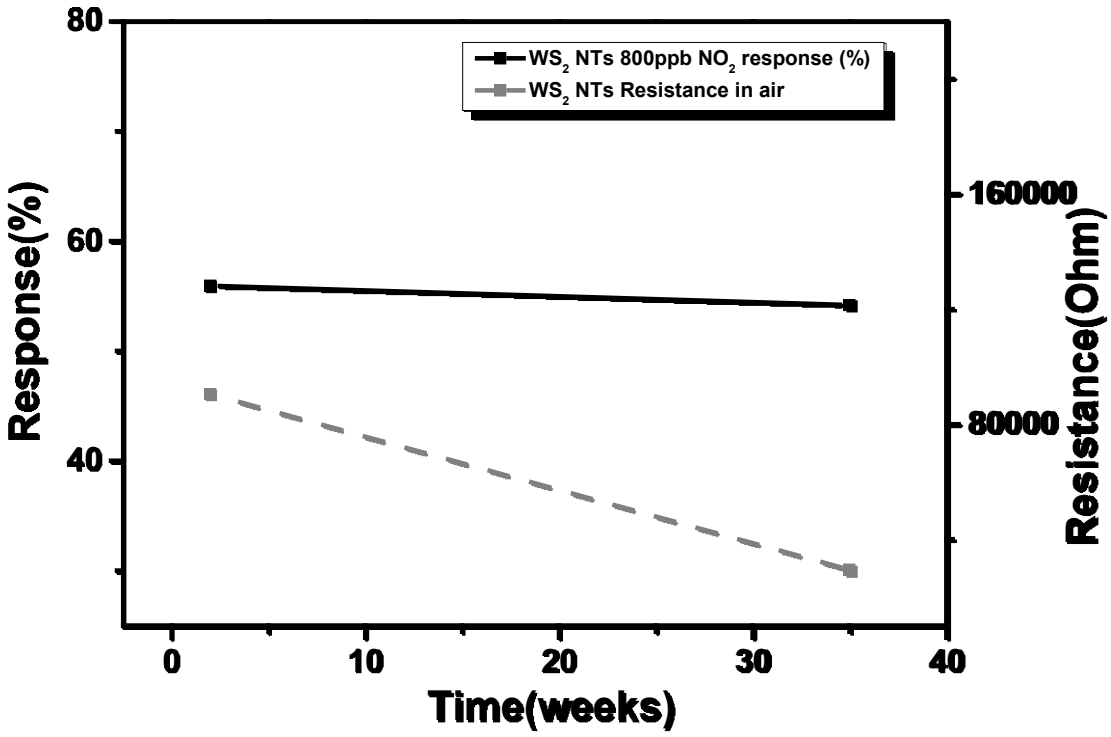

Figure S5: Long-term stability study. Evolution of the baseline resistance and sensor response to nitrogen dioxide over time. Upper panel: Stability study for WS_2 NFs. Lower panel: Stability study for WS_2-NTs.

Supporting Information

An ultrasensitive room-temperature H_2S gas sensor based on 3D assembly of Cu_2O decorated WS_2 nanomaterial

Aanchal Alagh*, Fatima Ezahra Annanouch*, Polona Umek[+], Carla Bittencourt, Jean Francois Colomer, Eduard Llobet*

Cross section of WO_3 and WS_2

Fig. S1 shows cross section of WO_3 and WS_2 nanomaterial. The thickness of WO_3 and WS_2 nanofilms were measured using a field emission scanning electron microscope equipped with an ETD detector. As depicted in Fig.S1, the thickness of WO_3 nanoneedles film was in the range of 6-7 µm, which after sulfurization changed to form much thicker films of approximately 31µm in width.

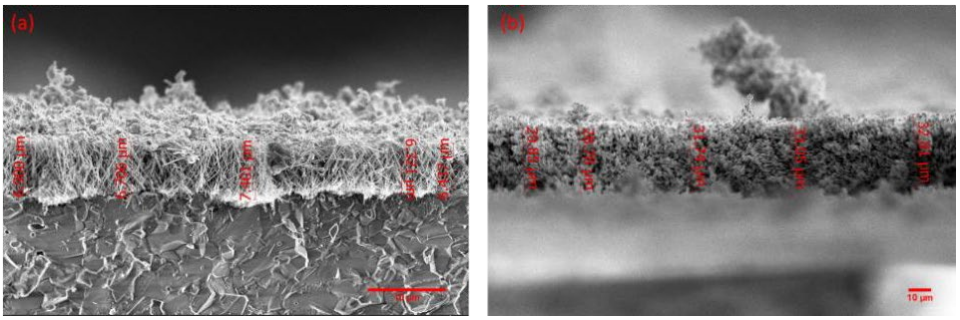

Figure S1 Cross section depicting thickness of (a) WO_3 nanoneedles (b) WS_2 nanotriangles/nanoneedles.

Submitted on 12 Februray 2021
An earlier version of this paper was presented at the IEEE sensors 2020 conference.
This project has received funding from the European Union's Horizon 2020 research and innovation programme under the Marie Skłodowska-Curie grant agreements No. 713679 and 823895, and from MININN-FEDER via grant no. RTI2018-101580-B-I00F.E.A. is a JdC fellow. E.L. is supported by the Catalan Institution for Research and Advanced Studies via the 2018 Edition of the ICREA Academia Award. CB and JFC are research associates of FNRS (Belgium).
Aanchal Alagh is a MSCA−COFUND PhD fellow at the Universitat Rovira i Virgili (e-mail: alagh.aanchal@urv.cat).
Fatima Ezahra Annanouch is a Post-Doctoral fellow at the Universitat Rovira i Virgili. (e-mail: fatimaezahra.annanouch@urv.cat).
Polona Umek is a research fellow at the Josef Stefan Institute in Ljubljana, Slovenia (e-mail: polona.umek@ijs.si).
Jean François Colomer is a research fellow of the Belgian National Fund for research at the University of Namur (e-mail: jean-francois.colomer@unamur.be).
Eduard Llobet is a professor at the Universitat Rovira i Virgili (e-mail: eduard.llobet@urv.cat).

Raman Spectrum of Cu_2O/WS_2

Fig.S2 depicts Raman spectrum obtained for the as-synthesized Cu_2O/WS_2 nanofilms. The spectrum depicts two sharp peaks at 349 cm^{-1} and 415 cm^{-1} which corresponds to the 2H-WS_2. No other peaks were obtained, which is possibly due to the low doping amount of Cu_2O (less than 3%).

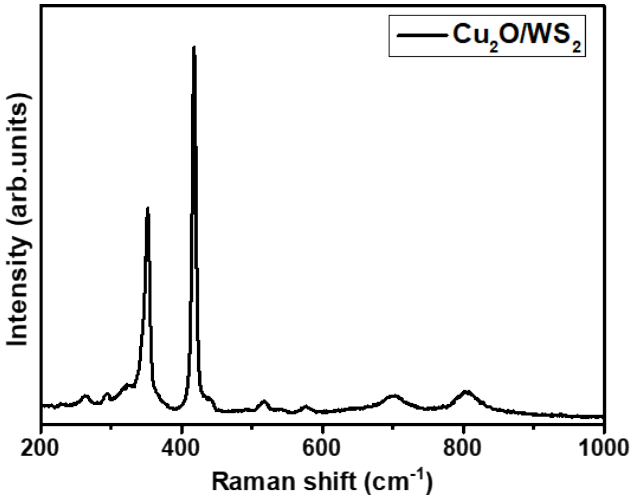

Figure S2 Raman spectrum of Cu_2O NPs doped WS_2 NTs/NNs.

Fig.S3 depicts the response and recovery time calculated for the Cu_2O/WS_2 sensor towards 40 ppm H_2S at a working temperature of 150˚C. The response and recovery time for pristine WS_2 sensor towards 40 ppm of H_2S gas were 230 s and 1710 s respectively. With the addition of Cu_2O NPs to WS_2 nanomaterial, the response and recovery time were reduced to 141 s and 328 s respectively.

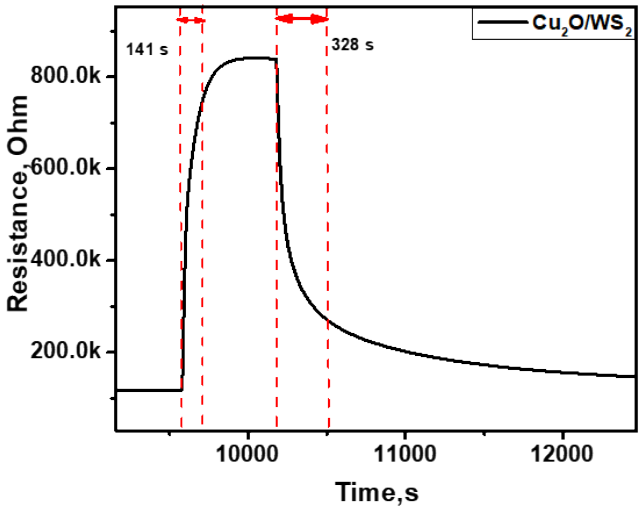

Figure S3 The response and recovery time of the Cu_2O/WS_2 sensor towards 40 ppm H_2S at a working temperature of 150˚C.

Fig.S4 depicts the long-term stability study. The stability of the fabricated sensors was monitored over a period of 7 months (approximately 29 weeks). H_2S measurements were repeated at regular intervals and the evolution of the baseline resistance as well as sensor response was examined. Although the baseline resistance shows a drift for both sensors over time, the gas sensing response of Cu_2O/WS_2 sensor towards H_2S shows good stability (Fig.S4(a,b)) and repeatability (Fig.S4(c)) . The sensing response was reduced compared to the initial measurements by only 16%.

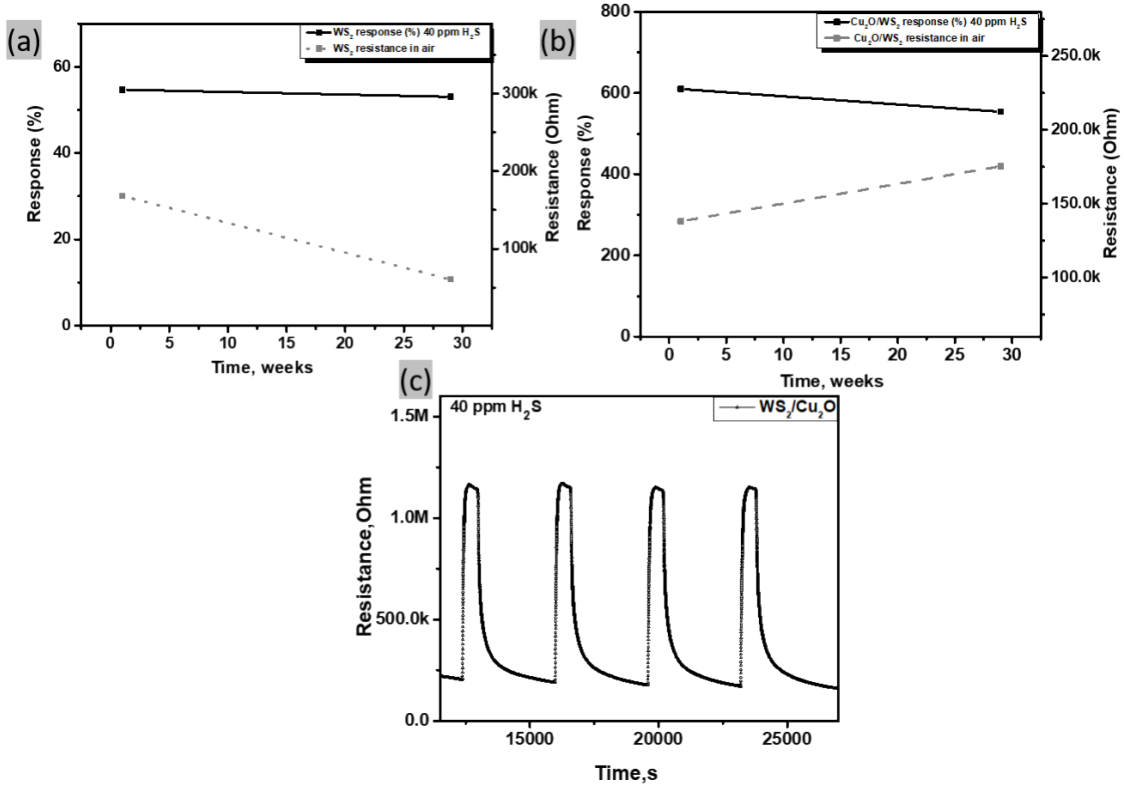

Figure S4 Long term stability study. Evolution of the baseline resistance and sensor response to H_2S over time. Stability study for (a) WS_2, (b) Cu_2O/WS_2, (c) electrical resistance towards 40 ppm H_2S at 150º C, recorded after 29 weeks.

The response towards other gases such as NO_2 and NH_3 was studied to examine the selectivity of the as fabricated Cu_2O/WS_2 sensor. The results obtained are summarized in Fig.S5 which are also compared with that of pristine WS_2 sensor. The results demonstrate the important role played by Cu_2O in enhancing the sensitivity and selectivity of WS_2 towards H_2S gas detection.

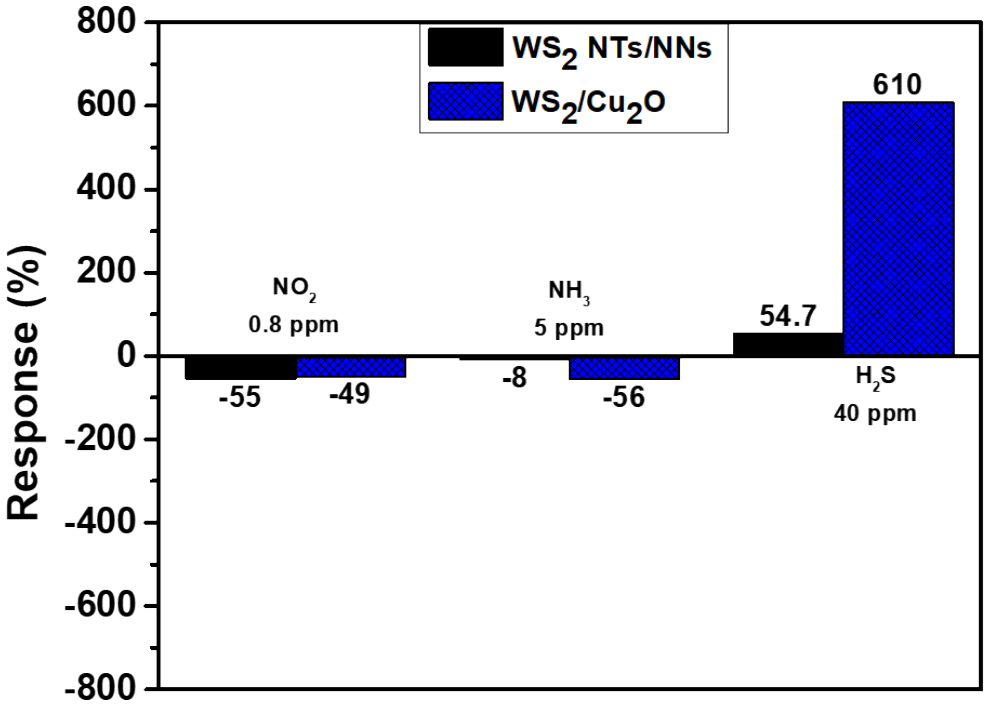

Figure S5 Response histogram of WS_2 NTs/NNs and Cu_2O/WS_2 sensors operated at 150 ºC.

Fig.S6 depicts the schematic diagram of the H_2S sensing process on the surface of the Cu_2O/WS_2 nanomaterial sensor.

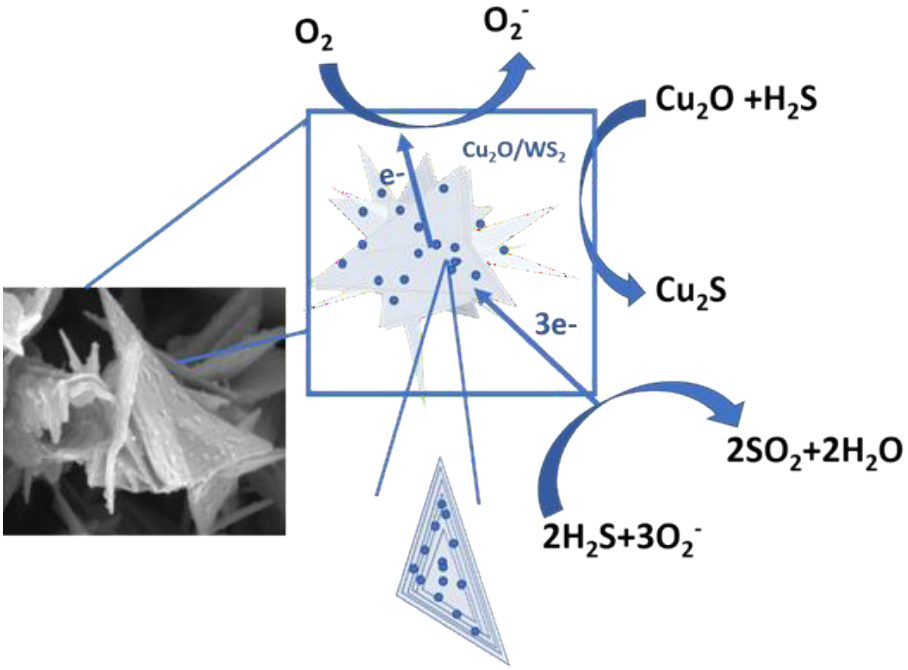

Figure S6 Schematic diagram of the H_2S sensing process on the surface of the Cu_2O/WS_2 nanomaterial sensor.

The sensing mechanism of WS2 nanostructure is based on charge transfer process. When the sensor is exposed to air, the O_2 molecules readily adsorb on the WS_2 surface to form chemisorbed oxygen species such as O_2^- at room temperature (see eq. 1 and 2) [1].

$$O_2\ (gas) \rightarrow O_2\ (ads)$$

$$O_2\ (ads) + e^- \rightarrow O_2^-\ (ads)$$

However, once the material is exposed to a reducing gas such as H_2S, this later donates electrons to the multi-layered WS_2, thereby decreasing the concentration of charge carriers (holes) which increases the overall resistance of the host matrix. Eq. 3 shows the chemical reaction occurring at the surface. The free electrons are released back to the surface of WS_2 [1].

$$2H_2S + 3O_2^- \rightarrow SO_2 + H_2O + 3e^-$$

Table S1 gives more insights by comparing the performance in the detection of H_2S reported in this paper with those found in the literature. From the results obtained, the fabricated Cu_2O functionalized WS_2 sensor shows outstanding gas responses with high sensitivity towards H_2S gas.

Table S1 Comparison of the sensing properties of H_2S resistive and FET type gas sensors based on different sensing material structures from the literature and the two WS_2 sensor types reported in this work.

Material	Concentration (ppm)	Operating temp.(˚C)	Response (%)	Sensitivity (Response /ppm)	References
Cu_20/WS_2	40	150	610	0.152	This work
Cu_20/WS_2	40	25	138	0.034	This work
NTs/NNs	40	150	54.7	0.013	This work
NTs/NNs	40	25	10.0	0.002	This work
CuO/MoS_2	30	RT	61	0.020	[2]
CuO-SWCNTs	50	125	28	0.005	[3]
SnO2/rGO	50	125	27	0.005	[4]
CeO2 NWs	50	RT	44	0.008	[5]
Al-ZnO	150	200	51	0.003	[6]
PANI-HCl/SSA	50	RT	47	0.009	[7]
Ti-ZnO	30	200	37	0.012	[8]

REFERENCES

[1] D. Liu, Z. Tang, and Z. Zhang, “Comparative study on NO2 and H2S sensing mechanisms of gas sensors based on WS2 nanosheets,” *Sensors Actuators, B Chem.*, vol. 303, no. 2, p. 127114, 2020, doi: 10.1016/j.snb.2019.127114.

[2] D. Zhang, J. Wu, and Y. Cao, “Ultrasensitive H2S gas detection at room temperature based on copper oxide/molybdenum disulfide nanocomposite with synergistic effect,” *Sensors Actuators, B Chem.*, vol. 287, no. February, pp. 346–355, 2019, doi: 10.1016/j.snb.2019.02.008.

[3] M. Asad and M. H. Sheikhi, "Highly sensitive wireless H2S gas sensors at room temperature based on CuO-SWCNT hybrid nanomaterials," *Sensors Actuators, B Chem.*, vol. 231, pp. 474–483, 2016, doi: 10.1016/j.snb.2016.03.021.

[4] J. Chu *et al.*, "Highly selective detection of sulfur hexafluoride decomposition components H2S and SOF2 employing sensors based on tin oxide modified reduced graphene oxide," *Carbon N. Y.*, vol. 135, pp. 95–103, 2018, doi: 10.1016/j.carbon.2018.04.037.

[5] Z. Li *et al.*, "Hydrothermally synthesized CeO2 nanowires for H2S sensing at room temperature," *J. Alloys Compd.*, vol. 682, pp. 647–653, 2016, doi: 10.1016/j.jallcom.2016.04.311.

[6] P. S. Kolhe, A. B. Shinde, S. G. Kulkarni, N. Maiti, P. M. Koinkar, and K. M. Sonawane, "Gas sensing performance of Al doped ZnO thin film for H2S detection," *J. Alloys Compd.*, vol. 748, pp. 6–11, 2018, doi: 10.1016/j.jallcom.2018.03.123.

[7] X. Dong, X. Zhang, X. Wu, H. Cui, and D. Chen, "Investigation of gas-sensing property of acid-deposited polyaniline thin-film sensors for detecting H2S and SO2," *Sensors (Switzerland)*, vol. 16, no. 11, 2016, doi: 10.3390/s16111889.

[8] P. S. Shewale and Y. S. Yu, "H2S gas sensing properties of undoped and Ti doped ZnO thin films deposited by chemical spray pyrolysis," *J. Alloys Compd.*, vol. 684, pp. 428–437, 2016, doi: 10.1016/j.jallcom.2016.05.178.

Supporting Information for:

PdO and PtO doped WS_2 boosts NO_2 gas sensing characteristics at room temperature

A. Alagh [a], *F. E. Annanouch* [a,*], *K. Al Youssef* [b], *C. Bittencourt* [b],

F. Güell [c], *P. R. Martínez-Alanis* [c], *M. Reguant* [c] *and Eduard Llobet* [a]

[a] Departament d'Enginyeria Electronica, Universitat Rovira i Virgili, Països Catalans 26, 43007 Tarragona, Spain.

[b] Laboratory of Plasma-Surface Interaction Chemistry (PSI Chem), University of Mons, Av. Nicolas Copernic 1, 7000 Mons, Belgium

[c] ENFOCAT-IN^{2}UB, Universitat de Barcelona, C/Martí i Franquès 1, 08028 Barcelona, Catalunya, Spain.

[*]Corresponding author: fatimaezahra.annanouch@urv.cat

AACVD reactor

Fig. S1 displays an image of the AACVD reactor used for the synthesis of pristine and functionalized WO_3 nanoneedles.

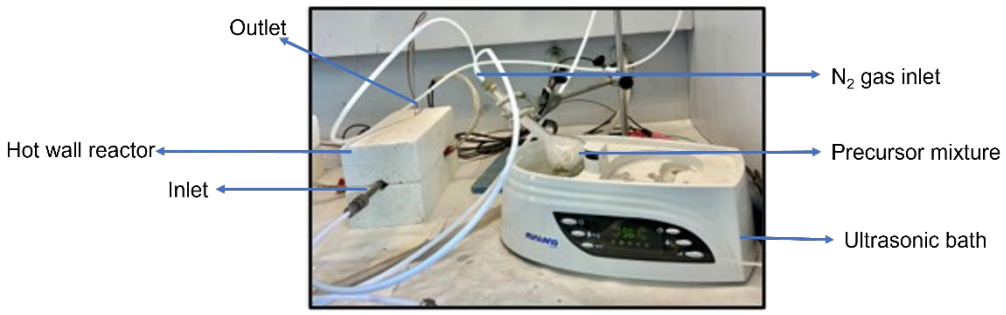

Fig. S1 Image of AACVD reactor.

Home-made APCVD reactor

Fig. S2

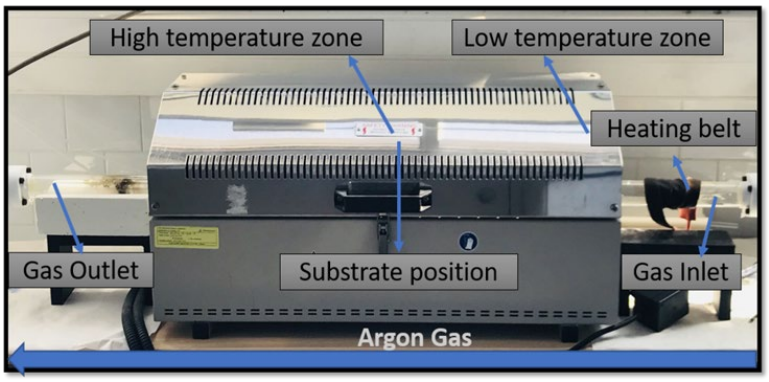

Fig. S2 Image of home-made APCVD reactor used for second step synthesis of WS_2.

XPS Spectra of WO_3 and WS_2 samples

Pristine, and functionalised samples were analysed and compared with the sulfurized samples using XPS spectroscopy. The XPS survey spectra in Fig. S3 shows the presence of W, C and O in WO_3 samples while for WS_2, an additional signal associated with the presence of sulphur atoms is observed.

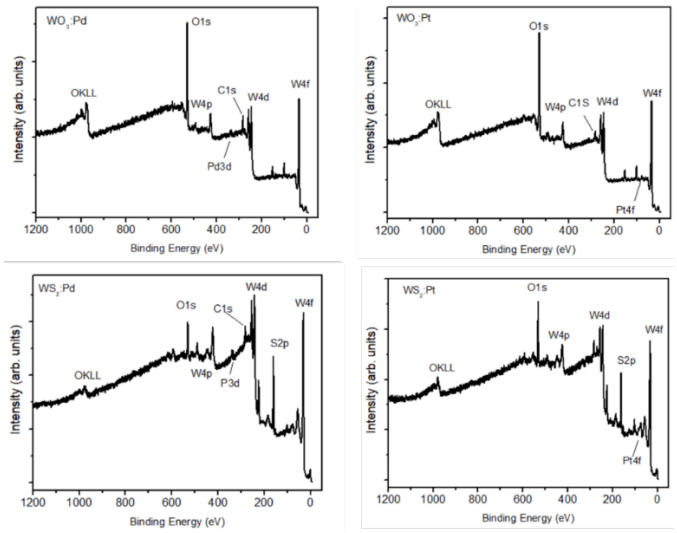

Fig. S3 XPS survey spectra shows the presence of WO_3 and WS_2 samples.

Figure S4 depicts four replicate measurement sequences towards NO_2 with gas concentration of 50 ppb. The sensing response of the doped sensors is around 6% whereas

pristine WS_2 shows no response at such a low concentration of NO_2. For 50 ppb of NO_2 gas concentration, the WS_2/PtO sensor displays little or no drift in response, whereas WS_2/PdO senor shows substantially higher drift in response. The high stability of the WS_2/PtO sensor can be ascribed to the high crystallinity of the WS_2/PtO composite.

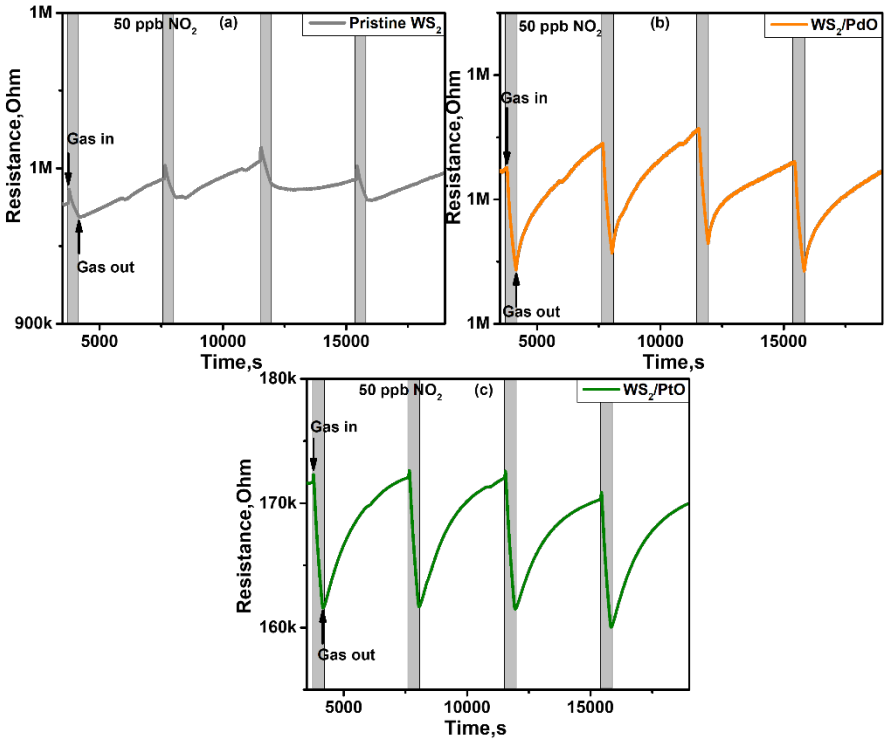

Fig. S4 Electrical resistance change of Electrical resistance change of (a) pristine WS_2 (grey), (b) WS_2/PdO (orange) and (c) WS_2/PtO (olive) towards NO_2 at 50 ppb, operated at room temperature.

Selectivity analysis

Fig.S5 displays the gas sensing performance of both doped and undoped sensors towards reducing gases such as, H_2, CO, NH_3, H_2S. Sensors that do not respond to a given analyte are excluded. For instance, Fig. S5 (a) and (b) displays the gas sensing properties of WS_2/PtO towards hydrogen (100 ppm) and carbon monoxide (50 ppm) gas, with 15.7% and 4.9% response for each target gas, respectively.

The other two sensors (pristine WS_2, as well as WS_2/PdO) showed negligible response towards these gases. Furthermore, only pristine WS_2 sensor showed an acceptable response when the sensors were subjected to NH_3 and H_2S gas (8.2% towards 10 ppm NH_3, whereas when exposed to 10 ppm H_2S the sensor response is determined to be 9%). Also, the resistance of the pristine WS_2 sensor, as well as that of the PtO/WS_2 sensor, increases in the presence of the target gas (reducing gas), indicating the p-type features of each. PdO/WS_2 sensor, on the other hand, displays no reaction to any of the four gases tested (NH_3, CO, H_2 and H_2S) indicating its superior selectivity towards NO_2 gas detection.

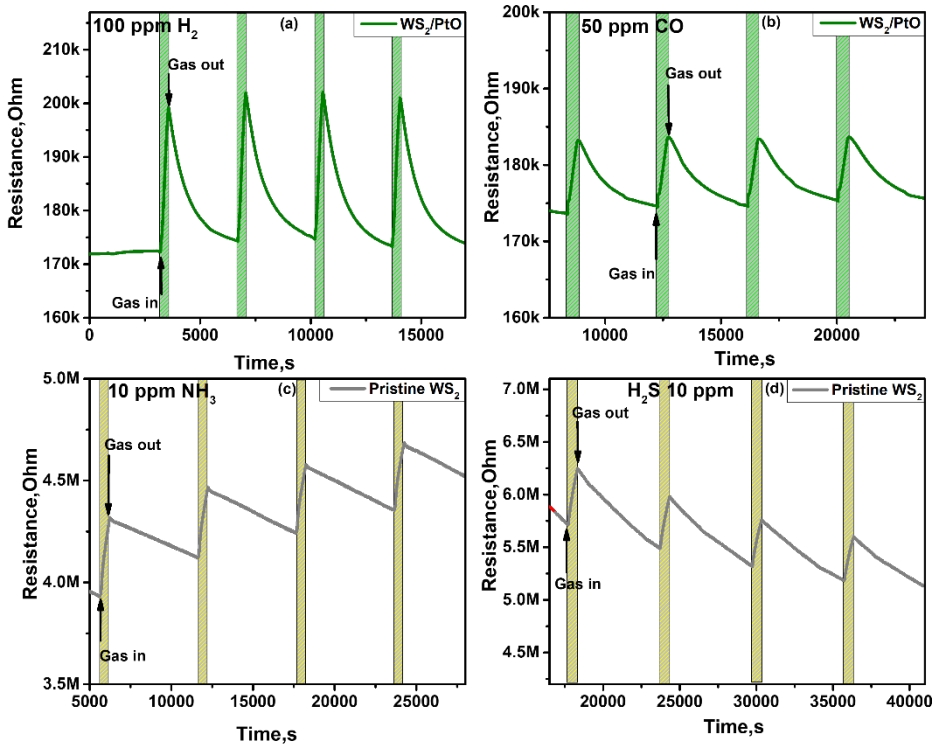

Fig. S5 Electrical resistance change of (a, b) WS_2/PtO sensor towards 100 ppm H_2 and 50 ppm CO, respectively, (c, d) pristine WS_2 sensor towards 10 ppm of NH_3 gas and 10 ppm H_2S gas, respectively, operated at room temperature.

Stability Study

Fig.S6 depicts the long-term stability study. The stability of the fabricated sensors was monitored over a period of 2.5 months (6 weeks). NO_2 measurements were repeated after humidity exposure and the evolution of the sensor response was examined. During the tested period, pristine WS_2 sensor showed a significant rise in the response with 24% as compared to doped sensors which were much more stable. The gas sensing response for PdO doped WS_2 was calculated to be 38.5% and for the PtO doped WS_2 it was 30%. While initially the sensing response for pristine WS_2, PdO/WS_2 and PtO/WS_2 were recorded to be 10.5%, 26.5% and 27.5%.

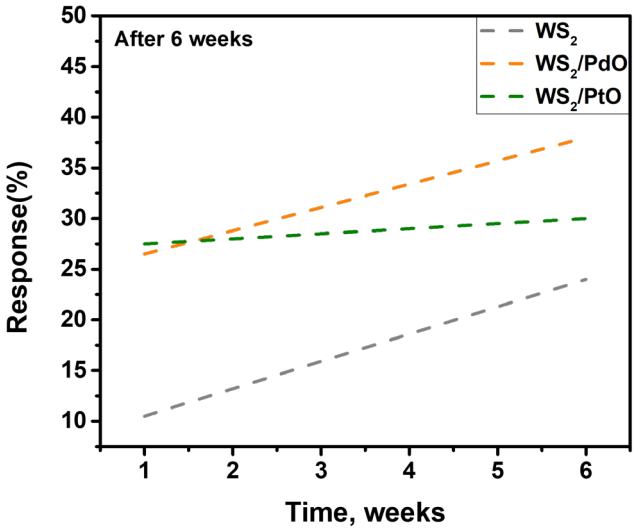

Fig. S6 Long term stability study for the responses of (a) WS_2, (b) PdO/WS_2 and (c) PtO/WS_2 towards 800 ppb NO_2 at room temperature, recorded after 6 weeks.

Supporting data for:

A robust gas sensor with bifunctional sensitivity and reliable anti-humidity ability based on WSe_2 nanoflower

Aanchal Alagh[a], Fatima Ezahra Annanouch[a], Ayrton Sierra-Castillo[b], Emile HAYE[c]

Jean-François Colomer[b], Eduard Llobet[a]

[b]: Department d'Enginyeria Electronica, Universitat Rovira I Virgili, Avenida Paisos Catalans 26,43007, Tarragona, Spain.

[b]: Research Group on Carbon Nanostructures (CARBONNAGe), University of Namur, Rue de Bruxelles 61, 5000 Namur.

[c]: Laboratoire d'Analyse par Réactions Nucléaires (LARN), Namur Insitute of Structured Matter (NISM), Université de Namur, Rue de Bruxelles 61, 5000 Namur.

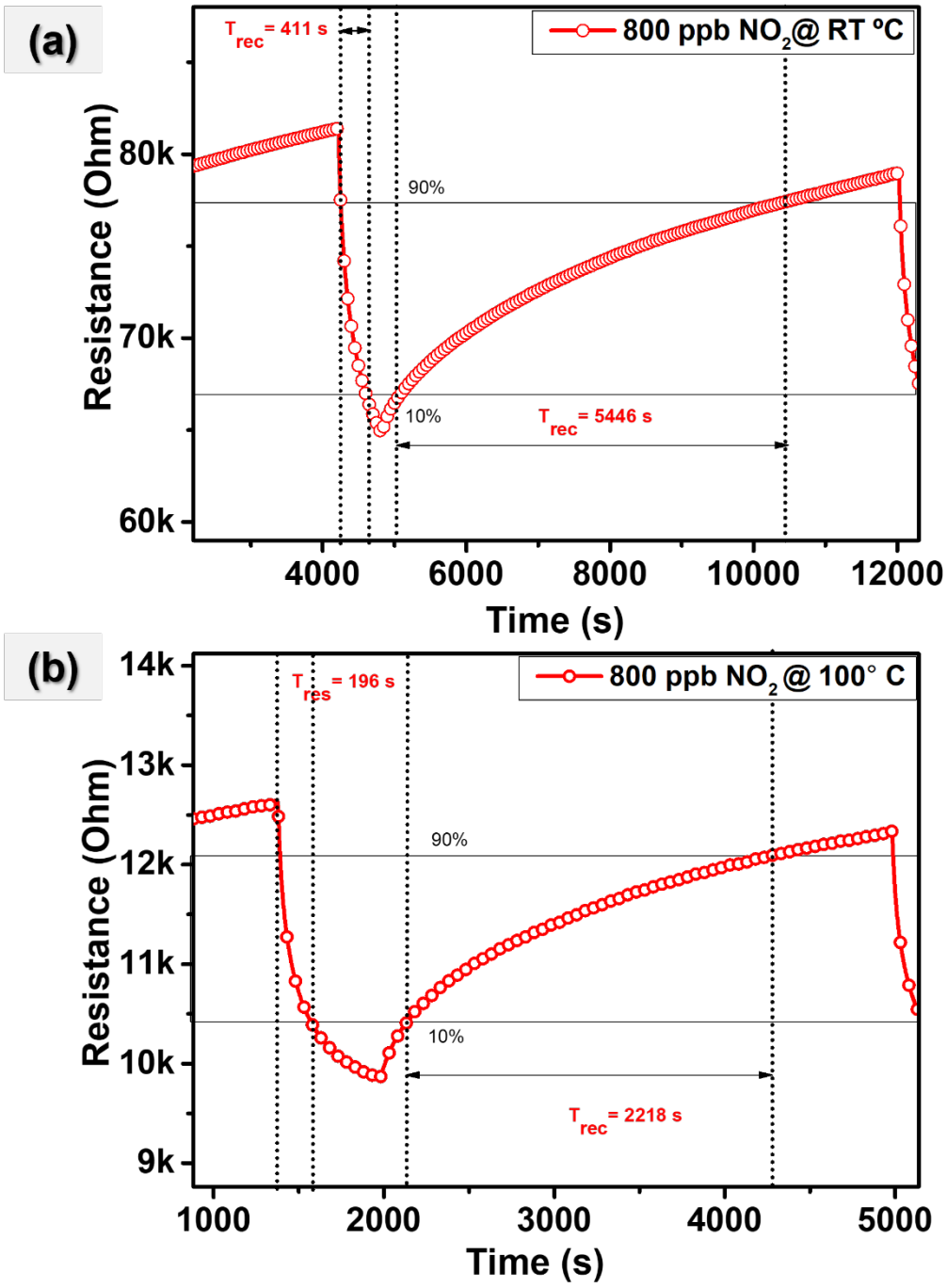

Fig.S 1 Response and recovery time of WSe_2 towards 800 ppb NO_2 at (a) room temperature, (b) at 100 ºC.

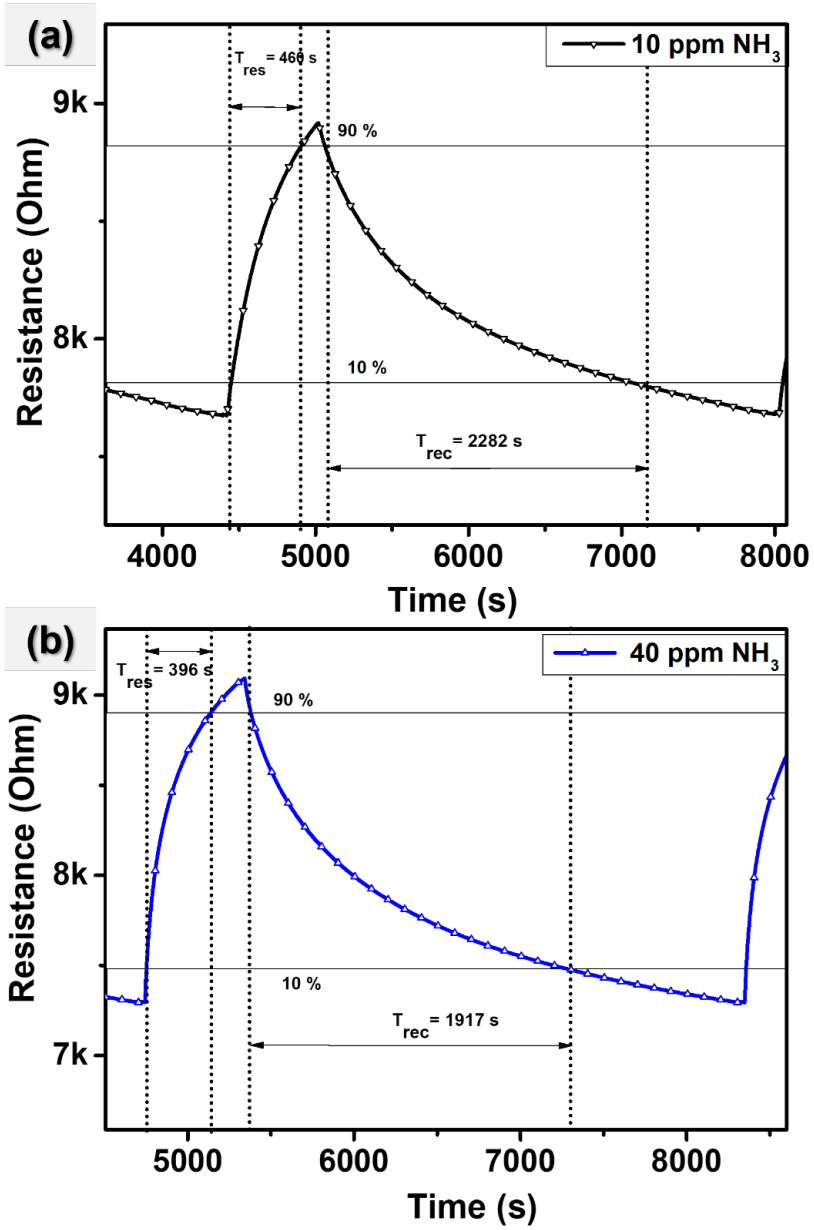

Fig.S2 Response and recovery time of WSe2 sensor towards (a) 10 ppm, (b) 40 ppm, NH_3 at 150 ºC.

Supporting Information of:

Controlled Growth of 3D Assemblies of Edge Enriched Multilayer MoS_2 Nanosheets for Dually Selective NH_3 and NO_2 Gas Sensors

Fatima Ezahra Annanouch [1*], Aanchal Alagh [1], Polona Umek [2], Juan Casanova [1], Carla Bittencourt [3] and Eduard Llobet [1]

[1] Departament d'Enginyeria Electronica, Universitat Rovira i Virgili, avenida Països Catalans 26, 43007 Tarragona, Spain.

[2] Department of Solid-State Physics, Jozef Stefan Institute, Jamova cesta 39, 1000 Ljubljana, Slovenia.

[3] Laboratory of Plasma-Surface Interaction Chemistry (PSI Chem), University of Mons, Av. Nicolas Copernic 1, 7000 Mons, Belgium.

Corresponding author

*Fatima Ezahra Annanouch: fatimaezahra.annanouch@urv.cat

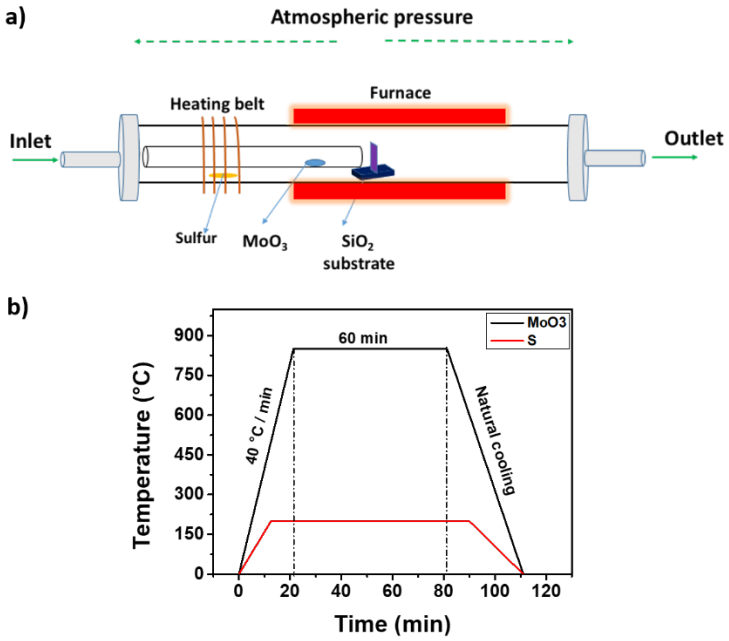

Fig.S1. (a) APCVD synthesis setup and (b) MoS_2 growth temperature profile.

Edge enriched 3D assembly of MoS_2 nanosheets based sensor was fabricated in our lab by connecting two platinum wires to the substrate using silver paste as depicted in Fig.S2. besides to this, a Platinum resistive heater was pasted on its backside in order to provide the temperature when needed. Finally, the hole sensor was wire-banded to a PCB.

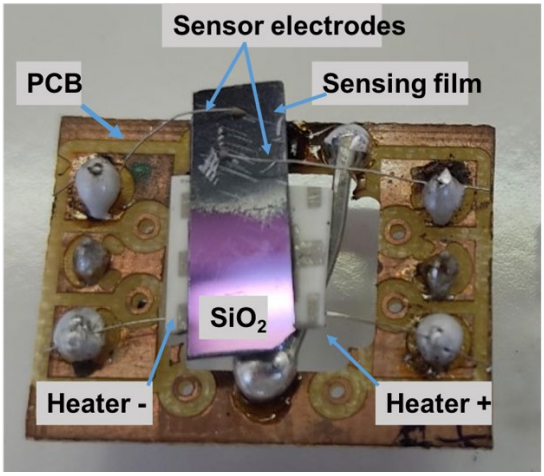

Fig.S2. Sensor photograph.

FESEM images of sample obtained at 10 ml /min of argon gas. As we can see, we have a dispersed nanotriangles over the substrate.

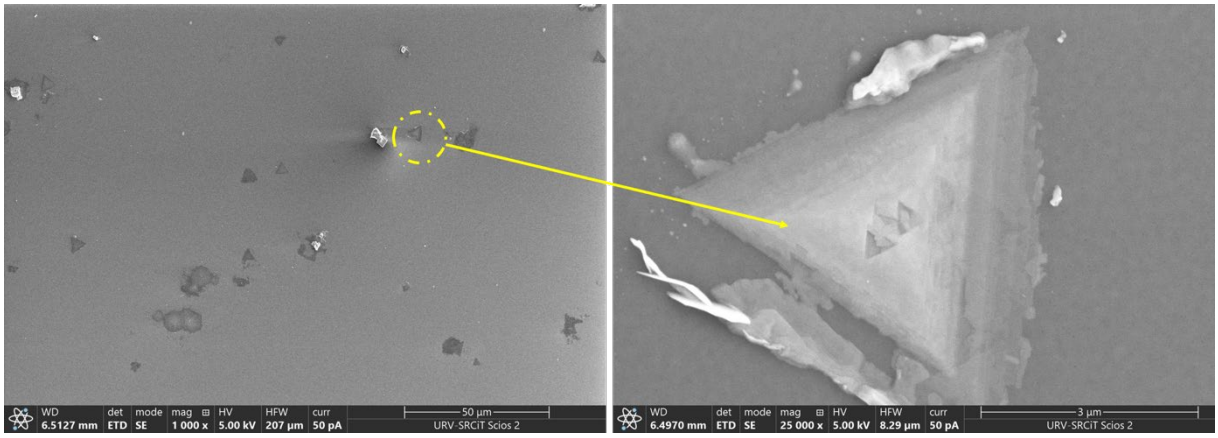

Fig.S3. FESEM images of MoS_2-10 sample.

FESEM images of sample obtained at 30 ml /min of argon gas. As we can see, we have thick layer of edge enriched 3D assemblies MoS2 nanosheets over the substrate.

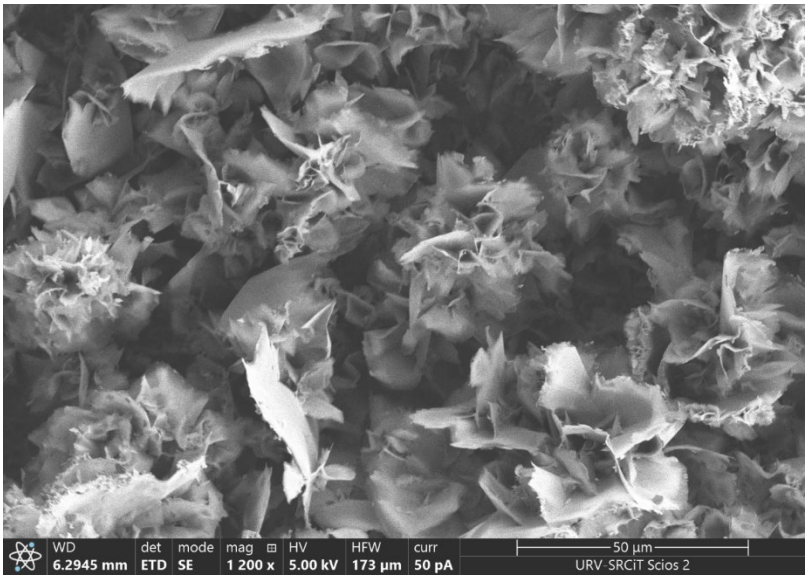

Fig.S4. FESEM images of MoS_2-30 sample.

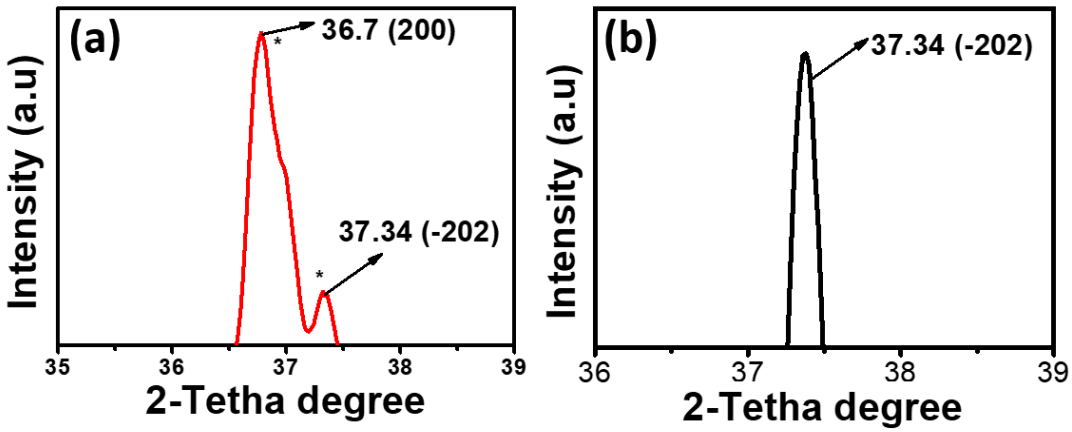

Fig.S5. Enlarged XRD peaks recorded between 36 º and 38º from MoS_2-30 and MoS_2-70 films.

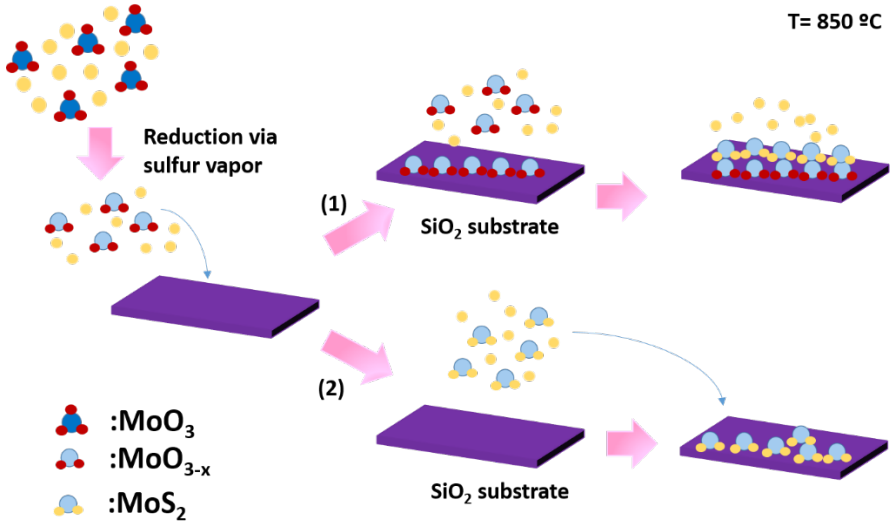

Fig.S6. growth mechanism of edge enriched 3D assembly of MoS_2 nanosheets.

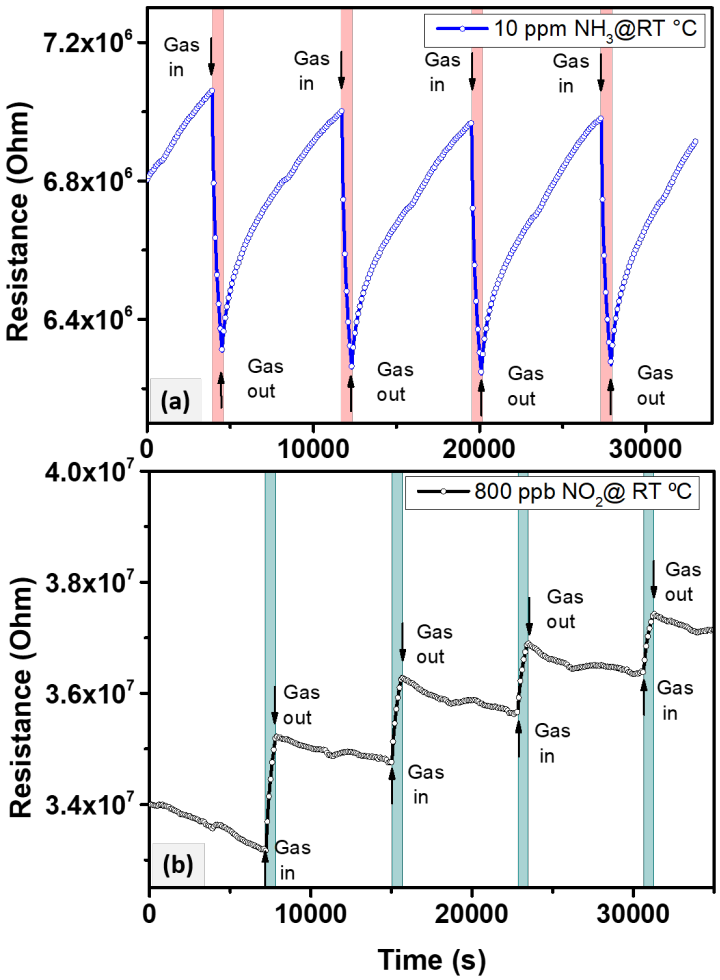

Fig.S7. sensor resistance changes as a function of time against (a) 10 ppm of NH_3 and (b) 800 ppb of NO_2, at room temperature.

Annex II
Publication List

Publications directly related with the thesis

1. **Aanchal Alagh**, Fatima Ezahra Annanouch, Polona Umek, Carla Bittencourt, AyrtonSierra-Castillo, Emile Haye, Jean François Colomer, Eduard Llobet, "CVD growth of self-assembled 2D and 1D WS_2 nanomaterials for the ultrasensitive detection of NO_2", **Sensors and Actuators B: Chemical,** vol. 326 (2021), 128813.doi: 1016/j.snb.2020.128813

2. **Aanchal Alagh**, Fatima EzahraAnnanouch, Polona Umek, Carla Bittencourt, Jean François Colomer, Eduard Llobet, "An ultrasensitive room-temperature H_2S gas sensor based on 3D assembly of Cu_2O decorated WS_2 nanomaterial," **IEEE Sensors Journal.** doi: 10.1109/JSEN.2021.3103925

3. **Aanchal Alagh**, Fatima Ezahra Annanouch, Polona Umek, Carla Bittencourt, AyrtonSierra-Castillo, Emile Haye, Jean François Colomer, Eduard Llobet, "PdO and PtO loaded WS_2 boosts NO_2 gas sensing characteristics at room temperature", **Sensors and Actuators B: Chemical,** vol. 364 (2022), 131905. doi: 10.1016/j.snb.2022.131905

Publications directly related with the thesis

1. Ernesto González, Juan Casanova-Chafer, **Aanchal Alagh**, Alfonso Romero, Xavier Vilanova, Selene Acosta, Damien Cossement, Carla Bittencourt and Eduard Llobet, "On the use of pulsed UV or Visible Light Activated Gas Sensing of Reducing and Oxidising Species with WO_3 and WS_2 Nanomaterials,"**Sensors,** vol. 21 **(**2021). doi: 10.3390/s21113736

Publications submitted for publication or in preparation

1. Fatima Ezahra Annanouch, **Aanchal Alagh**, Polona Umek, Juan Casanova, Carla Bittencourt, Eduard Llobet, "Controlled Growth of 3D Assemblies of Edge Enriched Multilayer MoS_2 Nanosheets for dually selective NH_3 and NO_2 gas sensors," **Under Revision** in **Journal of Materials Chemistry C.**

2. **Aanchal Alagh**, Fatima Ezahra Annanouch, Ayrton Sierra-Castillo, Emile Haye, Jean François Colomer, Eduard Llobet, "A robust gas sensor with bifunctional sensitivity and reliable anti-humidity ability based on WSe_2 nanoflower," **Under Revision.**

Publication in Proceeding (s):

1. **Aanchal Alagh**, Fatima Ezahra Annanouch, Eduard Llobet "Enhanced gas sensing characteristics of metal doped WS2 nanoflowers," **IEEE Xplore, 2021 International Conference on Sensors, IEEE**, Sydney, Australia. [Scopus]. doi:

10.1109/SENSORS47087.2021.9639580.

2. **Aanchal Alagh**, Fatima Ezahra Annanouch, Eduard Llobet "Single-step CVD synthesis of layered WS_2 films for NO_2 gas sensing," **IEEE Xplore, 2019 International Conference on Sensors, IEEE**, Montreal, Canada. 8956602 [Scopus]. doi:10.1109/SENSORS43011.2019.8956602

3. **Aanchal Alagh**, Fatima Ezahra Annanouch, Jean François Colomer, Eduard Llobet " 3D assembly of WS_2 nanomaterial for H_2S gas sensing application" **IEEE Xplore, 2020 International Conference on Sensors, IEEE**, Rotterdam, Netherlands. 165760 [Scopus].

Doi: 10.1109/SENSORS47125.2020.92787

Book Chapter (s)

1. Fatima Ezahra Annanouch, Juan Casanova-Chafer**, Aanchal Alagh**, Miriam Alvarado, Ernesto Gonzalez, Eduard Llobet. Nanosensors for Food Logistics. Nanosensors for Smart Agriculture. 1st ed., Elsevier; 2021.

Annex III

Contribution to conferences

- **Oral Presentation** on TMDs nanomaterials-based Gas Sensors, in Department of Chemistry, University of California, California, USA, 18th January 2022.

- **Oral presentation** on "2020 Enhanced Gas sensing characteristics of metal doped WS2 nanoflowers", in IEEE Sensors 2021 Virtual (Sydney, Australia 2021), 2 November 2021.
  Link: https://www.youtube.com/watch?v=TWHlHSCHg3U.

- **Invited talk** on "Transition metal dichalcogenide materials for gas sensing applications", in 16th International conference on Optical and Electronic Sensors COE 2020 (COE 2020), September 2020 (Remotely).

- **Oral presentation** on "3D assembly of WS_2 nanomaterial for H_2S gas sensing application", in IEEE Sensors 2020 Virtual (Rotterdam, Netherlands 2020), 25-28 October 2020.
  Link: https://www.youtube.com/watch?v=6Mp4nsgpkCs&ab_channel=IEEESensors

- **Poster presentation** on "Influence of morphology on gas sensing properties of WS_2) at 2020 Global Mosharaka Congress on Electrical Engineering (GMC-ElecEng 2020), Valencia, Spain, September 2020 (Remotely).

- **Poster presentation** on "Single-step CVD synthesis of layered WS_2 films for NO_2 gas sensing", in IEEE Sensors Congress held in Montreal, Canada, Oct 2019.

- **Poster presentation** in Joint training school-Chemical Sensors, Biosensors & Biochips: Sete, France, September 2019.

- **Poster presentation** on "CVD growth of two-dimensional semiconducting transition metal dichalcogenides for Gas sensing applications" in in Nanosen-AQM, workshop on Low-cost Sensors and Microsystems for Environment: Toulouse, France, May 2019.